ISSN 0911-5730
UVSOR-27
April 2000

UVSOR

ACTIVITY REPORT

1999

Ultraviolet Synchrotron Orbital Radiation Facility
Institute for Molecular Science

CONTENTS

Gas-phase spectorscopy

Solid state spectroscopy 1 (IR, VUV, etc)

Solid state spectroscopy 2 (XAFS, PES)

Surface & photochemistry

UVSOR

ACTIVITY REPORT

1999

edited by
E. Shigemasa, T. Gejo, M. Hosaka, H. Hagiwara

Preface

This Activity Report covers the research activities done by over 800 users from about 60 institutions at the UVSOR facility in 1999. This is the sixth volume in the red-covered Activity Report series for the second 10 years in UVSOR, where the first SR was emitted in November 1983. The improvement and upgrade projects of monochromators and end stations are under way. Unfortunately, since 1998 we have lost 15% of the total budget for the UVSOR facility. This budget cut policy has been applied to all the facilities under the Ministry of Education, Science, Sports and Culture (Monbusho). We have to reduce the beamtime and postpone the upgrade and the UVSOR-2 projects. Now we will try to get a special budget for the upgrade of the light source of UVSOR for the third 10 years. We hope that we can start the upgrade project in 2001.

For these six years, several UVSOR staff members were changed in spite of the small number, that is, three associate professors and four research associates. In the beamline division there are only two associate professors and two research associates. In FY99 one associate professor and one research associate were changed. After Associate Prof. Toyohiko Kinoshita moved to the University of Tokyo in November 1998, we had Dr. Eiji Shigemasa as a new associate professor from the Photon Factory in May 1999. He is in charge of science for free molecules. In November 1999 Dr. Shin-ichiro Tanaka was promoted to an associate professor of Nagoya University. In April 2000 Dr. Kazutoshi Takahashi will come as a new research associate from Tohoku University. On the other hand, in the light source division there are only one associate professor and two research associates. The machine group is indispensable to maintain and upgrade the UVSOR facility and realize the UVSOR-2 project. In September 1999 we lost Associate Prof. Hiroyuki Hama, who was in charge of the UVSOR-FEL(free electron laser) and UVSOR-2 projects but moved to Tohoku University. Fortunately, in March 2000 we can have Dr. Masahiro Kato as a new associate professor, He was in charge of the upgrade of Photon Factory, and now is in charge of the upgrade of UVSOR to get lower emittance, more straight sections and sophisticated insertion devices. Furthermore, we will try to augment a full professor position in the light source division to assure to the users the best light source for a long term.

March, 2000

Nobuhiro Kosugi
Director of UVSOR

Current Status of Light Source and Beam Lines

The UVSOR Accelerator Complex in 1999

Hiroyuki HAMA, Masahito HOSAKA, Shigeru KOUDA, Jun-Ichiro YAMAZAKI, Toshio KINOSHITA

UVSOR Facility, Institute for Molecular Science, Okazaki 444 Japan

1. General

Monthly statistics of the light source operation of the year 1999 are shown in Fig 1. These a couple of years we regularly have 4 shut-off terms for machine maintenance. In 1999, there were the new year shut-off (2-week), the spring term shut-off (4-week), the summer shut-off (4-week) and the fall term shut-off (2-week). Consequently the machine was totally operated for about 240 days (including test operations), and the integrated operation time reached approximately 2700 hours. In the spring shut-off term, pulsars for kicker magnets on the storage ring were replaced by new ones which employed IGBT switchings, and a new controller for charge and discharge of those pulsars was installed. Fall time of the bump orbit for the beam injection was reduced to 1 μs, so that the injection efficiency was improved. To avoid effects of ion-trapping, we have employed a partial filling operation so far. Number of filled buckets was further reduced to 11 from 12 after investigations during the shut-off. In addition to ordinary maintenance of accelerator devices, a klystron of the injector LINAC was replaced by new one in the summer shut-off term.

There was fortunately no serious trouble in the whole year. However the superconducting 4 T wiggler, which had been operated from December, 1998, was completely stopped in the beginning of June because of a fatal malfunction of the refrigerators. We have not decided yet whether the wiggler should be further operated. The wiggler system seemed to be replaced for stable operation, which means an extra budget is required. Continuation of the wiggler operation should be concluded from a view of scientific opportunities, so that a possibility of development of other insertion devices is expected to be considered in the discussion.

Another minor trouble was occurred on the RF

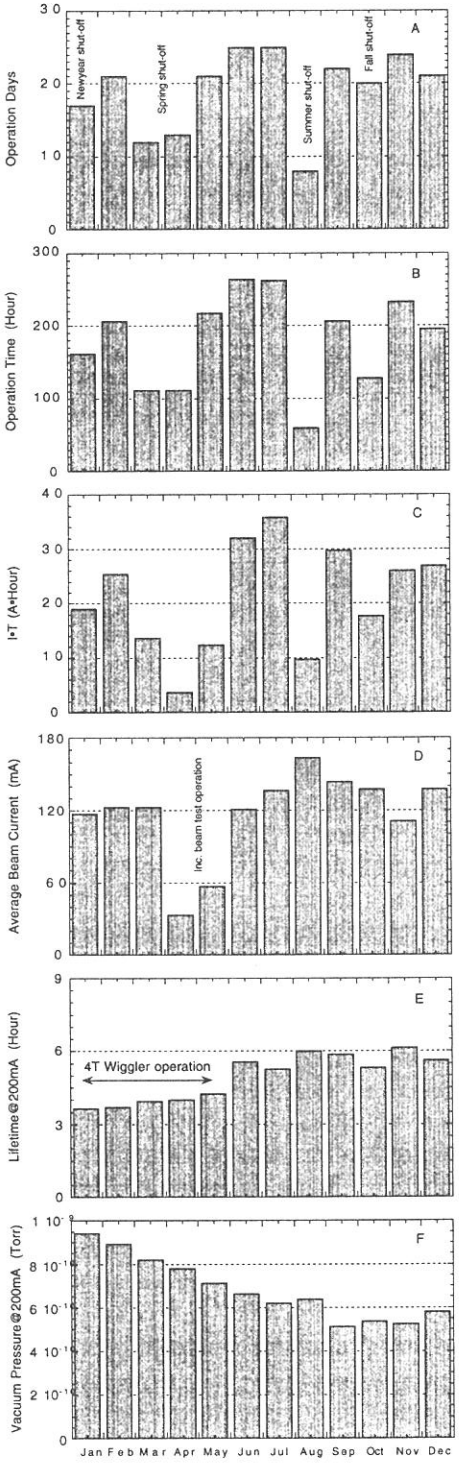

Fig. 1 Monthly statistics of the UVSOR light source in 1999. (A)The total operation days accumulated each month. (B)The total operation time. (C) The integrated beam current. (D) The averaged beam current. (E)The averaged beam lifetime at the multi-bunch beam current of 200 mA. (F)The averaged ring vacuum pressure at the multi-bunch beam current of 200 mA.

system of the storage ring, which was exposed in November. Reflected power from the main cavity has been increased, and then the RF power amplifier was frequently down because of safety. It was finally found that a circulator, which guides the reflected power into a water load, was malfunction. New one will be installed in March, 2000. By setting a tuning angle of the cavity small, the reflected power was reduced to be lower than a threshold power of the interlock system of the power amplifier in the ordinary multi-bunch operation.

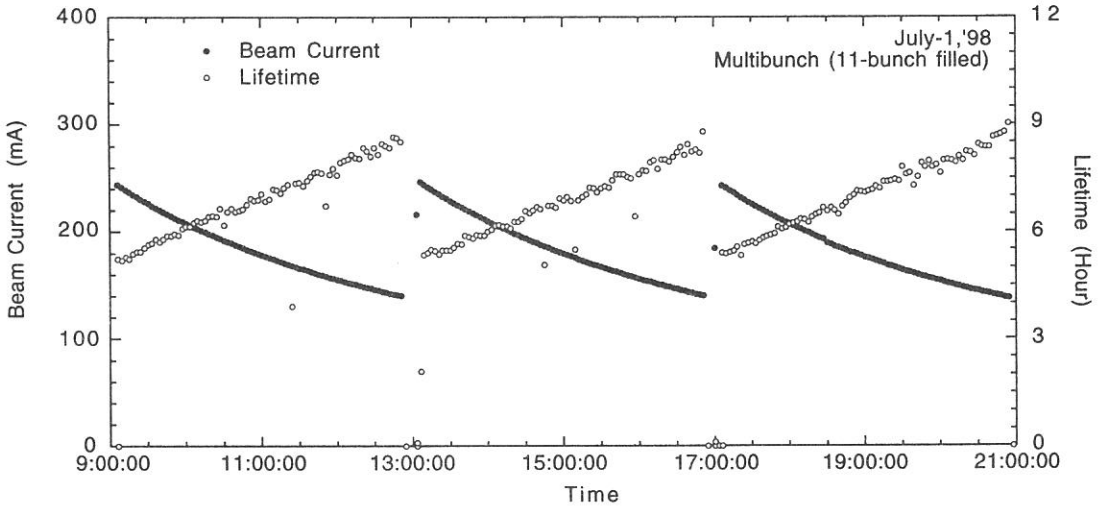

Fig. 2 Variations of the beam current and the lifetime in one-day operation with the multi-bunch mode (July-1, 1999).

Generally speaking, the operation of the UVSOR accelerators in 1999 was pretty stable and successful.

2. Improvement

As mentioned above, the kicker pulsars and the power supplier on the storage ring were replaced by new ones. In the injection scheme of the UVSOR accelerator system, 4-bunch train is extracted from the booster synchrotron. Because the flatness of the fast kicker pulse on the booster is imperfect, the overall horizontal emittance of the bunch train is very large. In order to obtain better injection efficiency, the fall time of the bump orbit of the ring should be fast to avoid beam loss at the septum after the first turn. By adjusting capacitance of the IGBT pulsar, the fall time of ~ 1 μs was achieved (former value was ~ 1.5 μs), so that the beam injection rate was improved to be 2 ~ 3 mA/s from 1 ~ 2 mA/s.

After the spring shut-off term, the beam orbit has been corrected after each beam injection. An on-line software for calculation of linear lattice parameters including effects of insertion devices was completed. This software was linked with an application for steering magnets control to change the beam orbit as one likes. Averaged rms orbit deviations in the horizontal and the vertical directions have been kept within ~ 50 μm and ~ 80 μm, respectively, in the user machine times.

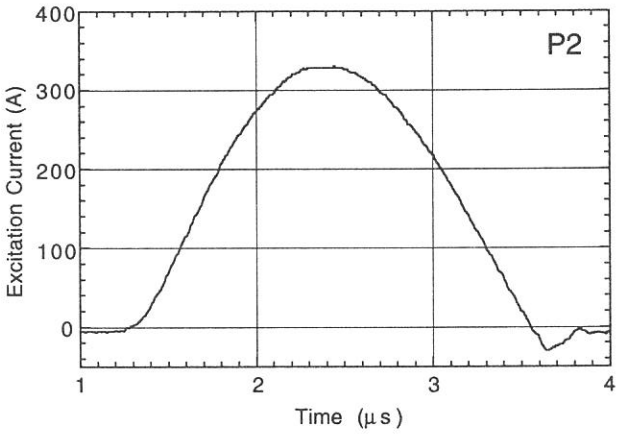

Fig. 3 Pulse shape of discharge current of a new IGBT pulsar for a kicker magnet.

ACCELERATOR COMPLEX

Injection Linac

Energy	15 MeV
Energy Spread	~ 1.6 MeV
Frequency	S-band 2856 MHz
Acceleration	2π/3 Traveling Wave
Length	2.5 m
Klystron Power	1.8 MW
Repetition Rate	2.6 Hz

Booster Synchrotron

Lattice Type	FODO
Energy	600 MeV
Beam Current	32 mA (8-bunch filled)
Circumference	26.6 m
Super Cell	6
Bending Radius	1.8 m
Betatron Tune	2.25 (horizontal)
	1.25 (vertical)
Momentum Compaction	0.138
Harmonics	8
RF Frequency	90.115 MHz
Repetition Rate	2.6 Hz

Storage Ring

Lattice Type	Chasman-Green
Energy	750 MeV
Critical Energy	425 eV
Super Cell	4
Bending Radius	2.2 m
Betatron Tune	3.16 (horizontal)
	1.43 (vertical)
Momentum Compaction	0.0264
Emittance	164 nm rad (horizontal)
RF Frequency	90.115 MHz
Harmonics	16
Beam Current	Multi-Bunch 200 mA
	Single-Bunch 70 mA
Life Time	4 h at 200 mA

Additional Equipment

Higher-Harmonic Cavity	3 x 90.115 MHz
Super-conducting Wiggler	4 T (maximum)
Undulator	for SR
Helical Optical Klystron	for Free Electron Laser

Control System

Preface: Based on Dual-Host system with CAMAC loop and friendly man-machine interface

Architecture

CPU	VAX4000 x 2
OS	VMS
Connection	DECNET & Local Cluster
Operating Console	X-servers
Interfaces	CAMAC serial loop
	GPIB
	RS232C
Languages	FORTRAN, C, PASCAL

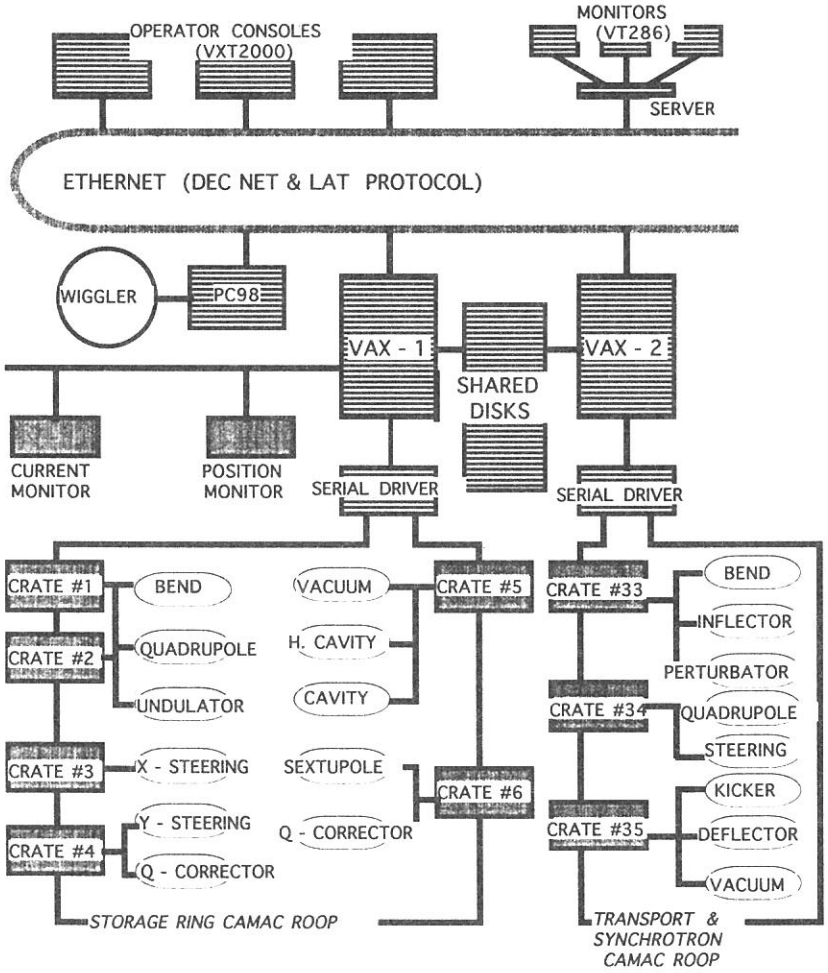

Scheme of Accelerator Control System "UCOSS"

Beam Lines in 1999

Masao KAMADA
UVSOR Facility, Institute for Molecular Science

There are 20 beam lines operational in UVSOR facility, 11 beam lines of which are opened beam lines for many users coming from outside of IMS, while the rest 9 beam lines are in-house beam lines dedicated to the research groups in IMS. The followings are the status of the beam lines in 1999.

<Open beam lines>

○BL1B

This beam line is one of the busiest beam line in UVSOR. The beam line has been used for general purposes in VUV region and has welcome many users all the time since the beam line has the following advantages. 1) It has large acceptance angles to provide high flux VUV light. 2) Standard measurements such as absorption, reflection, and luminescence can be conducted at low temperatures down to 10 K. 3) This beam line covers the wavelength ranges from 650 to 30 nm, which overlaps with those of the usual light sources in users' institute or university. 4) Since windows are available in the wavelength more than 110 nm, beginners can start their experiments by themselves without feeling any restriction. 5) The window makes possible for us to try many materials such as liquid, high-pressure, gaseous phase, high-vapor-pressure, bio-specimens, and so on. 6) Only usual vacuum techniques are required to conduct their experiments. 7) There is no similar beam line in other facilities in Japan.

In 1999, the computer control system of a 1-m Seya-Namioka monochromator has been renewed. The old control system consisted of motor drivers, encoder, limits, and a computer was replaced completely by the new system. The new system consists of components which can be supplied on commercial base. This improvement may make us easy for maintenance. The gratings were also exchanged by new ones. We installed two G3 and one G1 grating because of usefulness of the G3 grating in VUV region. The upgrade of a second-monochromator system will be done in 2000. We expect that this beam line can be used continuously in VUV region.

○BL2B1

This beam line consists of a grasshopper monochromator, a double-pass CMA, and coincidence analyzer. This beam line has been used mainly for surface science because useful equipment for surface science such as LEED, Auger, Ar-ion gun, and gas doser are installed at BL2B1. This beam line covers soft x-ray regions up to 800 eV and therefore useful for core level spectroscopy for C, N, and O elements. Photoelectron spectroscopy and electron-ion-coincidence spectroscopy can be carried out on adsorbed surface and bulk materials. Besides these spectroscopies, NEXAFS/XAFS are also powerful techniques for molecular science.

In 1999, a new version of an electron-ion-coincidence instrument has been installed, resulting in better efficiency in collecting data. An analyzing chamber for the experiments in UHV was also improved in order to install many apparatuses for surface science. Moreover, pre-mirror M2 was renewed and the trouble in driving mechanism of a Grasshopper monochromator was fixed, but not completely.

The performance of the monochromator is not good in comparison with similar beam lines in other facilities. This indicates that we must find our own idea such as an EICO method all the time in order to keep the activity of this beam line. We expect users' collaboration and proposal for future.

We would like to express our thanks to Prof. S. Nagaoka for his collaboration to maintain the activity of this beam line.

○BL3A1/BL3A2

These beam lines can share intense synchrotron radiation from a planar-type undulator. At BL3A1 the intense undulator radiation has been used without monochromator for SR-CVD, light-amplification, desorption, and luminescence experiments. At BL3A2, a constant-length SGM has been used with the undulator radiation for SR-laser combined experiments in gaseous phase.

In 1999, usual maintenance for vacuum systems has been done to keep activities at BL3A1/3A2. Besides this, the renewal program of the CL-SGM driving system at BL3A2 and also the improvement of the second-monochromators at BL3A1 have started. We have started thinking about a future plan of this beam line for coming century. Everybody having ideas and opinions is welcome.

○BL5A

This beam line consists of a high-resolution photoelectron spectrometer and a spin and angle resolved photoelectron spectrometer. Besides SR from a dipole magnet, circularly polarized radiation from a helical undulator can be used at BL5A.

In 1999, the mechanism of the pre-mirror VM for SGM-TRAIN monochromator was improved. This could solve the interference of the user experiments with the FEL studies. The powerful laser system consisting of a TiS laser, RegA, and OPA was also installed for user experiments.

○BL5B

This beam line was constructed for calibration of many optical elements and detectors in VUV and soft x-ray regions. Since there are no similar beam lines in other facilities, BL5B has been contributing to the various fields such as astro-science, nano-science, besides synchrotron science and technology.

In recent years, the mechanical and optical components were repaired. The program was also renewed from old digital controller to the computer control system. However, there are several points which should be improved to keep the performance of this beam line.

○BL6A1

The BL6A1 has been used as a unique IR and FIR beam line. It consists of FT-IR and FT-FIR interferometers and covers wide wavelength range from sub-milli to near IR. Lots of research studies such as high-pressure with DAC, magnetic circular Dichroism, and time-dependence have been carried out.

In 1999, the new Labview system for FT-FIR was commissioned. Many detectors and beam splitters are always maintained to keep the activity of this beam line. Another IR beam line is now under construction at Spring-8. This means not only many needs for IR beam lines with SR, but also the necessity and the possibility for the improvement of BL6A1. We started to discuss the improvement of this old but still powerful/useful beam line.

○BL7A

This beam line was constructed at the first construction stage of the UVSOR facility in mid of 1980 for soft x-ray spectroscopy. This beam line has been providing soft x-rays in the energy range from 0.6 to 3 keV without the 4T-wiggler and up to 6 keV with the wiggler. However, the mechanical problem happened on the cryogenics for the wiggler in 1998. In 1999, the 4T-wiggler was shutdown completely. We have decided to provide better SR from a dipole magnet with good crystals such as beryl, YB66, InSb, KTP, and alumna to cover the soft x-ray region less than 3 keV one hand, and to think deeply about the future of the wiggler and the BL7A with active users on the other hand.

○BL7B

The 3-m NIM at BL7B was constructed to provide good SR with a high resolving power in a wide wavelength range from near IR to VUV. Although the installation took long times,

users have started taking good data at He temperature and showed the good performance of BL7B in 1999. Few points still remain to fix and may be completely established in 2000.

We would like to express our thanks to working group, especially Profs. K. Fukui, K. Nakagawa, T. Kinoshita, and Dr. E. Okamura, for their efforts to construct this beam line.

○BL8A

This beam line has no monochromator and any special equipment. This means that users can install their own instruments which are brought from their institute or university. The UVSOR facility will support the users of course. For examples, a differential pump system can be provided for SR-CVD experiments. In 1999, the vacuum condition of the pre-mirror chamber and the differential pump system were improved.

○BL8B1

This beam line can provide soft x-rays with a high resolving power and cover the energy range of K-shell excitation in light elements. The TOF-mass instrument makes it possible to take ionization spectra of various molecules. Yield experiments on solid state phase are also available. In 1999, the alignment of the CL-SGM monochromator was improved to provide good linear polarization, which was monitored by a multi-layer polarizer

<In-house beam lines>

○BL1A

This beam line was constructed for solid state experiments in soft x-ray region. High performance photoelectron analyzer produces good data in recent years.

○BL2A

This beam line was constructed for experiments in gaseous phase and have produced a lots of scientific results. This beam line is now going to bio-science use under collaboration with bio-scientists in Okazaki institutes. Many apparatuses for experiments in gaseous phase have been removed in 1999. We would like to express our sincere thanks to all 2A users and active SR persons for their lots of efforts to construct this beam line and to keep activity of BL2A. We never forget the memorial fact that the first scientific data with using UVSOR had been obtained at 2A. We are also expecting many active bio-scientists who want to use UVSOR.

○BL2B2

The construction of a dragon-type new monochromator has commissioned in 1999. The good performance of a high resolving power will contribute experiments in gaseous phase soon.

○BL3B

This beam line consists of 3-m NIM and two-dimensional photoelectron analyzer. This has been used for experiments in gaseous phase. In 1999, the vacuum leakage happened into the monochromator and pre-mirror chamber, but fortunately the interlock system could protect the storage ring from the accident.

○BL4A/4B and BL6B

The re-arrangement of the beam lines at BL4A , 4B, and 6B has started in 1999. The SR-CVD instruments installed at 4B will move to BL4A, and the SR-STM system at BL4B will move to BL6B, since the IR station at BL6B was completely shutdown and the construction of a new soft x-ray beam line at BL4B was proposed.

○BL6A2

The optical elements including gratings and the control system were completely replaced by new ones in 1999. The micro-ESCA system will be installed to this beam line soon.

○BL8B2
The high-performance multi-channel photoelectron spectrometer is under installation. This is powerful for the angle-resolved photoelectron spectroscopy to investigate the relation of molecular orientation on the surface and the electronic states

Therefore, the UVSOR facility will have twenty stations operational; two soft-x-ray stations equipped with a double-crystal monochromator, nine extreme ultraviolet stations with a glancing incidence or a plane-grating monochromator, four vacuum-ultraviolet stations with a Seya-Namioka-type or a normal incidence-type monochromator, one (far) infrared station equipped with a FT interferometer, a multi-layer monochromator, and three white-light stations without any monochromator. In 1999, many and interesting results were obtained at UVSOR beam lines and they are presented in this activity report.

The UVSOR facility strongly asks all users to conduct their experimental procedures according to the beam line manuals and the guidebook. The persons who want to use the open and the in-house beam lines are recommended to contact with the following station master or supervisor and the representative, respectively. The persons who want to know updated information of the UVSOR facility are recommended to open http://www.uvsor.ims.ac.jp/.

Table I. Station masters and supervisors of open beam lines in 1999

Beam Line	Station Master	Sub Master	Supervisor
1B	M. Hasumoto	M. Kamada	M. Kamada
2B1	E. Nakamura	S. Nagaoka	M. Kamada
3A1	M. Kamada	E. Nakamura	M. Kamada
3A2	N. Kondo	T. Gejo	E. Shigemasa
5A	M. Hasumoto	M. Kamada	M. Kamada
5B	M. Hasumoto	E. Nakamura	E. Shigemasa
6A1	E. Nakamura	O. Matsudo	M. Kamada
7A	E. Shigemasa	N. Kondo	T. Kinoshita
7B	K. Fukui	M. Hasumoto	M. Kamada
8A	T. Gejo	E. Nakamura	E. Shigemasa
8B1	T. Gejo	N. Kondo	E. Shigemasa

Table II. Representatives of in-house beam lines in 1999.

Beam Line	Representative	Department/Facility
1A	N. Kosugi	VUV Photo Science
2A	N. Kosugi	VUV Photo Science
2B2	K. Mitsuke	VUV Photo Science
3B	K. Mitsuke	VUV Photo Science
4A	T. Urisu	VUV Photo Science
*4B	T. Urisu	VUV Photo Science
6A2	M. Kamada	UVSOR
*6B	K. Yakushi	Molecular Assemblies
8B2	T. Urisu	VUV Photo Science

*The new representatives of BL4B and 6B in 2000 are Profs. E. Shigemasa (UVSOR) and T. Urisu (VUV Photo Science), respectively.

Beam line of UVSOR

Beam Line	Monochromator, Spectrometer	Wavelength Region	Acceptance Angle(mrad) Horiz.	Vert.	Experiment
BL1A	Double Crystal	2.1 - 0.3 nm	4	1	Solid (photoemission)
BL1B	1-m Seya-Namioka	650 - 30 nm	60	6	Solid (absorption)
BL2A	1-m Seya-Namioka	400 - 30 nm	40	6	photoabsorption
BL2B1	2-m Grasshopper	60 - 1.5 nm	10	1.7	Solif & surface (photoemisson)
BL2B2	18-m Spherical Grating	60 - 6 nm	15	6	Gas (photoionization, photodissociation)
BL3A1	None (Filter, Mirror)	(U)	0.3	0.3	Solid & irradiation (photodissociation)
BL3A2	2.2-mConstant Deviation Grazing Incidence	100 - 10 nm	10	4	Gas & solid
		(U)	0.3	0.3	(photoionization & photodissociation)
BL3B	3-m Normal Incidence	400 - 30 nm	20	6	Gas (photoemission)
BL4A1	Multi-Layered-Mirror Monochromator	13 - 23 nm Mo/Si MLMs	16.6	12.8	Irradiation
BL4B	None		8.3	6	Irradiation
BL5A	None	(OK)			FEL
	SGM-TRAIN	250 - 5 nm	10	3	Solid (photoemission)
BL5B	Plane Grating	200 - 2 nm	10	2.2	Calibration, gas (photodissociation) & solid (absorption)
BL6A1	Martin-Puplett FT-IR	3000 - 30 mm	80	60	Solid (absorption)
	Michelson FT-IR	100 - 1 mm	80	60	
BL6A2	Plane Grating	650 - 8 nm	10	6	Solid & surface (photoemission)
BL6B	FT-IR	200 - 1.7 mm	70	25	Solid (absorption)
BL7A	Double Crystal	1.5 - 0.8 nm	2	0.3	Solid (absorption)
		1.5 - 0.2 nm (W)	1	0.15	
BL7B	3-m Normal Incidence	1000 - 50 nm	65	10	Solid (absorption)
BL8A	None (Filter)		25	8	Irradiation & user's Instrum.
BL8B1	15-m Constant Deviation Grazing Incidence	40 - 2 nm	10	1.5	Gas & solid (absorption)
BL8B2	Plane Grating	650 - 8 nm	10	6	Solid (photoemission)

SGM-TRAIN: spherical grating monochromator with translating and rotating assembly including normal incidence mount

U: with an undulator

W: with a wiggler

OK: with an optical klystron

BL1A

Soft X-Ray Beamline for Photoelectron-Photoabsorption Spectroscopy

BL1A is a soft x-ray beamline for photoelectron-photoabsorption spectroscopy. The beamline is equipped with a focusing premirror and a double crystal monochromator [1]. The monochromator serves soft x-rays in the energy range from 585 to 4000 eV by using several kind of crystals such as β-Al_2O_3, beryl, KTP ($KTiOPO_4$), quartz, InSb and Si crystals. The throughput spectra are shown in Fig. 1. Typical energy resolution ($E/\Delta E$) of the monochromator is about 1500 for beryl and IbSb.

For photoelectron-photoabsorption spectroscopy, an ultra-high-vacuum (UHV) apparatus is connected. The top view of the apparatus is shown in Fig. 2. It is equipped with a high-performance electron energy analyzer (SES-200, SCIENTA Co.). The pass energy can be varied between 1 and 500 eV. Using the apparatus, resonant photoelectron spectra for solid samples can be obtained with the total energy resolution of 0.7eV around hv=1000 eV.

Reference

[1] A. Hiraya et al., Rev. Sci. Instrum., **63** (1992) 1264.

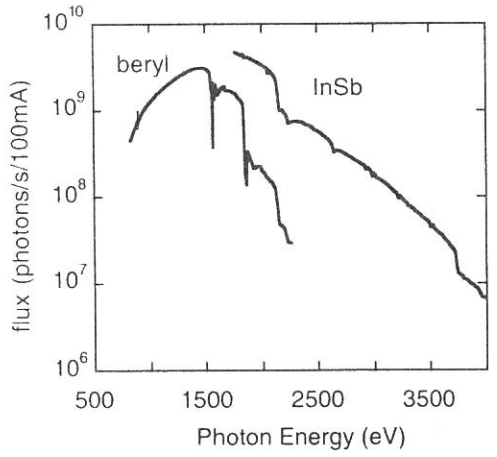

Figure 1. Throughput spectra of the double crystal monochromoator at BL1A.

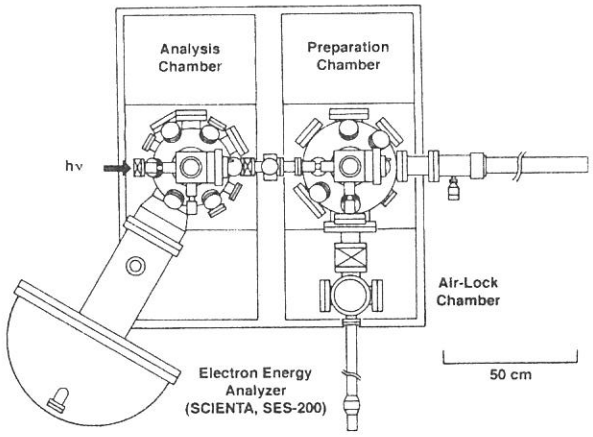

Figure 2. Top view of the UHV apparatus for photoelectron-photoabsorption spectroscopy.

Specification

Monochromator	: double crystal monochromator
Monochromator crystals (2d value, energy range)	: β-Al_2O_3 (22.53Å, 585-1609eV), beryl (15.965Å, 826-2271eV), KTP (10.95Å, 1205-3310eV), quartz (8.512Å, 1550-4000eV), InSb (7.481Å, 1764-4000eV), Si (6.271Å, 2104-4000eV)
Resolution	: $E/\Delta E$=1500 for beryl and InSb
Experiment	: photoelectron-photoabsorption spectroscopy for solid

BL1B

Seya-Namioka Monochromator for General Purpose in VUV Region

The beam line 1B has been used for many experiments such as absorption, reflectivity, photo-ionization, and luminescence in condensed phase. The system consists of a pre-mirror, a 1-m Seya-Namioka type monochromator, and a post-mirror. Three gratings with 600, 1200, and 2400 gr/mm can cover the wavelength range from 40 nm to 650 nm, and two post mirror make it possible to change the focus point. A long-focus mirror is usually used with a LiF window to separate a main chamber for spectroscopy in liquids and biospecimens, while a short-focus mirror is suited to solid-state spectroscopy. The output flux from this monochromator is about 10^{10} phs/s around 200 nm with 0.1 mm slits. The spectral distributions obtained with three gratings are shown in the figure, although they are not the best data because of the contamination of the mirrors and gratings due to the recent careless accident.

A second monochromator (Spex 270M) and a LN-cooled CCD detector (Princeton Inc.) are available for luminescence experiments, together with a liquid helium-flow type cryostat. A time-resolved system to observe luminescence and excitation spectra with three time-gates is also possible. The decay measurement is one of the highlights of this station. A couple of weeks are supplied for the decay measurements under single bunch operation. A TAC system is therefore one of the standard instruments at this beam line.

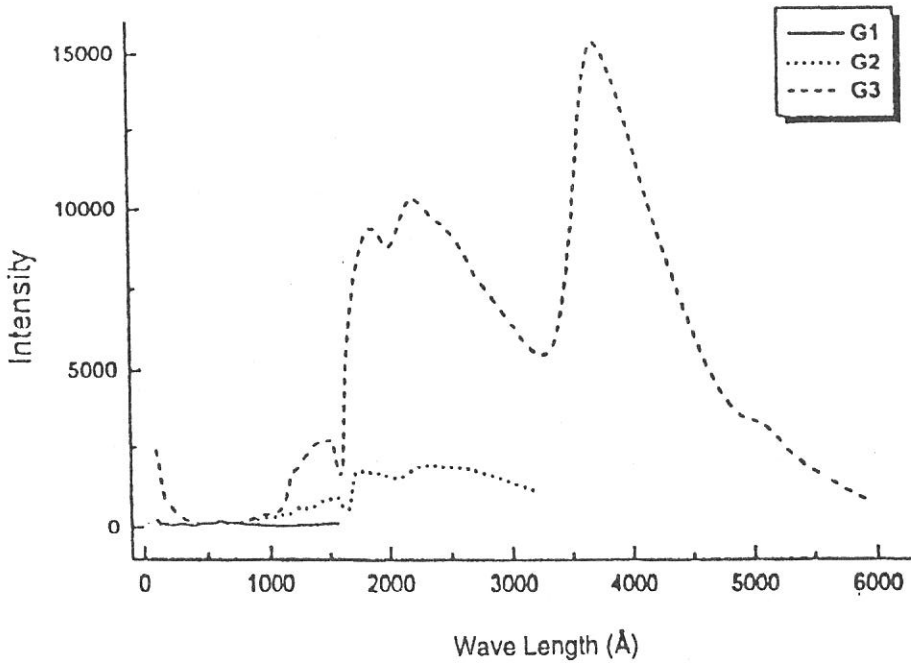

BL2A

Gas Phase Photoabsorption and Fluorescence Spectroscopy

Photoabsorption cross section and fluorescence excitation spectra of gaseous sample are simultaneously measured in a vacuum cell or effusive jet condition. The primary photons in the 30-400 nm region are dispersed by a 1-m Seya monochromator. Higher order light in the 80-120 nm range is suppressed by using a long channel with a cross section 2.5 × 5.0 × 170 mm long filled with argon gas at a pressure ≅0.3 Torr as shown in fig. 1. No filter is used between 30 and 80 nm since the photon flux at $\lambda<40$ nm is very weak (see fig. 1). The gas filter and cell are placed in a main chamber which is evacuated by a 5000 *l*/s diffusion pump (Varian, Model VHS10). A LiF window is used for the measurement at the $105<\lambda<210$ nm range as usual. Thus, the total photoabsorption cross section and fluorescence excitation spectra are available in the wide wavelength region 30-210 nm without or with little contamination by the higher order light.

Dispersed fluorescence and polarity of emission from the excited fragment are also measurable in addition to the total photoabsorption and emission cross sections. In the single bunch operation of synchrotron radiation with the period of 178 ns, a radiative life time can be measured.

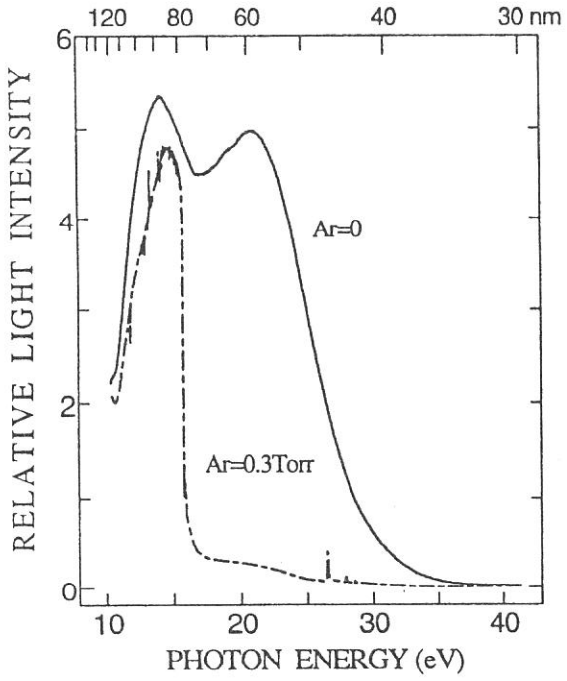

Fig. 1. Transmitted I_0 intensity with and without an Ar gas filter.

Specification

Monochromator : 1-m Seya
Wavelength range : 30-400 nm
Resolution : $\Delta E/E \cong 10^{-3}$ at 100 nm
Grating : 1200 *l*/mm blazed at 96 nm
Experiments :
- Vacuum cell or effusive jet
- Total photoabsorption cross section
- Fluorescence cross section
- Dispersed fluorescence
- Radiative lifetime
- Emission polarity

BL2B1

Soft-X ray beamline for solids and solid surfaces

BL2B1 is a beamline in order to study solids and solid surfaces by the use of photoabsorption and photoelectron spectroscopy. A 2-meter grazing incidence monochromator ('Grasshopper' type, Mark XV; Baker Manufacturing Co.) is installed. A 2400 l/mm grating has been installed since April 1994, and was replaced by a 1800 l/mm grating at March 1997. The resolving power is better than 600 at C-K edge (about 290 eV). Figure 1 shows the photoelectron yield from the Au mesh (10%-transmission) located near the position of a sample by the use of the 1800/mm grating. The dip around 300 eV is due to carbon contamination of optical elements.

The analyzing chamber is installed at the focusing point of the monochromized light. The pressure is less than $1x10^{-10}$ Torr. A double-pass CMA, a LEED optics, an ion-gun for sputtering, and a sample holder which can be cooled with liquid nitrogen and heated, etc. are equipped for the 'in-situ' measurements. The photoelectron spectroscopy including CIS (Constant initial state spectroscopy), CFS (Constant final state spectroscopy) can be measured using CMA, which is controlled by a personal computer. Samples can be transferred to the analyzing chamber from the air, through the preparation chamber in which sample treatments (e.g. cleaving, filing, and deposition) can be made.

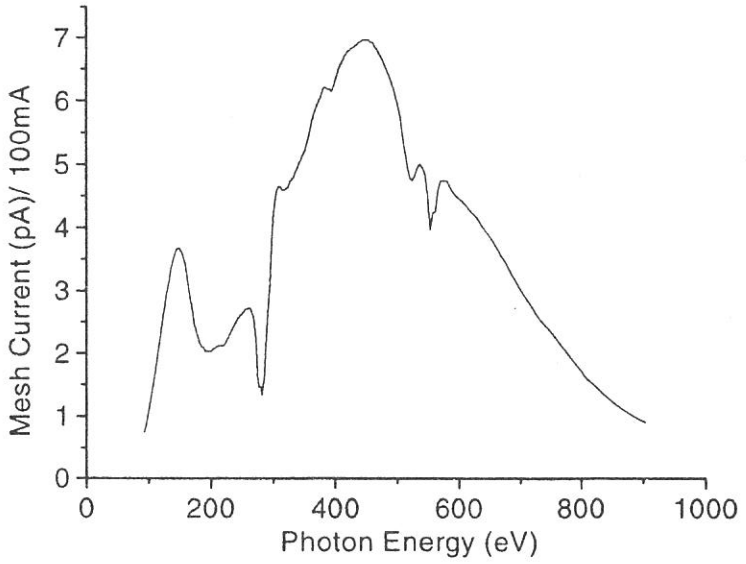

Figure 1. Photoelectron yield measured by the use of the Au mesh

Specification

Monochromator	:2m grasshopper type
Energy range	:95-1000 eV (1800 l/mm)
Resolution of photon	:<0.4eV at 300eV (1800 l/mm)
Resolution of photoelectron	:<0.3eV (hv=150eV)

Experiment : Photoelectron spectroscopy, X-ray absorption spectroscopy,

BL 3A1

Irradiation Port with Undulator Radiation

The beam line 3A1 has been used for various kinds of experiments with intense undulator radiation. In recent years, photo-desorption, photo-chemical reaction, SR-CVD, Photo-etching, irradiation damage effects in condensed phase, light amplification induced by core-level excitation, and so on have been carried out at the beam line 3A1. The luminescence from High-Tc superconductors, scintilator, and organic materials has been observed. Combination experiments with undulator radiation and lasers has also been successfully conducted for SR-induced desorption and SR-excited light-amplification.

A planar-type undulator installed in a long straight section of the UVSOR storage ring can provide an intense quasi-monochromatic radiation to beam lines 3A1 and 3A2. The photon energy range from 8 to 52 eV is covered by the fundamentals with K-values of 0.62-3.6 and higher harmonics are mixed in the spectral distribution of the undulator radiation in case of high K-values.

The beam line 3A1 has no monochromator between the undulator and a sample chamber. The radiation is introduced by a toroidal focusing mirror into the sample chamber through a pinhole of 1 mm in a diameter and metallic filters (Al, Sn, and In). A gold mesh is always installed in the sample chamber to monitor the incident photon flux. A typical spectral distribution measured with the monochromator at BL3A2 is shown in the figure. The photon flux provided with the gap of 60 mm is about $10^{14\text{-}15}$ phs/s on the samples.

A differential pumping system consisting of three TMP pumps can be available for the users who want to use gaseous materials. Visible and VUV second monochromators for luminescence measurements (Jobin-Yvon HR320 for visible range and home-made NIM monochromator for VUV range) are also provided. A He flow-type cryostat and a TAC system are useful for the time resolved experiments under a single-bunch operation.

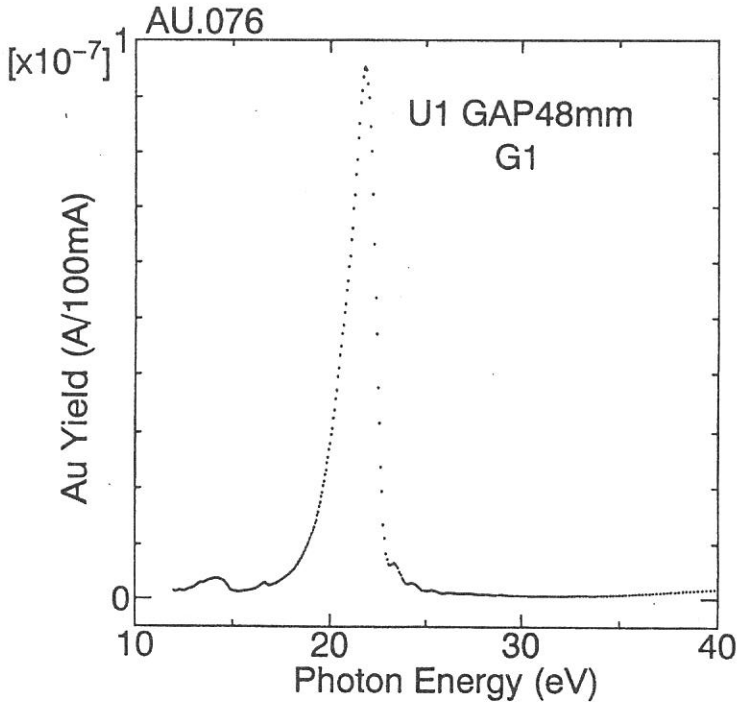

BL3A2

Gas-Phase Dissociative Photoionization Apparatus

This machine has been constructed to study the formation of multiply-charged ions and their dissociation processes. The monochromator is constant-deviation grazing-incidence type with 2.2m focal length and covers wide wavelength region(10-100nm) where many kinds of molecules and multiply-charged ions are effectively measured. High intensity photon beam is available by introducing the radiation emitted from the undulator to the monochromator. The apparatus contains an angle-resolved time-of-flight mass spectrometer (TOFM) equipped with automatic data acquisition system for photoion-photoion coincidence measurements. For full understanding of dissociative multiple photoionization, we detect the coincidence signals of two fragment ions produced from a parent ion, evaluate the kinetic energy release in "Coulomb explosion", and measure the angular distributions for the fragment ions. The sensitivity with respect to high-speed ions (several tens of electron volts) is much improved in comparison with commercial TOFMS.

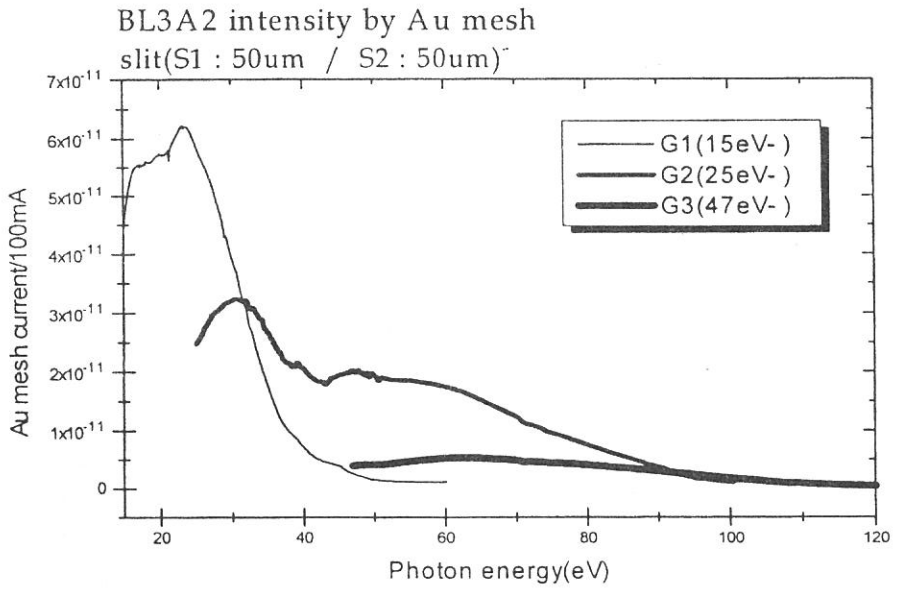

Specifications

monochromator	:	2.2m Constant-Deviation Grazing-incidence
Spectral range	:	10 - 100nm (15eV - 120eV)
Resolution	:	550 - 800 (0.03eV - 0.18eV)
Mass spectrometer	:	300
Length of the drift tube	:	0.2 - 1m
Rotatable angle	:	0 - 90° with respect to the photon beam

BL3B

Beam Line for Gas Phase Two-Dimensional Photoelectron Spectroscopy

This beam line is devoted to studies of elementary atomic and molecular processes induced by excitation of valence electrons. A monochromator is a vertically dispersed normal incidence type with 3m focal length and 10° angle between the incident and diffracted photon beams. The maximum wavelength resolution of 0.007nm is narrow enough to separate vibrational levels of excited states for various molecules. A main component in an experimental chamber is a spherical sector electrostatic energy analyzer which has been designed and setup for photoelectron spectroscopy. One can perform two-dimensional photoelectron spectroscopy with good resolution (≤ 30meV) in which the photoelectron yield is measured as a function of both photon energy and electron kinetic energy (binding energy). A two-dimensional spectrum, usually represented as a contour plot (*e.g.* Fig. 1), contains rich information on photoionization dynamics and properties of superexcited states. A great variety of interesting high-lying states involved in autoionization have been studied as follows: (1) a bound valence state of nitric oxide whose autoionization gives rise to a number of irregularly spaced peaks in its photoionization efficiency curve,[1] (2) the $(3\sigma_g)^{-1}(3\sigma_u)^1$ valence state of acetylene which dominates photoionization cross section and leads to strong vibrational excitation,[2] (3) Rydberg states of nitric oxide which undergo dissociation into N** + O($^1D^e$, $^3P^e$) followed by autoionizing transitions of the superexcited nitrogen atoms,[3] and (4) multiple-electron-excited Rydberg states of carbonyl sulfide which are primarily produced by conversion from the Rydberg states converging to $OCS^+(B^2\Sigma^+)$ and subsequently dissociate into S** + CO($X^1\Sigma^+$) giving rise to autoionizing transitions of the superexcited sulfur atoms.[4]

1) K. Mitsuke *et al.*, *J. Electron Spectrosc. Rel. Phenom.* **79**, 395 (1996).
2) H. Hattori and K. Mitsuke, *ibid.* **80**, 1 (1996); H. Hattori *et al.*, *J. Chem. Phys.* **106**, 4902 (1997).
3) Y. Hikosaka *et al.*, *ibid.* **105**, 6367 (1996).
4) Y. Hikosaka *et al.*, *ibid.* **107**, 2950 (1997).

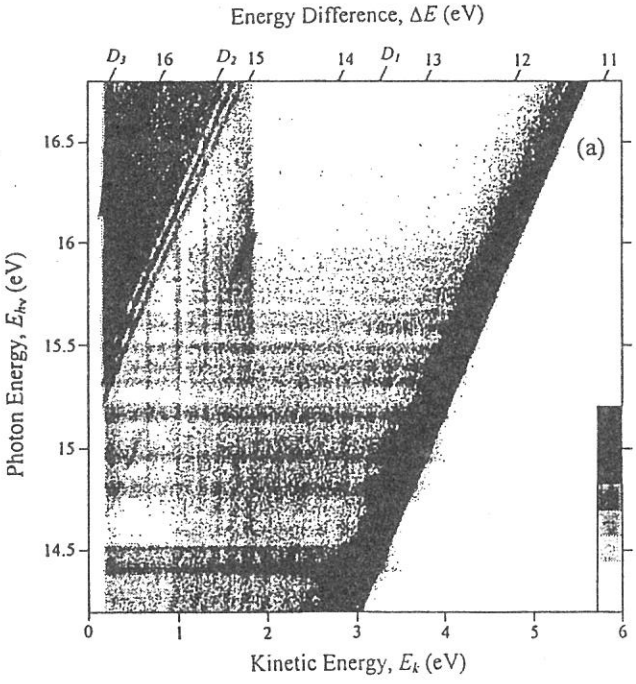

Figure 1. Two-dimensional photoelectron spectrum of OCS taken at the photon energy range from 14.2 to 16.8eV. The electron yield is presented by the plots with eight tones from light to dark on a linear scale.[4]

Specification

Monochromator : 3 m normal incidence
Wavelength range : 30 - 200 nm
Resolution : 0.007 nm at 100 nm

BL4A1

Multilayered-mirror monochromator beam line for the study of synchrotron radiation stimulated process

A multilayered-mirror (MLM) monochromator beam line designed specially for synchrotron radiation (SR) stimulated process experiments has been constructed for the first time. The most important point in constructing a MLM monochromator beam line for the study of SR-stimulated processes is the optimization of the beam line optics to obtain a large photon flux. The second most important point is to remove the background existing in the low energy region caused by the total reflection. Optimization concerning the reduction of the low-energy background due to the total reflection has been made for the combination of the Mo/Si MLMs and the C filter. Mo/Si MLMs have a (normal incident) reflectivity of over 60% can be made for the energy region around 100 eV, which contains the core electron binding energies of Al and Si (important materials in semiconductor processes). The beam line was designed by the criteria ; a beam spot size on the sample surface $\geqq 3\times3$ mm^2, a density of total irradiated photons $\geqq 10^{18}$ photons/cm^2 (for an irradiation time of a few tens of minutes to a few hours) and low-energy background $\leqq$ 1% of the output.[1]

[1] H. Mekaru, *et. al.*, Rev. Sci. Instrum., 70, 2601-2605 (1999).

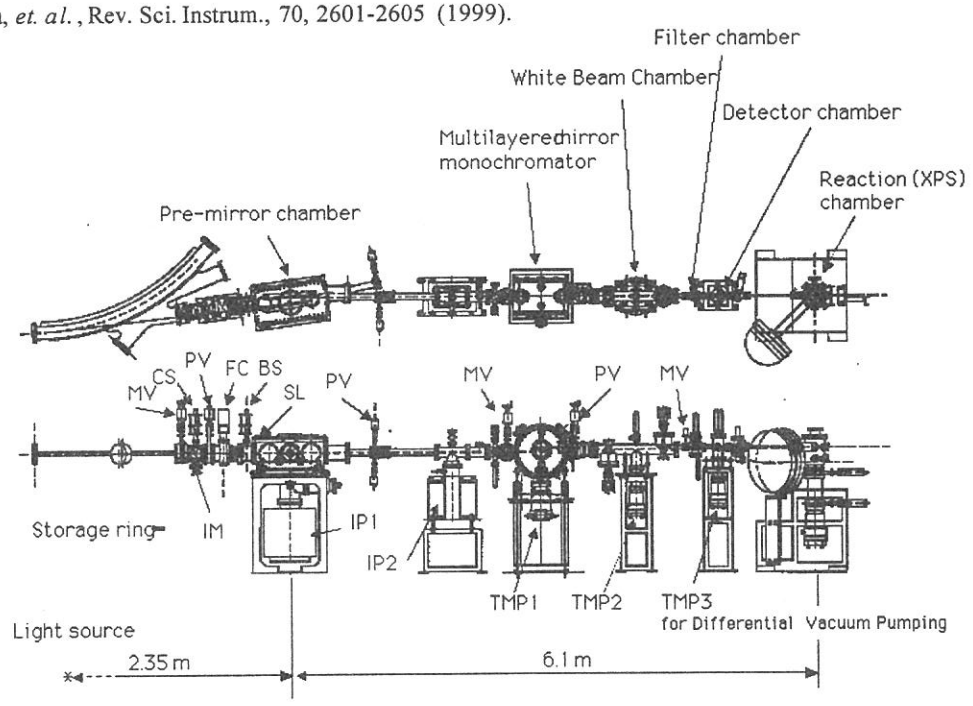

Figure 1. Top and side views of the MLM monochromator beam line (BL4A1) constructed at the UVSOR facility of the IMS.

Specifications

Monochromator	:Multilayered-mirror monochromator
Wavelength range	:13.3 - 22.5 nm
Resolution	:5 – 9 eV (FWHM)
Experiments	:Excitation energy dependence of the SR processing

BL 5A

Photoelectron Spectrometer for Solids and Surfaces

The beamline 5A is designed for spin- and angle-resolved photoelectron experiments for solids and surfaces with the circularly polarized synchrotron radiation from a helical undulator and for high-resolution photoelectron experiments with bending magnet radiation. The beamline consists of a Spherical Grating Monochromator with Translational and Rotational Assembly Including a Normal incidence mount (SGM-TRAIN), a spin- and angle-resolved photoelectron spectrometer, and a high-resolution photoelectron spectrometer.

The SGM-TRAIN is an improved version of a constant-length SGM to aim the following points; (1) wide energy range of 5-250 eV, (2) high resolving power, (3) use of linear and circular polarization, (4) reduction of second-order light, and (5) two driving modes by a computer control. The second-order light is well suppressed by using laminar-profile gratings and combinations of mirrors and gratings.

Specifications

1)Monochromator

Type:SGM-TRAIN
(two glancing-incidence and one normal-incidence)
Energy Range: 5-250 eV
Resolution: 0.5-80 meV with slits of 0.01mm
Flux: 3×10^{10} phs/sec at 120 eV with slits of 0.1 mm
(for bending manget radiation)

2) Main Instruments

Two-levels UHV chamber (1×10^{-10} Torr)
Hemi-spherical electron-energy analyzer
(OMICRON HR-125)
Spin- and Angle-resolved spectrometer
(low-energy diffused scattering type)
LEED of reverse type (OMICRON)
Ion-gun (ULVAC-Phi)
He-lamp for UPS
Low-temperature cryostat (>30 K)

3)Helical Undulator (Optical Klystron)

Number of periods	18
Period length	110 mm
Length of dispersive part	302.5 mm
Total length	2351.2 mm
Deflection parameter, Kx,y	0.07-4.6 (helical mode)
Deflection parameter, K	0.15-8.5 (planar mode)
Fundamentals	2-45 eV (Circular polarization)

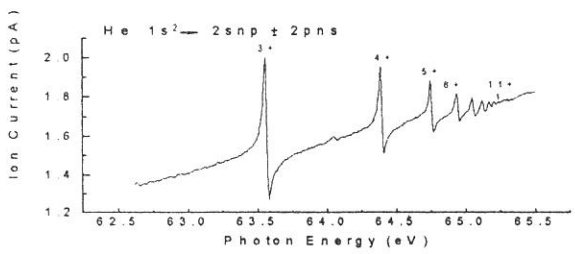

Fig. 1 He ionization spectrum

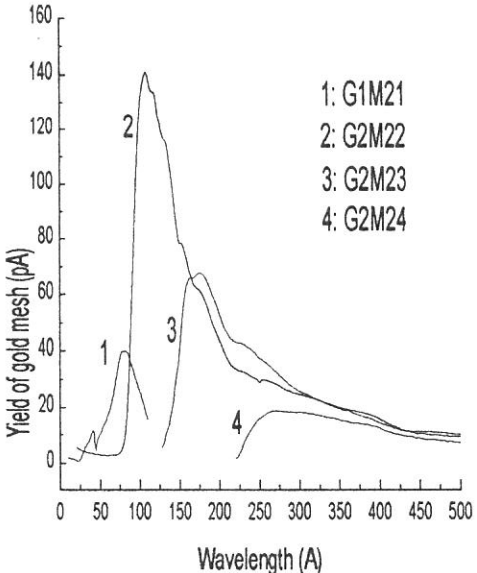

Fig. 2 Typical spectral distribution

Refs: M. Kamada et al., Rev. Sci. Instrum. 66, 1537 (1995), N. Takahashi et al., Jpn. J. Appl. Phys. 35, 6314 (1996).

BL5B

Calibration Apparatus of Optical Elements

BL5B has been constructed to calibrate optical elements. The beam line consists of a plane grating monochromator (PGM) and three chambers (Fig. 1). The chamber A is used for calibration of optical elements, the camber B for optical measurements of solids and the chamber C for photo-stimulated desorption (PSD) experiments. The chamber C is sometimes changed to a chamber for photoemission microscopy.

The calibration chamber is equipped with a goniometer. The goniometer, which was installed for the characterization of optical components, has six degrees for freedom; X-Y translation of a sample, and interchange of samples and filters. They are driven by vacuum pulse motors. Since the polarization of SR is essential for such measurement, axis of the rotation can be made in either horizontal or vertical direction (s- or p-polarization).

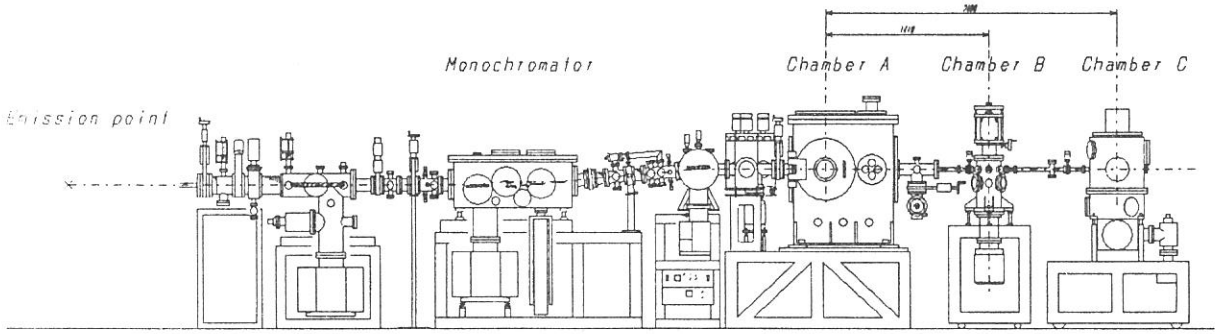

Figure 1. Schematic figure of BL5B spectrometer system.

Specification

Monochromator: Plane grating

Wavelength range: 2 - 200 nm (Fig. 2)

Resolution: $\lambda / \Delta\lambda = 300 \sim 500$

Experiments: Calibration of optical elements, absorption of solids, photo-stimulated desorption from rare gase solids, photoelectron microscopy.

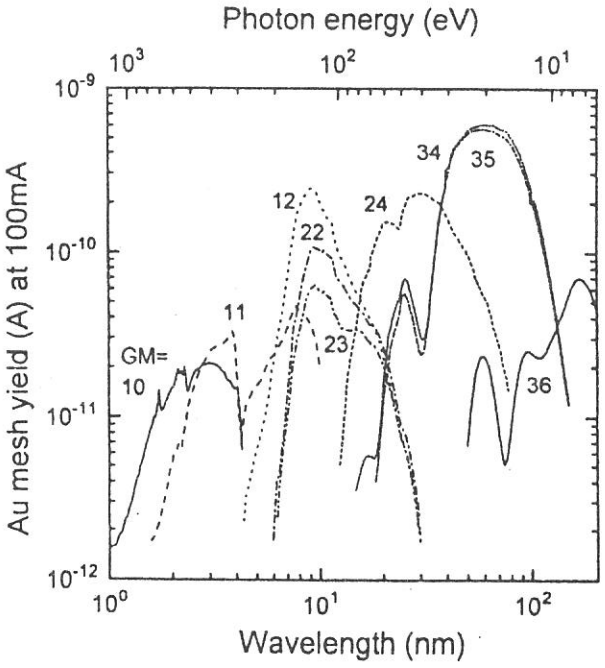

Figure 2. Throughput spectra of BL5B detected by a gold mesh (84% transmission).

BL6A1

Fourier-Transform Middle- and Far- Infrared spectrometers for solids

Synchrotron radiation of UVSOR covers a very wide energy region from soft-X ray to millimeter wave. BL6A1 was constructed in order to cover a long wavelength part in the spectral distribution from near infrared to millimeter wave. The beamline is composed of two kinds of interferometers, a Martin Puplett type and a Michelson type (Fig.1). The spectrum from 0.7 um to 2 mm is measureable by changing three kinds of detectors; MCT, Si-bolometer and InSb hot electron detector (Fig.2). Owing to the high brightness of the SR, the present spectroscopic system is especially favorable to the transmission and reflection measurements on tiny specimens.

In summer 1998, the control system for the Martin-Puplett type interferometer (SPECAC) was replaced owing to its lots of troubles. Most of the components in the control system were newly installed except the chopper controller and the PC. After some correction, the system is now under use regularly.

We have also installed new beamsplitters in the rapid scan type interferometer (Bruker IFS66V): Quartz(II) and myler(23 micron). It expands the measurable region.

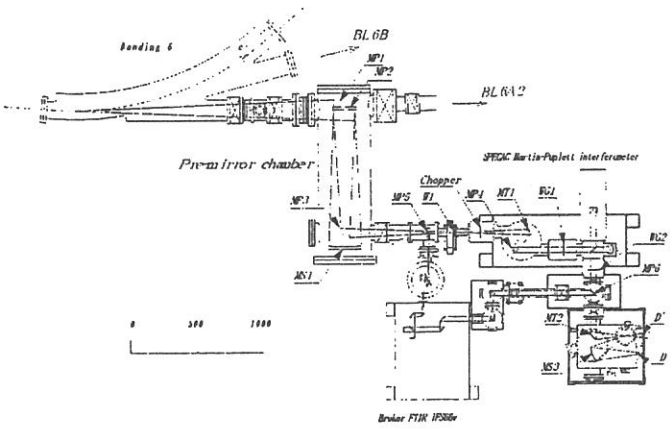

Fig.1 Top view of BL6A1.

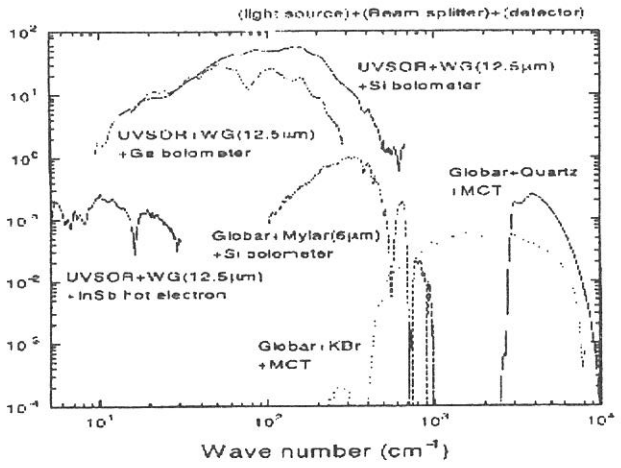

Fig.2 Throughput spectra of BL6A1.

Specification

Interferometers: a Martin-Puplett type and a Michelson type

Detectors: Si bolometer (20-1000 cm-1)

Ge bolometer (with polyethylene window, 30-300 cm-1)

Ge bolometer (with quartz window, 10-200 cm-1)

InSb bolometer (5-50 cm-1)

MCT (400-10,000 cm-1)

Photovoltaic type MCT (400-4000 cm-1, time response: 10 nsec)

Wavelength range: 5~300 cm-1 by the Martin-Puplett type interferometer

40~28,000 cm-1 by Michelson type interferometer

Experiments: Temperature dependence of reflectivity and transmission spectra, absorption under high pressure (up to 20 GPa), reflectivity under magnetic field (up to 8 T) and time-resolved spectroscopy.

BL6A2

Photoelectron Spectrometer for Solids and Surfaces

The beamline 6A2 has been used for photoelectron spectroscopy on solids and surfaces with bending magnet radiation. The beam line consists of a Plane Grating Monochromator (PGM), and an angle-resolved photoelectron spectrometer (ARUPS).

The PGM has several combinations of mirrors and gratings to cover wide energy range of 2-150 eV with less higher order light. Since the monochromator has no entrance slit, resolving power depends on the beam size and the divergence, but not only on the width of the exit slit. The ARUPS is mounted on the two-axes goniometer. The usual instruments for surface analyses are available. Recently, the combined experiments with SR and lasers are being carried out at this beam line. The upgrade of the BL6A2 is also in progress. The renewal of this beam line will be completed in 2000.

Specifications

1)Monochromator

Type:PGM
(Plane-Grating Monochromator)
Energy Range: 2-150 eV
Resolution: 0.1 eV at 70 eV with slit of 0.01mm
Flux: $1x10^{11}$ phs/sec at 120 eV with slit of 0.1 mm

2) Main Instruments

Two-levels UHV chamber ($1x10^{-10}$ Torr)
Hemi-spherical electron-energy analyzer
(two-axes)
LEED Optics (OMICRON)
Ar-ion gun (ULVAC-Phi)
Mode-locked Nd:YAG laser

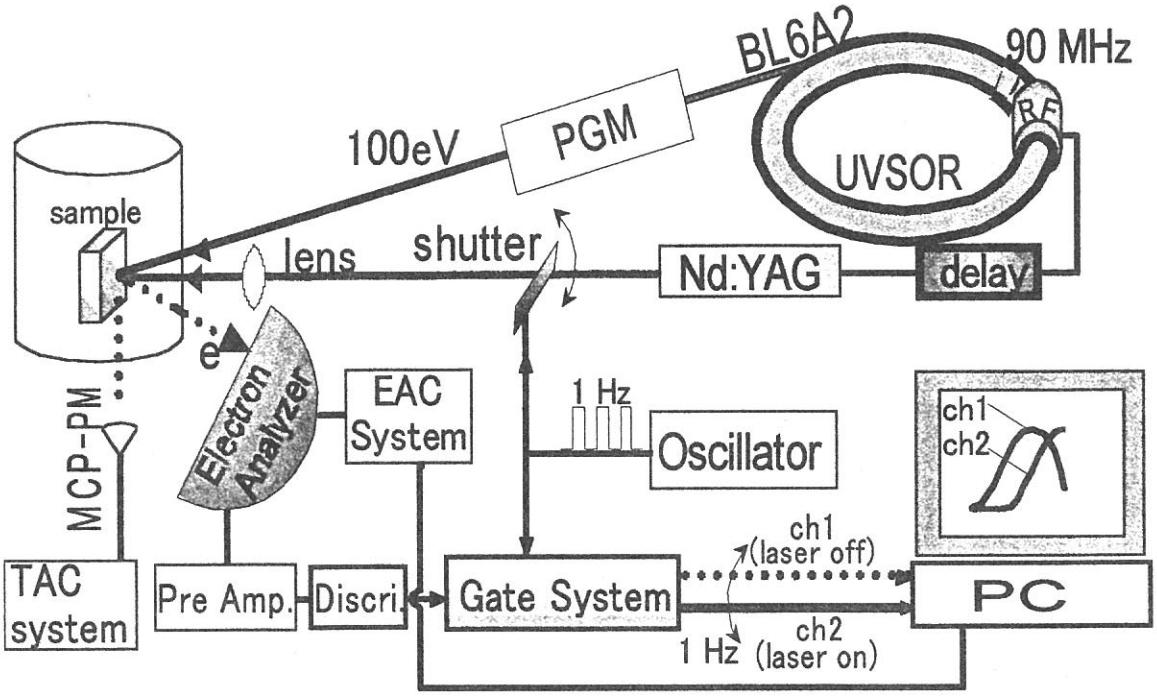

BL7A

Soft X-ray Spectrometer for Solids

The beamline BL7A equipped with a double crystal monochromator was constructed for spectroscopic investigation on solids in the soft X-ray range (0.6 to 5 keV). In order to make the EXAFS experiments at the Mg (~1300 eV) and Al (~1550 eV) *K*-edges possible, a pair of $KTiOPO_4$ [KTP] (011) crystals was introduced and its performance test was done in 1999. In the past, it has been necessary to use beryl and quartz crystals to approach these two edges. The combination of an artificial crystal, YB_{66}(400), with the wiggler has been another possibility to access the Al and Mg *K*-edges. However, YB_{66} is unsuitable for the radiation from the bending magnet, due to its low reflectivity, and there is a disadvantageous characteristic caused by a anomalous (600) reflection at the Y *L*-edge for carrying out the EXAFS experiments with the YB_{66} crystals.

Figure 1 shows the photon flux of the KTP monochromator crystals over the photon energy range 1200–3000 eV. It is found that the photon intensity from the KTP crystals without the wiggler is almost the same as that from the YB_{66} crystals combined with the wiggler. The ability to cover the Mg, Al, and Si *K*-edges with a single pair of the KTP crystals seems to be attractive for many users. Further details can be seen in this activity report (by Shigemasa).

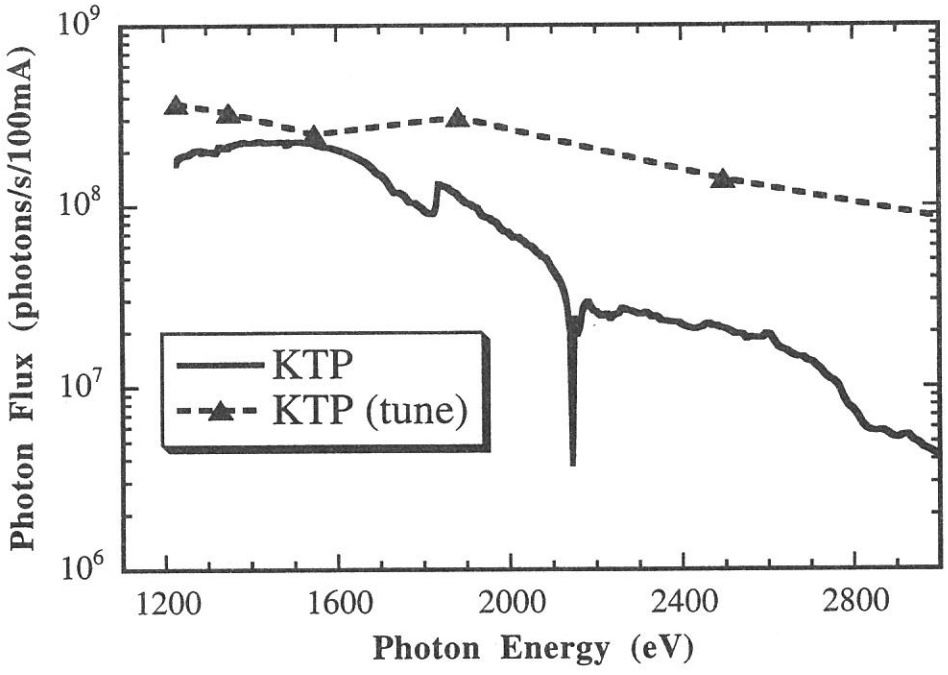

Figure 1. Throughput from KTP monochromator crystals on BL7A.

Specification

Monochromator: Double-Crystal

Energy range: 0.6～3.0 keV, without wiggler (～6.0 keV, with wiggler)

Experiments: X-ray absorption (by total electron- or fluorescence-yield methods)

BL7B

3m Normal Incidence Monochromator for UV, VIS and IR Spectroscopy of Solids

The reconstruction of the beamline BL7B has been almost completed. The 1m Seya-Namioka type monochromator was replaced to the 3m normal incidence monochromator (3m NIM; McPherson upgrade model of 2253) for the extended researches of the highest level with the higher resolution and intensity, the wider wave-length region available and so on. It will be also possible to utilize the linear and circular polarization inherent in synchrotron radiation (SR) and to realize some combined experimental systems, for example, with the synchronized laser to SR pulse or with the extended field. The outline of the new beamline is shown in Figure 1. The main parts of the system are a pre-mirror focusing system, a 3-m NIM and a post-mirror focusing system. The light from 50 to 1000 nm wavelength region is covered by changing three gratings *in situ*. Each spherical grating is original laminar type fabricated on SiO_2 and has effective grooved area of 120 x 40 mm^2. The 2 focusing positions are available for the experiments. At the position between 2 positions, LiF or MgF_2 window valve is installed. Therefore, the measurements for the organic materials, liquid and biochemical ones are possible at the 2^{nd} focal position.

This beamline is used for absorption, reflection and fluorescence measurements on various materials with higher performance (high energy resolution, high intensity, well-polarized light, short repetitive pulse light) not only on the VUV region but also in the near UV, VIS and near IR region. The performance of the beamline is presented in this activity report. The beamline has been opened to the users from April, 1999.

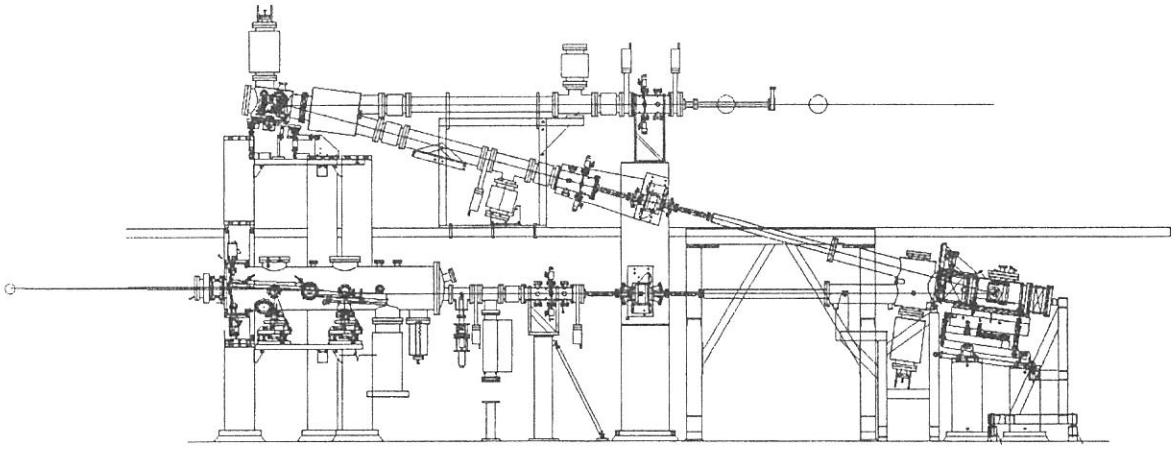

Specification

Monochromator	: 3m Normal Incidence Monochromator
Wavelength range	: 50 nm – 1000 nm
Typical resolution	: $E/\Delta E$ = 4000 – 23000 for 0.01 mm slits
Experiments	: absorption, reflection, fluorescence spectroscopy, mainly for solids

BL8A

Free Port

This beamline was constructed as a free port to which user can connect their own instruments. The beamline consists of a front end, a focusing premirror chamber and a separation chamber. Both focused and unfocussed beam can be used. A general purpose reaction chamber and a two (or three) stage differential pumping system are available for the experiments that use gas samples without window. With using three stage differential pumping system, gas pressure at the reaction chamber upto 0.5 torr can be used while keeping ultra high vacuum at the premirror chamber.

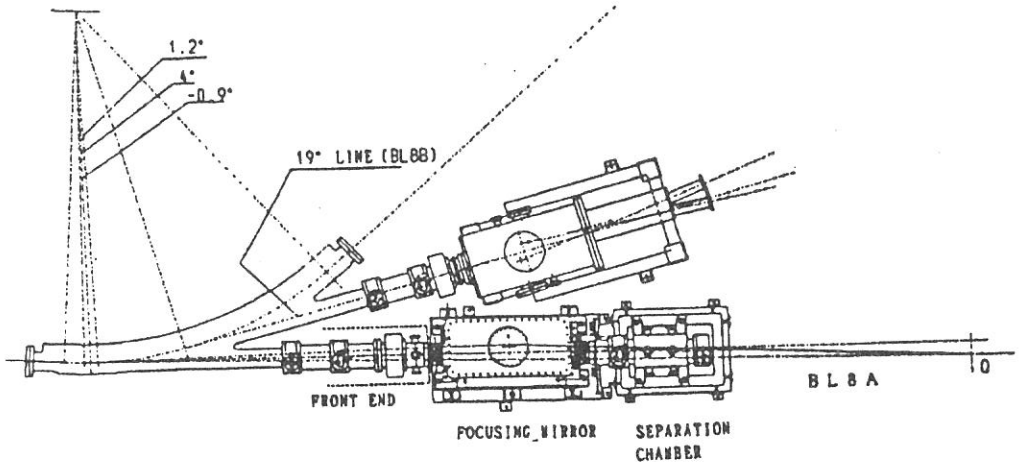

UP VEW OF BL8A

Specification

Spectral range : whole range of synchrotron radiation from UVSOR

Acceptance angle

Unfocused beam : 25 mrad (horizontal) × 8 mrad (vertical)
0.6 mrad (horizontal) × 0.6 mrad (vertical)
(with ϕ 3 mm aperture before sample)

Focused beam : 7.7 mrad (horizontal) × 8 mrad (vertical)

Beam spot size at focu : 3 mm (horizontal) × 2 mm (vertical)

Source - mirror distance : 2500 mm

Mirror - focus distance : 2807 mm

BL8B1

Photoabsorption and Photoionization Spectrometer

The beam line BL8B1 was constructed for observation of high resolution photoabsorption and photoionization experiments in the photon energy range from 30 to 800 eV, which includes the 1s core excitation energy of C, N and O atoms. For high resolution measurement among these energy, a constant-deviation constant-length spherical grating monochromator (CDCL-SGM) with three gratings (G1: R = 15 m; 1080 l/mm, G2: R = 15 m 540 l/mm, G3: R = 7.5 m; 360 l/mm) has been employed. The entrance and exit slit positions and directions of incident and exit photon beams do not change during its scan. Consequently, it provides us with a resolution (E/ΔE) of 4000 at 400 eV and of 3000 at 245 eV. A current of a Si diode reveals the absolute photon flux normalized by an ring current when two slit widths are 10 μm (Fig. 1).

Being Equipped at the downstream of the monochrometer, an chamber with a time-of-flight ion detector and a photoelectron detector, they allows us to measure photoelectron - photoion coincidence (PEPICO) and photoion - photoion coincidence (PIPICO) spectra. Measurements of absorption, electron yield and emission spectra of solid samples are also available.

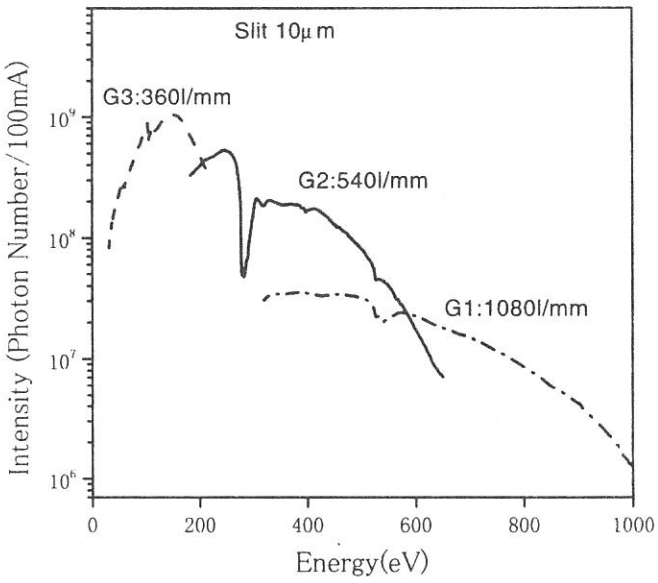

Figure 1. Absolute photon fluxes measured by a Si photodiode

Specification

Monochrometer	: 2.2 m constant-deviation grazing incidence
Wavelength range	: 30 to 800 eV
Resolution	: E/ΔE = 4000 at 400 eV and 3000 at 245 eV
Available Experiments	: Measurement of photoabsorption and photoionization spectra for gas and solid sample

BL8B2

Angle-Resolved Ultraviolet Photoelectron Spectrometer for solids

BL8B2 is a beamline for angle-resolved ultraviolet photoemission spectroscopy (ARUPS) system which is designed for measuring various organic solid such as molecular crystals, organic semiconductor, and conducting polymers. The beamline consists of a plane-grating monochromator (PGM), a sample preparation chamber with a fast entry Load-Lock chamber, a measurement chamber with an accurate manipulator for temperature dependence (base pressure 3×10^{-10} Torr), a cleaning chamber (base pressure 2×10^{-10} Torr), and a sample evaporation chamber (base pressure 3×10^{-10} Torr). The cleaning chamber is equipped with back-view LEED/AUGER, Ar^+ gun and an infrared heating units. The PGM consists of pre-mirrors, a plane grating, focusing mirror, and a post-mirror, with an exit slit. It covers the wide range from 2 to 150 eV with exchanging two gratings (G1; 1200 l/mm, G2; 450 l/mm) and five cylindrical mirrors. The toroidal mirror focuses the divergent radiation onto the sample in the measurement chamber. The spot size of the zeroth-order visible light at the sample surface is about $1 \times 1 mm^2$. The energy resolution at a slit width of 100 μm was found to be 0.004 - 0.3 eV in the wavelength range from 2 to 130 eV. A hemispherical electron energy analyzer of 25 mm mean radius with an angular resolution of 2° can be rotated around vertical and horizontal axes. The sample mounted on a manipulator can be also rotated around two axes.

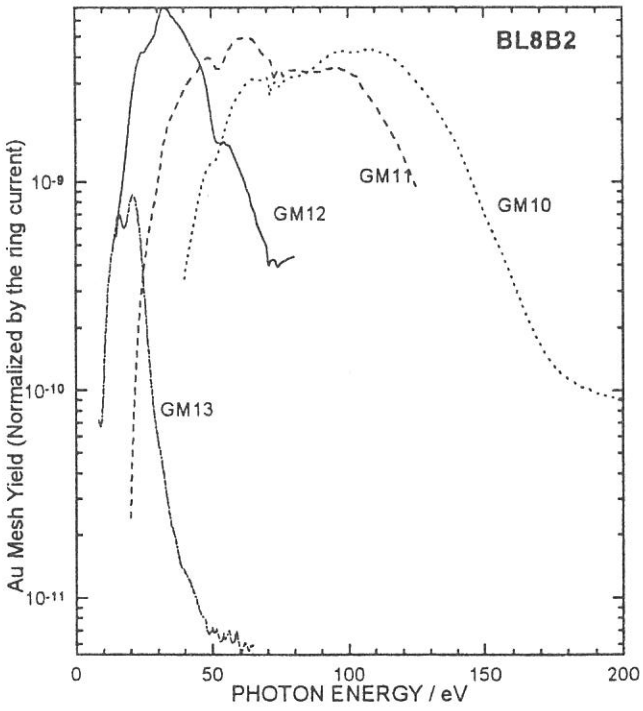

Figure Throughput spectra of plane-grating monochromator at BL8B2 with 100 μm exit slit.

Specification

Monochromator : plane grating monochromator
Spectral range : 2 - 130 eV
Resolution : 0.25 eV at 40 eV, as determined by the Fermi edge of gold.
Experiment : Ultraviolet Photoelectron Spectroscopy for various organic solids
Polarization : 85~91 % at 5000 Å

Open beam lines

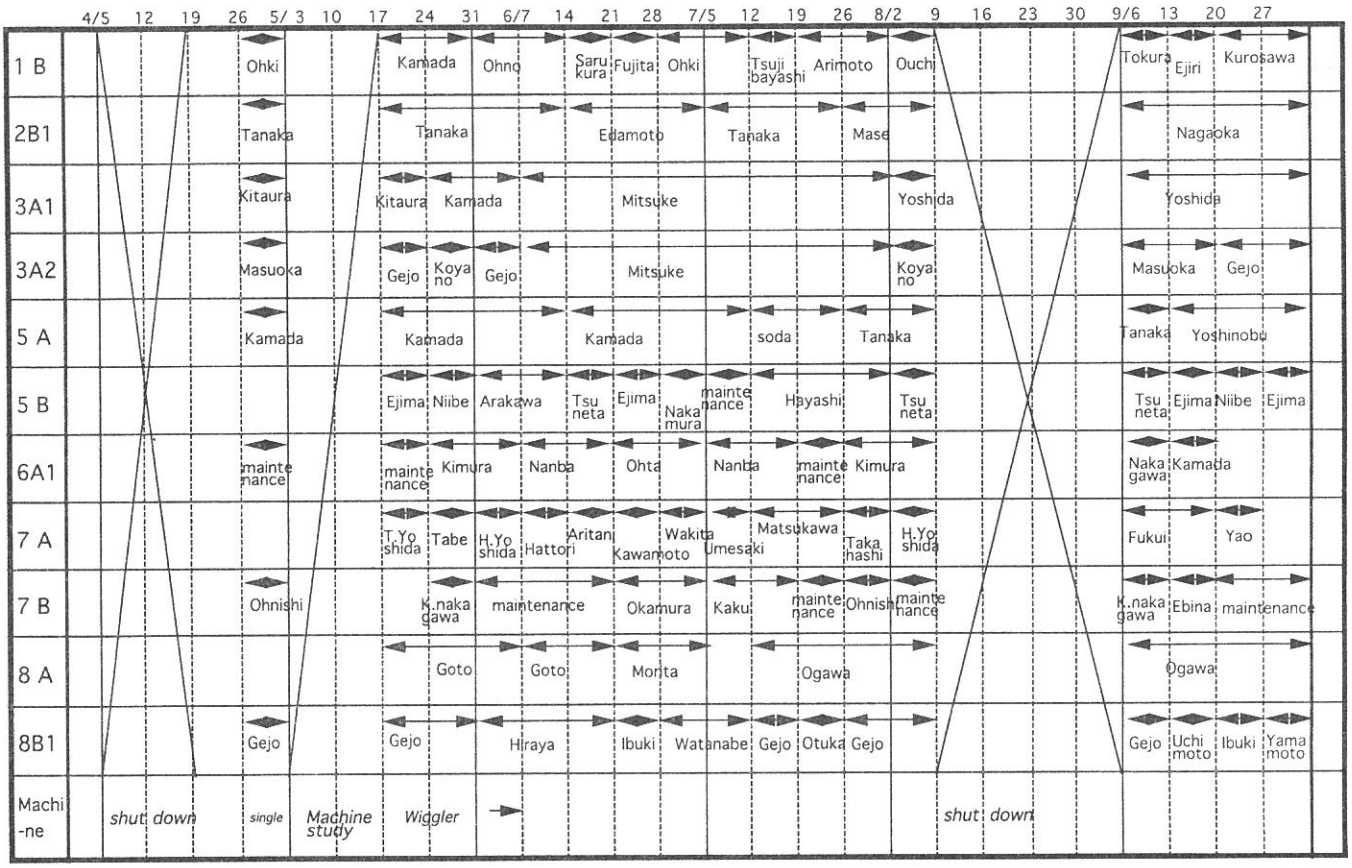

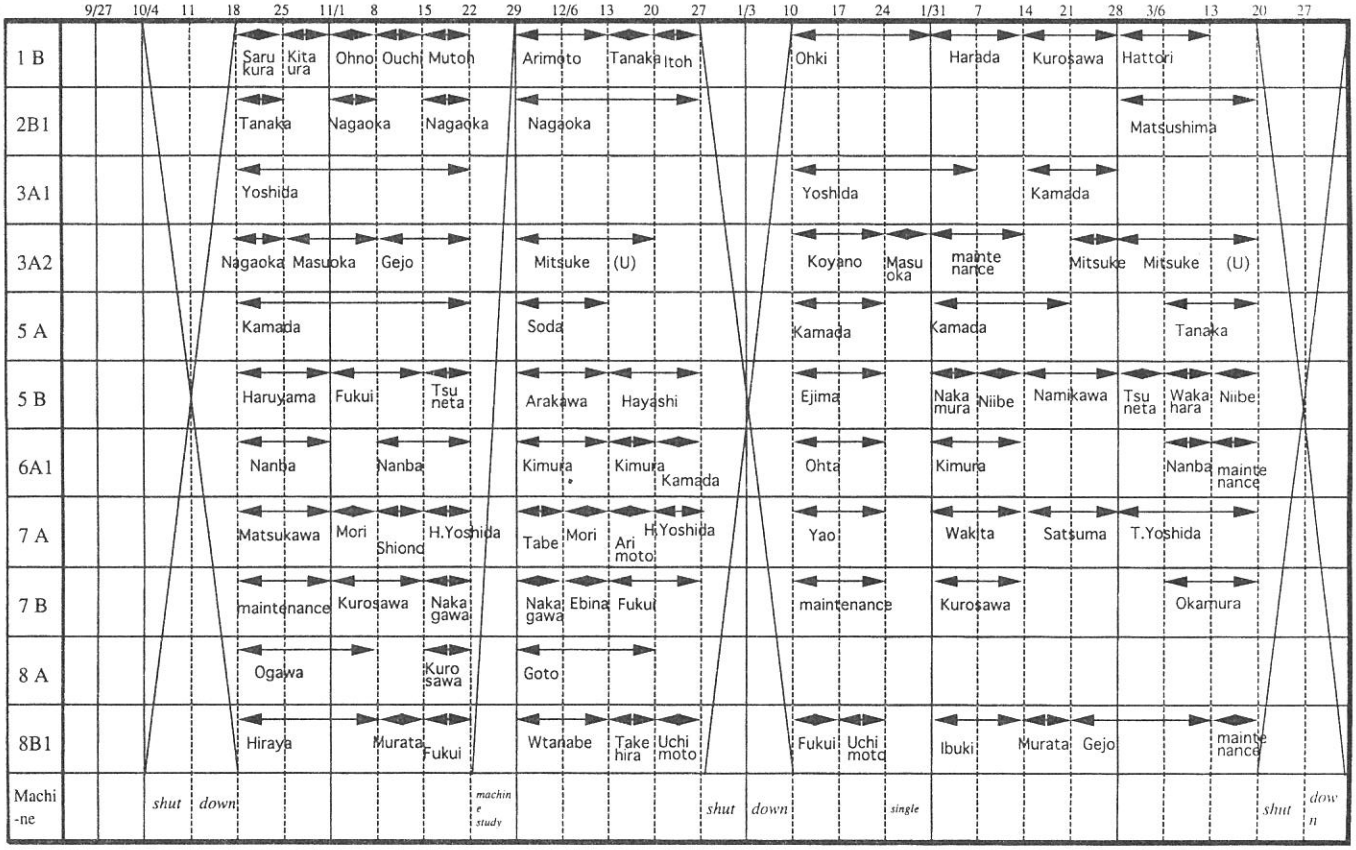

In-house beam lines

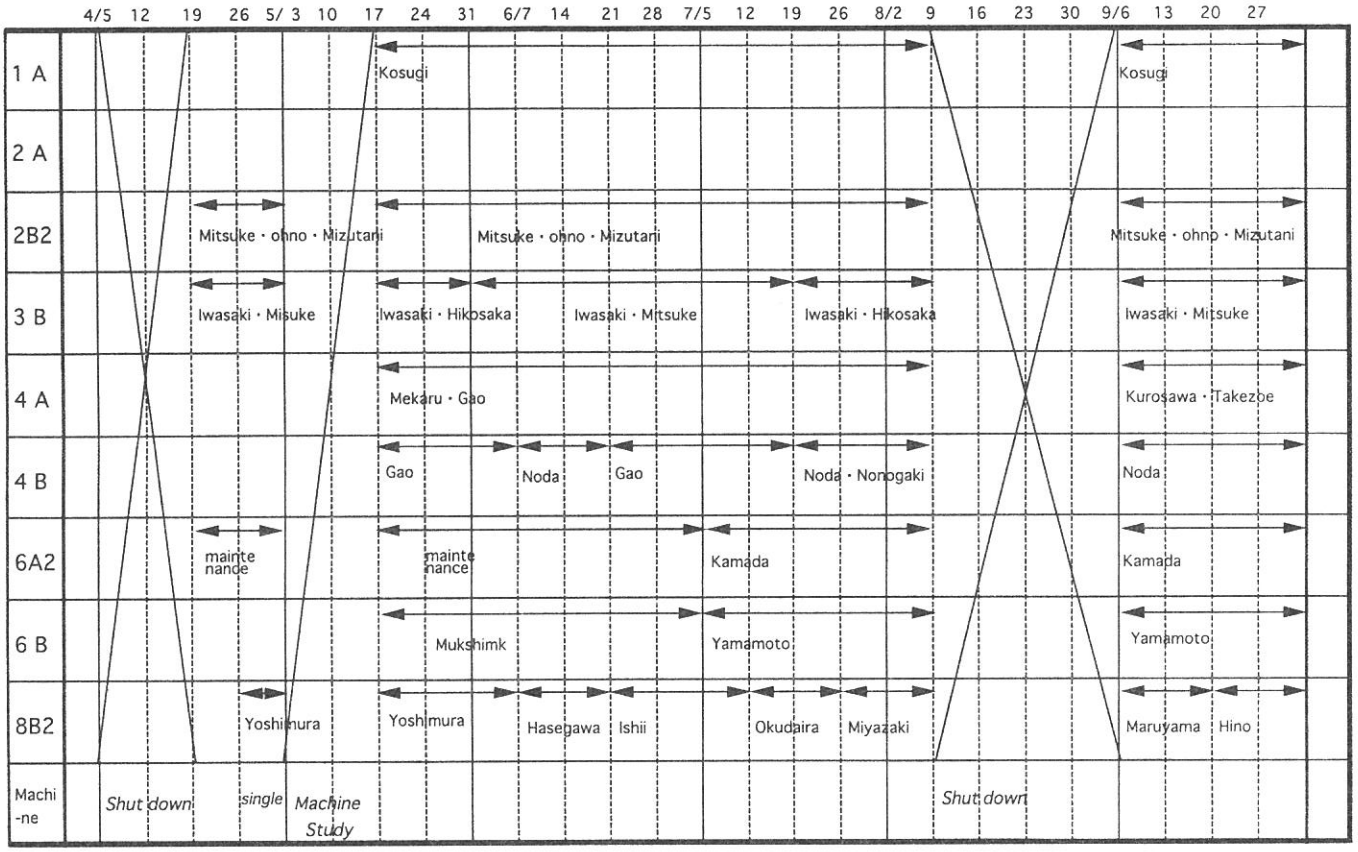

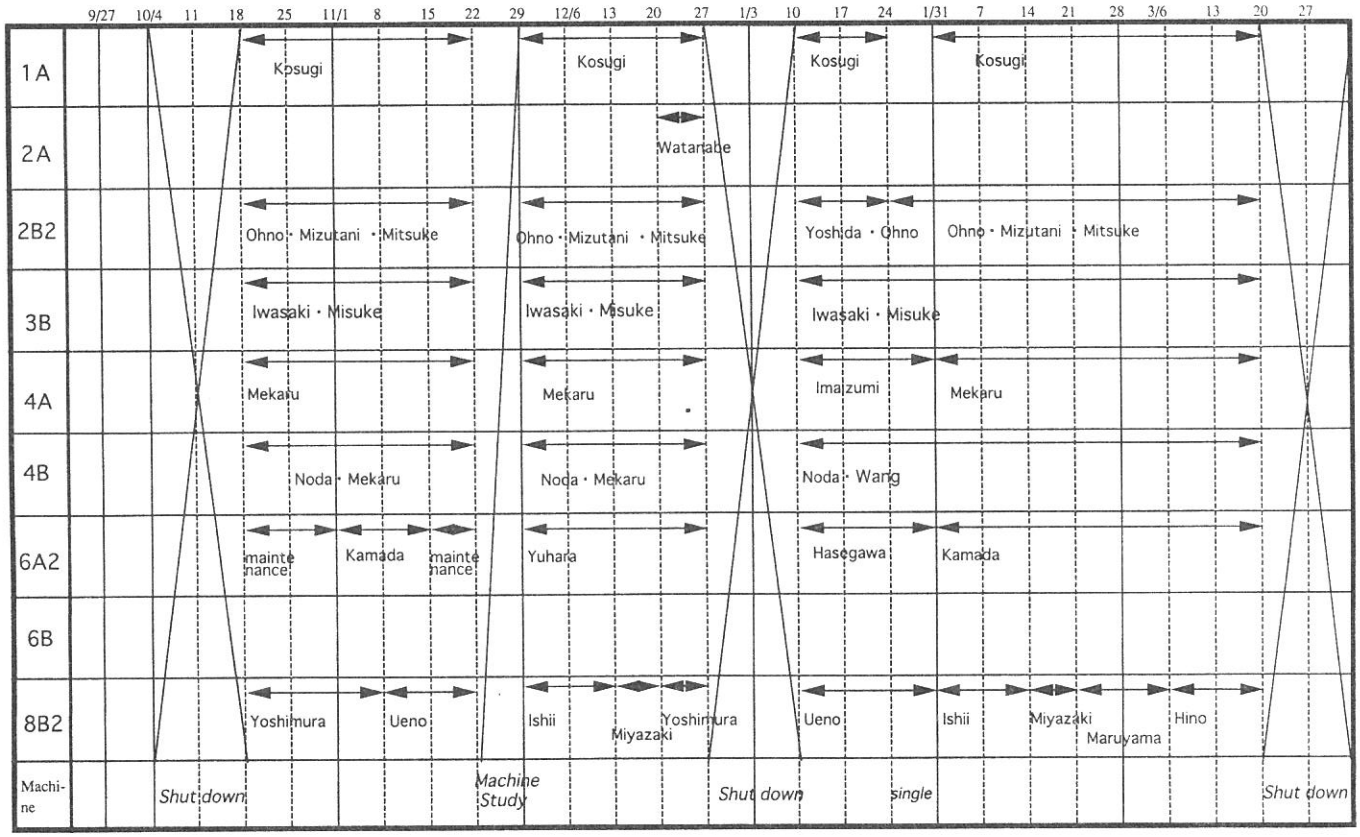

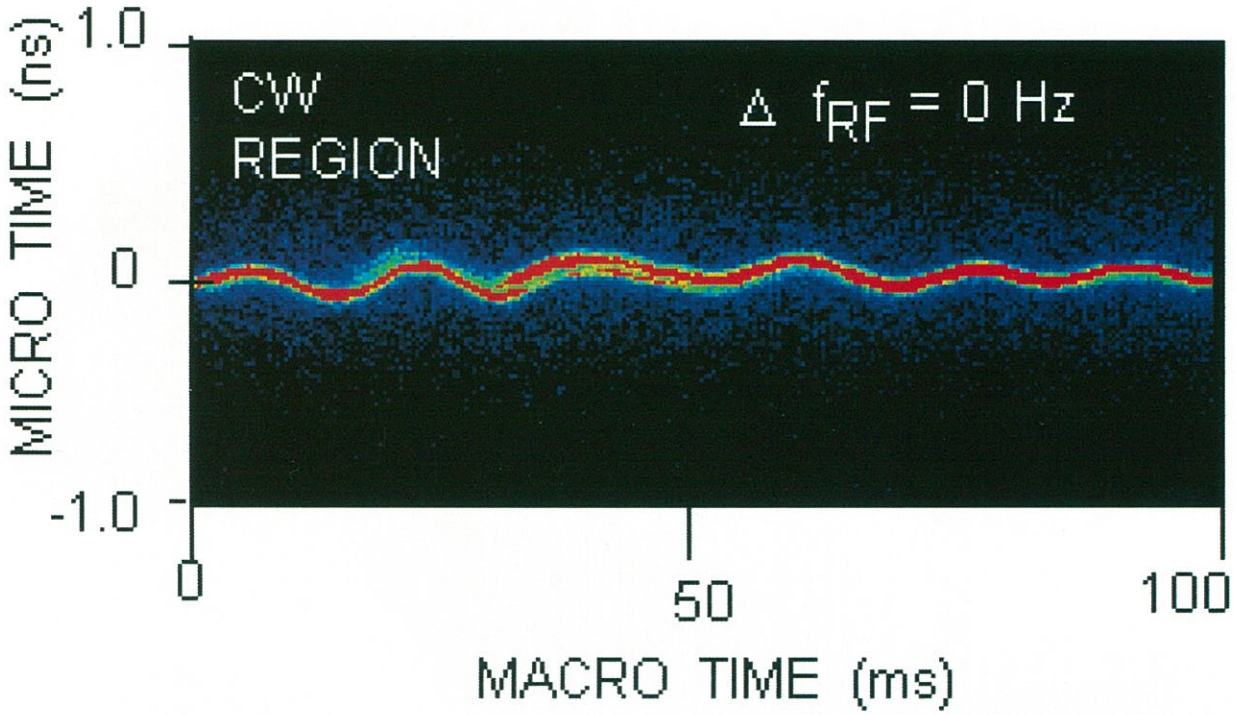

Beam Physics

Performance of the UVSOR-FEL with new optical cavity

Shigeru. KODA, Jun-ichiro YAMAZAKI, Masahito HOSAKA, and Hiroyuki HAMA
UVSOR Facility, Institute for Molecular Science, Myodaiji, Okazaki, 444-8585, Japan

After shutdown due to a conflict between the FEL mirror and the beam line BL5A, an FEL optical cavity and a control system were newly installed in the UVSOR-FEL[1,2]. The optical cavity was designed to reduce mechanical vibration, which is considered to spoil the lasing stability of the FEL. To escape from complicated mechanical resonances, the structure of the mirror chamber was simplified. Number of control axes for the cavity mirrors were reduced from ten axes of the former UVSOR-FEL[3] to five axes. In addition, to decrease mechanical vibrations, marble stones with weight of 2 t were employed as the bases of the optical cavity mirrors.

The first lasing of new FEL system was achieved in May, 1999. The lasing experiment was operated with an electron beam energy of 607 MeV with a maximum beam current of about 50 mA/bunch. An experiment at a visible wavelength of 520 nm was performed in order to check the FEL system and another experiment in the UV region was also carried out at a wavelength of 270 nm. Multi-layered mirrors of HfO_2/SiO_2 were used as the cavity mirror. Measured FEL spectra around 270 nm lasing are shown in Fig 1. The out-coupled power of the FEL was fairly stable in the CW region around the best synchronism between the electron bunch and the FEL micropulse. A measured intensity variation of 520 nm is shown in Fig. 2. The average power was 12 mW for the electron beam current of 30 mA/bunch, which corresponded to an energy of 1 nJ/pulse. Since observed rms width of an FEL micropulse in the CW region was approximately 10 ps, the out-coupled peak power reached at least 40 W. For the 270 nm lasing, a mirror with large transmission of 0.06% was employed for the backward mirror and the averaged lasing power was attained to be 10 mW for the electron beam current of 40 mA/bunch. Detuning dependence for the RF frequency was measured as two-dimensional time spectra by a dual-sweep streak camera. Typical cases are shown in Fig. 3. In a region of the small detuning around the best synchronism, a CW lasing was observed, which is shown as a case of $\Delta f_{RF} = 0$ Hz in Fig. 3. In the region of the large detuning of Δf_{RF}=10 Hz, a macropulse structure arose. Continuous lasing called quasi-CW was observed in the larger detuning region of Δf_{RF}=100 Hz. In the former UVSOR-FEL experiment, the lasing around the best synchronism was unstable and it was difficult to maintain the CW lasing [4]. In the new system, the CW region was clearly observed and stable in both points of the micropulse time jitter and the FEL intensity.

In summary, we carried out the FEL experiment with new optical cavity, which had the heavy and simple structure, and measured the lasing performances in visible and UV regions. The lasing stability was especially improved relative to former UVSOR-FEL and the stable lasing was easily maintained in the CW region.

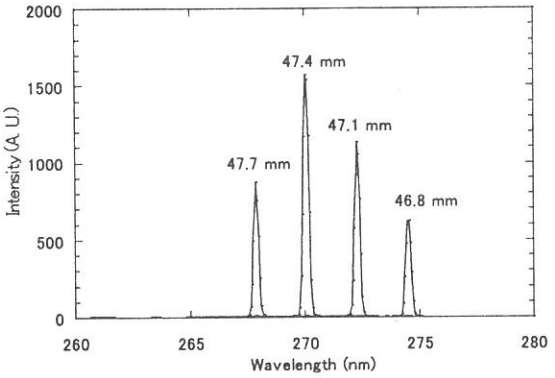

Fig. 1 Typical FEL spectra at wavelengths arround 270 nm for various gap lengths of the helical optical klystron.

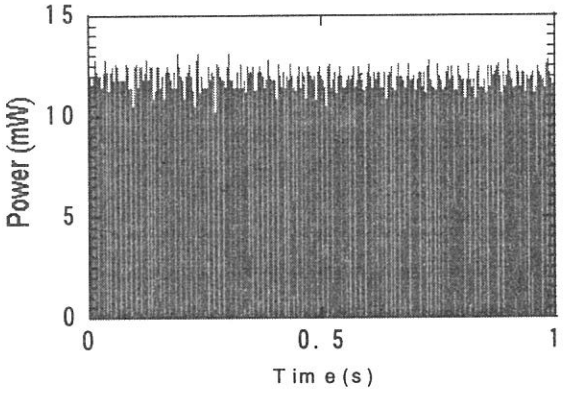

Fig. 2 Typical intensity variation at wavelength of 520 nm.

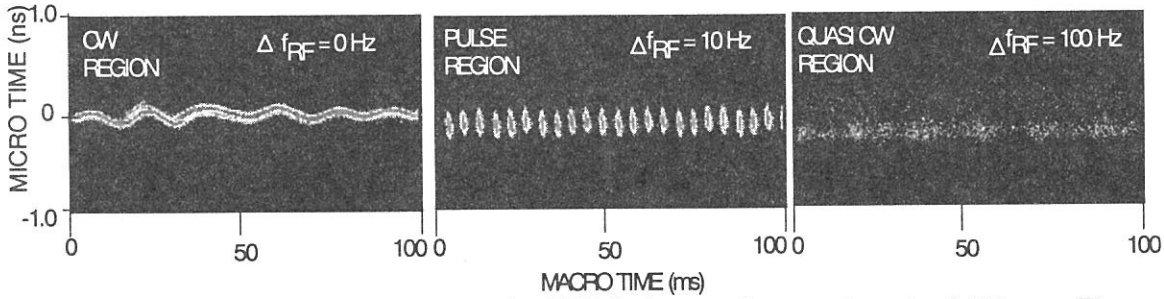

Fig. 3 Typical detuning dependence in the FEL lasing at the wavelength of 520 nm. Time structures of the CW, the pulse and the quasi-CW lasings were observed in order of detuning of the RF frequency. The rf frequency of the best synchronism was 90.101MHz.

References

[1] S. Koda, H. Hama, M. Hosaka, J. Yamazaki and K. Kinoshita, UVSOR Activity Report 1998, UVSOR-26 (1999)

[2] S. Koda, J. Yamazaki, M. Hosaka and H. Hama, Proceedings of 4th Asian Symposium on Free Electron Lasers and Korea-Russia Joint Seminar on High-Power FELs, Taejon, to be published.

[3] S. Takano, H. Hama and G. Isoyama, Nucl. Instr. and Meth. in Phys. Res. A331 (1993) 20.

[4] H. Hama, K. Kimura, M. Hosaka, Yamazaki and T. Kinoshita, Proceedings of the third Asian Symposium on Free electron Lasers, Ionics Publishin, Tokyo (1997) 17.

Development of a longitudinal feedback system for the UVSOR-FEL

Shigeru KODA, Masahito HOSAKA, Jun-ichiro YAMAZAKI and Hiroyuki HAMA
UVSOR Facility, Institute for Molecular Science, Myodaiji, Okazaki 444-0867

Synchronism between an FEL micropulse and an electron bunch is crucial to maintain lasing stability of storage ring FEL. However, in actual lasing, the synchronous condition is continuously disturbed by various factors such as thermal deformation of the optical cavity mirrors due to spontaneous radiation. We are developing a feedback system which corrects an longitudinal length of the optical cavity by changing the storage ring rf frequency. The control accuracy of the time deviation between the micropulse and the bunch has been required to be less than 10 ps that is the temporal width of the FEL micropulse. A phase detection technique was employed as a measurement method of the time deviation. The feedback system based on this method is different from systems developed in other FEL facilities of Super ACO[1] and Duke University[2].

The FEL light signal $f_{FEL}(t)$ and the electron bunch signal $f_e(t)$ can be expanded by harmonics of a round-trip frequency f_0 in the optical cavity as following

$$f_{FEL}(t) = f_0 \sum_{n=-\infty}^{\infty} F_{FEL}(2n\pi f_0) e^{2n\pi f_0 ti},$$

$$f_e(t) = f_0 \sum_{n=-\infty}^{\infty} F_e(2n\pi f_0) e^{2n\pi f_0 ti},$$

where n is a harmonic number and $F_{FEL}(2n\pi f_0)$, $F_e(2n\pi f_0)$ are Fourier transforms for the pulse shapes of an FEL micropulse and an electron bunch with angular frequency $\omega = 2n\pi f_0$, respectively. When the time deviation Δt of the micropulse signal occurred with respect to the electron bunch signal, the phase between the micropulse and the bunch is changed as $\Delta\phi = 2\pi n f_0 \Delta t$ in harmonic number of n. The time deviation Δt can be decided by measuring the phase $\Delta\phi$. The sensitivity for the time deviation is directly proportional to the number n in principle.

The schematic diagram of the feedback system is shown in Fig. 1. Band pass filters extract one harmonic component from signals of the electron bunch and the FEL light. The phase in the harmonic component is measured by a phase detector and then the rf frequency is controlled according to the detected phase. Considering the tradeoff between S/N ratio and the phase angle sensitivity, we measured the phase in a frequency component of 270 MHz, which corresponds to the 24-th harmonic component for the round-trip frequency f_0 of 11.3 MHz.

The flowchart of the feedback is shown in Fig. 2. The phase was converted to an amplitude signal by the phase detector. The signal is sampled by an ADC with sampling rate of 10^3 samples/sec, and an average phase deviation is calculated. When amplitude of the phase deviation exceeds one threshold value $\Delta\theta_{TH}$, the rf frequency is changed by values of $+\Delta f_{rf}$ or

$-\Delta f_{rf}$ to dump the time deviation. In the experiment, the value Δf_{rf} was set to be the minimum step frequency 0.1 Hz of the rf synthesizer. The ratio of $\Delta\theta_{TH}/\Delta f_{rf}$ was chosen to be equal to a measured ratio $\Delta\theta/\Delta f$ of the phase deviation $\Delta\theta$ for change Δf of the rf frequency in the CW lasing region.

The demonstration data of the feedback is shown in Fig. 3. The lines of upper and lower sides are the measured phase and the change of the rf frequency, respectively. The phase deviation of the FEL micropulse for the electron bunch was able to be maintained within range of σ=0.5 deg which means the time deviation of 5 ps.

The synchronism between the FEL micropulse and the electron bunch was successfully stabilized by the feedback system. As a next step, we are considering to develop more practical feedback system with faster response.

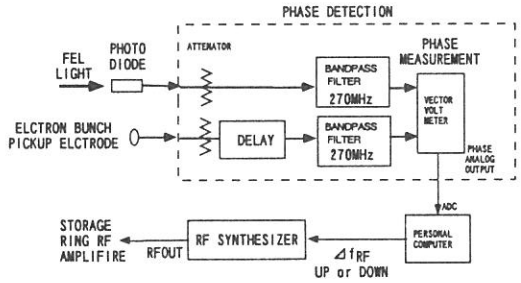

Fig. 1 Outline of the feedback circuit. The system consists roughly of the phase detection and the rf control.

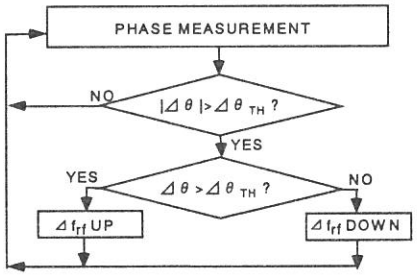

Fig. 2 Flowchart of the feedback program. The program repeats calculation of average phase and control of the rf synthesizer every one sec.

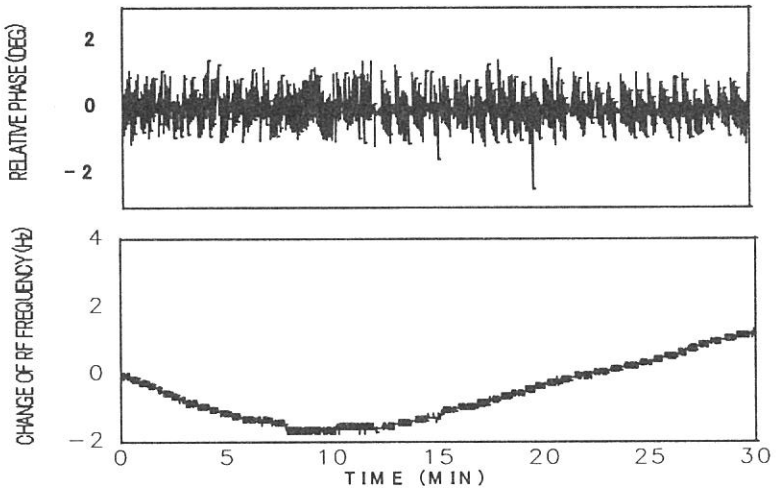

Fig. 3 Demonstration of the feedback operation. Measured phase (upper line) and changed rf frequency (lower line) are shown as a functions of time.

References

[1] M.E. Couprie, D. Garzella, T. Hara, J.H. Codarbox and M. Billardon, Nucl. Instr. and Meth. in Phys. Res. **A358**(1995) 374

[2] V. N. Litvinenko, et al, SPIE **2988**(1997)188

UVSOR

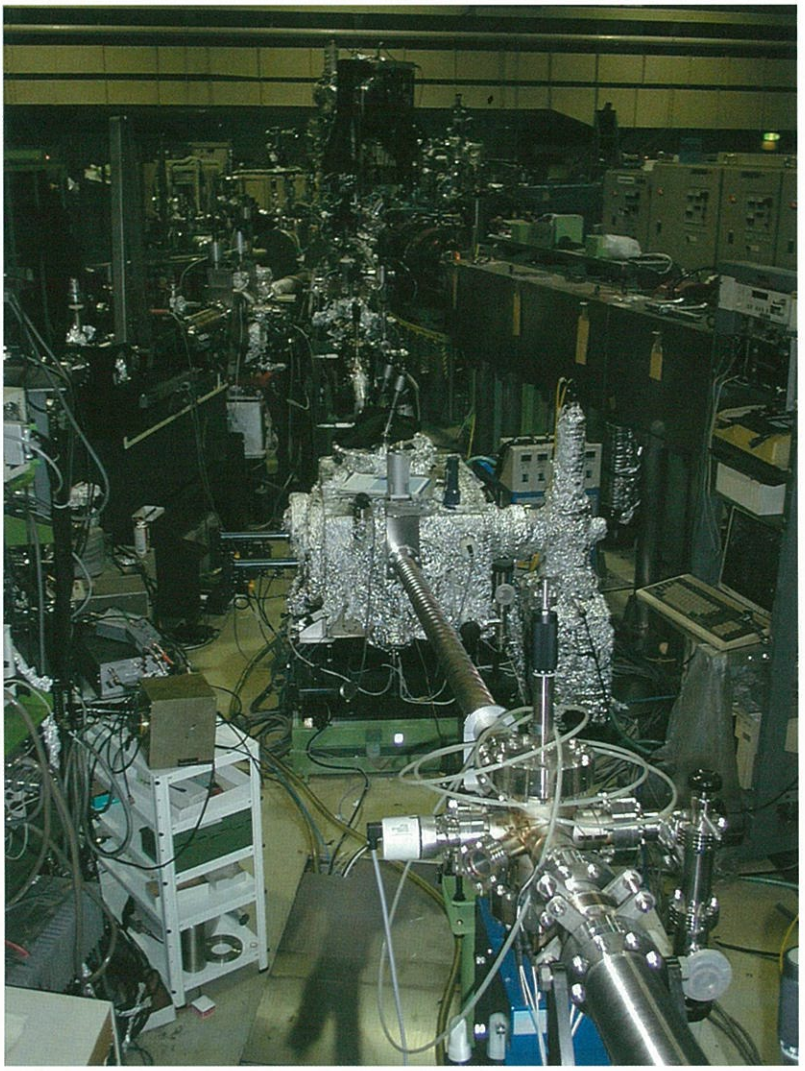

Instrumental Developments

Measurement of nonlinear momentum compaction factor in the UVSOR storage ring

Masahito HOSAKA, Jun-ichiro YAMAZAKI, Shigeru KODA and Hiroyuki HAMA
UVSOR Facility, Institute for Molecular Science, Okazaki 444-8585, Japan
Hitoshi TANAKA
Spring-8, Mikazuki, Sayo-gun, Hyogo 679-5198, Japan

There is a growing interest in operating of ring accelerator with extremely low momentum compaction factor. Such low momentum compaction factor, if attained, would lead to short bunched-beam that can be used for the generation of coherent radiation, and an isochronous condition that enables high power storage ring free electron laser. On the UVSOR storage ring, we have succeeded to operate the ring with momentum compaction factor reduced to one hundredth of the ordinal value by changing the dispersion function [1]. In the study we have found that nonlinear terms are serious problem to reduce momentum compaction factor further and precious study on them is needed, however there was no exact theoretical approach on them. Only recently Tanaka et al. have formulated a nonlinear dispersion function in storage ring and developed a code which gives higher order terms up to the fifth order [2]. In order to proceed with the study we have performed an experiment to observe the nonlinear behavior of momentum compaction factor and compared the result with the theoretical calculations.

The momentum compaction factors $\alpha_1, \alpha_2, \alpha_3, \ldots$ connect the momentum deviation dp/p to the fractional elongation $\Delta l/l$ as

$$\Delta l/l = \alpha_1(\Delta p/p) + \alpha_2(\Delta p/p)^2 + \alpha_3(\Delta p/p)^2 + \ldots . \tag{1}$$

Then a local value of the momentum compaction factor at a momentum deviation of dp/p can be written as

$$\alpha_{Local}(\Delta p/p) = \frac{d(\Delta l/l)}{d(\Delta p/p)} = \alpha_1 + 2\alpha_2(\Delta p/p) + 3\alpha_3(\Delta p/p)^2 + \ldots, \tag{2}$$

and the synchrotron oscillation frequency is given as

$$f_s = \frac{1}{2\pi}\sqrt{\frac{e\dot{V}_{RF}}{TE}\alpha_{Local}} = \frac{1}{2\pi}\sqrt{\frac{e\dot{V}_{RF}}{TE}\left[\alpha_1 + 2\alpha_2(\Delta p/p) + 3\alpha_3(\Delta p/p)^2 + \ldots\right]}, \tag{3}$$

where e, $\dot{V}_{RF}$, T and E are the electron charge, the slope of the RF field, the revolution time and the electron energy, respectively. Thus the nonlinear behavior of the momentum compaction factor can be investigated by measuring the synchrotron oscillation frequency as a function of the momentum deviation.

The experiment was carried out at the electron energy of 600 MeV, which is the maximum energy of the synchrotron and at the operation points of both positive and negative linear momentum compaction factor [3]. The synchrotron oscillation frequency was deduced through the collective synchrotron oscillation excited due to beam instability. We varied the RF frequency from the central value step by step until the acceptance limit and measured the synchrotron frequency as a function of the RF frequency. We also varied excitation current of focusing sextupole magnets in order to derive the dependence on sextupole strength. In Fig. 1, the experimental local momentum compaction factor (α_{Local}) deduced using Eq. (3) as a function of the deviation of the RF frequency is shown. As seen in the figure, nonlinear behavior due to the higher order momentum compaction factors ($\alpha_2, \alpha_3, \ldots$) is clearly observed. The central RF frequency ($\Delta f/f = 0$) in the figure was derived from the cross point that is independent of the value of the sextupole strength. This means that in the central RF frequency the electron beam passes through the averaged magnetic center of the sextupole magnets. The calculated local momentum compaction factor using the code [2] is also shown by the solid line in the figure. In the calculation, we have taken into account the higher order terms up to the fifth order (the maximum order obtained in the calculation code) and made a correspondence between the deviation of momentum and RF frequency as

$$\Delta f / f = -\left[\alpha_1 + \alpha_2(\Delta p / p) + \alpha_3(\Delta p / p)^2 + \alpha_4(\Delta p / p)^3 + \alpha_5(\Delta p / p)^4\right](\Delta p / p). \quad (4)$$

As seen in the figure, the calculated local momentum compaction factor agrees well with the experimental value. In order to confirm significance of the higher order terms of momentum compaction factor, we changed the maximum order of α included in the calculation and compared each value with the experimental ones. In the comparison, we found that up to the third order the calculation comes closer to the experiment as the maximum order increases, but on the calculation up to the forth order no actual improvement can be observed. This indicates that the contribution from more than the forth order terms is small and is obscured by the experimental errors. We think that source of the error comes from the incomplete modeling of the magnetic strength and the closed orbit distortion.

In this work, we have shown validity of the formalism by Tanaka et. al. up to the third order terms. More accurate study is needed to investigate further higher order terms and we are proceeding with it.

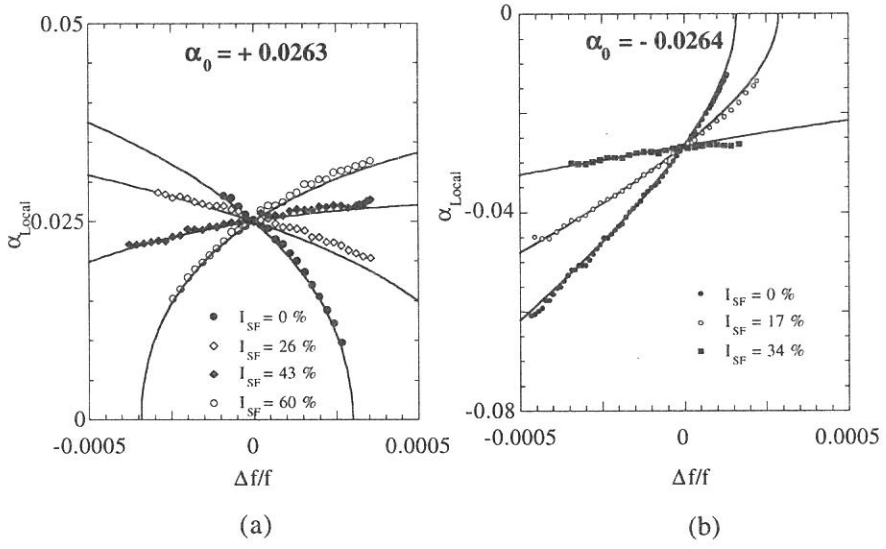

Figure 1. Variation of the local momentum compaction factor versus RF frequency for different sets of sextupoles , for positive (a) and negative first order momentum compaction factor. The solid line shows the calculated value.

References

[1] H. Hama et. al. Nucl. Instr. and Meth. A 329 (1993) 29.

[2] H. Tanaka et. al. Nucl. Instr. and Meth. A 431 (1999) 369.

[3] M. Hosaka et. al. Nucl. Instr. and Meth. A 407 (1998) 234.

(BL2B1)

Development of a new electron-ion coincidence analyzer

Kazuhiko Mase, Shin-ichiro Tanaka,[A] Eiji Ikenaga,[B] Kenichiro Tanaka,[B] Tsuneo Urisu[C]

Photon Factory, Institute of Materials Structure Science, High Energy Accelerator Research Organization, 1-1 Oho, Tsukuba 305-0801, [A]Department of Physics, Graduate School of Science, Nagoya University, Chikusa-ku, Nagoya 464-8602, [B]Department of Physics Science, Faculty of Science, Hiroshima University, Higashi-Hiroshima 739-8527, [C]Institute for Molecular Science, Okazaki 444-8585

Energy-selected electron ion coincidence (EICO) spectroscopy is an ideal tool for investigations of the ion desorption induced by electronic transitions, because it provides ion mass spectra for the ion desorption channels related to the selected electron transitions [1]. We have developed the first EICO apparatus combined with synchrotron radiation for the study of surface dynamics in 1996 [2]. A remodeled EICO analyzer was developed in 1998 the sensitivity of which was improved by the factor of 5 as compared with the second one [1]. In the present article, we describe the third EICO analyzer developed recently [3]. Every EICO analyzer was constructed on a 203-mm-diameter conflat flange as a bolt-on instrument, which consists of a cylindrical mirror analyzer (CMA) for detection of energy-resolved electrons, a time-of-flight ion mass spectrometer (TOF-MS) for ion detection and a retraction mechanism. Since the signal-to-background ratio of coincidence spectroscopy is linearly dependent on the collection efficiency of electrons and ions, the solid angles of CMA and TOF-MS were improved at every remodeling. Figure 1 shows a schematic diagram of the third EICO apparatus. In order to achieve a fair signal-to-background ratio within a reasonable data collection time, the solid angle of the CMA is designed to be 1.1 sr. The TOF-MS without a deflector is located coaxially with the CMA. With these reforms the signal-to-background ratio was improved by a factor of 5 as compared with the second one. The resolving power of the CMA was limited to $E/\Delta E = 100$ because of the large solid angle, the relatively large spot size of synchrotron radiation (1×1 mm^2) and ion extraction field (17 V/mm). The ion detection efficiency of the TOF-MS is 0.4. The EICO analyzer was attached to an ultrahigh vacuum chamber at the BL-2B1. The surface normal was set coaxial to the CMA and TOF-MS. A sample surface was excited by *p*-polarized radiation with an incident angle of 60° , and the emitted electrons were energy-selected and detected by the CMA, while the desorbed ions were mass-analyzed and detected by the TOF-MS. The ion counts were recorded as a function of the TOF difference between the energy-selected electron and the ion with a multi channel scaler (MCS) by taking the electron signal as the starting trigger. The ion desorbed in coincidence with the detected electron gives a coincidence signal at a specific TOF, while the ion irrelevant to the electron increases the background level. Since the selected electron kinetic energy corresponds to particular photoemission or Auger transitions, the coincidence signal intensity offers the yield of the ion desorption induced by the selected core-excitations or Auger transitions.

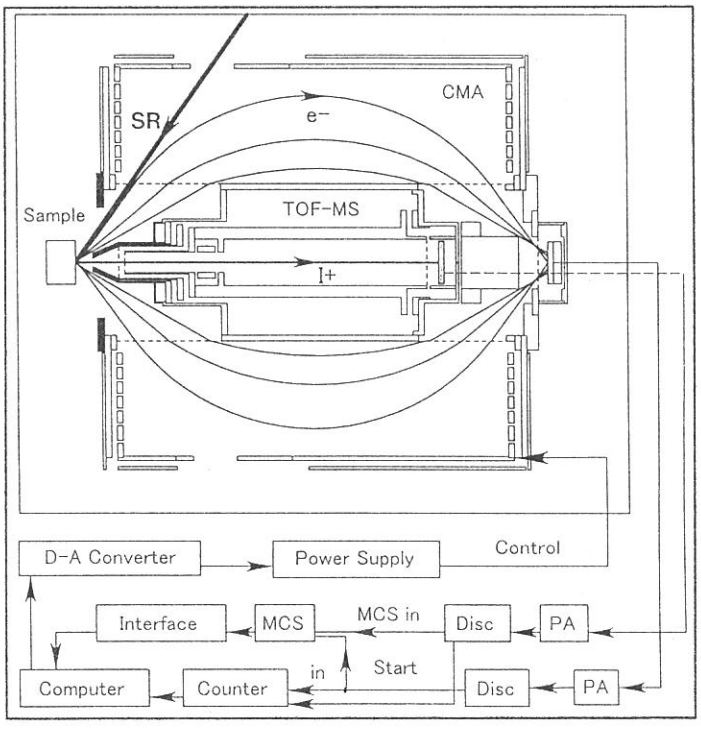

Figure 1. Schematic drawing of the third EICO apparatus.

References

[1] K. Mase *et al.*, *J. Electron Spectros. Relat. Phenom.* **101-103**, 13 (1999).

[2] K. Mase *et al.*, *Rev. Sci. Inst.* **68**, 1703 (1997).

[3] K. Mase *et al.*, *Surf. Sci.*, in press.

(BL2B2)

Performance of the Dragon-type monochromator

Masaki ONO[A], Hiroaki YOSHIDA[B], Hideo HATTORI[A] and Koichiro MITSUKE[A]

[A] *Department of VUV Photoscience, Institute for Molecular Science, Okazaki, 444-8585, Japan*
[B] *Department of Physical Science, Hiroshima University, Higashi-Hiroshima, 739-8526, Japan*

A Dragon-type monochromator has been newly constructed at the bending-magnet beamline BL2B2 of the UVSOR. The monochromator has been designed to cover the energy range of 20 – 200 eV with three gratings (G1 : 80 – 200 eV, G2 : 40 – 100 eV, G3 : 20 – 50 eV). A resolving power, $E/\Delta E$, of 5000 and a photon flux more than 1×10^{10} photons s^{-1} at 100 mA ring current are expected. The details of the monochromator were described in Ref. [1]. The optical alignment has been already finished. We have reported the performance of the monochromator, especially the resolving power and photon flux.

The resolving power has been evaluated from the ion yield spectra of the rare gas atoms ; the $3d_{5/2}^{-1}5p$ line of Kr (91.2 eV, exploited for G1 and G2) , $2snp + 2pns$ series of He (60 – 65 eV, for G2) and $3s^{-1}np$ series of Ar (25 – 30 eV, for G3). Figure 1 shows the ion yield spectrum of $3s^{-1}np$ series of Ar with a slit width of 100 μm. The series of the Rydberg states up to $n = 23$ is clearly observed. We have estimated the resolving power to be 12500 from the FWHM of the depression of $n = 18$ (2.3 meV) when the natural width, 0.23 meV calculated by n^{-3} rule, is ignored. The resolving power vs. slit width at 30 eV is shown in Figure 2. The solid line represent the dependence calculated theoretically by taking into account the entrance and exit slit widths, coma aberration and slope error of the grating [1]. The measured resolving power is higher than that expected.

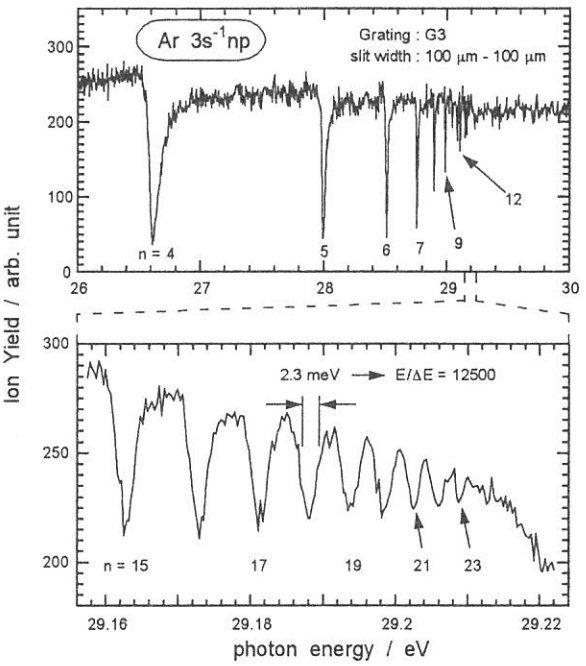

Fig. 1. Ion yield spectrum of $3s^{-1}np$ series of Ar with a slit width of 100 μm.

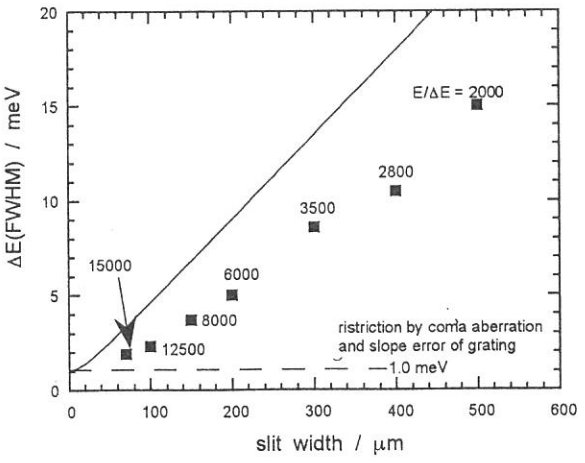

Fig. 2. Resolving power vs. slit width at 30 eV. The solid line shows the expected values [1].

The spectral shape of the $2snp + 2pns$ series of helium is asymmetric, and it is therefore difficult to estimate the resolution. However, the peaks become more symmetrical with increasing n because of the system resolution. Hence, we have judged the resolution based on the FWHM of the symmetrical peak. The resolution at 91.2 eV is obtained by fitting of the line shape of the $3d_{5/2}^{-1}5p$ peak of krypton to a Voigt function.

Figure 3 illustrates the resolving power and photon flux under the condition at the 100 mA ring current when both the entrance and exit slits are set to 100 μm wide. The solid line in the panel indicating the resolving power shows the expected values. Values of the resolving power measured at 30 eV and 60 eV are twice as high as those expected. It is lower than 5000 at 91.2 eV, though such performance has been predicted on the original design of the monochromator. At this energy the resolving power is also above the expected one. We have confirmation that the alignment procedure is fully completed.

The photon flux has been estimated by measuring the photocurrent of the gold mesh. The photon flux is more than 1×10^{10} photons s^{-1} in the region of 50 – 160 eV. In the region covered with G3 the photon flux seems to be low. However, the photon flux above 1×10^{10} photons s^{-1} has been achieved when the resolving power is lowered to 5000.

The alignment of the Dragon-type monochromator has been almost finished. The resolving power of 2000 – 8000 is available with the condition of the photon flux of 1×10^{10} photons s^{-1} at 100 mA ring current.

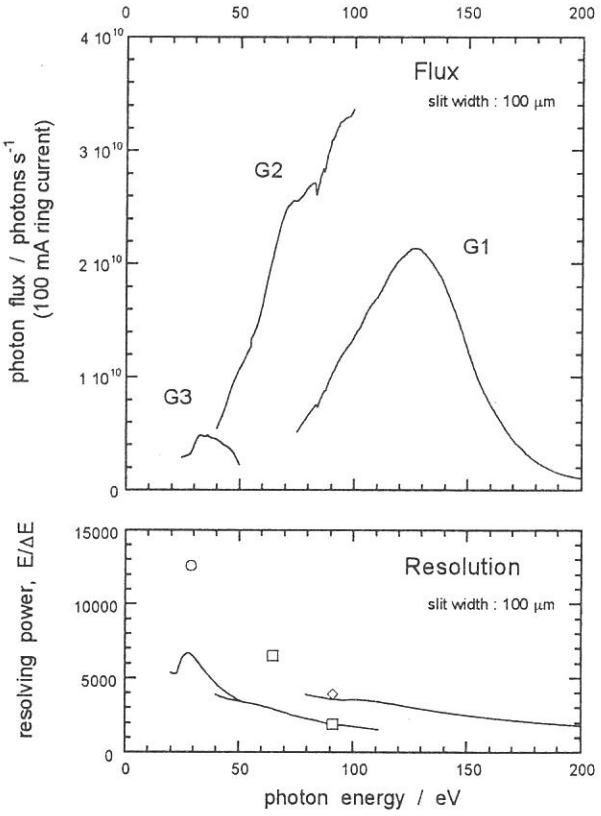

Fig. 3. Resolving power (down) and the photon flux at 100 mA ring current (up) when the entrance and exit slit widths are set to 100 μm. The solid lines in the lower panel show the expected values.

[1] H.Yoshida and K.Mitsuke, *J.Synchrotron Rad.* 5, (1998) 774.

(BL-4A)

Replacement of the new Pre-mirror Chamber in the beam line 4A

Harutaka Mekaru[a], Noritaka Takezoe[a], Hideyuki Noda[b], Hideaki Yanagita[c], Kazuhiro Kanda[d], Shinji Matsui[d], Kou Kurosawa[a], Eiken Nakamura[a], and Tsuneo Urisu[a]

[a]*Institute for Molecular Science, Okazaki, Aichi, 444-8585*
[b]*The Graduate University for Advanced Studies, Okazaki, Aichi, 444-8585*
[c]*Department of Electric and Electronic engineering, Miyazaki University, Miyazaki, Miyazaki 889-2192*
[d]*Laboratory of Advanced Science and Technology for Industry, Himeji Institute of Technology,, Ako, Hyogo 678-1201*

Since the beam line 4A1 and 4A2 are going to be used for experiments of fabricating nano-structures by SR-stimulated etching and thin film deposition, and for analysis of the SR-stimulated reaction by several *in situ* observation techniques, we established several criteria for the design of the beam lines. The beam spot size on the sample surface was designed to be $\geqq 3 \times 3$ mm^2. To obtain a large photon flux, we decided to use only one pre-mirror for focusing, designed so that it can accept as wide a horizontal divergence of the emitted beam from the light source as possible.

The pre-mirror of the beam line 4A1 is an elliptically-bent cylindrical quartz mirror with a Pt coating on its surface. (The radius of the cylindrical curvature is 253.0 mm and the longer and shorter radii of the elliptical curvature are, respectively, 4880 mm and 290 mm.) A length of the pre-mirror is 530 mm and a height is 30 mm. It was set at a point 2.35 m downstream from the light source point of the bending magnet with a grazing incident angle of 4 degrees. The horizontal and vertical acceptance angles of the pre-mirror are, respectively, 16.0 mrad and 13.0 mrad. The reflected beam is focused at a point 7.4 m downstream from the center of the pre-mirror and has an elliptical spot size of about 5 mm $\times$ 2 mm at this focus point.

The pre-mirror of the beam line 4A2 is also an elliptically-bent cylindrical quartz mirror with a Pt coating on its surface. (The radius of the cylindrical curvature is 210.0 mm and the longer and shorter radii of the elliptical curvature are, respectively, 7248 mm and 279 mm.) A length of the pre-mirror is 490 mm and a height is 30 mm. It was set at a point 2.35 m downstream from the light source point of the bending magnet with a grazing incident angle of 3 degrees. The horizontal and vertical acceptance angles of the pre-mirror are, respectively, 11.1 mrad and 13.0 mrad. The reflected beam is focused at a point 12.2 m downstream from the center of the pre-mirror.

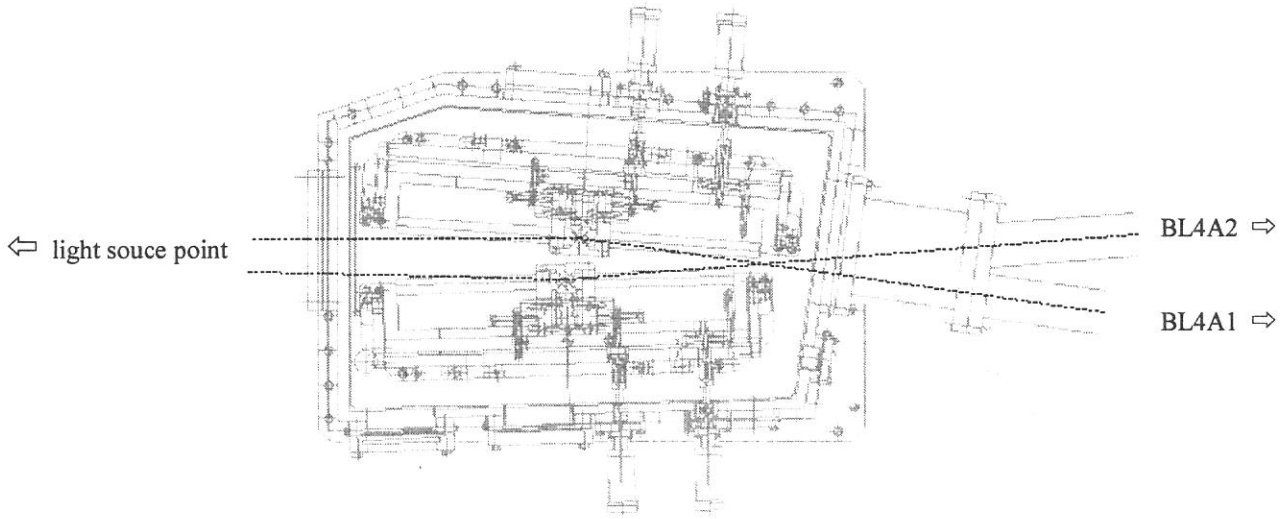

Figure 1. Top view of the pre-mirror chamber of the beam line 4A.

(BL8B1)

Improvement of the degree of liner-polarization at BL8B1

Tatsuo Gejo, Eiken Nakamura and Eiji Shigemasa
Institute for Molecular Science, Myodaiji, Okazaki 444-8585, Japan

It is well known that synchrotron radiation (SR) having a vertical spread of ~1 mrad from bending magnets is linearly polarized (more than 90%) horizontally. The degree of linear polarization depends on the detection angle for SR relative to the orbital plane of the electrons stored. This will be a maximum when the vertical position of the center of the first mirror matches with that of the orbital plane. At BL8B1 the degree of linear polarization was measured with the use of a soft X-ray multilayer polarizer and was determined to be about 0.6 [1]. This poor value was attributed to the fact that the vertical center of the acceptance angle of the first mirror was lower than the orbital plane.

The linear-polarization degree of monochromatized SR has been improved by the re-alignment of the beamline components (M1, M2, gratings, M3 and TOF chamber), with the help of well-polarized UV light. Fig. 1 shows the setup for monitoring the degree of linear polarization of the UV light. The vertical aperture of the diaphragm was placed in front of a UV filter and a polarizer. The width of the diaphragm was kept at 1mm during the measurements. In order to obtain only the central part of the photon beam, the polarization degree was monitored with the polarizer and a Si photodiode. Then, the position of the diaphragm was determined to be the polarization degree at maximum. After the determination of the central part of the SR beam, the heights of all the beamline components were moved so as to align the beam through the diaphragm. Consequently, we have moved them down 3mm to the ground level. The angle of the gratings was so important that a tilt angle of the monochromator was monitored during the re-alignment by a tilt sensor (Koku-Denshi MC100L) and was maintained at the fixed angle during the course of the experiments.

The improved polarization degree has been measured, again, by the soft X-ray multilayer polarizer and was determined to be more than 98%. This improvement will be particularly useful for Magnetic Circular Dichroism (MCD) measurements in core absorption.

Mr. Hayashi and Mr. Kondo at IMS deserve special thanks for their technical support. We are also indebted to Mr. Saito and Prof. Watanabe at Tohoku University for providing us the information on the degree of linear polarization.

[1] T. Hatano, W. Hu, M. Yamamoto and M. Watanabe, UVSOR Activity Report 1997, 64.

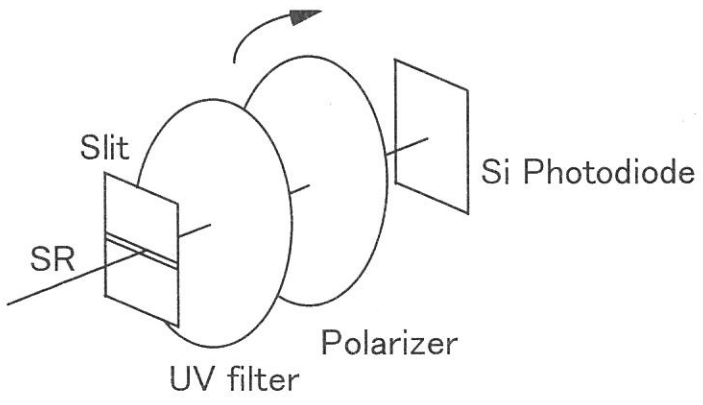

Fig. 1: The system for measurement of the polarization degree of UV light.

(BL4A2)

Design and Construction of BL-4A2 Beam Line for Nano-Structure Processing

N. Takezoe[1], H. Yanagida[1,2], K. Kurosawa[1], T. Urisu[1], H. Mekaru[1], H. Noda[3],
S. Matsui[4], K. Kanda[4] and H. Uchida[5]

[1]*Institute for molecular Science, Myodaiji, Okazaki, 444-8585, Japan*

[2]*Department of Electric and Electronic Engineering, Faculty of Engineering, Miyazaki University, Gakuenkibanadai-Nishi, Miyazaki, 889-2192, Japan*

[3]*The Graduate University for Advanced Studies, Myodaiji, Okazaki, 444-8585, Japan*

[4]*Laboratory of Advanced Science and Technology for Industry, Himeji Institute of Technology, Kamigori-cho, Ako-gun, Hyogo, 678-1205 Japan*

[5]*Electrical and Electronic Engineering, Toyohashi University of Technology, Tenpaku-cho, Toyohashi, 441-8580, Japan*

Nano structures must open new windows not only for surface physics and chemistry but also for electronic and photonic devices. Synchrotron radiation stimulated surface chemical reactions have been a most promising way to fabricate nano structures, because they offer a process with the advantages of high-site selectivity by core electron excitation and also free-of damage with atomic scale. Since a new beam line with higher flux is required for the processing, we have been designing and constructing BL-4A2 beam line for the nano structure fabrication.

We have been constructing a new beam line BL-4A2 which consists of white ray beam, ultra-high vacuum scanning tunneling microscope (UHV-STM) and photo-stimulated reaction chamber. In near future, we are going to join a near field optical microscope for monitoring optical properties with the atomic scale to them. Figure 1 shows the outline of the beam line, which consists of pre-focusing mirror (M1), secondary mirror (M2), monitor port, two differential pumping ports, reaction chamber and STM. An elliptically bent cylindrical mirror made of quartz coated with platinum is used as the pre-mirror. The reflected beam is focused at a point of 12.7 m down stream from the center of the pre-mirror and has a spot size of 8x6 mm^2. Low energy electron diffraction (LEED) is installed in the reaction chamber for in-situ characterization of substrate surfaces and also STM is for

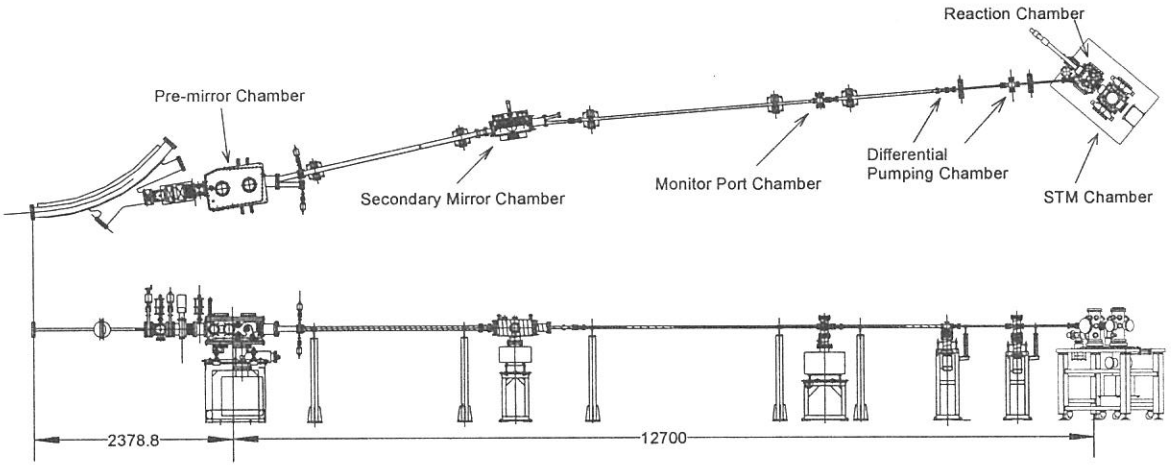

Figure 1. Schematic drawings of the BL-4A2 beam line with a reaction chamber and STM.

observation of the surface processes with atomic scale. We have a plan to make a photonic band-gap structures in a SiO_2 planer waveguide and study evanescent light from the waveguide surfaces with near field optical microscope.

First, we replaced the mirror chamber of the beam line BL4A with the new type of thing. In case of the new model chamber, when an optical-axis was considered a x-axis and a perpendicular on the floor was considered a z-axis, the tilting (ϕ) which moved around the x-axis, and a liner motion in the y-axis direction are possible. Though only the rotation which moved around the z-axis could be adjusted in case of the usual chamber by the liner motion feedthroughs in the vacuum. Helium neon laser was irradiated from the downstream side of the beam line to adjust the optical-axis, without SR. It is because the front-end valve has the atmosphere leak and it is dangerous to keep the pre-mirror chamber atmospheric pressure for a long time. Each degree of vacuum of the pre-mirror chamber and the secondary-mirror chamber reaches 9.8×10^{-10} Torr and 3×10^{-10} Torr at present. However, a mirror of a BL4A2 inside the pre-mirror chamber, which should be faced on the xy-plane, is slanted and it was proved that a beam form warped in the parallelogram. It can think that this is because a displacement occurred in the holder by the vibration when a HELICOFLEX of the pre-mirror chamber were secondary tightened. The pre-mirror chamber will atmosphere leak on that occasion, and alignment will be done with the SR because the valve exchange of the front end is done when it is shut down next time. Therefore, the adjustment of the STM2 chamber that is an end station is being made in the present. We must attain the ultra high vacuum of 10^{-11}Torr level to do in-situ observation with STM. Besides, because it had to get rid of mechanical vibrations, usual exhaust was reconsidered and improved as the figure 2. A sputter ion pump of 400 m^3/s, a non-evaporable getter pump and a nitrogenous trap are attached to the bottom part of the STM chamber, and a TMP(turbo molecular pump) of 300 l/s is attached to the top and the TMP of 50 l/s is connected in series. The sputter ion pump of 200 m^3/s is attached to the reaction chamber. A present degree of vacuum is 8×10^{-11} Torr though heating of the sample holder and nitrogenous cooling aren't being done. Therefore, it will reach the degree of a vacuum that it aims at while an experiment is being done.

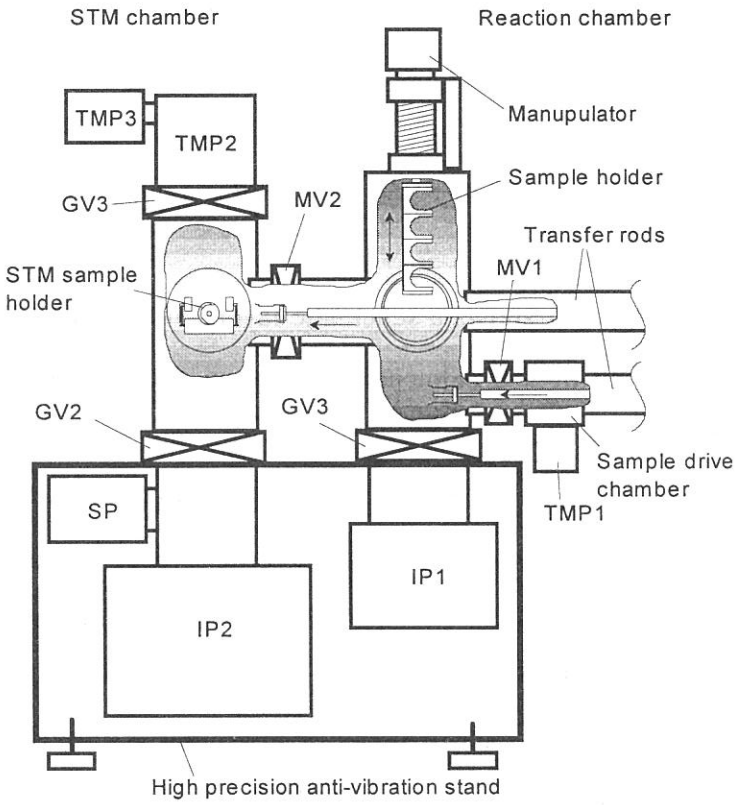

SP: Non-evaporable Getter Pump
GV1, 2, 3: Gate Valves
MV1, 2: Manual Gate Valves
TMP1, 2, 3: Turbo Molecular Pumps (1&3; 50 l/s, 2; 300 l/s)
IP1, 2: Sputter Ion Pumps (1; 0.2 m^3/s, 2; 0.4 m^3/s)

Figure 2. Schematic drawings of the improved exhaust system of the end-station.

(BL4B)

Design for a new monochromator on BL4B

Yasutaka Takata, Tatsuo Gejo, and Eiji Shigemasa
Institute for Molecular Science, Okazaki 444-8585, JAPAN

Recent conceptual and technological improvements to monochromators for synchrotron radiation have enabled us to realize various studies on vibrational spectroscopy in the soft x-ray range (100 ~ 1000 eV), which contains the *K*-shell thresholds of chemically important elements like C, N, and O, even without the use of undulator radiation [1]. At the UVSOR, there is only one monochromator for high resolution spectroscopy in the photon energy region of interest (250–550 eV). A maximum resolving power of 4000 at 400 eV is achievable with this monochromator, but due to a little complicated scanning mechanism, it has difficulty maintaining such high resolution in the entire photon energy range. Design study for a new monochromator at BL4B has recently been started in order to improve the situation. A Varied-line-spacing Plane Grating Monochromator (VPGM) has been chosen for this work. Thanks to the availability for high quality gratings and simple scanning mechanism, VPGM seems to be one of the most trustworthy monochromators to realizing high resolution in the soft x-ray range.

Figure 1 shows a schematic layout of the optical elements of the present VPGM. In front of all optical elements, there is an aperture, located 1.9 m from the source position. The usual setting of this aperture is 3.8 $mm_V \times 14.3$ mm_H, which limits the half acceptance angle to 1 $mrad_V \times 3.75$ $mrad_H$. The radiation is deflected horizontally by a cylindrical mirror M_0. This also serves as a vertical focusing mirror (sagittal focusing), which focuses the radiation onto an entrance slit S_1. A cylindrical mirror M_1 is located 1.1 m behind M_0, and focuses the radiation horizontally. M_0 and M_1 (Si substrates) are cooled from both sides by water-cooled copper blocks coated with Ni. A spherical mirror M_2 is one of the most important optical element to realizing high resolution, which focuses the radiation through S_1 onto an exit slit S_2. Two holographically ruled laminar profile plane gratings with the varied-line-spacing are designed to cover the energy range from 100 eV to 700 eV. The gratings with the groove densities of 266.7 and 800 l/mm cover the spectral ranges of 100–250 and 250–700 eV, and are interchangeable without breaking the vacuum. The

including angle of the gratings is 174°, and the fixed entrance- and exit-slit arm lengths are 4.0 and 4.006 m. A refocusing mirror M_3 has a toroidal shape, which focuses the monochromatized radiation at the sample position. The incidence angle of M_3 is 87.5°, in order to make the exit beam horizontal. All the gratings and mirrors are coated with Au.

The resolution of the present monochromator was studied by ray-tracing simulation as well as analytical estimation. As a result, it is found that a resolving power E/ΔE of more than 5000 is achievable over the energy range from 250 to 700 eV with one single grating having the groove density of 800 l/mm. It is also seen that the beam size (FWHM) at the sample position is smaller than 0.4 $mm_V \times 0.6$ mm_H, even with full size openings of the entrance and exit slits. The throughput photon flux estimated ranges from 10^8 to 10^{10} photons/sec for the ring current of 100 mA, with a resolving power of 5000.

References

[1] Y. Kitajima et al., J. Synchrotron Rad. **5**, 729 (1998).

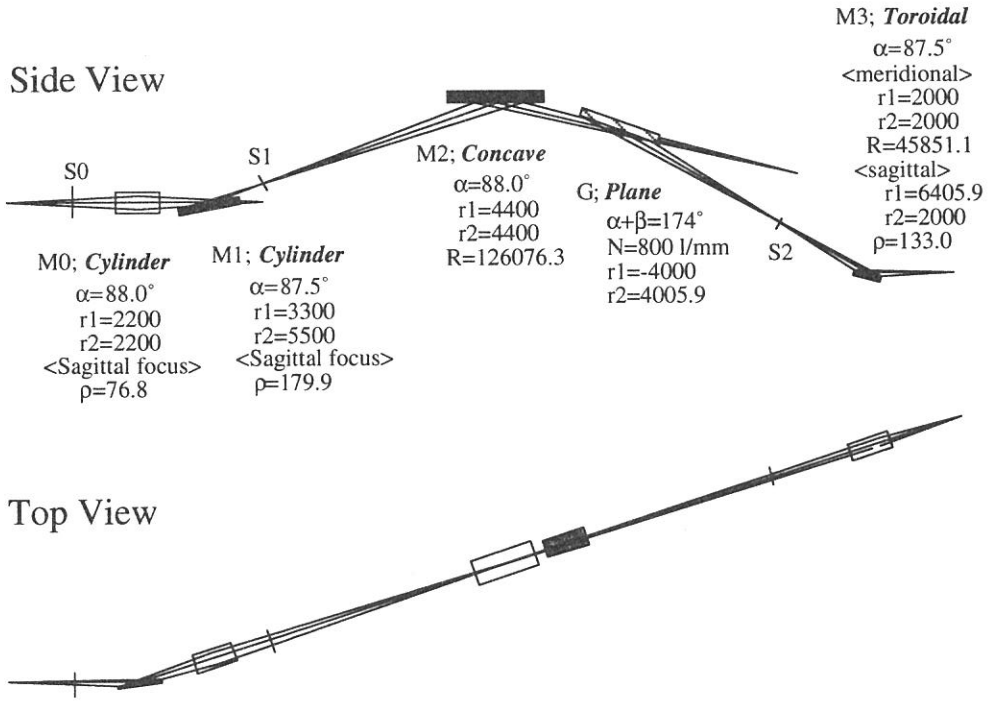

Figure 1. Schematic layout of the designed monochromator.

BL5B

Two-color reflection multilayers for He-I and He-II resonance lines for microUPS using Schwarzschild Objective

Takeo EJIMA, Yuzi KONDO, and Makoto WATANABE
Research Institute for Scientific Measurements, Tohoku University, 2-1-1 Katahira, Aoba-ku, Sendai, 980-8577

Two-color multilayers reflecting both He-I (58.4 nm) and He-II (30.4 nm) resonance lines have been designed and fabricated for reflection coatings of Schwarzschild objectives of micro ultraviolet photoelectron spectroscopy (UPS) instruments. They were designed to consist of top layers and piled double layers so that their reflectances for both He-I and He-II resonance lines are more than 20 %. Fabricated are multilayers of SiC(top layer)-Mg/SiC(double layers) and SiC(top layer)-Mg/Y_2O_3 (double layers), and their reflectances for the He-I and the He-II are 23 % and 17 %, and 20 % and 23 %, respectively.

KEYWORDS: multilayer, He-I, He-II, resonance line, ultraviolet, reflection coating, mirror

1. Introduction

Photoelectron micro-spectroscopy is powerful method to investigate electronic structures of condensed matters of small size and those consisting of grains.[1] In laboratories, He-I (58.4 nm) and He-II (30.4 nm) resonance lines are used for ultraviolet photoelectron spectroscopy (UPS). Changing the exciting photon energy for photoelectron spectroscopy is important to obtain partial density of states (p-DOS) of valence bands.[2] Even if the energies of the initial states are same, symmetries of final states excited by He-I and He-II lines are different. The difference is due to the dependence of the transition matrix element on the exciting photon energies.[2,3] Therefore, the p-DOS with different symmetries can be seen even if the photoelectrons are emitted from valence states with the same binding energy. For example, the Ce 4f p-DOS's in $CeSi_2$ were obtained using He-I and He-II lines.[4] Therefore, the microUPS instruments of the practical use are very promising tool if the suitable demagnifying optical elements for both resonance lines are available.

The Schwarzschild objective (SO) is one of microfocusing optical elements in ultraviolet and soft x-ray regions.[5] In the SO unit, the mirror surfaces should be coated with high reflectance materials for normal incidence. One of such materials is the multilayer of the piled double layers consisting of two materials with period of more than 10 (usual multilayer). However, the usual multilayer has a high reflectivity at only a certain wavelength for a fixed angle of incidence.

Therefore, in this paper, special *two-color* multilayers reflecting both He-I and He-II resonance lines have been designed and fabricated for reflection coatings of the SO units in microUPS instruments.

2. Design and fabrication of *two-color* multilayers

There are several materials which reflect He-I line efficiently (> 20 %) by their single layers. However, there are no such materials for He-II line, so that usual multilayers are required. Extinction coefficients of materials are generally larger for He-I line than for He-II line. Therefore, the *two-color* multilayer was designed to be composed of the top single layer reflecting He-I line with high transmittance for He-II line and the usual multilayer reflecting He-II line under the top layer.

To obtain high reflectance at interfaces, two materials were selected according to the following principle. The principle is that, the absolute value of the difference of Fresnel reflection coefficients (*abs.*) between two materials has to be as large as possible at the design wavelength.[6] (The Fresnel coefficient of the vacuum is 0.) Adding to this, the imaginary parts of these Fresnel coefficients (*im.*) which are proportional to the extinction coefficients have to be as small as possible to minimize the absorption of the light.

In Figs. 1(a) and 1(b), Fresnel reflection coefficients of various materials for He-I and He-II resonance lines at the angle of incidence of 0° are plotted in the complex-plane using the Henke's and the Palik's data.[7-9] The single layer of SiC was chosen for the He-I reflection, because in SiC the *abs.* is large for He-I line as shown in Fig. 1(a), and the *im.* is small for He-II line as shown in Fig. 1(b). The piled double layers of Mg/Y_2O_3 and Mg/SiC were chosen for the He-II reflection. In the case of Mg/Y_2O_3 multilayer, the *abs.* between Mg and Y_2O_3 is large as shown in Fig. 1(b), so that the high reflectance can be achieved by a small number of layers. In the case of Mg/SiC multilayer, the *abs.* between Mg and SiC is small, but the *im.* of each material is small, so that the high reflectance can be achieved by a large number of layers.

Calculations of reflectance of the multilayers are performed using the recurrent method with extension as for the number of materials.[6] The *two-color* multilayers were designed to have reflectances of more than 20 % for both He-I and He-II lines. Through the calculations, the thickness of the layers in the SiC (top layer)-Mg/SiC (double layers) and the SiC (top layer)-Mg/Y_2O_3 (double layers) were determined. The former multilayer has an advantage of being composed of only two materials. Calculated reflectances are presented as dashed curves in figure 2. The angle of incidence to all multilayers is 10° in the figure.

All samples were fabricated by magnetron sputtering. The sputtering system (ANELVA SPL-500) is of a vertical type with the targets and substrates placed vertically. Mg was dc-sputtered with an input power of 100 W, and SiC and Y_2O_3 were rf-sputtered with input power of 200 W. The Ar pressure was 2.0 mTorr for all the depositions, while the base pressure was 2.0×10^{-6} Torr. The multilayers were deposited onto commercially avail-

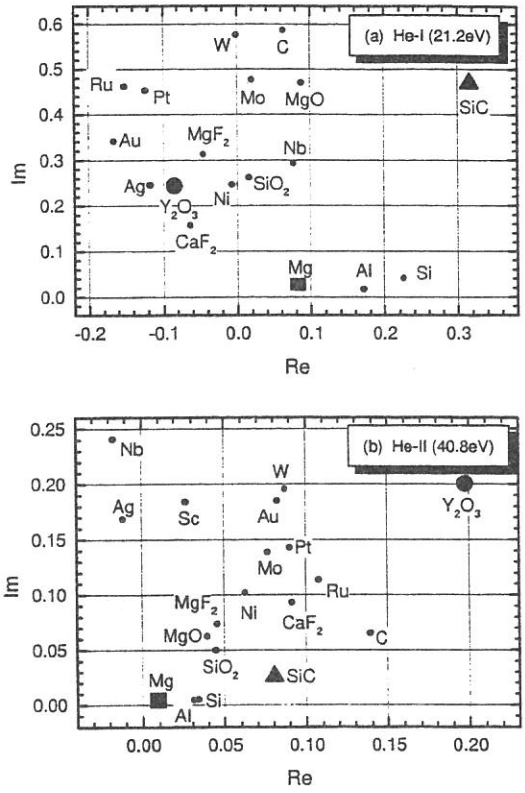

Fig.1: Fresnel reflection coefficients of various materials for He-I (58.4 nm), (a), and He-II (30.4 nm) resonance lines, (b).

able 4 inch (10.16 cm) Si wafers. Effective deposition rate of Mg, SiC, and Y_2O_3 are 0.12 nm/s, 0.02 nm/s, and 0.04 nm/s, respectively. The film thickness was measured by an x-ray diffractometer within 5 % error for the top layers and 2 % error for the double layers.

3. Results and Discussion

Reflectances of *two-color* multilayers were measured with a reflectometer at the beamline BL5B.[10] In this experiments, we used the combinations of the G3 grating and the M25 mirror for the 25–60 nm range and the G3 grating and the M26 mirror for the 50–70 nm range. An average resolving power $\lambda/d\lambda$ was about 500. The resolution of the angle of incidence was about 1° in reflection measurements.

In Fig. 2, reflectances of SiC(14.4 nm)-Mg(10.4 nm)/SiC(6.1 nm) multilayer at the angle of incidence of 10° are presented. In the figure, the left and right solid curves represent experimental results obtained by the G3-M25 and G3-M26 combinations, respectively. The dashed curve represents the calculated result. In the figure, the measured reflectance shows the rise around 28 nm, becomes maximum (20 %) at 31 nm and decreases toward 33 nm. From 33 nm to 40 nm, the reflectance is less than 10 % showing small oscillation. Above 40 nm, the reflectance increases toward the longer wavelength. Comparing experimental result obtained by G3-M25 combination with calculated ones, spectral shapes and absolute values of reflectances resemble to each other between 30 nm and 40 nm. The measured reflectance obtained by the G3-M25 combination did not connect smoothly to that obtained by the G3-M26 combination between 50 nm and 60 nm. The reflectance obtained by G3-M26 combination increases from 20 % to 30 % as the wavelength increases from 50 nm to 70 nm. The measured reflectance obtained by G3-M26 does not differ much with the calculated one above 55 nm. Therefore, we supposed the discrepancy may be due to the effect of the higher order light in the output light in the G3-M25 combination. Therefore, we adopted the results of the G3-M26 combination as the obtained values of the reflectances for He-I line. The reflectance of the SiC-Mg/SiC for the He-I is 23 % and for the He-II, 17 %.

In this study, the reflectance of the SiC-Mg/Y_2O_3 was also measured. It was 20 % for the He-I and 23 % for the He-II. The detailed results will be reported elsewhere.

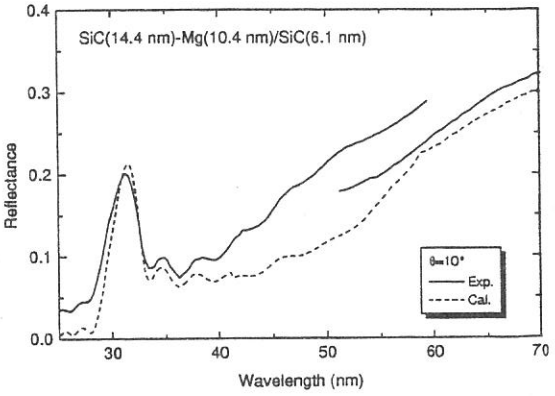

Fig.2: Measured reflectance of SiC-Mg/SiC multilayers for 10° angle of incidence.

References

1) *see for instance,* H. W. Ade: Nucl. Instrum. Methods Phys. Res. **A319** (1992) 311.
2) *Photoemission in Solids I*, ed. M. Cardona and L. Ley, (New York, Springer-Verlag, 1978).
3) J. J. Yeh and I. Lindau: At. Data Nucl. Data Tables **32** (1985) 1.
4) M. Grioni, D. Malterre, P. Weibel, B. Dordel and Y. Baer: Physica **B 38–43** (1993) 186.
5) see for instance, F. Cerrina: J. Imag. Sci. **30** (1986) 80.
6) M. Yamamoto, S. Nakayama and T. Namioka: SPIE Vol. **984** (1988) 160.
7) *Handbook of Optical Constants of Solids*, ed. E. D. Palik, (San Diego, Acad. Press. Inc., 1985).
8) B. L. Henke, P. Lee, T. J. Tanaka, R. L. Shimabukuro and B. K. Fujikawa: At. Data Nucl. Data Tables **27** (1985) 1.
9) B. L. Henke, J. C. Davis, E. M. Gullikson and R. C. C. Perera: Lawrence Berkley Laboratory **LBL-26259** and a diskette containing the data (1988).
10) M. Sakurai, S. Morita, J. Fujita, H. Yonezu, K. Fukui, K. Sakai, E. Nakamura, M. Watanabe, E. Ishiguro and K. Yamashita: Rev. Sci. Instrum. **60** (1989) 2089.

(BL5B) **On the diminishment of the high order light in the extreme ultraviolet region**

*M.Nakamura, *A.Yamazaki, *K.Shiomi, and #I.Yoshikawa

* *Faculty of Earth and Planetary Science, University of Tokyo, Bunkyo-ku, Tokyo 113-0033*

\# *Institute of Space and Astronautical Science, Sagamihara, Kanagawa 229-8510*

We plan to optically observe ion and neutral atom distributions in space plasma environment. Ions and atoms resonantly scatter the solar emissions in extreme ultraviolet region. Our targets are helium ion emission at 30.4nm (HeII emission), helium atom 58.4nm (HeI emission) and oxygen ion 83.4nm (OII emission). Intensity of emission is proportional to column density of particles along the line of the sight, so optical observations bring to us the macroscopic particle distribution.

Japan's Mars orbiter Planet-B (NOZOMI) was launched in July 1998 to the parking orbit around the earth and now is cruising to the Mars orbiter. The eXtreme UltraViolet (XUV) scanner is onboard the NOZOMI spacecraft and observes resonantly scattered light from helium atoms and ions. We succeeded to observe the terrestrial plasmasphere by detecting HeII emission [1] and the emission reflected from the surface of the moon on the parking orbit, and in the cruising phase to the Mars detect HeI and HeII emission from the interplanetary medium.

Also we are developing a mirror for detecting OII emission. In this machine time, we examine the characteristics of SOR beam at BL-5B and build the method to produce monochromic beam, which includes no high order light in extreme ultraviolet region, especially from 20nm to 100nm of wavelength. Finally, we measure transmittance of thin metal filters, reflectivity of multilayer-coated mirrors and quantum efficiency of Micro Channel Plates (MCPs) detector with the monochromic beam.

Method to produce monochromic light.

In the latest machine time, we confirm that an Al/Mg/Al filter removes the high order light in 25-50nm wavelength region and make the monochromic light beam produced to the calibration chamber. As the same way, we tried to remove high order light in other region with Al 430.6nm-thickness filter, Sn 354.5nm filter, and In 583.0nm filter. Figure 1 shows diffraction patterns of beams transmitting the Sn filter at the wavelength of 58.4nm. This pattern has no high order line, therefore, it is clear that the beams consist of one specific wavelength light. Furthermore we measure transmittances of some metal filers and compare the ones evaluated with discharged light source. The results are shown as Figure 2a, 2b, and 2c, which represent the transmittance of Al 149.2nm, Sn 184.0nm, and In 158.0nm filter, respectively. We conclude that high order cut filter have good performance.

Quantum efficiency of MCPs

The quantum efficiency measurement of backup MCPs for the XUV is effective to estimate

temporal development of the detectable efficiency on flight. So we revalue quantum efficiency of a reference MCPs for laboratory at 30.4nm and 58.4nm. We evaluate the efficiency by the comparison between the output current from absolutely calibrated photodiode and the count rate of the MCPs, to be 5% at 58.4nm and 10% at 30.4nm.

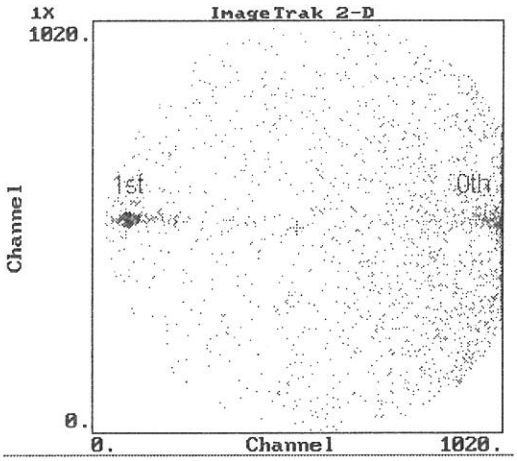

Figure 1. The diffraction pattern of 584nm light through Sn filter.

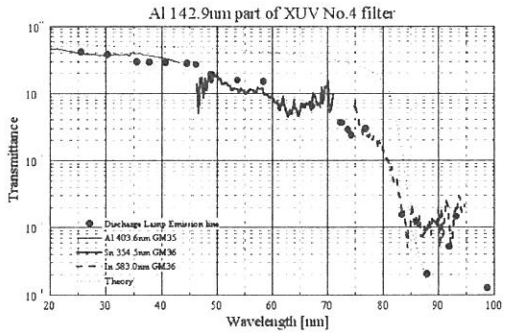

Figure 2a. The transmittance of Al filter.

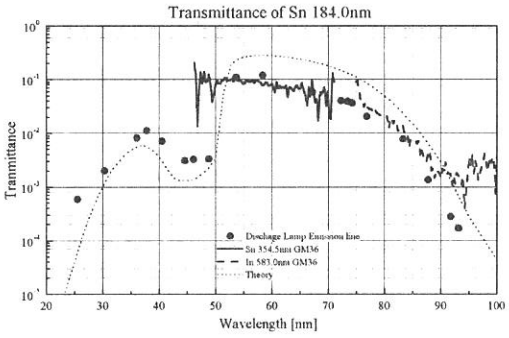

Figure 2b. The transmittance of Sn filter.

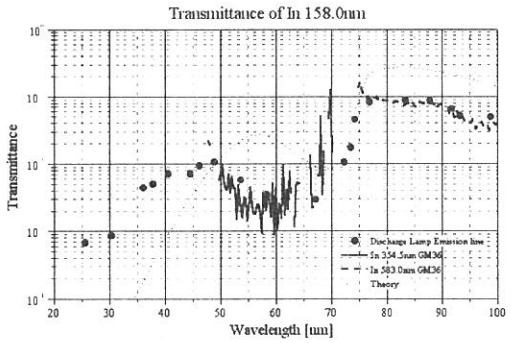

Figure 2c. The transmittance of In Filter

Reference

[1] Nakamura,M., I.Yoshikawa, A.Yamazaki, K.Shiomi, Y.Takizawa, M.Hirahara, K.Yamashita, Y.Saito, and W.Miyake, Terrestrial Plasmaspheric Imaging by an Extreme Ultraviolet Scanner on Planet-B, *Geophys. Res. Lett., 27,* 141, 2000.

(BL5B)

Contrast Measurement of Reflection Mask for Extreme Ultraviolet Lithography

Masahito Niibe, Takeo Watanabe, Hajime Nii, Takeshi Tanaka and Hiroo Kinoshita

Laboratory of Advanced Science &Technology for Iudustry, Himeji Institute of Technology,

3-1-2 Koto, Kamigoori, Ako-gun, Hyogo 678-1205 Japan

Extreme Ultraviolet Lithography (EUVL) is attracting much interest and actively studied as a new technology to fabricate semiconductor devices in near future generations. In the EUVL method, multilayer mirrors are used not only in the demagnifying projection optical system but also in the reflection masks to print IC patterns on wafers. The reflection masks have currently been developed for the wavelength of 13.5 nm and have been prepared by patterning metal thin films as absorber materials deposited on EUV reflecting substrates coated by Mo/Si multilayers. Although Au, Ge, W, and Ni have been used as a absorber metal previously, the studies on absorber materials and their processing method are insufficient.

We chose chromium, Cr, and tantalum, Ta, metals as a new absorbing material for EUVL reflection mask. These metals are frequently used in photomask or X-ray mask for lithography and their fabrication processes are well investigated. Figure 1 shows the calculated transmittance of EUV light for various metals at the wavelength of 13.5 nm. As shown in Fig. 1, the transmittance (or absorbing ability) of Cr and Ta metals for the EUV light is nearly equal to that of tungsten, W.

We have fabricated the reflection masks with Cr or Ta metal absorbers deposited on top of Mo/Si multilayer reflectors. The Cr absorber mask with absorbing film thickness of 44 nm was patterned by conventional lift-off technique. The schematic diagram of the fabrication process of Ta absorber mask is shown in Fig. 2. The Ta absorbing layer with 100 nm thickness was deposited on top of the multilayer with 10-nm-thickness SiO2 etch-stop layer. The Ta absorber mask was patterned by ECR-plasma etching technique.

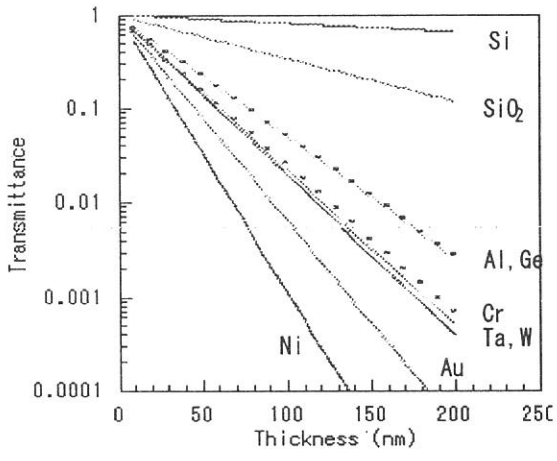

Fig. 1. Transmittance of metals at the wavelength of 13.5 nm.

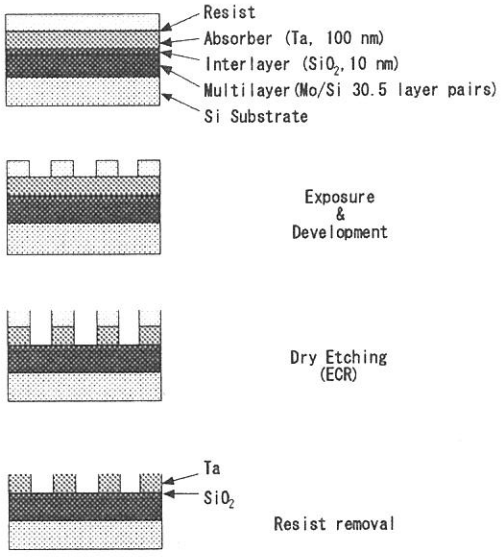

Fig. 2. Fabrication process of Ta absorber reflection mask

The mask contrast measurement was carried out by synchrotron radiation source beamline with plane-grating monochromater around the wavelength of 13.5 nm (UVSOR BL-5B). A silicon membrane with thickness of 150 nm was used as a low-pass filter. In the mask with 3" Si wafer substrate, we made a reflectivity measurement pattern of 4 mm square in addition to resolution evaluation patterns illustrated in Fig. 3. The contrast was measured by measuring the reflectivity of reflecting and absorbing parts of the patterns using movable stage in the reflectivity measurement system.

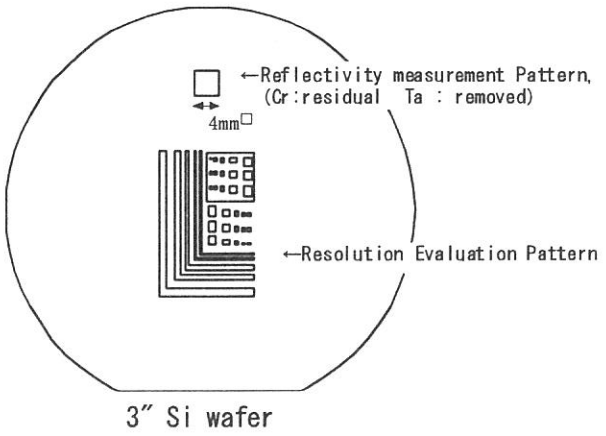

Fig. 3. Mask patterns of the present study

The peak reflectivity of the non-processed surface of Mo/Si multilayer deposited by a RF-magnetron sputtering method was about 62%. For the Cr absorber (44 nm thickness) mask, measured peak reflectivities at the reflecting and absorbing parts of the processed patterns were about 59% and 4.9%, respectively. The reflection contrast of the Cr absorber mask was about 12. On the other hand for the Ta absorber (100 nm thickness) mask, measured peak reflectivities at the reflecting and absorbing parts of the processed patterns were about 50% and 0.48%, respectively. The reflection contrast was about 105. From an AFM observation we got a roughness value of 1.3 nm(rms) on the surface of SiO2 etch-stop layer of the Ta absorber mask. The reduction of the peak reflectivity at the reflecting part of Ta absorber mask would be coursed by both absorption and scattering of light by SiO2 etch-stop layer.

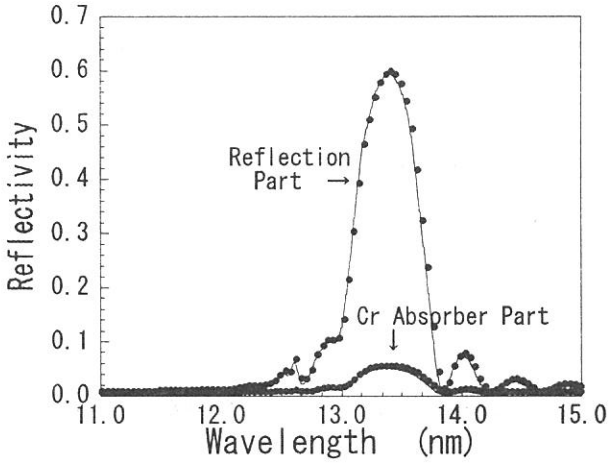

Fig. 4. Reflectivity of the Cr absorber reflection mask

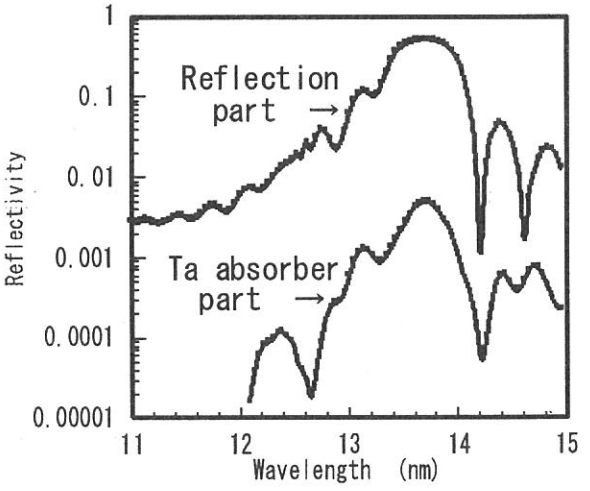

Fig. 5. Reflectivity of the Ta absorber reflection mask

It is noted that the masks were prepared at about one year before the reflectivity measurements and had been kept in the normal air. However there was no significant degradation of the reflectance or surface quality of the reflection masks.

(BL7A)

Performance of KTP monochromator crystals

Eiji Shigemasa
UVSOR, Institute for Molecular Science, Okazaki 444-8585, JAPAN

A variety of monochromator crystals with different 2d spacings is required for providing the monochromatized radiation in the soft x-ray region (0.7–3.5 keV) with double-crystal monochromators. Above about 1.7 keV, semiconductor crystals such as InSb and Si are available and it is known that such crystals are thermally strong and can endure long exposure to the intense X-rays even from the 4T wiggler , which is installed in the straight section upstream of the B7 bending magnet. Below this energy, the Al (~1550 eV) and Mg (~1300 eV) *K*-edges lie. It had been necessary to use beryl and quartz crystals to approach these two edges. However, these crystals are quite sensitive to radiation damage with considerable degradation in performance. Furthermore, the beryl and quartz crystals contain the Al and Si elements, respectively. This property prevent users from performing EXAFS measurements at the Mg and Al *K*-edges.

The combination of an artificial crystal, YB_{66}(400), with the wiggler has been another possibility to access the Al and Mg *K*-edges at BL7A in the past [1]. Their low reflectivity makes YB_{66} unsuitable for the radiation from the bending magnet. The focusing mirror system for the wiggler radiation was successfully installed in 1998 [2]. The basic ability to cover the Mg, Al, and Si *K*-edges with a single pair of monochromator crystals is very fascinating, but there is a disadvantageous property for the EXAFS experiments with the YB_{66} crystals, that is, two positive glitches at 1385 and 1438 eV caused by anomalous scattering for the (600) reflection at the Y L_{III} (2080eV) and L_{II} (2156eV) edges. It is quite hard to compensate the glitches completely even though the cutoff mirror is introduced.

In order to meet the demand to perform the EXAFS experiments at the Mg and Al *K*-edges in the UVSOR, a pair of $KTiOPO_4$(011) (KTP) crystals has been introduced and its performance test has been carried out on BL7A and BL1A. Figure 1 shows the photon intensity of the KTP monochromator crystals over the photon energy range 1200–3000 eV, comparing with those from other crystals. The silicon photodiode from IRD Co. was used to estimate the photon flux for each pair of crystals. The solid line represents the photon flux

for the KTP crystals measured after the optimization at 1500 eV, and the solid line with black circles indicates that the intensity was measured at each data point showed by the circles after the optimization. Comparing with these two curves, it is clear that the detuning by the irradiation happens, even against the radiation from the bending magnet. However, it can easily be seen that the photon flux from the KTP crystals without the use of the wiggler radiation is almost the same as that from the YB_{66} crystals combined with the wiggler and the focusing mirror system. The weak structure around 1800 eV and sharp drop around 2150 eV on the curve corresponding to the KTP crystals are attributed to the Si *K*-edge jump of the photodiode and to the P *K*-edge absorption of the KTP crystals, respectively. The excellent ability to cover the Mg, Al, and Si *K*-edges without any structures is quite suitable for performing the EXAFS measurements at the Mg and Al *K*-edges.

References

[1] T. Kinoshita et al., UVSOR Activity Report 1997, p. 62.
[2] T. Kinoshita et al., UVSOR Activity Report 1998, p. 41.

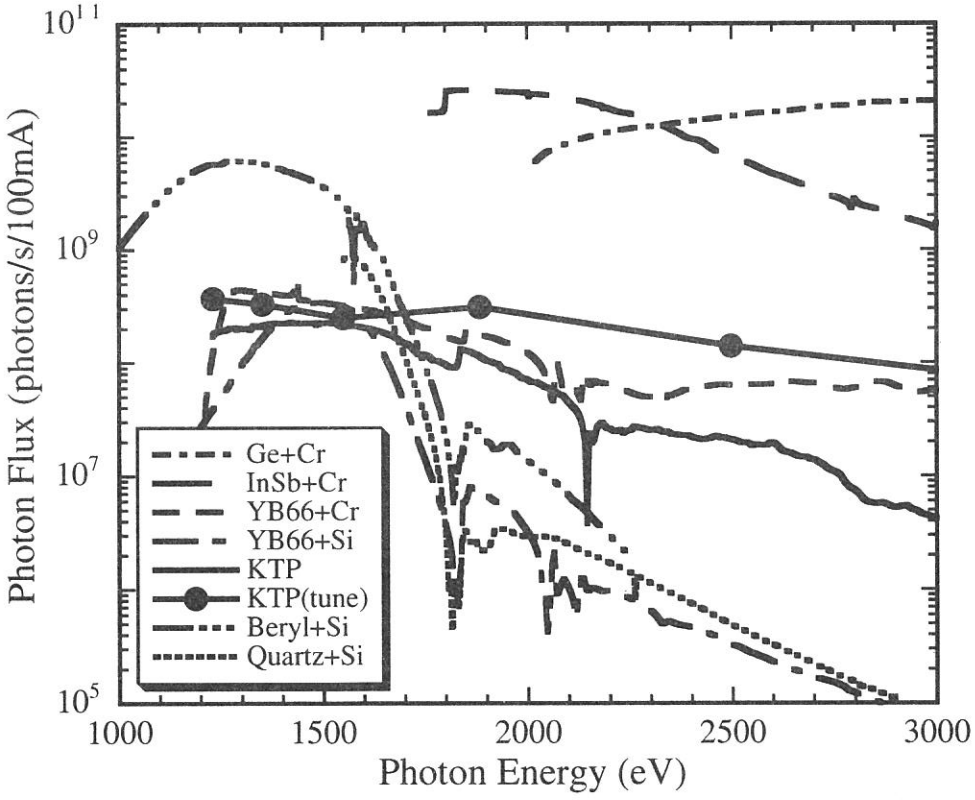

Figure 1. Throughput from KTP monochromator crystals on BL7A, in comparison with those for several combinations of the focussing mirrors and the monochromator crystals. Except for KTP, the 4T wiggler radiation was used as a light source.

(BL7B)

Present Performance of BL7B 3m Normal Incidence Monochromator

Kazutoshi FUKUI, Hiroshi MIURA[1], Hideyuki NAKAGAWA[1], Iwao SHIMOYAMA[2],
Kazumichi NAKAGAWA[3], Hidekazu OKAMURA[4], Takao NAMBA[4],
Masami HASUMOTO and Toyohiko KINOSHITA[5]

Institute for Molecular Science, Okazaki 444-8585, Japan

Fax +81-564-54-7079, fukui@ims.ac.jp

[1] *Faculty of Engineering, Fukui University, Fukui 910-8507, Japan*

[2] *Japan Atomic energy Research Institute, Ibaraki 319-1195, Japan*

[3] *Faculty of Human Development, Kobe University, Kobe 657-8501, Japan*

[4] *Faculty of Science, Kobe University, Kobe 657-8501, Japan*

[5] *SRL-ISSP, University of Tokyo, KEK-PF, Tsukuba 305-0801, Japan*

The beamline BL7B at the UVSOR facility for solid-state spectroscopy has been opening for users from April 1999. This beamline is reconstructed on the basis that the synchrotron radiation is still an important light source, not only for the VUV region but also for the UV, VIS and IR regions, owing to the wavelength continuity of synchrotron radiation with no structure. Then, this 3 m normal incidence monochromator (modified version of McPherson model 2253) covers the 50 – 1000 nm range with three gratings. The optical design and setup has been reported in Ref. 1.

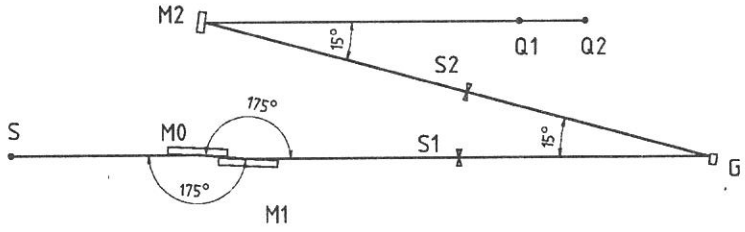

Fig. 1

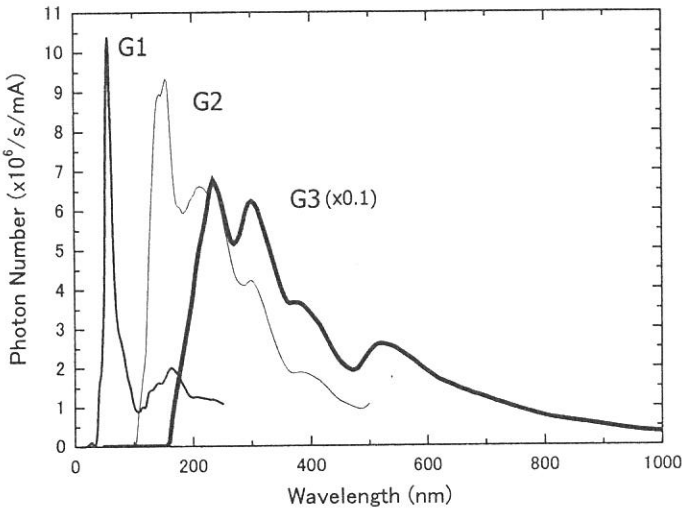

Fig. 2

The outline of the new beamline is illustrated at BL7B page of Status of UVSOR in this report. The optical design is also shown in Fig. 1. The design parameters of the optical elements are summarized in Table 1, 2 and 3 in Ref. 2 without coating material of G2 as mentioned after. The coverange of the three gratings in design is

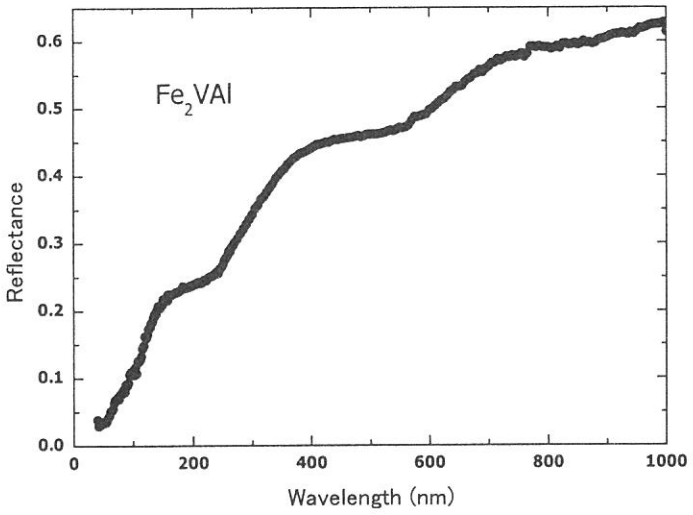

Fig. 3

50 – 150 nm for G1, 80 – 300 nm for G2 and 150 – 1000 nm for G3. This beamline covers the wide wavelength range, so that the reduction of the higher order light becomes important. Good purity of the monochromated light is almost fulfilled over whole wavelength by using the low wavelength cut filters such as LiF, quartz, pyrex glass and colored glasses.

Figure 2 shows the output spectra of BL7B. Both entrance and exit slits are 50μm. LiF and quartz filters are used in G2 and G3 spectra, respectively. Re-coating from Al to Au of G2 gives us the sufficient flux increase at higher energy of G2 region. It is difficult to estimate the intensity of the scattered light, but comparison between the spectra with and without the filters represents that the intensity ratio of the visible scattered light to the average output is expected less than 0.5%. Figure 3 shows Fe_2VAl reflectance spectrum as an example of the wide range measurements. Details of the spectrum will be seen in Ref.3.

References

[1] K. Fukui, H. Nakagawa, I. Shimoyama, K. Nakagawa, H. Okamura, T. Nanba, M. Hasumoto and T. Kinoshita, J. Synchrotron Rad. 5 (1998) 836.

[2] K. Fukui, H. Nakagawa, I. Shimoyama, K. Nakagawa, H. Okamura, T. Nanba, M. Hasumoto and T. Kinoshita, UVSOR Activity Reprot 1998, 1999, p. 42.

[3] H. Okamura, J. Kawahara, T. Nanba, S. Kimura, K. Soda, U. Mizutani, Y. Nishino, M. Kato, I. Shimoyama, H. Miura, K. Fukui, K. Nakagawa, H. Nakagawa, T. Kinoshita, Phys. Rev. Lett., in press.

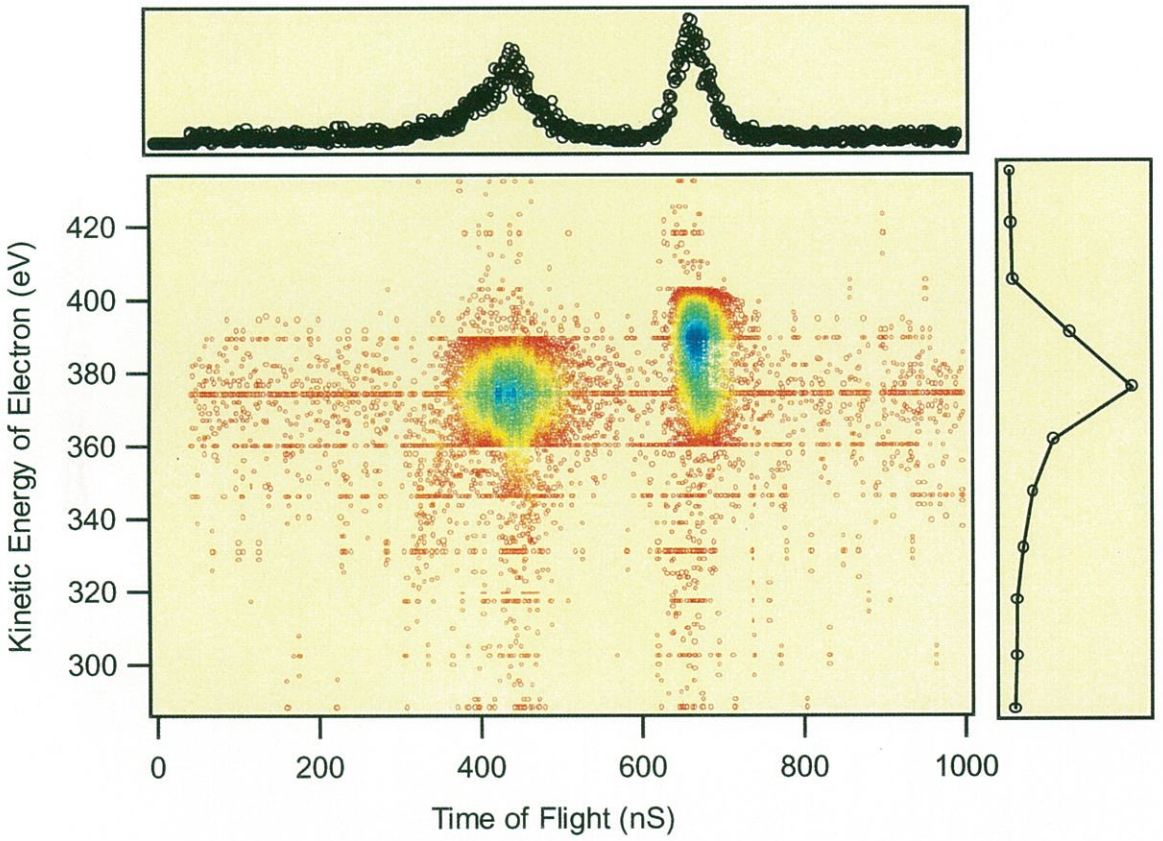

Gas-phase Spectroscopy

BL2B2, 3A2, 3B, 8B1

(BL3A2)

Two-dimensional imaging technique for measuring translational energy and angular distribution of ionic photofragments

Tatsuo Gejo, Eiken Nakamura, Eiji Shigemasa and Norio Saito[A]

Institute for Molecular Science, Myodaiji, Okazaki 444-8585, Japan

[A] *Electrotechnical Laboratory, Umezono, Tsukuba-shi, 305-0045, Japan*

During the last decade, the dynamics of molecules in the valence energy regime has been investigated by preparing excited state at well-defined energy, and analyzing photoelectron energy and angular distribution of ionic photofragments involved. Two-dimensional (2D) imaging technique is one of the most powerful tools for obtaining this information because 2D data and its simple calculation on the basis of momentum conservation law, provide Newton diagram of photofragments, which leads to dynamical process involved immediately

At beamline 3A2 of UVSOR, we have tested this two-dimensional imaging system using a position sensitive detector (PSD) (Roendek). Last year, although, we successfully measured the image of N^+ and N_2^+ signals from nitrogen molecules in the valence excitation region (20-100 eV), significant noise level excluded us from analyzing data. Therefore, we have improved mechanics and electronics as follows:

1) Molecular beam was replaced with an effusive beam from a nozzle.
2) The flight region of photofragments was made shorter.
3) A new TDC system (Lecry4208) was introduced, allowing us to develop our software system.

The system mainly consists of accelerator lens, a PSD and an electronic system for data analysis and a computer. After the gas passes synchrotron radiation (SR) region, less than one molecule per one photon beam on the average undergoes ionization and/or dissociation. The direction of polarization of SR is parallel to the axis of TOF tube (10 cm). After the acceleration by the ion lens, ionic fragments fly through the TOF tube and hit the PSD. The determination of the impact position on the detector is based on the time delay between two signals from each end of a the wire behind the MCP. The position is obtained by the subtracting of time when each two signals arrive, providing us its velocity and direction in the center-of-mass frame. Fig. 1 shows the 2D imaging of N_2^+ after the excitation of the valence electrons. This figure indicates that the interaction region was relatively large because the photon beam was not well focused.

With this technique, we will try to perform the triple coincidence in the ionic fragmentation following inner-shell excitation.

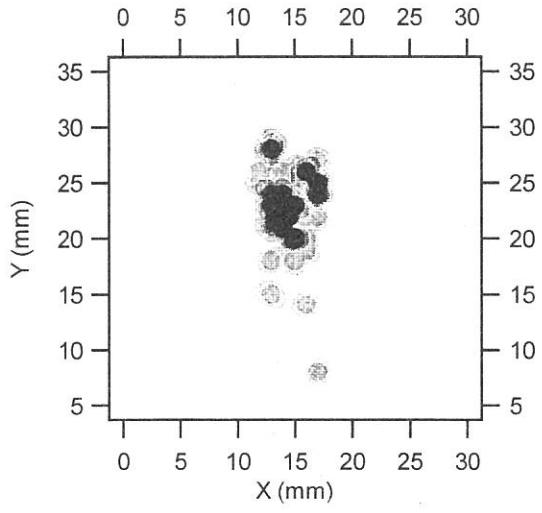

Fig. 1: 2D imaging from N_2^+.

(BL3A2)

Single- and double-photoionization of nitrogen dioxide (NO_2) and ionic fragmentation of NO_2^+ and NO_2^{2+}

Toshio MASUOKA

Department of Applied Physics, Faculty of Engineering,, Osaka City University, Sugimoto 3, Sumiyoshi-ku, Osaka 558-8585

Doubly charged molecular ions are produced in abundance at high energies. However, since molecular double ionization (m^{2+}) is usually followed by the production of an ion pair ($m_1^+ + m_2^+$, dissociative double ionization) doubly charged molecular ions are rare or non-existent in the mass spectra of many molecules. In the determination of double-photoionization cross section (σ^{2+}), it is essential to include both the stable m^{2+} ions (if they exist) and the $m_1^+ + m_2^+$ ion pairs. Another problem is that the m_1^+ ion is produced from m^+ or m^{2+} at excitation energies where dissociative single and double photoionization take place concomitantly. It is desirable to determine how many m_1^+ ions are produced respectively from m^+ and m^{2+}.

In the present study, molecular and dissociative single- and double-photoionization processes of nitrogen dioxide are examined in the photon energy region of 37-120 eV by use of time-of-flight mass spectrometry and the photoion-photoion-coincidence method together with synchrotron radiation. The TOF mass spectra and the PIPICO spectra were measured at an angle of ~55° with respect to the polarization vector where the second-order Legendre polynomial is close to zero. Under these conditions, the effects of anisotropic angular distributions of fragment ions are minimized [1].

Shown in Fig. 1 is a typical time-of-flight mass spectrum measured at a photon energy of 100 eV by using the rf frequency as the start input of a TAC under the single bunch mode. The spectrum is complicated because two or three bunches pass the front end of the beam line in the time range of the mass spectrum. The ratio of double to single photoionization is shown in Fig. 2. Above 100 eV, the ratio exceeds 0.2. This ratio may be regarded as a lower limit of σ^{2+}/σ^+ because the O^++O^++N channel of NO_2^{2+} is not included in the evaluation of σ^{2+} and discrimination effects against energetic ions produced in dissociative double photoionization has not been corrected. However, it should be noted that the correction due to the latter effects is at most about 10% since the average kinetic energy release is about 10 eV at 100 eV for the N^++O^+ dissociation channel and about 7 eV for the O^++NO^+ channel [2]. Since the total photoabsorption cross section of NO_2 in this photon energy region has been reported by Au and Brion [3], the σ^{2+}/σ^+ ratio can be converted to the absolute cross sections for the single and double photoionization.

Ion branching ratios for the individual ions respectively produced from the parent NO_2^+ and NO_2^{2+} ions are determined separately, thus enabling more detailed study of the dissociation processes of the NO_2^+ and NO_2^{2+} ions. These results are shown in Figs. 3 and 4. Looking at the ion branching ratios of NO_2^+, we notice that there is no outstanding variation in the fragmentation as a function of photon energy. Only the O^+ ion increases with photon energy. The thresholds for the O^++NO^+ and N^++O^++O dissociation channels of NO_2^{2+} are at 34.7±0.5 and 43.6±0.2 eV, respectively. These thresholds observed in the present study are in good accordance with those reported previously [4]. The O^++NO^+ dissociation channel of NO_2^{2+} is dominant below 90 eV and above this energy the N^++O^++O channel is a main dissociation process. Charge localized dissociation products, N^{2+} and O^{2+}, are observed above 60 eV.

REFERENCES

[1] T. Masuoka, I. Koyano, and N. Saito, J. Chem. Phys. **97**, 2392 (1992).

[2] T. Masuoka, unpublished data.

[3] J. W. Au and C. E. Brion, Chem. Phys. **218**, 109 (1997).

[4] P. G. Fournier *et al.*, J. Chem. Phys. **89**, 3553 (1988); J. H. D. Eland, Mol. Phys. **61**, 725 (1987).

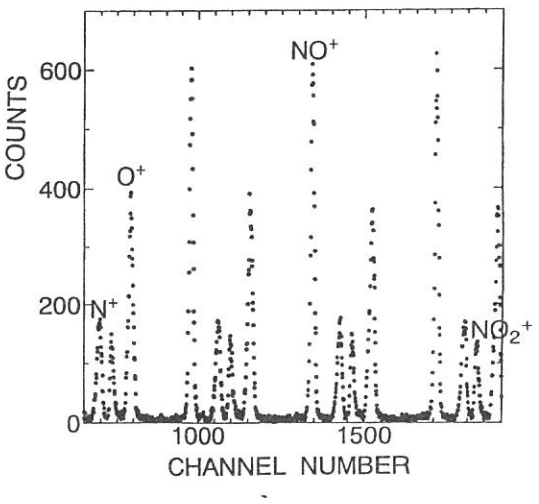

FIG. 1. A typical time-of-flight mass spectrum measured at a photon energy of 100 eV by using the rf frequency as the start input of a TAC under the single bunch mode operation.

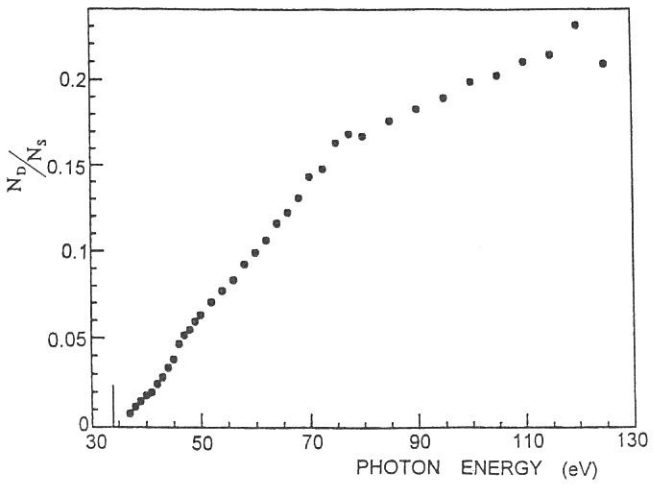

FIG. 2. Ratios of double to single photoionization cross section of NO_2.

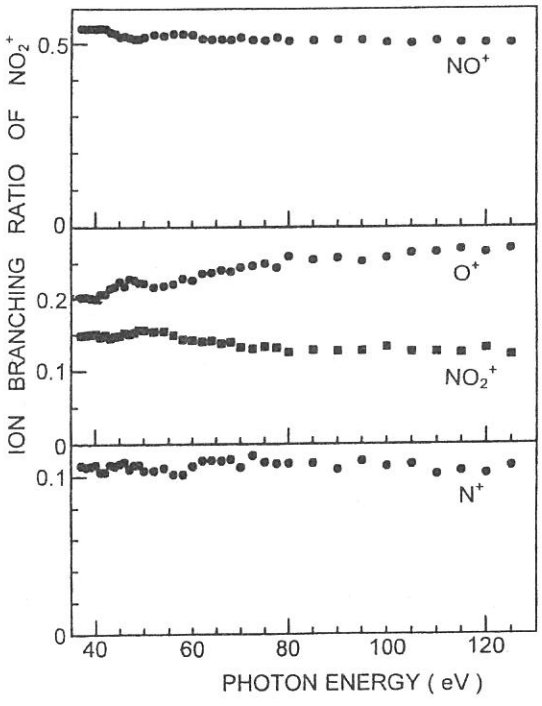

FIG. 3. Ion branching ratios of single photoionization of NO_2.

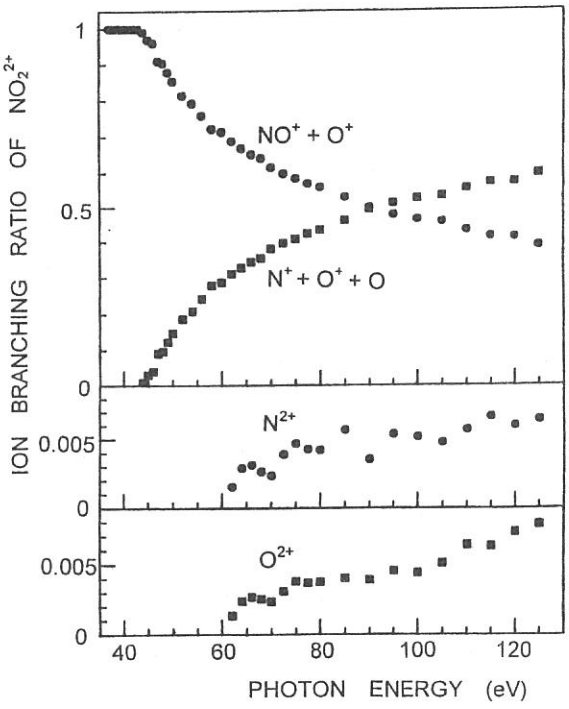

FIG. 4. Ion branching ratios of double photoionization of NO_2.

(BL3A2)

Laser Induced Fluorescence Excitation Spectroscopy of CN($X\ ^2\Sigma^+$, v = 0) Produced by VUV Photoexcitation of CH_3CN

Masakazu MIZUTANI, Hiromichi NIIKURA[A] and Koichiro MITSUKE

Department of Vacuum UV Photoscience, Institute for Molecular Science, Okazaki 444-8585, Japan
[A]The Graduate University for Advanced Studies, Okazaki 444-8585, Japan

It is important to measure the internal distribution of neutral fragments resulting from VUV photoexcitation of gas phase molecules because the internal distribution contains information on predissociation dynamics of superexcited states. However, detection of neutral fragments is difficult by means of conventional methods such as mass spectrometry and photoelectron spectroscopy. Unless the fragments experience radiative transition, fluorescence spectroscopy is ineffective.

The pump-probe experiment combining synchrotron radiation and a laser is expected to be one of the most effective method for probing ionic and neutral fragments resulting from VUV photoexcitation. We have developed laser induced fluorescence (LIF) excitation spectroscopy of ions prepared by VUV photoexcitation with synchrotron radiation. The rotational states of N_2^+($X\ ^2\Sigma^+$, v = 0) produced from N_2 or N_2O are resolved and their distribution is analyzed.[1-3] Following these experiments, we are trying to realize LIF excitation spectroscopy of neutral fragments produced by VUV photoexcitation.

A molecular beam of the sample gas of CH_3CN is expanded from a multi-capillary nozzle and subjected to photoexcitation with an intense undulator radiation (E_{SR} = 18 eV) which is supplied as the zeroth order light of a grazing-incidence monochromator. Formed neutral fragments, CN($X\ ^2\Sigma^+$, v''=0), are excited to the $B\ ^2\Sigma^+$, v'=0 state by irradiation of the second harmonic of a mode-locked Ti:sapphire laser. The fluorescence due to the transition ($B\ ^2\Sigma^+$, v'=0) → ($X\ ^2\Sigma^+$, v''=1) is detected by using a combination of an input optics, a secondary monochromator and a photon-counting system including a photomultiplier. As far as we know, there is no experimental work on laser spectroscopy of the CN($X\ ^2\Sigma^+$) radicals produced by VUV photoexcitation of CH_3CN. The signal intensity is estimated to be very low because the cross section for the formation of CN($X\ ^2\Sigma^+$) is no more than 1 Mb.

In order to improve the collection efficiency of the fluorescence, we are planning to improve the input optics. The revised optics consists of spheroidal and spherical mirrors and a optical fiber.

References

1) M. Mizutani, H. Niikura, A. Hiraya and K. Mitsuke, *J. Synchrotron Rad.* **5** (1998) 1069-1071.
2) K. Mitsuke, M. Mizutani, H. Niikura and K. Iwasaki, *Rev. Laser Eng.* **27** (1998) 458-462.
3) H. Niikura, M. Mizutani and K. Mitsuke, *Chem. Phys. Lett. in press.*

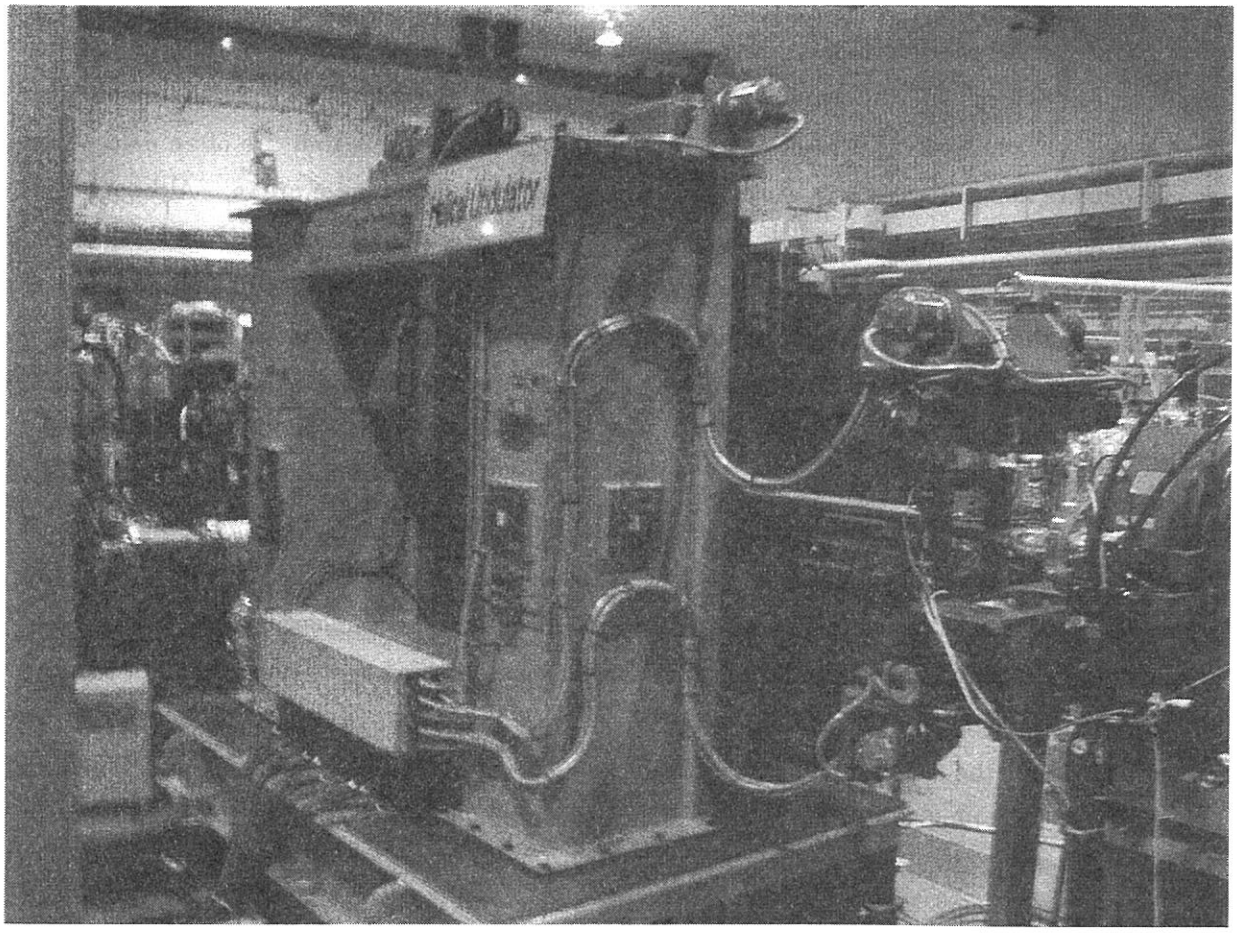

Helical Undulator

(BL3A2)

Fragmentation of $Cl_3SiC{\equiv}CSi(CH_3)_3$ vapor following Si:2*p* core-level photoexcitation. A search for a site-specific process in complex molecules

Shin-ichi Nagaoka and Joji Ohshita[A]

Institute for Molecular Science, Okazaki 444-8585 and [A]Department of Applied Chemistry, Faculty of Engineering, Hiroshima University, Higashi-Hiroshima 739-8527

Synchrotron radiation has provided a powerful means to obtain information about core-level excitations, and the dynamic processes following the core-level excitations in molecules have long been a subject of interest. In contrast to valence electrons that are often delocalized over the entire molecule, the core electrons are localized near the atom of origin. Although core electrons do not participate in the chemical bonding, the energy of an atomic core-level in the molecule depends on the chemical environment around the atom. A shift in the energy levels of core electrons that is due to a specific chemical environment is called a chemical shift.

Monochromatized synchrotron radiation can excite core electrons of an atom in a specific chemical environment selectively, discriminating the core electrons from those of like atoms having different chemical environments. This site-specific excitation often results in site-specific fragmentation, which is of importance in understanding localization phenomena in chemical reactions and which is potentially useful for synthesizing materials through selective bond breaking. Studies of the site-specific fragmentation of organosilicon molecules would also be of interest from the viewpoint of photochemical vapor deposition using synchrotron radiation in the processes of semiconductor fabrication.

To elucidate the site-specific fragmentation, we have studied the spectroscopy and dynamics following core-level photoionization of various molecules condensed on surfaces [1-4]. In contrast to the cases of $Cl_3SiSi(CH_3)_3$ and $F_3SiCH_2Si(CH_3)_3$, the site-specific fragmentation was clearly observed in the mass spectra of $F_3SiCH_2CH_2Si(CH_3)_3$ (FSMSE) in the vapor phase [2,3]; production of $SiCH_3^+$ and SiF^+ ions is enhanced by Si[Me]:2*p* and Si[F]:2*p* excitations, respectively. It is considered that the site-specific fragmentation is observed in molecules in which the two Si sites are located far apart and, thus, electron migration between the two Si-containing groups is not effective. In the present study, we studied the fragmentation of $Cl_3SiC{\equiv}CSi(CH_3)_3$ (CSMSA) vapor following Si:2*p* core-level photoexcitation to elucidate the effect of the unsaturated bond (C ≡C) between the two sites.

CSMSA was synthesized for the first time in this study with the reaction of $BrMgSiC{\equiv}CSi(CH_3)_3$ and $SiCl_4$. The experiments were performed using a time-of-flight spectrometer with variable path length, coupled to a constant-deviation grazing incidence monochromator installed on the BL3A2 beamline [5].

Figure 1 shows the total photoionization efficiency curve of CSMSA. Figure 2 shows an example of the photoionization mass spectrum of CSMSA taken in the photoelectron-photoion

coincidence (PEPICO) mode at a photon energy of 105 eV. Assignments are given in the figure. Figure 3 shows plots of the ratios of the integrated intensities of $SiCH_3^+$ and $SiCl^+$ peaks in the photoionization mass spectrum to the total photoion intensity ($I_{ion}/I_{tot\text{-}ion}$) as a function of photon energy. In contrast to the case of FSMSE, $I_{ion}/I_{tot\text{-}ion}$'s for $SiCH_3^+$ and $SiCl^+$ are similar to each other in CSMSA, except for the increase in the $I_{ion}/I_{tot\text{-}ion}$ for $SiCl^+$ at 110 eV. The site-specific fragmentation of CSMSA is less remarkable than that of FSMSA. Further investigations are clearly needed on the reason for this difference.

[1] S. Nagaoka, K. Mase, M. Nagasono, S. Tanaka, T. Urisu and J. Ohshita, J. Chem. Phys. 107, 10751 (1997).

[2] S. Nagaoka, T. Fujibuchi, J. Ohshita, M. Ishikawa and I. Koyano, Int. J. Mass Spectrom. Ion Processes 171, 95 (1997).

[3] S. Nagaoka, K. Mase and I. Koyano, Trends Chem. Phys. 6, 1 (1997).

[4] S. Nagaoka, K. Mase, M. Nagasono, S. Tanaka, T. Urisu, J. Ohshita and U. Nagashima, Chem. Phys. 249, 15 (1999).

[5] T. Masuoka and S. Nagaoka, Trends Chem. Phys. 3, 13 (1994).

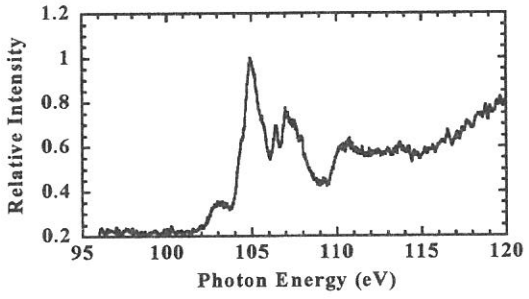

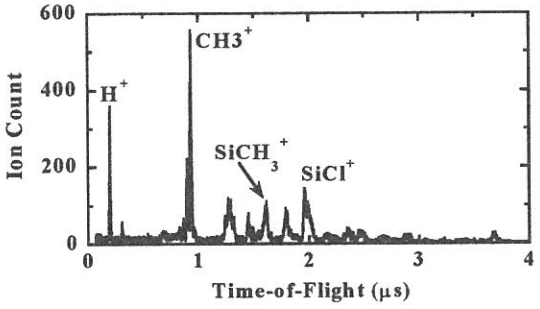

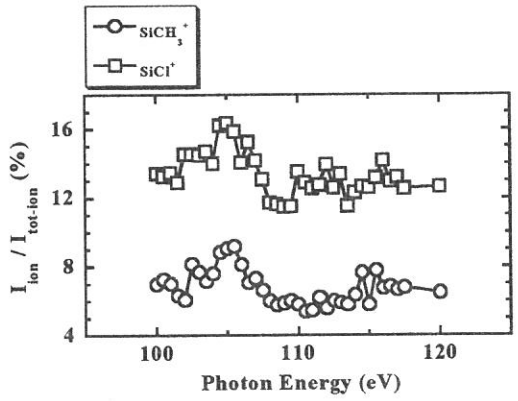

Figure 1 (upper left-hand side). Total photoionization efficiency curve of CSMSA. The slit widths of the monochromator were 0.2 mm, giving an optical resolution of 0.04 nm.

Figure 2 (upper right-hand side). Photoionization mass spectrum of CSMSA taken by excitation at 105 eV in the PEPICO mode. The slit widths of the monochromator were 0.2 mm, giving an optical resolution of 0.04 nm. Data collection time was 450 s.

Figure 3 (bottom). $I_{ion}/I_{tot\text{-}ion}$ for $SiCH_3^+$ and $SiCl^+$ in CSMSA as a function of photon energy. The slit widths of the monochromator were 0.2 mm, giving an optical resolution of 0.04 nm.

(BL3A2)

Rotational State Distribution of $N_2^+(X^2\Sigma_g^+, v = 0)$ formed by N_2O.

Hiromichi Niikura*, Masakazu Mizutani** and Koichiro Mitsuke**

*The Graduate University for Advanced Studies, ** Institute for Molecular Science,

Myodaiji, Okazaki, 444-8585, Japan.

The rotational temperature of $N_2^+(X\ ^2\Sigma_g^+, v = 0)$ formed by undulator radiation excitation of N_2O at 18.556 eV reduces to be 200 - 230 K from 300 K in the course of the dissociation [1]. Dissociation leading to $N_2^+(X\ ^2\Sigma_g^+) + O(^3P)$ is known to be promoted at E_{SR} = 18.556 eV by autoionization of the $3d\pi$ Rydberg state to the $N_2O^+(B^2\Pi)$ state. The energy released at a time of dissociation, referred to here as the *available* energy E_{avl}, are distributed to the fragment rotational energy in addition to the initial rotational energy of the parent $N_2O^+(B\ ^2\Pi)$, E_{avl} is defined by

$$E_{avl} = E_{SR} - E_{elec} - D_0 = I_E - D_0 \qquad (1)$$

where E_{SR} is the excitation photon energy for the $3d\pi$ Rydberg state (E_{SR} = 18.556 eV), D_0 is the NN-O bond dissociation energy (17.25 eV measured from the electronically ground state of N_2O), E_{elec} is the kinetic energy of the ejected electron, and I_E is the ionization energy for a vibrational state of N_2O^+ ($B\ ^2\Pi$).

The available energy is calculated from an Eq. 1 to be 3200 - 10500 cm^{-1} depending on I_E. On the other hand, the average rotational energy of the N_2^+ ($X\ ^2\Sigma_g^+$, v = 0) fragment is obtained from T = 220 K to be 150 cm^{-1}. The percentage of the rotational energy of $N_2^+(X\ ^2\Sigma_g^+, v = 0)$ to the available energy is thus only 1.5 - 5 %. This small fraction of the fragment rotational energy indicates that the available energy is distributed dominantly to the relative translational energies of N_2^+ and O and/or to the fragment vibrational energy.

The impulsive model assumes that the molecules dissociate so rapid that the available energy can not randomizes to the all phase space equally but is specified by the geometry at a instance of dissociation. The distribution of the available energy to the fragment rotational and/or vibrational energy of fragments are evaluated by using E_{avl}, the masses of the three atoms and the bond angle, θ ,of $N_2O^+(B\ ^2\Pi)$ in its equilibrium geometry. Unfortunately, the exact equilibrium geometry of N_2O^+ ($B\ ^2\Pi$) has not been elucidated yet because of a strong vibronic coupling between two electronic states located at around 17.5 eV whose configurations are expressed as $(2\pi)^{-2}$ $(3\pi)^1$ and $(1\pi)^{-1}$. It is possible that the ion with the former configuration has a bent equilibrium geometry on account of the accommodation of an electron in the π^* orbital. Therefore, we calculate the average rotational energy of $N_2^+(X\ ^2\Sigma_g^+, v = 0)$ as a function of θ by a similar procedure to that reported by *Levine* and *Valentini [2]* who have assumed a *stiff* NN bond and no vibrational excitation (*modified* impulsive model). For simplicity, we make further assumptions: The bond length of NN-O is equal to that of N-NO, the three atoms have the same mass, and the dissociation is assumed to proceed on the plane where the three atoms are located. The contribution of the bending motion to the fragment rotational energy is disregarded. A space-fixed Cartesian coordinate system is employed with the origin at the center of mass of N_2O^+. The rotational angular momentum of $N_2O^+(B\ ^2\Pi)$ perpendicular the molecular plane, namely, J_C, is taken as the initial angular momentum even in the C_s bent geometry.

Figure 1 shows the calculated rotational energy of $N_2^+(X\ ^2\Sigma_g^+, v = 0)$ as a function of θ when E_{avl} takes a value of 3200 cm^{-1}, assuming that the dissociation takes place from the vibrational ground state of $N_2O^+(B\ ^2\Pi)$, *i.e.*, at the lowest peak of the vibrational band (I_E = 17.65 eV) in the reported photoelectron spectrum. Two rotational energies were calculated which correspond to two extreme cases: the high J limit and low J limit. Those are classified by the direction between the initial rotation of $N_2O^+(B\ ^2\Pi)$ and the repulsive force generated at a time of dissociation. In the low J limit the calculated curve once goes down to zero and goes up again with decreasing bond angle. The increase in the rotational energy with decreasing bond angle is attributed to the increase in the component of the rotational angular momentum of $N_2^+(X\ ^2\Sigma_g^+, v = 0)$ resulting from the repulsive force. The dashed line at the rotational energy of 200 cm^{-1} shows the initial rotational energy of $N_2O^+(B\ ^2\Pi)$ at 300 K. The rotational energy of $N_2^+(X\ ^2\Sigma_g^+, v = 0)$ is smaller than that of the parent $N_2O^+(B\ ^2\Pi)$ at $\theta \geq 130°$ and $\theta \geq 165°$ in the low-J and high-J limits, respectively. This clearly suggests the possibility of less rotational excitation in $N_2^+(X\ ^2\Sigma_g^+, v = 0)$ than in $N_2O^+(B\ ^2\Pi)$ at $\theta \geq 130°$. The LIF spectrum of $N_2^+(X\ ^2\Sigma_g^+, v = 0)$ has demonstrated that the average rotational energy of $N_2^+(X\ ^2\Sigma_g^+, v = 0)$ is smaller than that of $N_2O^+(B\ ^2\Pi)$. From these considerations, we can draw the conclusion that the equilibrium bond angle for the vibrational ground state of $N_2O^+(B\ ^2\Pi)$ is larger than ~ 130°.

References

[1] H. Niikura, M. Mizutani and K. Mitsuke, Chem. Phys. Letters, 317 (2000) 45.

[2] H. B. Levene and J. J. Valentini, J. Chem. Phys., 87 (1987) 2594.

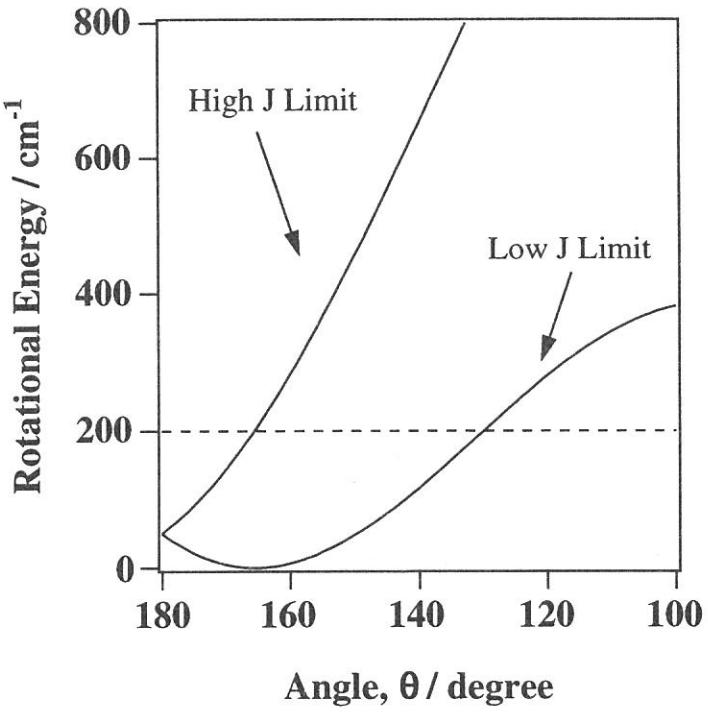

Figure 1. Calculated rotational energies of the N_2^+ fragment as a function of the bond angle θ on the basis of the modified impulsive model. Two rotational energies were calculated which correspond to the high J and low J limit (see text). The dashed line at the rotational energy of 200 cm^{-1} shows the initial rotational energy of N_2O^+ at 300 K.

(BL-3B)

Development of a new angle-resolved energy analyzer for photoelectron spectroscopy of polarized atoms

Kota IWASAKI and Koichiro MITSUKE

A Institute for Molecular Science, Myodaiji, Okazaki 444-8585 , Japan

A new angle-resolved electron energy analyzer incorporating a position sensitive detector (PSD) has been designed to measure the angular distribution of photoelectron from polarized rare gas atoms in BL3B. There are two ways to obtain the angular distribution of photoelectrons: rotating an energy analyzer with respect to its the symmetric axis or using angle-resolved energy analyzer. The former is simpler than the latter one, however the latter one gives promise of achieving good angular resolution and wide angular acceptance simultaneously. We think that an angle-resolved analyzer is needed to measure complicated angular distributions of photoelectrons caused by the atomic alignment with relatively short accumulation time of signals.

The following specifications are required for developing the analyzer available in the present experiment.

1. Photoelectrons should be detected with relatively good energy resolution that is smaller than the energy difference 177meV between $Ar^+(^3P_{1/2})$ and $Ar^+(^3P_{3/2})$. Since the energy resolution is generally proportional to the transmission energy, high resolution can be obtained in an analyzer of low transmission energy. However, we should consider the fact that transmission efficiency of an analyzer decreases as the transmission energy is reduced. The transmission energy is therefore expected to be larger than 3eV.

2. In our experiment, target atoms are excited with linearly polarized synchrotron radiation (SR) and ionized with YAG laser (532nm). Both two light beams intersect each other in the right angle, and the YAG laser beam is introduced to pass through an entrance slit and an exit hole of the electron analyzer. The exit hole should be designed to avoid the scattering of the laser light. Therefore, the width of the slit, defining the energy resolution, is determined from the diameter of the laser beam (ϕ2mm).

3. Angular resolution of a spherical analyzer equipped now in the end station of BL3B is about 8 degrees; this value is equal to the angular acceptance and not enough for our purpose. We intend to achieve better angular resolution and wider angular acceptance.

Considering these factors, we have newly designed a conical analyzer consisting of a set of an inner and outer conical deflector electrode, cylindrical lenses, a gas cell and a PSD unit as shown in Figure 1. Photoelectrons emitted in the gas cell are accelerate between the cell and an extractor electrode, then focused on an entrance slit by the cylindrical lenses. The trajectories of electrons between the inner and the outer conical electrodes are similar to those expected for a conventional parallel-plate analyzer. However, the conical analyzer

has rather larger energy dispersion and larger angular aberration than the parallel-plate analyzer. Energy selected electrons ejected from the conical deflector electrodes are detected with the PSD mounted behind the analyzer which consists of a resistive anode encoder of an effective diameter 40mm and micro-channel plates. The energy resolution is expressed as

$$\frac{\Delta E}{E} = \frac{\Delta R}{1.11R} + k_1\alpha + k_2\alpha^2 \approx \frac{1}{30},$$

where R denotes the distance between the entrance and exit slits, α the angular deviation of electrons about the mean trajectory of the incident electrons in the dispersion plane, and k_1 and k_2 angular aberration coefficients. On the other hand, the conical analyzer is incapable of focussing in the azimuth direction. The azimuth angular resolution is thus determined from the diameter of the sample volume (ϕ1mm) and the position sensitivity of PSD, and we expect the resolution of 1.5 degree. With fixing the PSD at certain position, the angular distribution can be measured in the range of 25 degrees at once. By rotating PSD about the synchrotron radiation propagation axis, we can obtain the photoelectron angular distribution from –5 to 95 degrees with respect to the electric vector of SR.

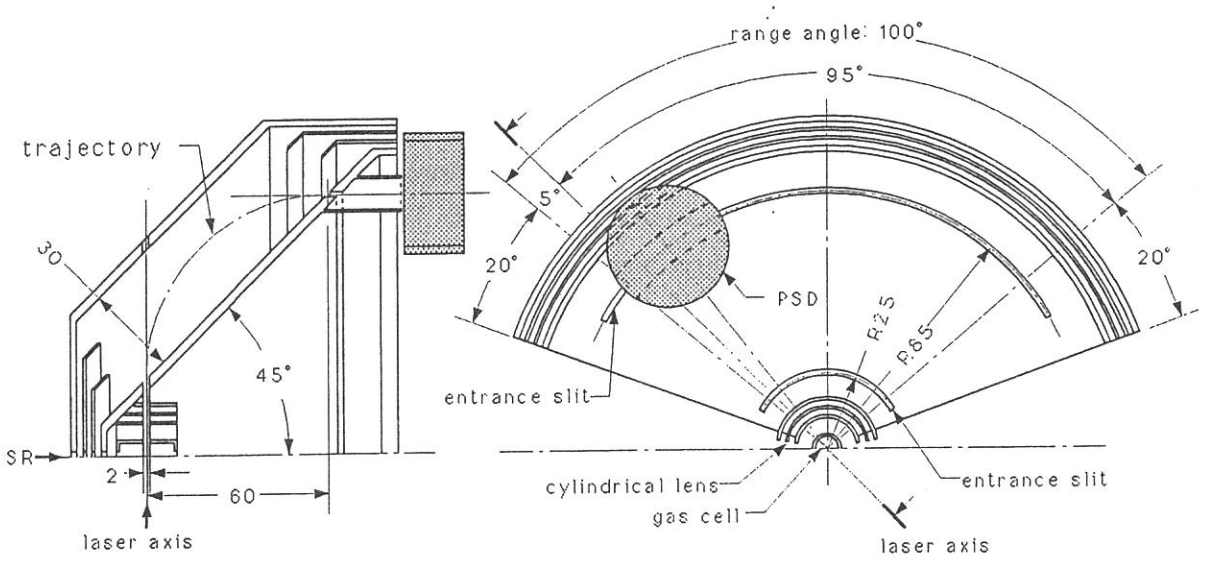

Figure 1. Schematic diagram of the conical analyzer. The principal electrodes of the analyzer are depicted by taking a cross sectional view on the plane which includes the propagation vectors of the laser and SR (left), and by taking a top view (right).

(BL8B1)

Site-selective fragmentation of core-excited acetylacetone

Hiroaki YOSHIDA, Takatoshi YANAGIHARA , Takashi TOKUSHIMA, Yasunori SENBA,

Katsutoshi SHIRASAWA, Katsura KAMIMORI, Atsunari HIRAYA

Department of Physical Sciences, Hiroshima University, Kagamiyama, Higashi-Hiroshima

739-8526, Japan

Site-selective fragmentation of acetylacetone ($CH_3COCH_2COCH_3$) after an excitation of oxygen 1s electron has been studied. Ion yields of m/e=15 (CH_3^+) and 43 (CH_3CO^+) obviously increase at an oxygen 1s→π^* excitation by comparing pre-edge excitation. On the other hand, ion yield of only m/e=15 (CH_3^+) shows a prominent enhancement at an oxygen 1s ionization region. Precursor states of these fragmentation processes are discussed from a viewpoint of resonant and normal Auger decay processes.

Experiments were carried out at BL8B1 of UVSOR. Synchrotron radiation from bending magnet is dispersed by a constant-length-type spherical-grating monochromator. Energy resolution (E/ΔE) of the monochromator is set to about 500 at 500eV. Produced ions are detected by a reflectron-type time-of-flight mass spectrometer. Mass resolution (m/Δm) is about 600 for zero-energy ions.

Total ion yield curve in the oxygen K-edge region in Fig.1 shows a remarkable peak structure at 531.4eV. By comparing the peak position to that of acetone $(CH_3)_2CO$, 530.4eV, the peak is assigned to O1s→$\pi^*_{C=O}$ resonance. A broad structure above about 540eV is ascribed to transitions to the ionization continuum of oxygen 1s electron. Mass spectra were obtained at the energy of a) pre-edge, b) π^*, and c) ionization continuum (Icont) excitations. Contributions by pre-edge excitation were subtracted from raw spectra for π^* and Icont in Fig.2. Ion yields of the specific mass number such as m/e=15 (CH_3^+) and 43(CH_3CO^+) obviously increase at an oxygen 1s→$\pi^*_{C=O}$ excitation by comparing pre-edge. Resonant Auger decay around C=O, which produces a single-charged ion, would weaken the strength of either C-C bond neighboring C=O as shown below.

i) $H_3C\text{-}C{=}O^*\text{-}CH_2COCH_3 \rightarrow H_3C^+\text{—}C{=}O\text{-}CH_2COCH_3 \rightarrow H_3C^+\text{-} \quad \text{-}C{=}O\text{-}CH_2COCH_3$

ii) $H_3C\text{-}C{=}O^*\text{-}CH_2COCH_3 \rightarrow H_3C\text{-}C^+{=}O\text{—}CH_2COCH_3 \rightarrow H_3C\text{-}C^+{=}O\text{-} \quad \text{-}CH_2COCH_3$

CH_3^+ and CH_3CO^+ are, thus, produced effectively after an excitation of oxygen 1s electron to $\pi^*_{C=O}$ orbital. On the other hand, only m/e=15 (CH_3^+) ion yield prominently enhanced at an

oxygen 1s ionization region. Normal Auger decay around C=O, which produces a double-charged ion, would weaken the strength of both C-C bonds neighboring C=O as shown below.

iii) $H_3C\text{-}C{=}O^+\text{-}CH_2COCH_3 \rightarrow H_3C^+—C{=}O—{}^+CH_2COCH_3$

$\rightarrow H_3C^+\text{-} \quad C{=}O \quad \text{-}{}^+CH_2COCH_3$

Coulomb explosion caused by a hole-hole repulsion initially makes ion pairs of CH_3^+ and $CH_2COCH_3^+$. The fact that m/e=57 ($CH_2COCH_3^+$) is not observed in the mass spectra suggests the sequential dissociation of $CH_2COCH_3^+$ into various kinds of fragments. As a result, only CH_3^+ is produced effectively after an ionization of oxygen 1s electron.

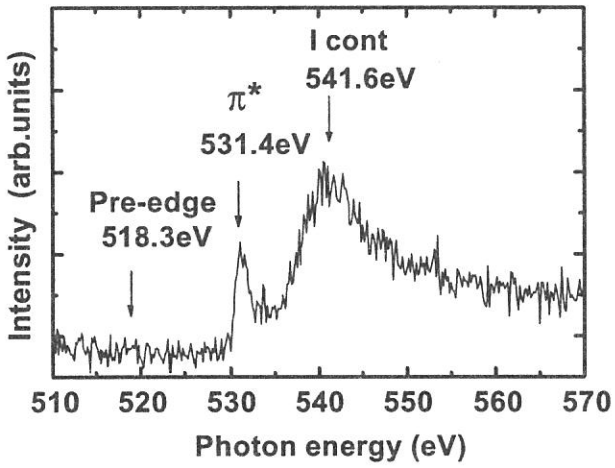

Fig.1 Total ion yield of acetylacetone in the oxygen K-edge region.

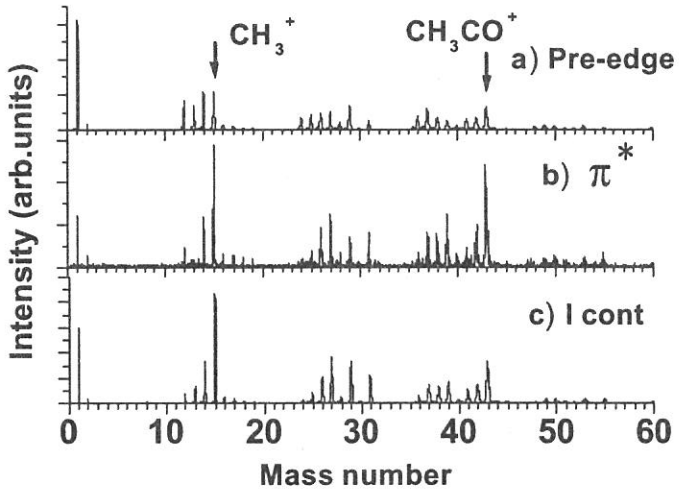

Fig.2 Mass spectra of acetylacetone following a) pre-edge, b) O1s→π*, and c) O1s→ ionization continuum (Icont) excitations. Contributions by pre-edge excitation were subtracted from raw spectra for π* and Icont.

(BL8B1)

The measurement of PEPICO spectra at BL8B1 with photoelectron energies being selected

Tatsuo Gejo, Kazuhiko Mase, Shin-ichiro Tanaka, Shin-ichi Nagaoka
Eiji Ikenaga[A] and Iwao Shimoyama[B]
Institute for Molecular Science, Myodaiji, Okazaki 444-8585, Japan
[A]Faculty of Science, Hiroshima Uviv., Higashi-Hiroshima 739, Japan
[B]Faculty of Science, Kobe Univ., Kobe 657-8501, Japan

Fragmentation and ionization process of inner-shell excited molecules has been investigated by the excitation with synchrotron radiation. When one measures time-of-flight (TOF) spectra of ionic fragments generated from these core-ionized molecule, selecting the energy of the double charged ion energy by photoelectron analyzer allows us to select a defined initial state. This measurement is called PEPICO (photoelectron-phootion-coincidence) or AEPICO (Auger electron-photoion-coincidence) spectroscopy.

A CMA type electron energy analyzer with a TOF apparatus has been constructed and installed at beamline 8B1 in UVSOR for the measurement of the PEPICO spectra. TOF spectra have been observed with photoelectron energies being selected by this analyzer. In order to evaluate this analyzer we used soft X-ray of synchrotron radiation as a photon source and N_2 and CO_2 as target molecules.

Fig. 1 shows the 2D image of PEPICO spectra, in which the TOF spectra was shown with selecting a given photoelectron kinetic energy. The peak around 420 ns can be attributed to the N^+ and those around 650 ns arise from N_2^+. In this figure, strong correlation between Auger electron around 390 eV and the generation of N_2^+ has been observed, suggesting that N_2^+ are mainly generated via $3\sigma_g^{-1}$ Auger decay process. With this technique, we will try the triple coincidence of ionic fragments of molecules.

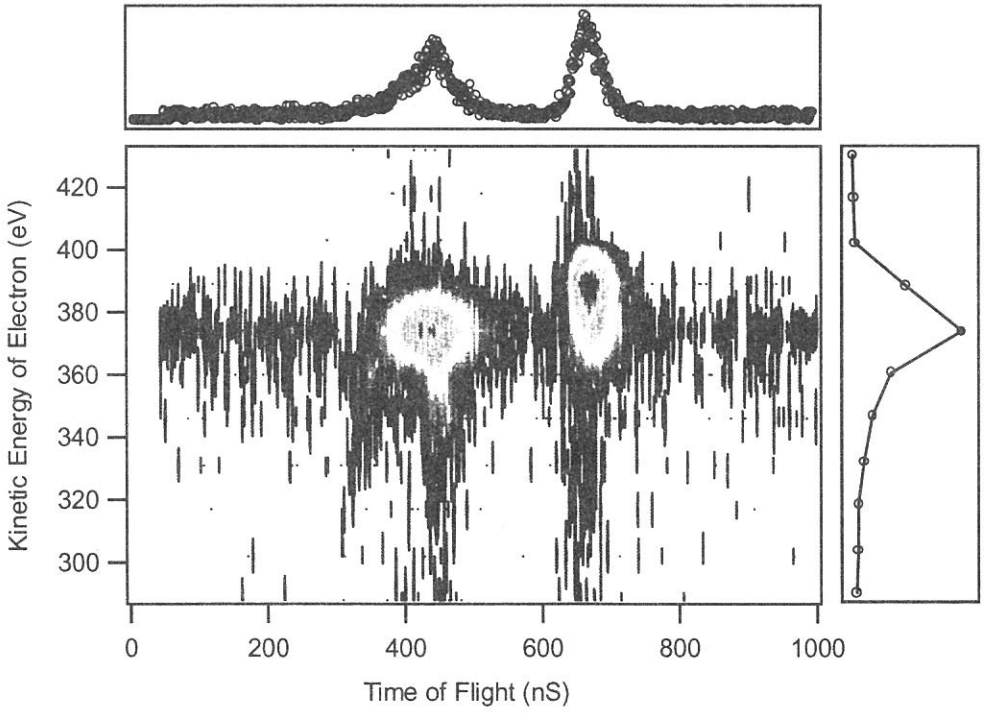

Fig. 1: PEPICO spectra of N_2.

UVSOR

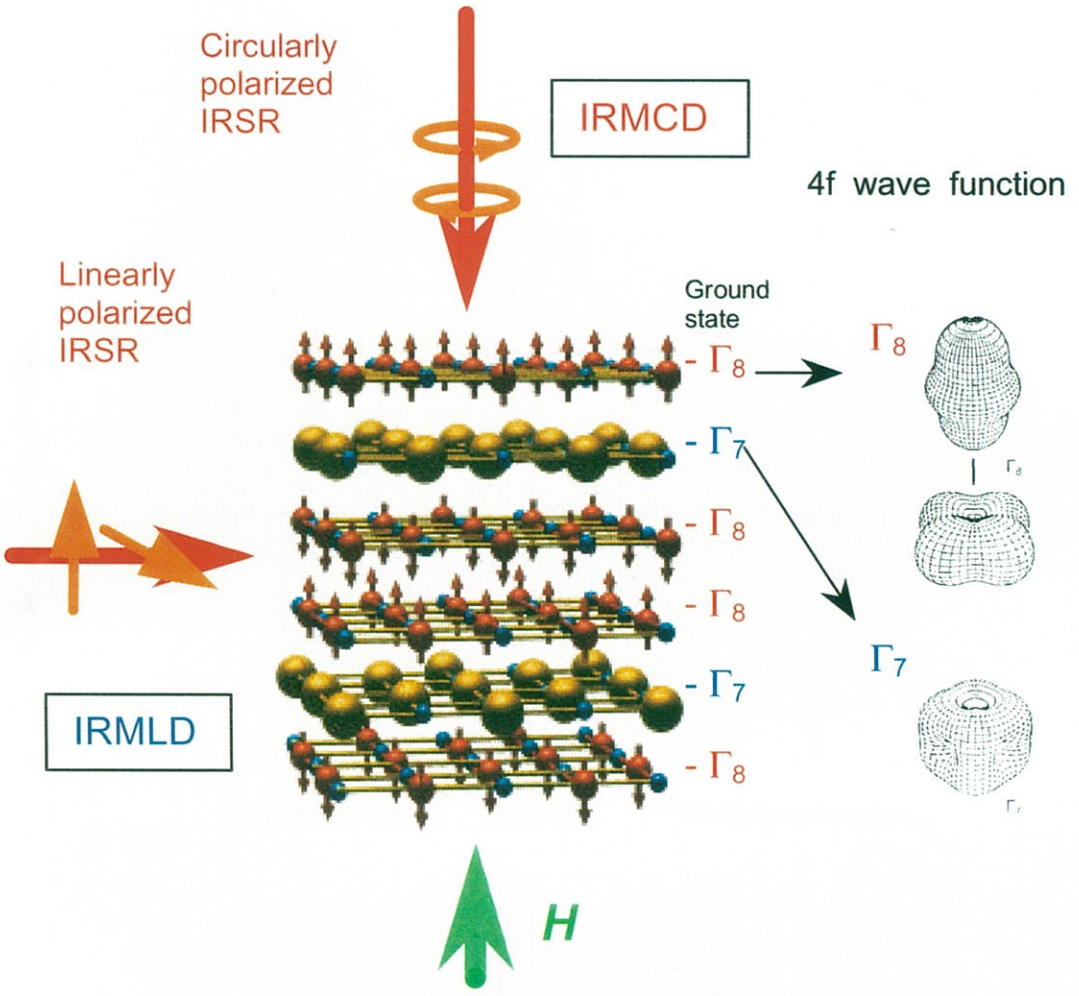

Solid State Spectroscopy I

(IR, VUV, etc)

BL1B, 3A1, 6A1, 7A, 7B

BL1B

LiCAF crystal as a new vacuum ultraviolet optical material with transmission down to 112 nm

M. Sakai[1], M. Kozeki[1], Z. Liu[1], H. Ohtake[1], N. Sarukura[1], Y. Miyazawa[2], K. Shimamura[3], S. L. Baldochi[3], K. Nakano[3], N. Mujilatu[3] and T. Fukuda[3]

[1] Institute for Molecular Science (IMS), Okazaki, Aichi 444-8585, Japan

[2] Research and Development Department, Optron Inc., Toride, Ibaraki 302-0032, Japan

[3] Institute for Materials Research, Tohoku University, Sendai, Miyagi 980-8577, Japan

Recently, various new fluoride crystals have been developed as the host crystals for new solid-state tunable ultraviolet and infrared laser materials. Ce:LiCAF and Ce:LiSAF are attractive solid-state lasers with their practical tuning region from 288 to 315 nm [1, 2]. To improve laser performance, further spectroscopic studies of these materials will be necessary, including accurate band-gap measurement of the host crystal. In addition, optical material for the ultraviolet and vacuum ultraviolet region has become much more important for the deep ultraviolet lithographic technology required for the semiconductor processing technology of the next century and vacuum ultraviolet spectroscopy using synchrotron orbital radiation.

Crystals of LiCAF, LiSAF and LiF were grown by the Czochralski method. The sample was about 1-mm thick. To measure the transmission edge of various fluoride materials at room temperature, an experiment was performed at Ultraviolet Synchrotron Orbital Radiation Facility (UVSOR). Figure 1, indicates the transmission spectrum of various fluoride samples. According this figure, transmission edge of LiCAF, LiSAF and LiF were 112 nm, 116 nm and 136 nm, respectively. From the transparent wavelength shorter than that of conventional LiF, the non hydroscopic nature of LiCAF, and the better mechanical properties compared with LiF, LiCAF is shown to be an ideal optical material for the vacuum ultraviolet region.

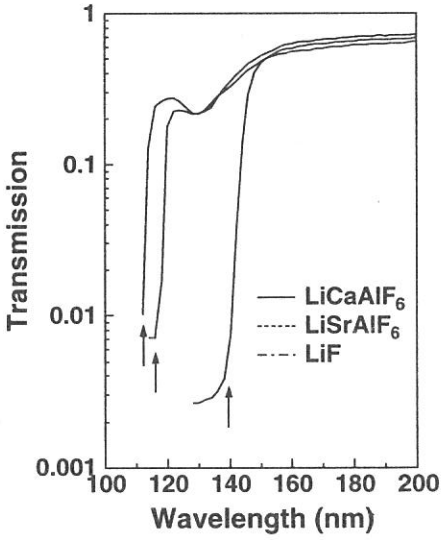

Fig. 1

The authors are grateful to Mr. M. Hasumoto, Dr. T. Gejo, and Prof. K. Kamada for their experimental support and stimulated discussion.

References

[1] See, for example, C. D. Marshall, S. A. Payne, J. A. Speth, W. F. Krupke, G. J. Quarles, V. Castillo and B. H. T. Chai: J. Opt. Soc. Am. B. **11** (1994) 2054-2057.

[2] See, for example, Z. Liu, S. Izumida, H. Ohtake, N. Sarukura, K. Shimamura, N. Mujilatu , S. L. Baldochi and T. Fukuda: Jpn. J. Appl. Phys., **37** (1998) L1318 –L1321

(BL1B)

Surface Excess of Dye Molecules at Gas/Water Interface Determined by Single-Photon Ionization Spectroscopy

Toshio Ishioka, Koichiro Seno, Shinya Sasaki, and Akira Harata

Department of Molecular and Material Sciences, Interdisciplinary Graduate School of Engineering Sciences, Kyushu University, Fukuoka, 816-8580 Japan

The understanding of molecular behavior at gas/water interface is of central importance in surface science, film technology, and environmental chemistry. For decades, they have been studied by methods such as surface tensiometry and radiochemical methods, yielding mostly information on the macroscopic level of interface. The recently developed nonlinear optical methods, such as second-harmonic generation (SHG), sum-frequency generation (SFG), and multi-photon ionization, have been providing essential information on microscopic molecular states of surfaces since they have specific sensitivity of 'just' interface. Though they are excellent in selectivity at interfaces, the mechanism of multi-photon process is usually complex and difficult to analyze quantitatively because resonant states often intervene in those processes. To solve above problem, we have tried to measure simple single-photon ionization spectra of dye molecule using synchrotron radiation, and compare the results with those of two-photon ionization and surface-tension measurements.

The experimental setup for single-photon ionization is shown in Fig. 1. Synchrotron photon-energy from 4.7 to 6.8 eV was used as an excitation source. The beam power was calibrated using a photomultiplier tube (Hamamatsu Photonics, R955) after each measurement. The beam was irradiated on the water surface containing various concentration of Rhodamine B (RhB). The solution was kept in a stainless-steel vessel so that high voltage was appliable between water surface and electron-trapping electrode settled in the gas. The photoionization current was measured using a current meter (Keithley, 617). Two-photon ionization experiment was carried out using third-harmonic (355 nm, 5 ns) of Nd:YAG laser (Minilite, Spectra Physics). Experimental configuration of two-photon ionization was approximately the same except for the excitation source and cell dimension. Surface tension was measured by a surface-pressure meter (Model HMB, Kyowakaimen, Japan) equipped with a glass plate of Wilhelmy type. RhB (reagent grade, Nacalaitesque, Japan) was used as received and dissolved into pure water. Water was purified until resistivity reached higher than 18 MΩcm by Milli-Q system (Milli-Q Academic, Millipore).

The normalized one-photon ionization spectra of RhB is shown as Fig. 2. All derived spectra obey a empirical 5/2 power law represented by

$$I = C\, E_{ex}^{2.5} = C\, (h\nu - E_{th})^{2.5} \qquad (1)$$

where E_{ex} is the excess energy of the ionized pair; C is the proportionality constant; and E_{th} is the ionization threshold. The abscissa in Fig. 2 should give the E_{th} value of eq.1. The derived threshold energy for RhB lies at 5.5–5.6 eV and does not depend on the bulk concentration, which would imply neither the chemical state of RhB nor the length from the surface are largely changed.

At fixed photon energy, the photoionization intensity should be linear with the number of photoionizing molecule at probe area. In Fig.2, the signal intensity at fixed photon energy above E_{th} monotonously increases with RhB concentration because surface density increase with bulk concentration. If linearity with surface concentration (which is equal to the thermodynamic definition of 'surface excess' when dilute solution is used) and photoionization intensity can be assumed, the adsorption isotherm can be discussed. In Fig. 3, the intensity of photoionization is plotted against bulk concentration, and obviously, it obeys Langmuir isotherm which was denoted by

$$\Gamma/(\Gamma_{max}-\Gamma) = \beta c \qquad (2)$$

where Γ and Γ_{max} denote surface excess and saturated surface excess, respectively; β is the adsorption parameter; and c is the bulk concentration of adsorbate. The result that RhB obey Langmuir isotherm is coincident with the result of two-photon ionization and surface tension measurement. Table 3 summarizes the result of adsorption parameter derived from these methods. They agree within a factor or two and show these methods are reliable to measure surface excess of RhB. Small deviation of each experimental value was, however, observed in Table 3, which may imply the difference of probe region (probe depth from surface) of these methods. Further discussion would be carried out in future articles.

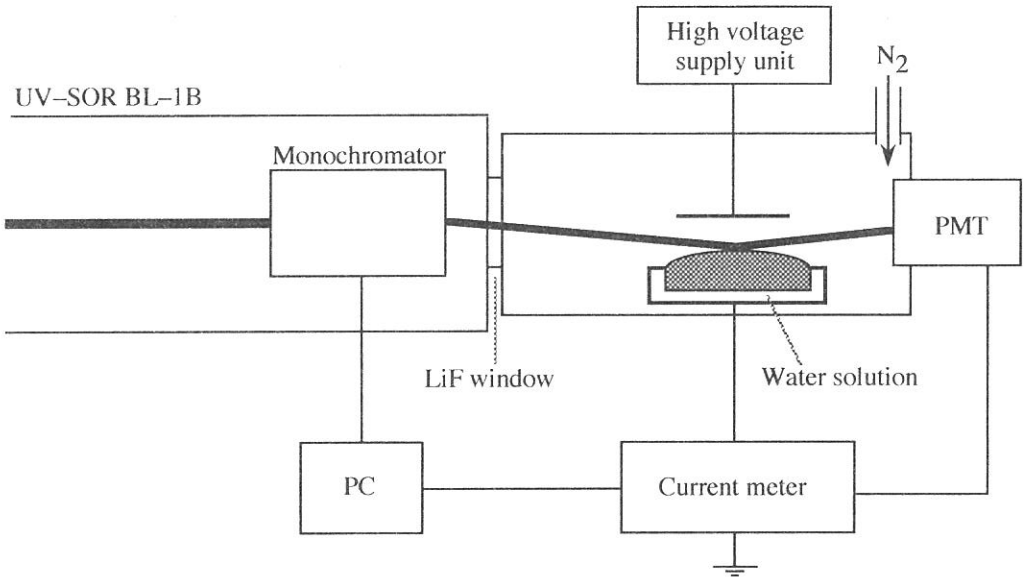

Fig. 1 Schematic diagram of the photoionization spectrometer using SOR light.

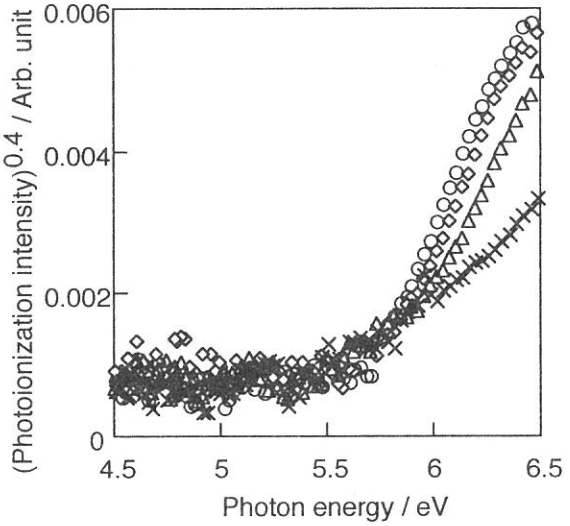

Fig. 2 Bulk concentration dependence of RhB on single-photon ionization spectra of water surface. Each RhB concentration was $1.0*10^{-4}$ M(circle), $1.0*10^{-5}$ M (lozenge), $2.0*10^{-6}$M (triangle), and $3.0*10^{-7}$ M (cross).

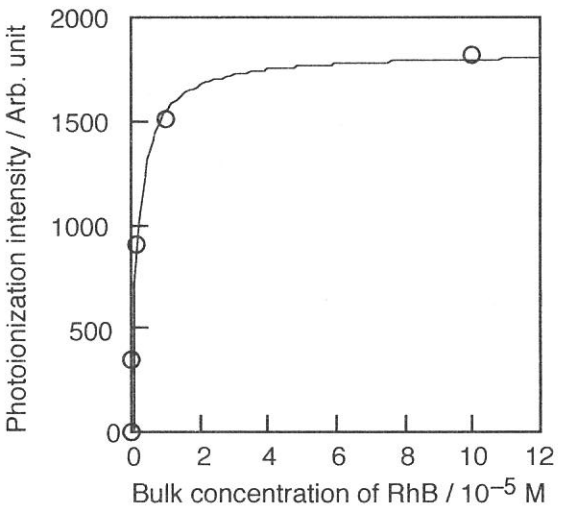

Fig. 3 Adsorption isotherm RhB onto water surface by single-photon ionization. The fitting was carried out using Langmuir isotherm.

Table 1 Adsorption parameter of RhB onto water derived by various methods.

Method	β / 10^5 mol^{-1} dm^3 *
single-photon ionization	5.2
two-photon ionization	3.9
surface tension	8.2

*) Langmuir isotherm: $\Gamma / (\Gamma_{sat}-\Gamma) = \beta a$; Γ(surface excess), Γ_{sat}(saturated surface excess), a (activity in bulk phase), β (adsorption parameter).

(BL1B) Reflection and luminescence spectra of $CaWO_4$ and $ZnWO_4$ crystals grown by flux method

Minoru ITOH, Michihiro HORIMOTO, Shuji OISHI[1] and Masami FUJITA[2]

Department of Electrical and Electronic Engineering, Shinshu University, Nagano 380-8553
[1] *Department of Environmental Science and Technology, Shinshu University, Nagano 380-8553*
[2] *Maritime Safety Academy, Wakaba, Kure 737-8512*

The second-group metal tungstate family has extensive applications and therefore has been intensively studied during the past half a century. However, there are still unanswered questions concerning the nature of the optical transitions; e.g., the importance of defects and impurities on the luminescence properties. Until now, all the crystals investigated have been grown from the melt by the Kyropoulos or Bridgman technique. This may introduce some local deformation due to thermal stress into the large-volume crystals. The growth method using flux has several principal advantages; the resultant crystals are relatively free of thermal stress and has a lower concentration of lattice imperfections, compared to the melt-grown crystals. In the present experiment, we have, for the first time, investigated the optical properties of $CaWO_4$ and $ZnWO_4$ crystals grown by the flux method. Calcium tungstate crystallizes in a scheelite (stolzite) structure, while zinc tungstate has a raspite (wolframite) structure.

Well-formed crystals of $CaWO_4$ were grown in Na_2WO_4 flux. The crystal growth was conducted by heating mixtures at 1100 °C for 5 h, followed by cooling to 500 °C at a rate of 5 °C/h [1]. Crystals of $ZnWO_4$ were prepared in Na_2O-WO_3 flux. The heating conditions for $ZnWO_4$ growth were almost the same as those in the case of $CaWO_4$ growth. Both crystals obtained were colorless and transparent, with flat surfaces. The X-ray diffraction indicated that our crystals of $CaWO_4$ and $ZnWO_4$ are single-phased.

A solid curve of Fig. 1 represents the reflection spectrum of $CaWO_4$ measured at 6 K under near-normal incidence configuration. There exist a sharp exciton band at 5.96 eV and a broad doublet structure in the spectral range between 8 and 12 eV. This spectrum is similar to the previous result obtained in ref. [2], although our doublet structure is larger in intensity than theirs. The reflection spectrum of $ZnWO_4$ is shown by a solid curve in Fig. 2. One can see a strong band peaking at 5.00 eV with sub-structures on the low- and high-energy sides, and a weak doublet structure in the 8－12 eV range. To our knowledge, there seems to be no reflection data of $ZnWO_4$ to be compared to our spectrum.

The $CaWO_4$ and $ZnWO_4$ emit a single luminescence peaking at 2.85 and 2.40 eV under excitation in the exciton-band region at 6 K, respectively. The spectra are shown in Fig. 3, where the collections were made for the dispersion of the analyzing monochromator and for the spectral response of the detection system. The excitation spectra for these two bands are shown by dotted curves in Figs. 1 and 2. It is evident that the 2.85- and 2.40-eV bands are an intrinsic feature to the respective systems, because they are stimulated with photons above the onset of the lowest exciton reflection bands. The 2.40-eV luminescence of $ZnWO_4$ exhibited two decay components at 6 K; fast one (1.2 ± 0.2 μs) and slow one (21 ± 1 μs). Decay measurement was not carried out for the 2.85-eV luminescence in $CaWO_4$. At 295 K, both emission bands are thermally quenched by 50%.

When $CaWO_4$ is excited around 4.6 eV on the low-energy side of the exciton band, two weak emission bands appear at about 2.45 and 2.70 eV. They are most likely due to lattice imperfections. On the other hand, no other luminescence was observed in $ZnWO_4$.

According to a recent band structure calculation of some tungstate crystals [3], the main exciton peaks in Figs. 1 and 2 would be ascribed to the optical transitions from the O 2*p* states to the W 5*d* states. It is, therefore, supposed that the 2.85-eV emission band of $CaWO_4$ arises from radiative annihilation of excitons self-trapped on WO_4 molecular groups in which four oxygen ions form the tetrahedron with a tungsten ion at the center. On the other hand, the emission band at 2.40 eV in $ZnWO_4$ is attributed to excitons self-trapped on octahedral WO_6 groups in which a tungsten ion is surrounded by six oxygen ions. The luminescence in monoclinic tungstate crystals of raspite-type appears at the energy lower than that in tetragonal ones of scheelite-type. This general trend has nicely been confirmed for $PbWO_4$ by our recent experiment [4].

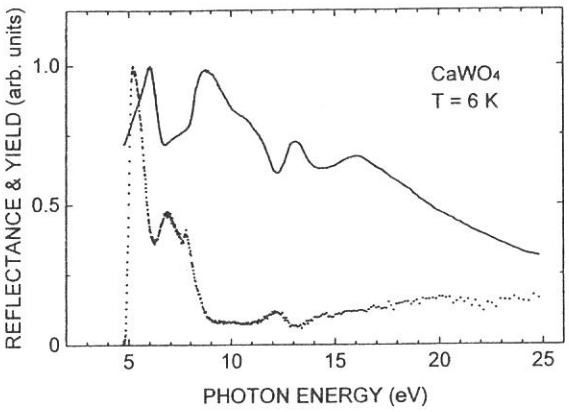

Fig. 1. $CaWO_4$: reflection spectrum (solid curve) and excitation spectrum (dotted curve) for the 2.85-eV band.

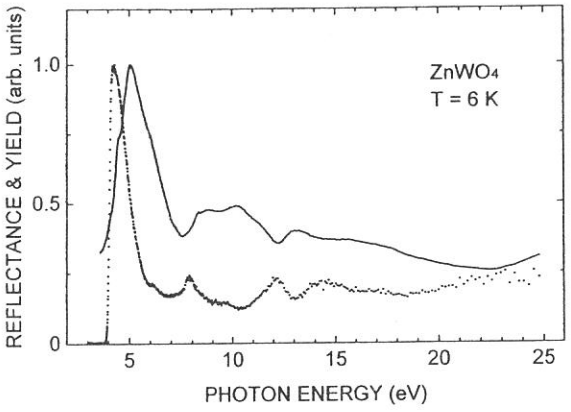

Fig. 2. $ZnWO_4$: reflection spectrum (solid curve) and excitation spectrum (dotted curve) for the 2.40-eV band.

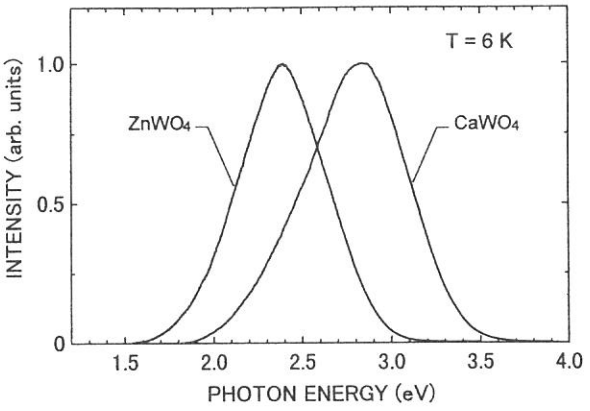

Fig. 3. Luminescence spectra of $CaWO_4$ and $ZnWO_4$ excited at 6 K with 5.15- and 4.45-eV photons, respectively.

[1] S. Oishi and M. Hirao: Bull. Chem. Soc. Jpn. **63** (1990) 2721.

[2] R. Grasser, E. Pitt, A. Scharmann and G. Zimmerer: Phys. Status Solidi (B) **69** (1975) 359.

[3] Y. Zhang, N. A. W. Holzwarth and R. T. Williams: Phys Rev. B **57** (1998) 12738.

[4] M. Itoh, D. L. Alov and M. Fujita: J. Lumin. (in press).

(BL1B)

Photoluminescence in amorphous silicon oxynitride grown by plasma-enhanced chemical vapor deposition

Hiromitsu *KATO*, Kwang Soo *SEOL**, Makoto *FUJIMAKI***, Takashi *NOMA****, Takashi *WATANABE*, and Yoshimichi *OHKI*
Department of Electrical, Electronics, and Computer Engineering,
Waseda University, Shinjuku-ku, Tokyo 169-8555.
* Applied Laser Chemistry Lab., RIKEN (The Institute of Physical and Chemical Research),
Hirosawa, Wako-shi, Saitama 351-0198.
** Research Fellow of the Japan Society for the Promotion of Science.
***Engineering Department 1, MOS-LSI Division, Semiconductor Company, Sanyo Electric Co. Ltd,
Oizumi-Machi, Gumma 370-0596.

Category 4. Solid- & liquid-phase spectroscopy 1 (IR, VUV, etc)

I. EXPERIMENTAL PROCEDURES

The amorphous silicon oxynitride (a-SiO_xN_y) films were deposited on a silicon monocrystal substrate by plasma enhanced chemical vapor deposition at a substrate temperature of 400 °C using SiH_4, N_2O and N_2 as monomer gases. The thickness of these films was about 100 nm. By changing the flow rate of SiH_4, samples A to E shown in Table I were obtained. The ratio of y/x was measured using X-ray photoelectron spectroscopy (JEOL JPS-90MX). Photoluminescence (PL) spectra, PL excitation (PLE) spectra and PL decay profiles were measured using synchrotron radiation (SR) at BL1B line in UVSOR. The PL and PLE spectra were measured under multi bunch operation mode at 14 K, and the PL decay profiles were measured at 14 K by a time-correlated single photon counting technique under single-bunch operation mode.

II. RESULTS AND DISCUSSION

Figure 1 (a) shows the PL spectrum of sample B excited by 5.0 eV photons. Intense PL is observed at 4.4 eV. Figure (b) shows the PLE spectrum of the 4.4 eV band. As shown in Fig.1 (b), the 4.4 eV band has two PLE bands at 5.0 eV and 7.3 eV. Figure 2 shows decay profiles of the 4.4eV band excited at 5.0 eV (a) and 7.3 eV (b). The data were fitted by the least-squares method with the time derivative of a stretched exponential function,

$$I(t) \propto (\beta/\tau)(\tau/t)^{1-\beta}\exp(-(t/\tau)^{\beta}). \qquad (1)$$

Here, τ and β are the effective lifetime and a parameter which takes a value of $0<\beta<1$, respectively. This is consistent with many reports which revealed that the luminescence decay in many amorphous materials is described by the above equation. The lifetime of the 4.4 eV band is 3.4 ns under the 5.0 eV excitation and is 2.2 ns under the 7.3 eV excitation. These values agree well with the ones reported for the lifetime of 4.4 eV band due to the oxygen vacancy (≡Si-Si≡, '≡' denotes bonds with three separate oxygen atoms) in the oxygen-deficient-type bulk SiO_2. The 4.4 eV band in SiO_2 is considered to be due to an electronic transition from the excited singlet state to the ground state. The oxygen vacancy in SiO_2 also gives rise to a PL band at 2.7 eV, which is due to an electronic transition from the excited triplet state to the ground state. Since this 2.7 eV band involves a thermally activated intersystem crossing, its intensity decreases as the temperature decreases. These characteristics, namely, the concurrence of two PLs at 2.7 and 4.4 eV, the PLE spectrum and the lifetime of the 4.4 eV band, and the temperature dependence of the 2.7 eV band agree quite well with those of the PL bands shown in Fig.1. This indicates that sample B includes oxygen-deficient SiO_2.

Figure 3 shows the PL spectrum (a) of sample E excited at 5.0 eV and the PLE spectrum (b) monitored at 2.6 eV. The 4.4 eV band does not appear, indicating that the oxygen-deficient SiO_2 was not present. For comparison, the PL and PLE spectra are also shown for hydrogenated amorphous silicon nitride (a-SiN_x:H) deposited by low-pressure chemical vapor deposition. In both samples, the 2.6 eV band is seen. From Fig.3 (b), it is considered that both the 2.6 eV band in sample E and the 2.6 eV band in SiN_x are excited by interband photon absorption. The subtle difference in the photon energy at which the PLE spectrum starts to rise is presumably due to the difference in the optical absorption edge in the two materials. The lifetime τ is 3.2 ns for sample E and 3.7 ns for SiN_x, while β is 0.39 and 0.40. This good agreement indicates that the two PLs are caused by the same mechanism. The 2.6 eV band of SiN_x is considered to be related to recombination of electrons and holes, generated by interband photon absorption. It is therefore considered that the 2.6 eV band in sample E is caused by the same mechanism, and that sample E includes, at least partially, the structure of SiN_x.

As a function of y/x, the change of the two PL intensities, 2.6 eV and 4.4 eV, clearly shows that the contribution of PL from SiN_x is weak if y/x is small and becomes stronger when y/x becomes larger. This indicates that the present samples, SiO_xN_y, are not a perfect compound, and includes, at least partially, SiO_2 and SiN_x. The ratio of SiN_x and SiO_2 depends primarily on the ratio y/x.

Table I. The y/x ratio and refractive index for SiO_xN_y films examined.

Sample	y/x	refractive index
A	0.054	1.49
B	0.112	1.52
C	0.125	1.54
D	0.148	1.56
E	0.161	1.59

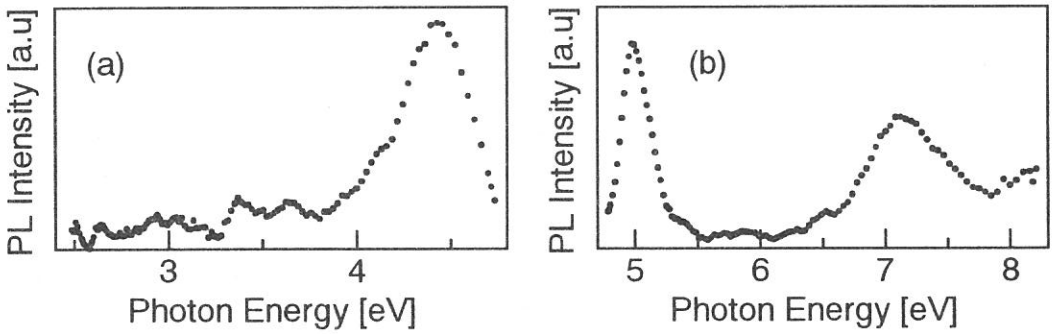

FIG.1. PL spectrum (a) of sample B at 14 K excited by 5.0 eV photons and PLE spectrum (b) of the 4.4 eV band.

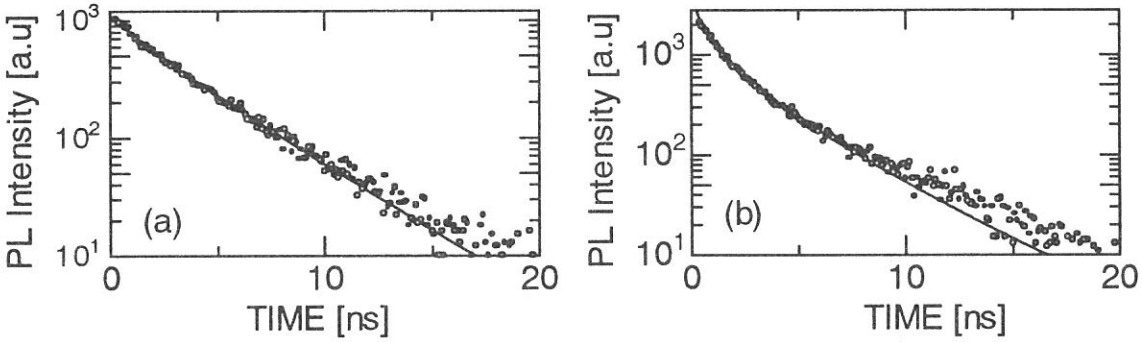

FIG.2. Decay profiles of the 4.4 eV band excited at 5.0 eV (a) and 7.3 eV (b) for sample B. Solid curves are drawn by assuming the stretched exponential function, Eq. (1).

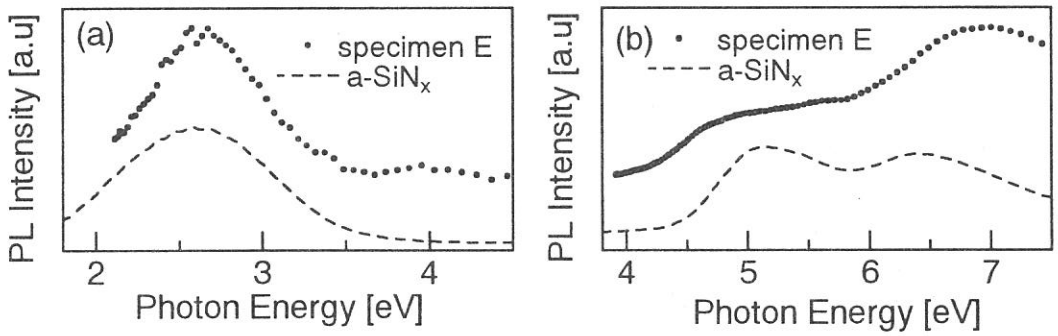

FIG.3. PL spectrum excited by 5.0 eV photons (a) and PLE spectrum of the 2.6 eV PL band (b) for sample E (solid curves) and SiN_x (broken curves).

(BL1B)

Reflection Spectra of Hydrogen-Bonded Ferroelectric $PbDPO_4$

Noriaki KIDA, Nobuhito OHNO[A], Yoshihiko YAMAZAKI[A] and Masao KAMADA[B]

Research Center for Superconducting Materials and Electronics, Osaka University, Suita, Osaka 565-0871, Japan
[A] Division of Electronics and Applied Physics, Graduate School of Engineering, Osaka Electro-Communication University, Neyagawa, Osaka 572-8530, Japan
[B] UVSOR Facility, Institute for Molecular Science, Okazaki, Aichi 444-8585, Japan

Lead monohydrogen phosphate $PbHPO_4$ (LHP) is a hydrogen-bonded ferroelectric material. It shows a second-order structural phase transition from a monoclinic Pc to a paraelectric $P2/c$ at T_C=310 K. The PO_4 tetrahedra are linked to linear chains by short O-H-O bonds and not cross-linked to one another, in contrast to well studied KH_2PO_4 (KDP) [1]. Therefore, LHP and its isomorphic compounds are regarded as quasi-one dimensional ferroelectrics. The most famous phenomenon of the hydrogen-bondend ferroelectric materials is the isotope effect — Curie point T_C corresponding to the onset temperature of ferroelectric order increases by substituting deuterium for hydrogen atoms —. In deuterium compound of LHP, $PbDPO_4$ (DLHP), T_C increases to about 450 K [2].

Up to now, optical response of LHP and $PbHAsO_4$ (LHA) has been investigated [3]. The clear direct excitonic transitions are observed at the fundamental absorption edge. These transitions are assigned due to intra-cationic Pb^{2+} transitions ($6s \rightarrow 6p$). The Urbach rule holds well for the absorption edge of LHP. The conversing energy is found to be different between ferro- and paraelectric phases. The temperature profile of the steepness parameter (σ) of LHP derived from Urbach slope exhibits an anomalous behavior. Moreover, the observed temperature-dependent σ is well scaled to that of the spontaneous polarization (P_S) with the scaling factor $\sim 1/2$. Recently, Noba and Kayanuma have theoretically shown that excitons in the ferroelectric phase are strongly affected by the Stark effects induced by the local fields due to the hydrogen ordering [4]. It is interesting to study the optical properties of DLHP, to see the isotope effect on the electronic structure of LHP.

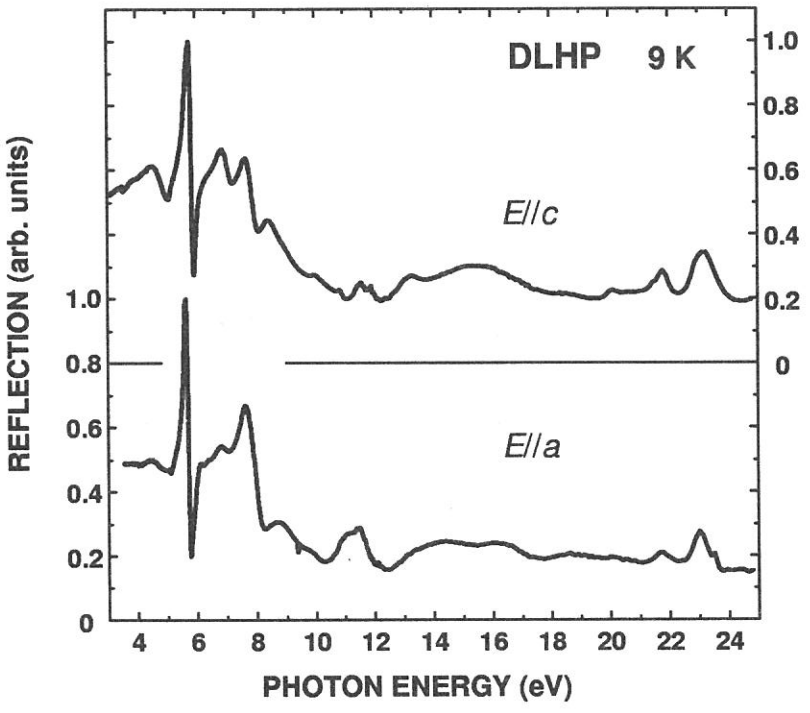

Figure 1: Polarized reflection spectra of DLHP for $E//a$ (lower) and $E//c$ (upper) at 9 K. Each spectrum is normalized at maximum.

Table 1: The first direct exciton transition energy E_1, the exciton binding energy E_B and the band-gap energy E_G for DLHP and LHP ($E//a$).

	E_1 (eV)	E_B (eV)	E_G (eV)
DLHP	5.63	0.67	6.30
LHP	5.62	0.67	6.29

In the present investigations, reflection spectra of a single crystal of DLHP have been investigated for the first time in the VUV region up to 25 eV by using polarized synchrotron radiation at the BL1B beamline. The specimens of DLHP grown from the conventional gel-growth method were used for optical measurements.

Figure 1 shows the reflection spectra of a single crystal of DLHP for polarization parallel to the crystallographic a-axis ($E//a$) and the c-axis ($E//c$), respectively, measured at 9 K. The direction of P_S is in the ac plain, nearly close to the a-axis. Distinguished sharp peaks with dispersive structure are observed at the absorption edge at 5.63 eV for $E//a$ and at 5.77 eV for $E//c$. In LHP, these structures are located at 5.62 eV for $E//a$ and at 5.77 eV for $E//c$. These transitions have been ascribed to the cationic transition Pb^{2+} ($6s \rightarrow 6p$) based on the comparative results of the isomorphic compound LHA as well as KDP [3]. Hence, the first excitonic bands in DLHP are assigned as cationic-intraband transition of Pb^{2+} ions as in LHP. With increasing temperature, these structures shift to the lower energy side. They are clearly seen even at room temperature. This fact indicates that the exciton has a large binding energy (E_B).

A clear shoulder structure is observed on the higher energy side of the first direct exciton transition for $E//a$ at 6.13 eV. This transition peak is assigned to the n=2 state of exciton Rydberg series. We adopt the hydrogen-like energy model and estimate E_B and the band-gap energy (E_G) of DLHP as summarized in Table 1 together with LHP.

Spectral profile and peak energy positions are resemble to those of LHP. These results suggest that the electronic state of exciton is not affected by the *statical* hydrogen atoms. Hence the change of σ with temperature as observed in LHP is responsible for the *dynamics* of surrounding atoms.

The structures around 22 eV are attributed to the Pb^{2+} $5d \rightarrow 6p$ core excitons. Sharp peaks at 21.7 eV and 23.0 eV for $E//a$ are assigned to the transitions from the $^1S_0$ state to the $^3P_1$ and $^1P_1$ excited states, as in the cases of LHP and lead halides [3, 5]. As compared with LHP and LHA, these structures are more clearly seen in DLHP. An additional structure on the higher energy at 23.5 eV for $E//a$ is probably due to the transition to the $^3D_1$ state.

We thank Dr. D. J. Lockwood for kindly providing single crystals of DLHP.

References

[1] F. Jona and G. Shirane, Ferroelectric Crystals, p63 (Dover, United States, 1993).

[2] K. Deguchi and E. Nakamura, J. Phys. Soc. Jpn. **57**, 413 (1988).

[3] N. Kida, N. Ohno, K. Deguchi, and M. Kamada, J. Electron Spectrosc. Relat. Phenom. **101-103**, 603 (1999); N. Ohno and N. Kida, Ferroelectrics **223**, 389 (1999); N. Kida, Bussei Kenkyu (Kyoto) **63**, 477 (1999) [in Japanese]; N. Kida, N. Ohno, and M. Kamada, UVSOR Activity Report **1998**, 86 (1999).

[4] K. Noba and Y. Kayanuma, Phys. Rev. B **60**, 4418 (1999).

[5] M. Fujita, H. Nakagawa, K. Fukui, H. Matsumoto, T. Miyanaga, and M. Watanabe, J. Phys. Soc. Jpn. **60**, 4983 (1991).

(BL-1B)

Multiplication process of free excitons in $CsPbCl_3$ crystal

Mamoru KITAURA and Akimasa OHNISHI[A]

Fukui National College of Technology, Sabae 916-8507

[A]*Department of Physics, Yamagata University, Yamagata 990-8560*

Excitation spectra for luminescence in the energy region exceeding the band-gap energy by several times are know to contain information on multiplication process of electronic excitations (EE's). [1] In the present work, we measured the excitation spectrum for the free exciton luminescence in $CsPbCl_3$ crystals at BL-1B beam line of UVSOR and investigated the multiplication process of EE's in this material.

$CsPbCl_3$ single crystals were grown from melt in sealed quartz ampoules by the Bridgman method. The crystal samples were mounted on a Cu holder of a liquid helium cryostat and were cooled down to 15 K by thermal conduction. The free exciton luminescence was detected with a photomultiplier (Hamamatsu R955) through a grating monochromator (Jobin-Yvon HR320). The excitation spectra measured were corrected for both the spectral distribution and reflection losses of an excitation light.

Figure 1 shows the excitation spectrum for the free exciton luminescence of $CsPbCl_3$ at 15 K. For reference, the reflection spectrum at 15 K is also shown by a broken line. In spite of the correction for reflection losses of an excitation light, the excitation spectrum for the free exciton luminescence exhibits dips at reflection peaks. The dips should be connected to nonradiative annihilation of EE's at the crystal surface, because optical excitation at the reflection peaks with high absorption coefficient creates high concentrated EE's at the crystal surface.

The free exciton luminescence is excited with photons in the whole absorption region. It drastically increases its intensity in the energy range of 9.5-12.5 eV, and reaches almost twice that at 9 eV where one photon creates one *e-h* pair. Such increase in the intensity of the free exciton luminescence takes place beyond three times the band gap energy. These results undoubtedly satisfy a condition for multiplication processes of EE's. Heiderich *et al.* [2] measured the reflection spectrum of $CsPbCl_3$ and assigned reflection structures between 8 and 10 eV to electronic transitions from the VB of Cl 3*p* states to higher lying Cs 6*s* conduction states. Furthermore, they calculated its energy band structure and presented that the Cs 6*s* conduction states lie above the conduction band (CB) bottom of Pb 6*p* orbitals by 2.9 eV. It is worth noting that the energy between the Cs 6*s* and the Pb 6*p* states is almost equal to that of the lowest exciton peak. On this basis, the following situation will be supposed for the increase in the free exciton luminescence intensity in the 9.5 - 12.5 eV range. Hot photoelectrons optically created in the Cs 6*s* conduction states will release their kinetic energies through an inelastic scattering on valence electrons, and then relax into the conduction band bottom. The released kinetic energies are transferred to cause secondary excitation of the valence electrons. As a result, a free exction is secondarily produced besides an initially created *e-h* pair. The production of a free exciton

and an *e-h* pair results in the twice value of the free exciton luminescence intensity at 12.5 eV. Therefore, we attribute the increase in the 9.5 - 12.5 eV range to secondary formation of free excitons due to an inelastic scattering of hot photoelectrons in the Cs 6*s* conduction states on valence electrons.

In the 12.5 - 15 eV range, the free exciton luminescence is slightly enhanced. Since this energy range includes contribution of electronic transitions from Cs 5*p* core levels to the CB [2], such a slight enhancement in the free exciton luminescence originates from creation of Cs 5*p* core holes. From ref. 2, the energy between the top of the Cs 5*p* levels and the bottom of the VB is estimated to be about 3 eV. This value is almost equal to the band-gap energy and is enough to excite valence electrons into the CB bottom. It is thus possible to generate secondary valence excitation, when the Cs 5*p* core holes combine with valence electrons to decay nonradiatively. Therefore, we attribute the enhancement in the 12.5 - 15 eV range to secondary formation of *e-h* pairs accompanied by nonradiative decay of a photohole in the Cs 5*p* core levels.

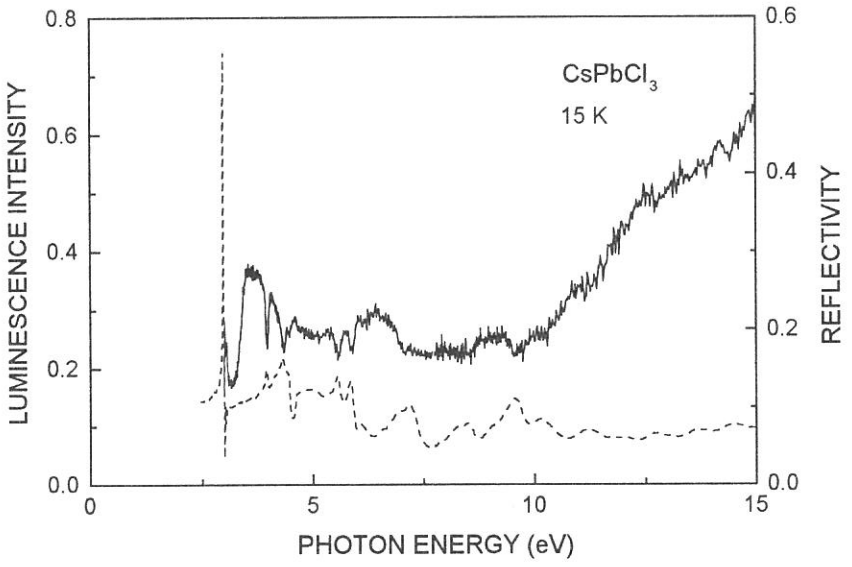

Fig. 1: Excitation spectrum for the free exciton luminescence line of $CsPbCl_3$ observed at 15 K. For reference, the reflectivity spectrum at 15 K is shown by a broken curve.

References

[1] A. Lushchik, E. Ferdbach, R. Kink and Ch. Lushchik: Phys. Rev. B, **53** (1996) 5379.

[2] K. Heidrich, W. Schafer, M. Schreiber, J. Sochtig, G. Trendel and J. Treusch: Phys. Rev. B, **24** (1981) 5642.

(BL-1B)

Reflection Spectra of $(C_2H_5NH_3)_2CdCl_4$ Single Crystal

Akimasa OHNISHI, Ken-ichi TANAKA, Takafumi OTOMO,
Takehisa YOSHINARI and Mamoru Kitaura[A]
Department of Physics, Yamagata University, Yamagata 990-8560
[A]*Fukui Department of Physics and Mathematics, National College of Technology, Sabae 916-8507*

We have studied the lowest exciton absorption of $(C_2H_5NH_3)_2CdCl_4$ single crystal and reported that the upper valence band (VB) and the lowest conduction band (CB) are constructed from the Cl 3*p* and Cd 5*s* states, respectively.[1] In the present work, we measured the optical reflection spectra of $(C_2H_5NH_3)_2CdCl_4$ up to 30 eV and investigated the energy band structure and the nature of optical transitions.

$(C_2H_5NH_3)_2CdCl_4$ single crystals were grown by slow evaporation method from the aqueous solution of $C_2H_5NH_3Cl$ and $CdCl_2$ at room temperature in dark. The measurements of reflection spectra for the polarization perpendicular to the *c*-axis (E ⊥ c) were carried out at BL-1B of UVSOR equipped with a 1m Seya-Namioka type monochromator. The spectral distribution of the incident light and the reflection light from the sample crystals was detected by a photomultiplier (Hamamatsu R105) coated with sodium salicylate, which is placed inside the sample chamber.

Figure 1 shows the reflection spectrum of the cleaved surface of $(C_2H_5NH_3)_2CdCl_4$ at 7 K in the range of 3 - 30 eV for the polarization E ⊥ c. The reflection spectrum is more refined than the previous report.[2] A sharp peak (X_1) is observed at 6.20 eV with an additional structure (X_2) appearing as the shoulder at 6.35 eV. The energy difference between the structures X_1 and X_2 is 0.15 eV and is comparable with the spin-orbit splitting energy of a Cl atom. Further, the peak energies of the structures X_1 and X_2 are almost same as the 1*s* exciton peaks of $CdCl_2$.[3] Thus, we attribute the structures X_1 and X_2 to the excitonic transition from the Cl 3*p* VB to the Cd 5*s* CB. A small hump (X_3) is observed at 6.97 eV. This hump may be due to the n = 2 exciton series of $(C_2H_5NH_3)_2CdCl_4$. A sharp peak (A) is also observed at 8.19 eV.

Figure 2 shows temperature dependence of reflection spectra (E ⊥ c) of $(C_2H_5NH_3)_2CdCl_4$ in the range of 5 - 10 eV. The reflection spectra were measured at temperatures of 7 - 280 K. Up on raising the temperature from 7 K, the X_1 peak at 6.20 eV shifts continuously to the low energy side, as indicated by a line. On the other hand, the peak A at 8.19 eV indicates the discontinuous low-energy-shift by 0.1 eV between 190 K and 220 K, as indicated by another lines. Such a discontinuous peak-shift is most likely caused by the structural phase transition taking place at 216.2 K in $(C_2H_5NH_3)_2CdCl_4$.[4] When the phase transition occurs, the relative arrangement between the NH_3 heads and the adjoining Cl ions largely changes, while that between the Cd ions and the Cl ions hardly changes. On the analogy of NH_4Cl crystal in which the NH_4 ions form the *s*-like CB,[5] we suppose that the peak A at 8.19 eV originates from the electronic transition from the Cl 3*p* VB to the second CB constructed from the *s*-like states of NH_3 heads.

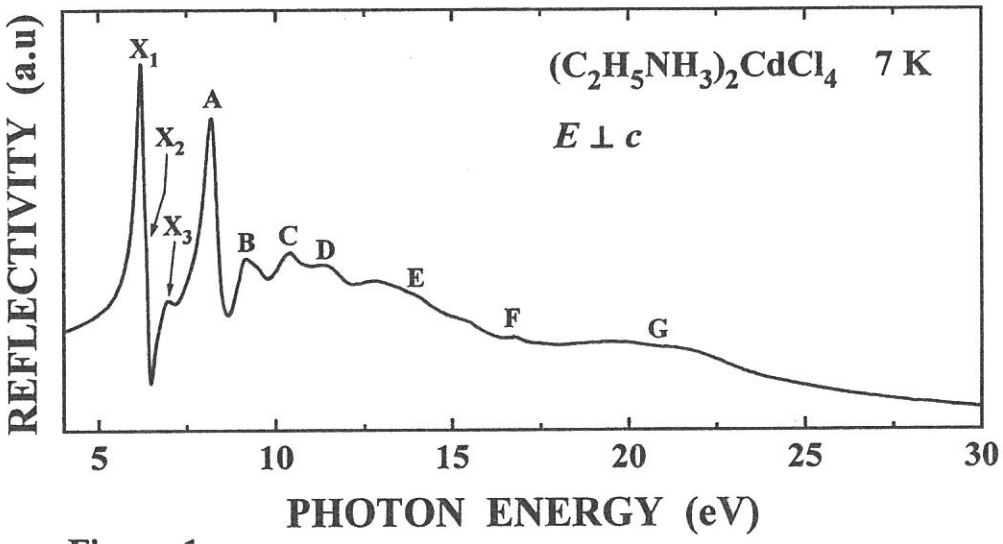

Figure 1

References

1)A. Ohnishi, K. Tanaka and T. Yoshinari: J. Phys. Soc. Jpn. **68** (1999) 288.

2)T. Yoshinari, T. Nanba, S. Shimanuki, M. Fujisawa, T. Matsuyama, M. Ikezawa and K. Aoyagi: J. Phys. Soc. Jpn. **58** (1989) 2276.

3)M. Fujita, H. Nakagawa, H. Matsumoto, T. Miyanaga, M. Watanabe, K. Fukui, E. Ishiguro, Y. Fujii and Y. Sakisaka: J. Phys. Soc. Jpn. **59** (1990) 338.

4)G. Hhapuis: Phys. Status Solidi a **43** (1977) 285.

5)H. Yamashita: J. Phys. Soc. Jpn. **29** (1990) 338.

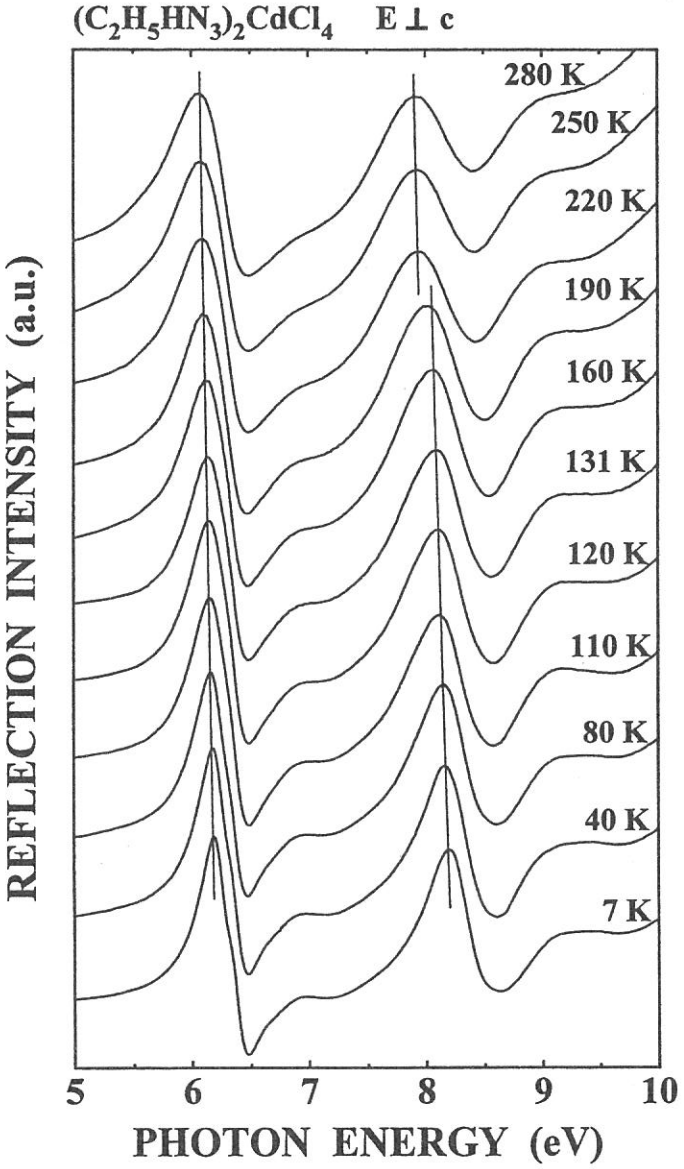

Figure 2

(BL1B)

Absorption Spectra and Optical Constants of Uniaxially Drawn Polyethylene Naphthalate Films

Isuke **OUCHI**, Ikuo **NAKAI**[A], Masao **KAMADA**[B] and Shin-ichiro **TANAKA**[B]

Faculty of Engineering, Tokushima Bunri University, Shido, Kagawa 769-2193
[A] Faculty of Engineering, Tottori University, Koyama, Tottori 680-8552
[B] UVSOR, Institute for Molecular Science, Myodaiji, Okazaki 444-8585

Polyethylene naphthalate (PEN) has a similar molecular structure as polyethylene terephthalate (PET), having a naphthalene ring in place of benzene in the main chain. As a film, it has somewhat better physical and chemical properties than PET in a practical sense; it is utilized for various products as electric insulators, capacitors, videotape bases, APS photographic bases etc. Structures and properties of PEN films have been studied by many researchers, but not so extensively as in PET. As for the electronic spectra, absorption spectra in solution[1] and in films[2] were reported; photochemical phenomena like coloration[3], fluorescence[4] have been treated to some extent; soft x-ray absorption was also studied[5,6]. However, the spectra relating to the deeper levels of valence electrons have not been examined so far; only a few studies have been made for PET too in this region.[7] The present study is being made to examine the electronic spectra of PEN in the deeper levels of valence electrons.

The measurement was made at the BL-1B where the Seya-Namioka type monochromator was equipped. Film samples of PEN were supplied from the Film Research Laboratory of Teijin Limited: amorphous undrawn films of 100 μm, uniaxially 4 times drawn films of 90 μm and biaxially drawn films of 40 μm.

The measurement procedure was the same as for the previous case of PET[8] but with an improvement. Namely, in the process of obtaining a reflection spectrum from a measured multiple reflection, more rigorous treatment was made for the spectrum in the semi-transparent region. Instead of approximating the calculated reflection to a straight line in the region, measured transmission data at each wavelength was put in the Kato's formula[9]; the transmission measurement was made separately by use of a Shimazu UV spectrometer: UV2400(PC)S.

Reflection spectra of PEN films uniaxially drawn by 4 times are shown in Fig.1 after correcting multiple reflection, where the reflection intensity of the film having its draw axis parallel to the electric vector of the incident light is more intense than that perpendicular, except in the region between 1600A and 2000A..

The phase of the reflected light was calculated from these data of reflection spectra using the Kramers-Kronig relation. Contribution to the integral from shorter and longer side wavelengths was counted by Roessler's method as in the previous study. Complex refractive indices and complex dielectric constants were computed by use of Fresnel equations; then, absorption coefficients were obtained from the extinction coefficients. Calculated refractive indices at 5000A agreed reasonably well with the values separately measured by Abbe's refractometer, guaranteeing the validity of the present treatment

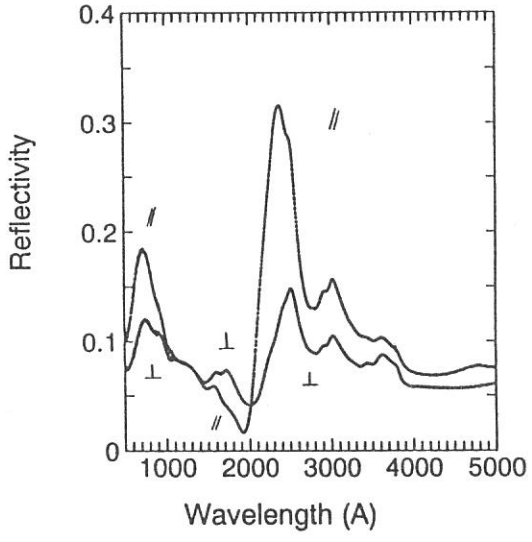

Fig. 1. Reflection spectra of uniaxially drawn (x4) PEN films. Multiple reflection is already corrected..

Fig. 2 shows the converted anisotropic absorption spectra of uniaxialy 4 times drawn PEN films. The absorption band of the longest wavelength has two peaks at 3560A and 3370A. They look rather perpendicular band; but it was slightly parallel according to the old data obtained by transmission method using extremely thin cast and drawn film. (Here, parallel band means that the electric vector parallel to the axial direction of the drawn film is absorbed more than that perpendicular to the axis, and perpendicular band is opposite.). Probably, the difference would be within the error caused by various approximation utilized in the Kramers-Kronig conversion. Nevertheless, the absorption coefficient at this band is much larger than that of the longest wavelength in a uniaxially drawn PET film. Second band is of parallel polarity and has three peaks at 2990A, 2890A and 2760A. Third band is very intense and has also parallel polarity and peaks at 2500A, 2390A and 2250A. Fourth band is perpendicular and peaks at 1700A. Polarity of the band peaking at 1550A is difficult to tell. Sixth band at 800-900A is strong and also has about same intensity either for parallel and perpendicular. General feature of the absorption spectra looks similar to that of PET exhibited in the previous report[8], whereas the detail is fairly different.

As an example of the optical constants obtained, refractive index and extinction coefficient of the uniaxially drawn (x4) PEN of parallel alignment is shown in Fig. 3. Detailed analysis should still to be made.

The authors are thankful to Mr. N. Takagi, Film Research Laboratory, Teijin Limited, for supplying film samples to us.

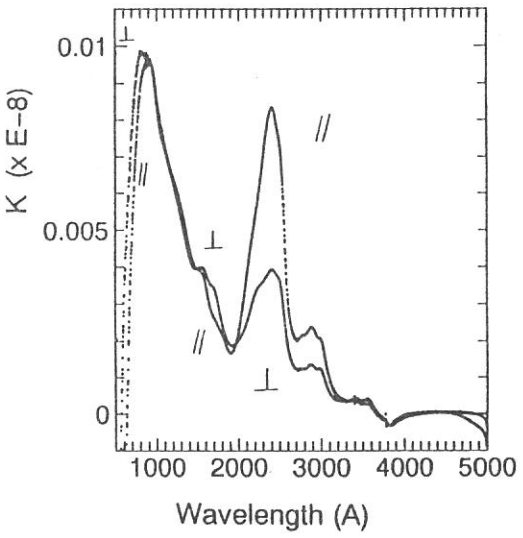

Fig.2. Converted absorption spectra of uniaxially drawn (x4) PEN films.

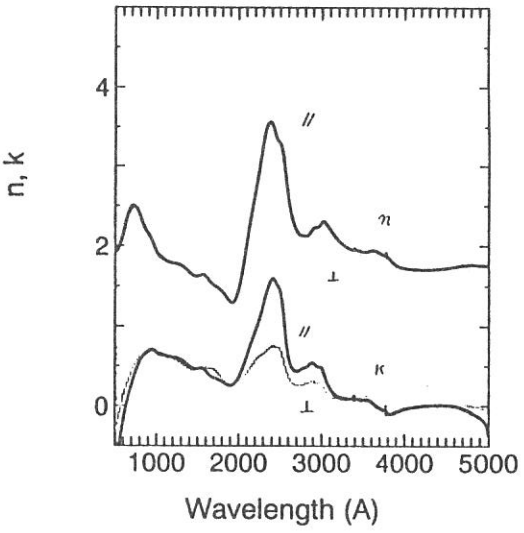

Fig. 3. Refractive index and extinction coefficient of a uniaxially drawn (x4) PEN films.

1) P-S.R. Chung et al., J. Appl. Polym. Sci., 24 (1979) 1809.
2) I. Ouchi, Rep. Progr. Polym. Phys. Jpn., 22 (1977) 437.
3) I. Ouchi et al., J. Appl. Polym. Sci., 20 (1976) 1983.
4) I. Ouchi et al., Polym. Adv. Technol., 10 (1999) 195.
5) I. Ouchi et al., Polym., J., 27 (1995) 127. J. Electr. Spectr. Rel. Phenom., 78 (1996) 363.
6) E.G. Rightor et al., J. Phys. Chem., 101 (1997) 1960.
7) M. Chitaib et al., Phys., Rev. B, 44(1997) 1960.
8) I. Ouchi et al., UVSOR Act. Rept. 1998, (1999) 88.
9) R. Kato, J. Phys. Soc. Jpn., 16 (1961) 2525.

(BL1B)

Reflection Spectra of Excitons in Orthorhombic $SnBr_2$

Yoshihiko YAMASAKI and Nobuhito OHNO

Division of Electronics and Applied Physics, Graduate School of Engineering, Osaka Electro-Communication University, Neyagawa 572-8530, Japan

Optical properties of Pb halides have been studied extensively so far by several groups. Especially, luminescence studies of these materials have been carried out since they give complimentary information on the photolysis phenomena. There are two types of luminescence in $PbCl_2$ and $PbBr_2$ at low temperatures [1,2]. One is the UV (B) luminescence produced under the excitation in the first exciton region, attributed to the radiative decay of self-trapped excitons at Pb^{2+} ion sites in $PbCl_2$ ($PbBr_2$). The other is the BG luminescence stimulated by photons with energies above the band gap, which originates from tunneling recombination of holes released from some trapping centers with electrons trapped at the Pb_2^{3+} self-trapped electron (STEL) centers [3].

Orthorhombic Sn halides, $SnBr_2$ and $SnCl_2$, have the same crystal structure (space group *Pmnb*) and the similar electronic configurations as orthorhombic Pb halides. It is interesting to know the electronic structures and exciton states in Sn halides. However, optical properties of these materials have not been revealed clearly so far [5-7]. In the present study , we have measured polarized reflection and absorption spectra of orthorhombic $SnBr_2$ using synchrotron radiation at the BL1B line of UVSOR facility.

Figure1 shows the reflection spectra up to 12 eV for polarization *E//a*, *E//b* and *E//c* measured at 12 K. As clearly seen, structures in the energy region of 3-8 eV show pronounced polarization dependence. The reflection spectra at the absorption edge are shown in expanded scale in Fig. 2. We can see a prominent peak at 3.409 eV for *E//a*, two peaks at 3.410 eV and 3.463 eV for *E//b*, and a peak at 3.461 eV and a weak hump at 3.412 eV for *E//c* polarization. These structures are obviously ascribed to the lowest exciton transitions. The splitting energy of the exciton for *E//b* polarization is 53 meV. The observed first exciton peaks in $SnBr_2$ are considerably sharp as compared with those in orthorhombic Pb halides. The polarization dependence of the first exciton band is well interpreted as a cationic interband transition in Sn^{2+} ($5s \rightarrow 5p$) under the crystal field with C_S symmetry.

We can see a small hump on the higher energy side of the first exciton band for *E//b* and *E//c* polarizations as indicated by arrows in Fig. 2. They are located at 3.486 eV for *E//b* 3.485 eV for *E//c*, probably due to n=2 state of exciton Rydberg series. The exciton binding energy is estimated as 32 meV assuming the hydrogen-like energy model. It is to be noted that there has been no report on the observation of higher exciton series in orthorhombic Pb halides.

Absorption spectra near the fundamental absorption edge were also measured in the temperature range 10 to 300 K. The logarithmic plot of the absorption spectrum near the absorption edge is found to give a straight line, that is, the absorption tail of $SnBr_2$ is well described as Urbach rule. Temperature dependence of the Urbach slope gives the high-temperature value of the steepness parameter $\sigma_0 = 0.74$ (0.70) and the

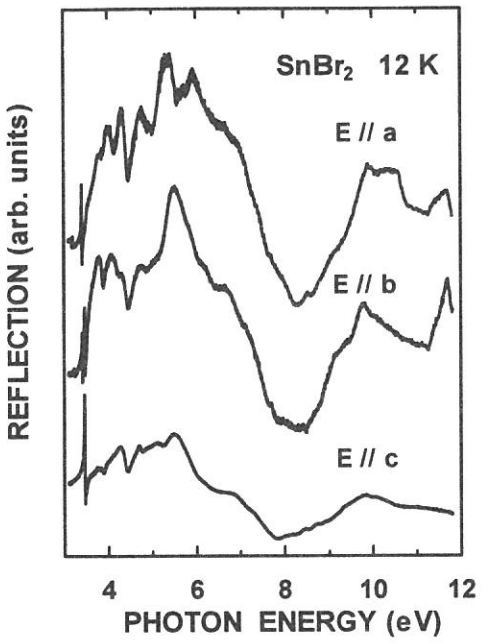

Fig. 1. Polarized reflection spectra of orthorhombic $SnBr_2$ at 12 K.

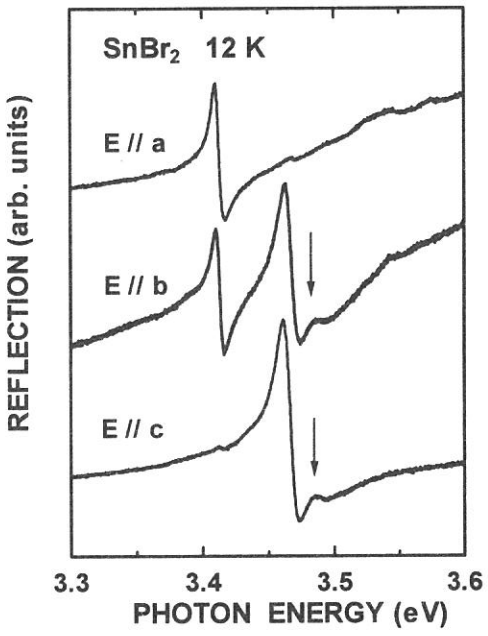

Fig. 2. Polarized reflection spectra of $SnBr_2$ in the first exciton region measured at 12 K.

effective phonon energy $h\omega_p = 24$ meV (13 meV) for $E//a$ ($E//b$) polarization. The small values of σ_0 indicate that the exciton-phonon interaction is in a strong case, and the excitons are unstable and easily self-trapped in $SnBr_2$.

In summary, polarized reflection spectra of orthorhombic $SnBr_2$ have been investigated by using synchrotron radiation. The first exciton bands with pronounced polarization dependence have been found at around 3.4 eV in the reflection spectra. Absorption spectra near the fundamental absorption edge are found to obey Urbach rule, suggesting that excitons are self-trapped in $SnBr_2$.

References

[1] M. Kitaura and H. Nakagawa: J. Electron Spectrosc. and Relat. Phenom. **9** (1996) 171.
[2] M. Kitaura and H. Nakagawa: J. Lumin. **72-74** (1997) 883.
[3] S.V. Nistor, E. Groovaert and D. Schoemaker: Phys. Rev. **B48** (1993)9575.
[4] M. Fujita, H. Nakagawa, K. Fukui, H. Matsumoto,T. Miyanaga and M. Watanabe: J. Phys. Soc. Jpn. **60** (1991) 4393.
[5] A.S. Voloshinovskii, S.V. Myagkota, N.S. Pidsyrailo and Z.A. Khapko: Opt. Spectrosc. (USSR) **52** (1982) 457.
[6] N.S. Pidsyrailo, A.S. Voloshinovskii, N.G. Stan'ko and Z.A. Khapko: Sov. Phys. Solid State **24** (1982) 708.
[7] A.S. Voloshinovskii: Phys. Solid State **35** (1993) 1588.

(BL1B)

Study on the defects in silica irradiated by a nuclear reactor

Tomoko Yoshida[1], Tetsuo Tanabe[1], Tatsuya Ii[2], Takanobu Hara[2], Shunsuke Muto[1] and Yoshitaka Inaki[3]

[1]*Center for Integrated Research in Science and Engineering, Nagoya University, Nagoya 464-8603, Japan*

[2]*Department of Nuclear Engineering, Graduate School of Engineering, Nagoya University, Nagoya 464-8603, Japan*

[3]*Department of Applied Chemistry, Graduate School of Engineering, Nagoya University, Nagoya 464-8603, Japan*

Introduction

Neutron irradiation and radiation effects on silica glasses are one of the main concerns for their application as optical windows, insulators and optical fibers in fusion reactors as well as fission reactors.[1,2] Recently, dynamic effects of the irradiation in silica glasses have been observed as degradations of their good transparency, high electrical resistivity, low optical absorption and luminescence during in-reactor irradiation.[1-5] In order to investigate dynamic effects of in-reactor irradiation on silica, we have tried to make in situ luminescence measurement of silica glasses induced by in-reactor irradiation. The in-reactor luminescence from silica was found to be a powerful technique to observe dynamic effects on the electrical property of silica, since the luminescence was directly associated with the electron excitation process under the irradiation. So far, we found that the luminescence mainly originates from the defects in silica due to an electron excitation during irradiation. However, the detailed dynamic effects on silica glass are still unknown. For example, the intrinsic defects existing in silica glasses make our understanding of the defects formation process very difficult. And the influence of the OH content in silica on the luminescence is also still an open question.

In the present study, optical absorption measurements for the irradiated samples have been carried out to obtain information of the defects produced by the reactor irradiation.

Experimental

The samples used in this work were fused silica glasses (T-1030 and T-2030) and synthesized silica glasses (T-4040) of 13 mm diameter and 2 mm thickness produced by Toshiba Ceramics, Japan with different OH content. Nominal impurity levels in these samples are listed in Table 1.

In-reactor irradiation have been carried out using the nuclear reactor YAYOI at the University of Tokyo. YAYOI was operated with a power of 0.5 or 1.5 kW (the neutron flux were about 2×10^{15} n/m^2 s and 6×10^{15} n/m^2 s, respectively) with an average neutron energy of 1.3 MeV and γ ray level was about 3.0 kGy/h.[6] The irradiation temperature was not controlled but kept below 323 K because of small output power of the reactor.

Optical absorption were measured at room temperature using synchrotron radiation at the beam line 1B station (BL-1B) attached with 1m Seya-Namioka monochromator at UVSOR, Institute for Molecular Science, Okazaki, Japan, operated at electron energy of 750 MeV. Optical absorption spectra were detected by a photomultiplier (Hamamatsu R105).

Results and Discussion

Fig. 1 shows the optical absorption spectra of low-OH fused silica glass (T-2030) irradiated in the reactor and that of unirradiated one. The fluence of the neutron in the irradiated sample was estimated as ca. 2.8×10^{19} n/m^2. In the spectrum of the unirradiated one (Fig. 1a), optical-absorption bands at ca. 5.1, 6.2 and 7.6 eV were observed, which is a clear indication of the existence of various intrinsic oxygen deficiencies in the unirradiated sample. The band at 7.6 eV is characteristic of the oxygen-deficient-type amorphous SiO_2 [7] and known as E center (≡Si-Si≡). And the absorption band appearing around 5 eV has been reported as the B_2 center [8] which has been attributed to either an oxygen vacancy (≡Si-Si≡) or twofold coordinated silicon (0-Si-0). The origin of the absorption band at around 6.2 eV is not clear, although this band was observed

for the KrF laser irradiated silica sample. [9] In the absorption spectrum of the irradiated sample (Fig. 1b), the band at 7.6 eV grow and a new band at 5.8 eV corresponding to E' center (≡Si) [10] appeared, indicating the increase in the number of E and E' centers by the in-reactor irradiation. On the other hand, as shown in Fig. 2a, the optical absorption spectrum of the unirradiated high-OH synthesized silica glass (T-4040) had no significant band in the region from 2 eV to 7.5 eV. The in-reactor irradiation (the neutron fluence of 2.7×10^{20} n/m^2) brought the intense absorption bands at 5.1, 5.8 and 7.6 eV assigned to B_2, E' and E centers. Thus, the optical absorption spectra clearly showed the production of various types of oxygen deficiencies such as B_2, E and E' by the irradiation. These defects should be produced mainly by the atomic displacement and electron excitation effects during in-reactor irradiation.

Table 1
Nominal impurity levels in silica glasses (in ppm)

Sample	Al	Fe	Na	K	Cu	B	OH
Fused silica (T-1030)	8	0.4	0.8	0.8	0.02	0.3	200
Fused silica (T-2030)	8	0.8	1	1	0.02	0.3	1
Synthesized silica (T-4040)	0.1	0.05	0.05	0.05	<0.01	<0.01	800

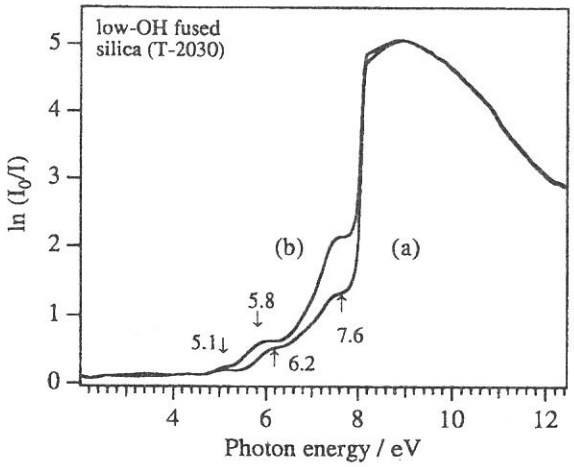

Fig. 1 Optical absorption spectra of (a) an unirradiated low-OH fused silica glass (T-2030) and (b) the reactor irradiated one (neutron fluence is 2.8×10^{19} n/m.)

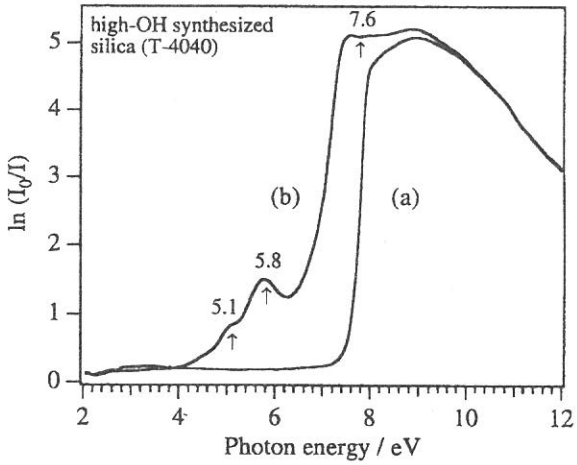

Fig. 2 Optical absorption spectra of (a) an unirradiated high-OH synthesized silica glass (T-4040) and (b) the reactor irradiated one (neutron fluence is 2.7×10^{20} n/m.)

References

[1] F. W. Clinard, Jr and L.W. Hobbs, Physics of Radiation Effects in Crystal (Elsevier, Amsterdam, 1986) p. 442.

[2] Proc. US/Japan Workshop on Dynamic Effects of Irradiation in Ceramics, Santa Fe, November 11-14,1992, Los Alamos National Laboratory Report LA-UR-92-4400 (1992)

[3] E. H. Farnum et al., J. Nucl. Mater. 191/194 (1992) 548.

[4] E. R. Hodgson, J. Nucl. Mater. 191/194 (1992) 552.

[5] T. Shikama et al., J. Nucl. Mater. 191/194 (1992) 544 and 575.

[6] M. Nakazawa and A. Sekiguchi, Radiation Dosimetry Data for Reactor YAYOI, Interior Report of University of Tokyo, R0037 in Japanese.

[7] R. Tohmon, H. Mizuno, Y. Ohki, K. Sasagane, K. Nagasawa and Y. Hama, Phys. Rev. B 44 (1989) 1337.

[8] L. Skuja, J. Non-Cryst. Solids 149 (1992) 77.

[9] A. Anedda, C. M. Carbonaro, R. Corpino and F. Raga, Nucl. Instr. and Meth. B 141 (1998) 719.

[10] R. Boscaino, M. Cannas, F. M. Gelardi, M. Leone, Nucl. Instr. and Meth. B 116 (1996) 373.

(BL3A1)

Amplification of impurity-associated Auger-free luminescence in $Rb_{1-x}Cs_xCl$ (x = 0.18) mixed crystals by undulator radiation

M. Itoh, S. Asaka,[1] M. Kamada[2] and V. B. Mikhailik[3]

Faculty of Engineering, Shinshu University, Nagano 380-8553

[1] *Equipment Development Center, Institute for Molecular Science, Okazaki 444-8585*

[2] *UVSOR Facility, Institute for Molecular Science, Okazaki 444-8585*

[3] *Lviv Franko State University, Kyryla i Mefodia str.8, 290005, Lviv, Ukraine*

A new mechanism of light amplification and laser action effects has been examined in BaF_2 [1], for which the hole transitions between the core and valence bands have a primary importance. This experiment has demonstrated a principal possibility to achieve lasing in compounds exhibiting Auger-free luminescence (AFL). Since the AFL arises from radiative transitions between the completely filled valence and core bands, the creation of empty (hole) states in the lower core bands means formation of the inverted population between these two bands at any excitation intensity. This idea was successfully tested in BaF_2 [1], but, as it turned out, the certain threshold of pumping power was needed to the amplification. This is probably because a part of the AFL is reabsorbed by metastable self-trapped exciton states in BaF_2. It is of great interest to extend similar experiments to other AFL-emitting materials in order to test their potentialities for laser action.

The compounds exhibiting impurity-associated AFL are supposed to be very promising candidates for the purpose mentioned above. This type of luminescence has been found in AFL-free alkali halides containing alkali or halogen impurity ions that form the impurity states in the energy gap between the host valence and outermost-core bands, which provides an additional channel for radiative decay of the core holes generated on the impurity states. The impurity-associated AFL yield in $Rb_{1-x}Cs_xCl$ can exceed the intrinsic AFL yield in pure CsCl [2]. In the present experiment, we have thus investigated this mixed crystal with x = 0.18.

The undulator radiation at BL3A1 provides quasi-monochromatic light with $\Delta\lambda/\lambda$ = 5% at 36 eV (photon flux: ~ 10^{15} photons/sec·mm^2) and at 15 eV (photon flux: ~ 10^{14} photons/sec·mm^2). A freshly cleaved 1 mm-thick sample was mounted on a rotatable holder installed in a vacuum chamber. The undulator radiation was incident at nearly 45° on the sample surface. Two flat multiple-dielectric coated mirrors (the reflectivity R = 100 and 90% in the 260-320 nm range) were placed near the sample in the direction perpendicular to the exciting radiation. The best collimation of the optical cavity was attained when the images of the iris diaphragms formed by He-Ne laser light reflected from the front and back mirrors were coinciding with each other. The luminescence was observed without using lenses through a monochromator equipped with a PM tube. A single-photon counting technique was applied to decay profile measurements. All the experiments were performed at room temperature.

Figure 1 shows luminescence spectra taken under no collimation (broken line) and the best collimation (solid line). The excitation was made with 36-eV photons, which corresponds to the transition from the deep-lying Rb 4p core state to the conduction band. The AFL spectra consist of the main band at 275 nm, the high-

energy band at 240 nm and the low-energy tail around 325 nm. An important feature in Fig. 1 is that the peak intensity of the 275-nm band is enhanced by a factor of 2.6 when the mirrors are adjusted for the best collimation. Similar enhancement was also confirmed under the excitation with 15-eV photons, corresponding to the Cs 5*p* core state → conduction band transition. The enhancement factor was about 1.7 in this case, in spite of the fact that the photon flux at 15 eV is one order of magnitude smaller than that at 36 eV. Furthermore, from Fig. 1, one may see a sharpening of the 275-nm band under the best collimation. These observations indicate the amplification of the impurity-associated AFL in $Rb_{1-x}Cs_xCl$ mixed crystals.

In the lower part of Fig. 2 are shown decay profiles of the 275-nm band excited with 36-eV photons under (a) the best collimation and (b) no collimation. By assuming a single exponential decay for the curve (b), we obtained a decay constant of 0.9 ± 0.1 nsec, in good agreement with the previous result. The decay profile of curve (a) is different from that of curve (b). This fact is clearly seen in the upper part of Fig. 2, where the dotted curve was obtained by subtracting the curve (b) from the curve (a). It appears that a faster component grows up in the peak region of the curve (a). Such a shortening of the luminescence decay profile is a characteristic feature of stimulated emission.

The above results confirm the validity of our anticipation about the promising potentialities of the compounds with impurity-associated AFL for light amplification, using the inverted population arising from impurity-core level excitation.

The authors acknowledge Mr. Y. Bokumoto and Mr. J. Murakami for their assistance in the experiment.

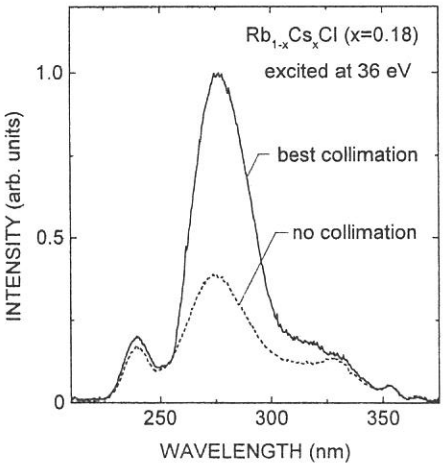

Fig. 1. Luminescence spectra of $Rb_{1-x}Cs_xCl$ (x = 0.18) excited with 36-eV photons under no collimation and the best collimation.

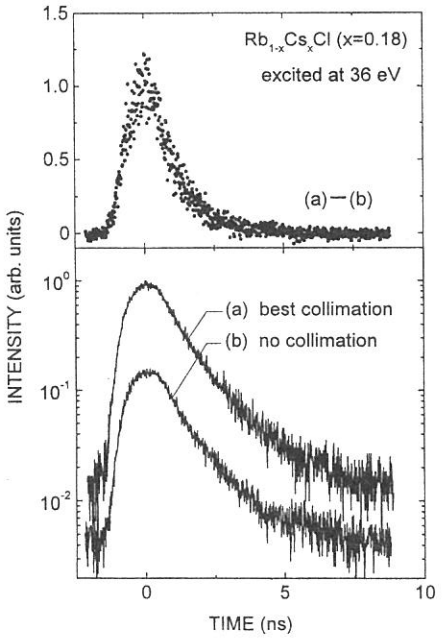

Fig. 2. Decay profiles of the 275-nm band excited at 36 eV; lower part. Subtraction of (b) from (a); upper part.

[1] M. Itoh and H. Itoh: Phys. Rev. B **46** (1992) 15509.

[2] A. S. Voloshinovskii, M. S. Mikhailik, V. B. Mikhailik, E. N. Mel'chakov, P. A. Rodnyi, C. W. E. van Eijk and G. Zimmerer: J. Lumin. **79** (1998) 107.

(BL5B)

Optical Properties of Amorphous Chalcogenide Semiconductors

Koji HAYASHI

Department of Electrical and Electronic Engineering, Gifu University, Gifu 501-1193, JAPAN

Amorphous chalcogenide semiconductor materials, such as a-As_2S_3, a-As_2Se_3 and a-Se etc., show a variety of photoinduced phenomena. Therefore, these materials are expected as materials for optoelectronic devices. A lot of work have been done on the photoinduced phenomena of these amorphous semiconductor materials and various mechanisms have been proposed for these photoinduced phenomena[1,2]. However, the details of the mechanisms are still unknown. These phenomena were studied by exciting outer core electrons with the irradiation of the visible light with the energy corresponding to the optical bandgap or sub-bandgap. Little attention has been give to photoinduced effects by exciting inner core electrons with the irradiation of higher energy photon. To obtain a wide knowledge of the photoinduced effects, it is necessary to investigate photoinduced phenomena on wide energy region. In the previous reports[3,4], we reported the photoinduced effects in amorphous chalcogenide films by the irradiation of the vacuum ultra-violet (VUV) light. That is, photodarkening is occurred by the irradiation of the VUV light and the darkened state is removed by annealing at near the glass-transition temperature. In our recent study, we observed interesting photoinduced change in the photoconductivity and the total photoyield of amorphous chalcogenide films by the irradiation of the VUV light[5-7]. In the present work, we measure the VUV reflection spectra and the total photoyield spectra in these materials in order to study the photoinduced effects of those optical spectra by the irradiation of the bandgap light and the VUV light.

The samples used for measurements were amorphous arsenic trisulfied (a-As_2S_3). Thin films of a-As_2S_3 were prepared onto quartz substrates by conventional evaporation technique. For the measurements of the total photoyield spectra, an electrode using Al contact was fabricated first on the substrate before depositing the amorphous film. A typical thickness of an amorphous film was around 0.7 μm. The samples were annealed at 443K (near the glass transition temperature) for two hours in a vacuum. The experiments were performed at room temperature at the BL5B beam line of the UVSOR facility of the Institute for Molecular Science in Okazaki. For the measurements of the reflection spectra, the incident angle was near normal to the sample surface and the reflectivity was measured by a silicon photodiode. The reflection spectra were obtained by normalizing the spectra by the spectrometer system response.

Figure 1 shows the VUV reflection spectrum of a-As_2S_3 at room temperature in the photon energy region between 35 eV and 55 eV. One main peak and interfering pattern were observed at this energy region. This peak around 44 eV corresponds to the 3d core level of As atom. Figure 2 shows the total photoyield spectrum of a-As_2S_3 at room temperature in the same photon energy region. As you see in the figure, the peak corresponding to the 3d core level of As atom was also observed in the total photoyield spectrum. Further analysis of these spectra is now in progress. We pay attention to the photoinduced effects near this energy region. We now are investigating photoinduced change on these spectra. The detailed experiments and analysis will be done in the next step.

This work was partly supported by grants-in-aid for Scientific Research from the Ministry of Education, Science and Culture of Japan and the OGAWA Science and Technology Foundation

REFERENCES

[1] Ke. Tanaka, Rev. Solid State Sci., 4(1990)641.
[2] K. Shimakawa, A. Kolobov, and S. R. Elliott, Adv. Phys., 44(1995)475.
[3] K. Hayashi, D. Kato, and K. Shimakawa, UVSOR Activity Report 1995, p128.
[4] K. Hayashi, D. Kato, and K. Shimakawa, J. Non-Cryst. Solids., 198-200(1996)696.
[5] K. Hayashi, A. Hirai, and K. Shimakawa, UVSOR Activity Report 1996, p116.
[6] K. Hayashi, UVSOR Activity Report 1997, p118.
[7] K. Hayashi, UVSOR Activity Report 1998, p105.

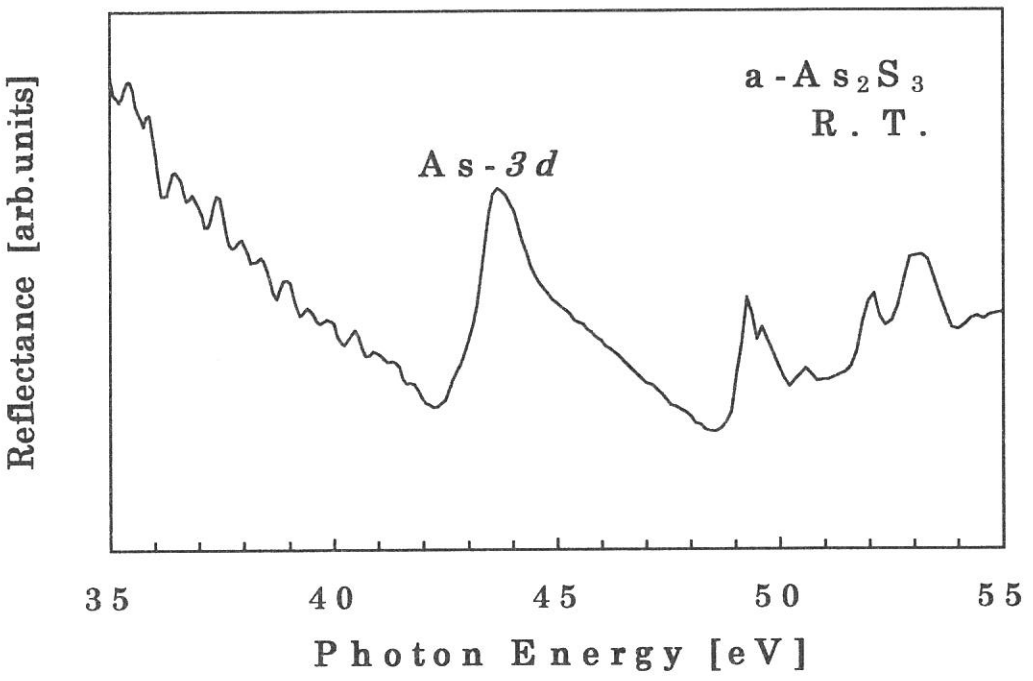

Fig. 1 Reflection spectrum of a-As_2S_3 at room temperature.

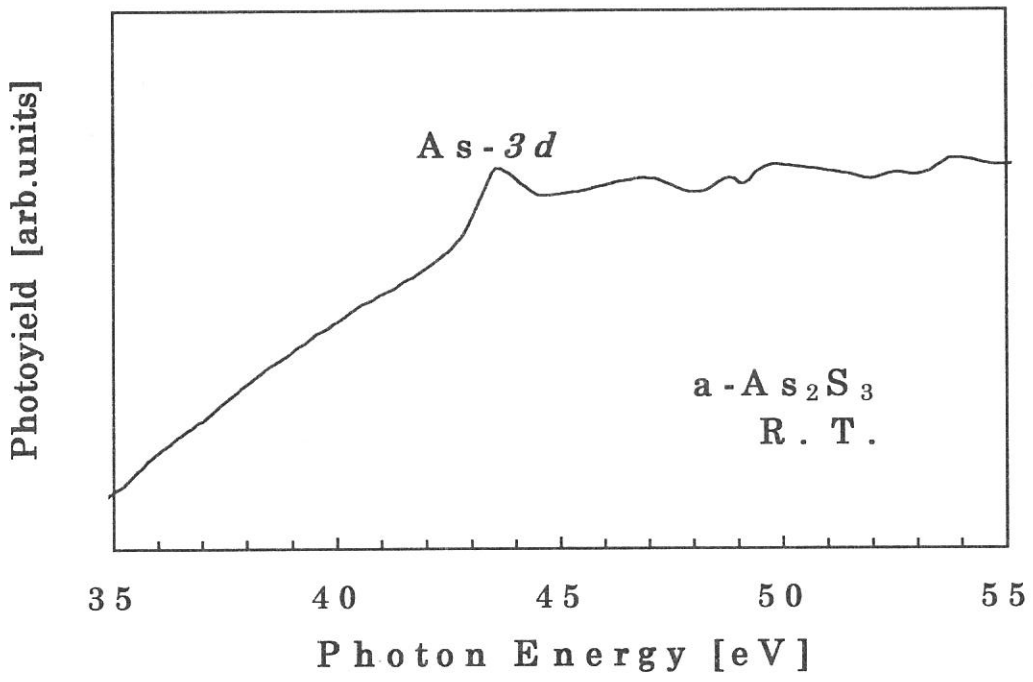

Fig. 2 Total photoyield spectrum of a-As_2S_3 at room temperature.

Vacuum-ultraviolet reflectance spectroscopy of transition-metal oxides

Yasujiro TAGUCHI[1], Eiji SAITOH[1], Yoshinori ONOSE[1],
Tadayuki OSAKI[1], Kyoko ISHIZAKA[1], Taka-hisa ARIMA[2], and Yoshinori TOKURA[1]

[1]*Department of Applied Physics, University of Tokyo, Tokyo 113-8656*
[2]*Institute of Materials Science, University of Tsukuba, Tsukuba 305-8573*

The discovery of high-Tc cuprate superconductor by Bednorz and Muller in 1986 has aroused great interest in strongly correlated electron systems in general, and 3*d* transition-metal oxides in particular. One of the most important characteristics for the correlated electron systems is the drastic re-construction of electronic structure over an energy scale of eV with changes of temperature, doping concentration, and/or external field. Therefore, optical reflectivity measurement over a wide energy range and the optical conductivity spectra derived from the reflectivity spectra provide us with very useful information about the strongly correlated electron systems.

In this beam time, we measured the reflectivity spectra of several transition-metal oxides, including Mn-, Ni-, Cu-, and Mo-oxides, for an energy range of 4 eV < E < 35 eV at room temperature. The measured reflectivity data, together with the lower-enegy data measured at University of Tokyo, were used to derive the optical conductivity spectra or dielectric function via the Kramers-Kronig analysis. As an example, the imaginary part of the dielectric function of pyrochlore-type Mo-oxide is shown below. This compound is known as showing geometrical frustration of magnetism, and exhibits an anomalous ferromagnetic state at low temperatures. The absorption bands indicated as A and B correspond to transitions from O 2*p* to Mo t_{2g} state and the bands denoted as C and D are due to the transition between O 2*p* and Mo e_g levels. The splitting (A and B, C and D) may be caused by the final state Hund's-rule coupling with the Mo t_{2g} spin. The structure indicated as E and the broad band lying at its higher-energy side correspond to the transition from O 2p to Sm 5d and/or Mo 5s/5p states.

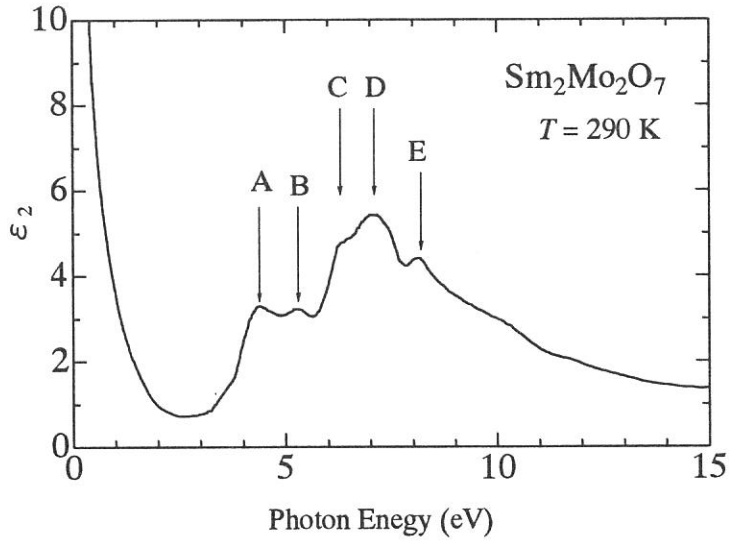

(BL6A1)

Temperature Dependence Millimeter Wave Reflection Measurements of Secondary Battery Substances $Li_{1-x}Ni_{1+x}O_2$

Hitoshi Ohta, Atushi Ueda, Yuichi Miura, Kenji Hazuki, Takao Nanba[A], Atushi Hirano[B] and Ryoji Kanno[B]

Department of Physics, Faculty of Science, Kobe University, 1-1 Rokkodai, Nada, Kobe 657-8501
[A]The Graduate School of Science and Technology, Kobe University, 1-1 Rokkodai, Nada, Kobe 657-8501
[B]Department of Chemistry, Faculty of Science, Kobe University, 1-1 Rokkodai, Nada, Kobe 657-8501

Recently, the study of $LiNiO_2$ is interesting because it is a promising material for the positive electrode of the Li ion secondary batteries. We found the drastic increase of the reflection of $LiNiO_2$ above 300 K in the millimeter wave region previously [1, 2]. We suppose that this increase of reflection is related to the motion of Li ion in the system. We extended our study to the low energy region down to 5 cm^{-1} and also trying to extend to the study of $Li_{1-x}Ni_{1+x}O_2$ [3, 4]. This year we extended our study to x=0.11 case.

The reflection measurements of x=0.11 sample have been performed in the spectra region from 5 to 60 cm^{-1} using the beam line BL6A1 of UVSOR. For the measurement below 22 cm^{-1}, low pass filter was used. The temperature was changed from 79 to 380 K. The gold plate was used as a reference and InSb detector was used as a detector. Figure 1 shows our results for x=0.11 sample. Overall reflection is low compared to the previous results of x=0 and x=0.05 samples [4]. Especially the increase of the reflection of x=0.11 sample is small as the temperature is increased above 300 K. The reflection above 300 K statrts to increase from 50 cm^{-1} in the case of x=0.11 while that of x=0 sample increase steeply below 10 cm^{-1}. Comparing three samples, which are x=0, 0.05 and 0.11, the increase of the reflection becomes steeper as x is decreased. This tendency seems to have correlation with the fact that the non-stoichiometry degrades the charge and discharge characteristics significantly. From the point of view of the application, the reflection measurements of $Li_{1-x}NiO_2$ are important as a next step.

[1] H. Ohta *et al.*: UVSOR Activity Report 1996 (1997) 182.
[2] H. Ohta *et al.*: proceedings of ICTMC (2000).
[3] H. Ohta *et al.*: UVSOR Activity Report 1997 (1998) 128.
[4] H. Ohta *et al.*: UVSOR Activity Report 1998 (1999) 158.

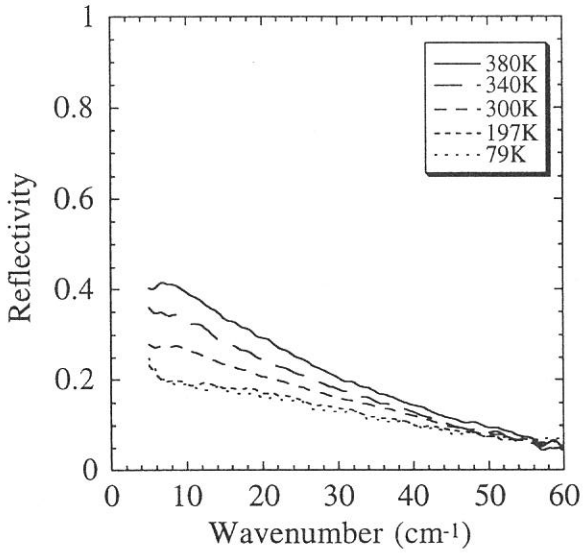

Fig. 1 The reflection spectra of x=0.11 sample.

(BL6A1)

Optical Response Of $CuIr_2X_4$ (X=S,Se) Due To Metal-Insulator Transition

M.Hayashi[1], M.Nakayama[1], T.Nanba[1], T.Matsumoto[2], J.Tang[2] and S.Nagata[3]

1.*Graduate School of Science and technology, Kobe University, Nada-ku, 657-8501, Kobe, Japan*

2.*National Research Institute for Metals, 1-2-1Sengen, Tsukuba, 305-0047, Japan*

3.*Department of Materials Science and Engineering, Muroran Institute of Technology, 27-1 Mizumoto-cho, Muroran, 050-8585, Japan*

$CuIr_2X_4$(X=S,Se) are spinel-type compound. $CuIr_2Se_4$ is a metal at atmospheric pressure but shows a stabilization of insulating phase from metal phase under high pressure [1]. $CuIr_2S_4$ undergoes a temperature-induced metal-insulator transition (M-I transition) at around 226K [2,3]. The magnitude of the energy gap in the insulating phase was estimated to be 0.094 eV by the electric resistivity data in the temperature range between 140K and 200K.[1,2] From X-ray diffraction measurement[3], $CuIr_2S_4$ was found to possess a normal cubic structure in the metallic phase and to be distored to a tetragonal structure in the insulating phase. However, additional some superstructure spots that cannot be assigned simply by tetrahedrally distored spinel structure were found in the low phase. The details of the structure is still unknown in the insulating phase.[3] Band calculations[4] based on a FLAPW method and photoemission data [5] showed the existence of Ir5*d*-S3*p* hybridization band near the Fermi level (E_F). It is therefore very interesting to know the fine electronic structure very close to the E_F by low energy optical excitation methods.

The temperature dependence of the optical reflection spectrum of the polycrystalline sample of $CuIr_2X_4$ (X=S and Se) was measured in the energy region of 0.005-6 eV. The energy resolution was kept to be 4 cm^{-1}. In the energy range below 0.015 eV, infrared synchrotron radiation at the UVSOR Facility of Institute for Molecular Science in Okazaki was used as a light source using a Martin-Puplett interferometer. The optical conductivity spectrum ($\sigma(\omega)$) was obtained from a Kramers-Kronig transformation of the R- spectrum. which was extrapolated by Hagen-Rubens' relation $R(\omega) \propto 1 - a\sqrt{\omega}$ in the lower energy side of the spectrum and by a well known function of $R(\omega) \propto b\omega^{-4}$ in the higher energy side.

Figs.1 and 2 show the measured R- (*a*) and the σ-spectra (*b*) of $CuIr_2S_4$ and $CuIr_2S_{e4}$ at various temperatures. From the Drude-like R spectra, $CuIr_2S_{e4}$ was found to hold metallic properties through the whole temperature range at atmospheric pressure although it exhibits the R-spectra with many peaks structure as cooling down to 30 K. On the other hand, the R-spectrum of $CuIr_2S_4$ showed a strong temperature-dependence. Above 222 K, the R-spectra showed an abrupt rise below 0.3eV which corresponds to a so-called plasma frequency due to the collective motion of free carriers. As temperature decreases below 221 K, such metallic behavior was completely suppressed (the occurrence of M-I transition) and many phonon-like structures appeared in the narrow energy region of 0.035eV-0.052eV. In the insulating phase, the energy gap was estimated to be about 0.1eV from the abrupt decrease in the intensity of the σ-spectra, which is almost consistent with 0.094eV given by electric resisitivity data [1,2]. A new band appeared at 0.4eV and gradually grew instead of the band around 0.7eV in the metallic phase as cooling, so as to compensate the decrease in intensity of the Drude component. In this way, by low energy optical excitation experiment, we resolved the fine change in the electronic structure within the overall change in the density of state observed in the photoemission spectroscopy. The σ-spectrum in the metallic phase was well fitted by the superposition of two Drude and two Lorentz functions (see Fig. 3). The existence of two Drude components suggests that at least two kinds of energy levels go across the E_F. This is consistent with the band calculation results of $CuIr_2S_4$ which indicates two conduction bands in the direction of X-Γ of the B.Z. Conduction bands in $CuIr_2S_4$ consist mainly of Ir5*d* and S3*p* hybridization.

References
[1]J.Tang,T.Furybayashi,T.Kosaka,s.Magata,Y.Kato,h.Asano,and T.Matsumoto, Rev.High Pressure Sci. Technol. 7(1998)496.
[2] S.Nagata, T.Hagino, Y.Seki and T.Bitoh, PhysicaB 194-196 (1994) 1077.
[3]T.Furubayashi, T.Matsumoto, T.Hagino, S.Nagata, J.Phys.Soc.Jpn 63 (1994) 3333.
[4]T.Oda, M.Shirai, N.Suzuki and K.Motizuki, J.Phys.:Condens.Matter 7 (1995) 4433
[5]J.Matsuno, T.Mizokawa, A.Fujimori, D.A.Zatsepin, V.R.Galakhov, E.Z.Kurmaev,Y.Kato and S.Nagata, Phys.Rev.B 55 (1997) 15979.

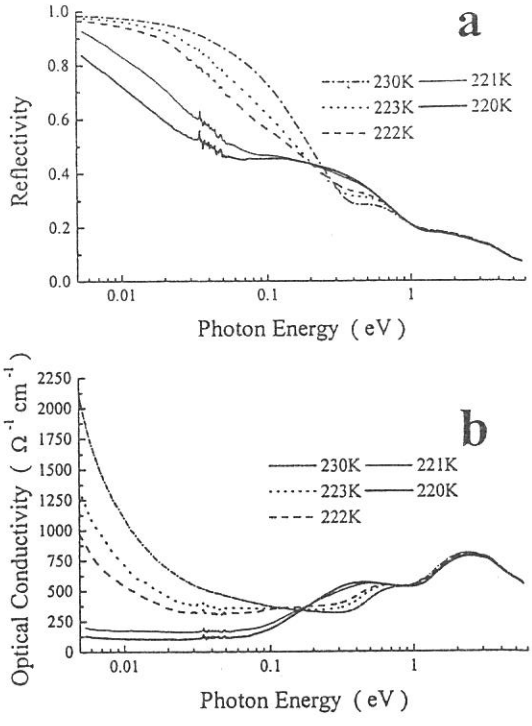

Fig.1 Reflection (*a*) and the σ-spectra (*b*) of $CuIr_2S_4$ at the temperatures of 230-220 K.

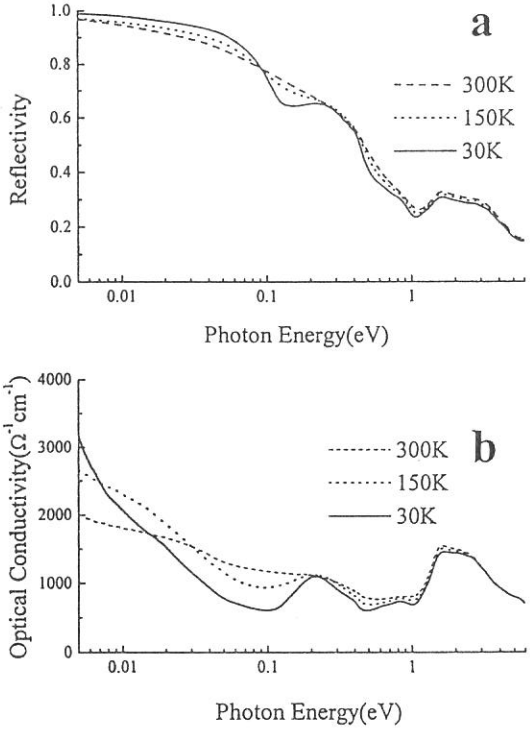

Fig.2 Reflection (*a*) and the σ-spectra (*b*) of $CuIr_2Se_4$ at 300,150 and 30K.

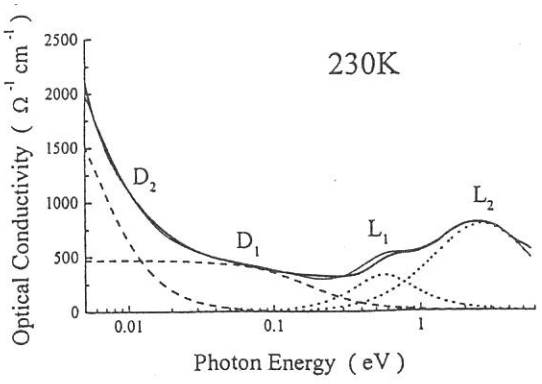

Fig3. Decomposition of the σ-spectrum of $CuIr_2S_4$ at 230K into two Drude (D_1 and D_2) and two Lorentz (L_1 and L_2) functions. The thick solid line represents an experimental curve and the thin solid one the summation of the fitting curves.

(BL6A1)

Optical Conductivity Spectra in the Magnetically Ordered States of CeBi

Shin-ichi Kimura[1], Mitsuru Okuno[1], Hideaki Kitazawa[2], Giyu Kido[2] and Takashi Suzuki[2]

[1]*Graduate School of Science and Technology, Kobe University, Nada-ku, Kobe 657-8501*
[2]*Physical Properties Division, National Research Institute for Metals, 1-2-1 Sengen, Tsukuba, 305-0047*

Cerium-monopnictides (Ce*X*; *X* = N, P, As, Sb, Bi) have complex magnetic phase diagram with the eleven layered magnetic structure. The origin of the magnetic phase diagram and the magnetic structure attract attention and many experimental and theoretical researchers have been investigating over two decades.

Last year, we started the magnetic reflectivity (MR) and the magnetic circular dichroism (MCD) experiments of CeSb in the infrared region using UVSOR for the investigation of the electronic structure in the magnetically ordered states.[1] In this year, we performed the measurement of the MR and MCD of CeBi, that also has a complex magnetic phase diagram, and we report the experimental result in this paper.

CeBi was grown by the Bridgman method with a tungsten furnace.[2] The measured surface is along (100)-plane and was prepared by a cleavage in a helium atmosphere. Since the material is easy to be oxidized, it was mounted to the sample holder of a cryostat in the helium atmosphere and was set to the center of the superconducting magnet in a short time.

The temperature dependence of optical conductivity spectra of CeBi at zero magnetic field and the assigned magnetic structure by neutron scattering[3] are shown in Fig. 1. The spectrum strongly changes with temperature. Particularly, the spectrum in the AF1-phase is strongly changes with changing temperature in spite that this material in the temperature range is assigned in the same phase by neutron

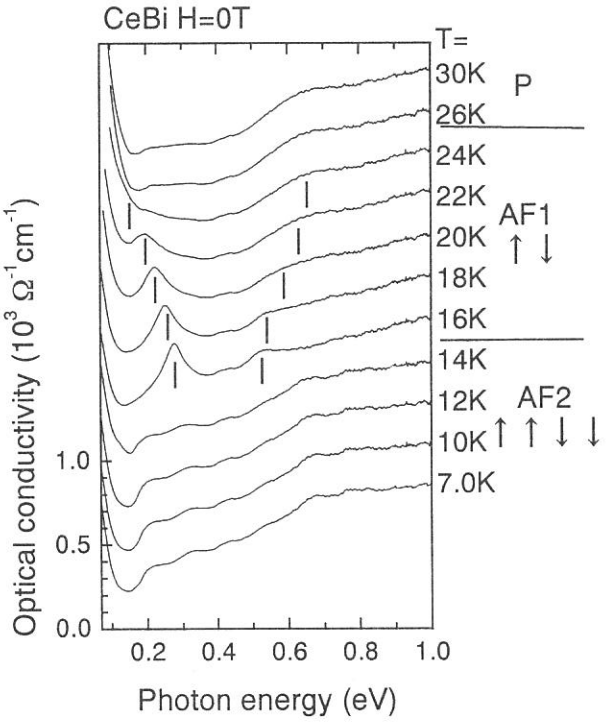

Fig. 1. Temperature dependence of the optical conductivity at zero magnetic field of CeBi. The depicted magnetic structures are referred from neutron scattering data.

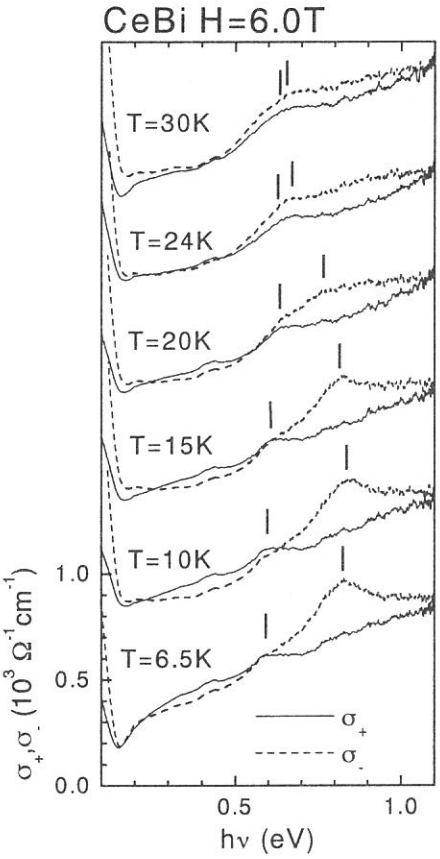

Fig. 2. Temperature dependence of the MCD optical conductivity ($\sigma_+(\omega),\sigma_-(\omega)$) at 6 T of CeBi.

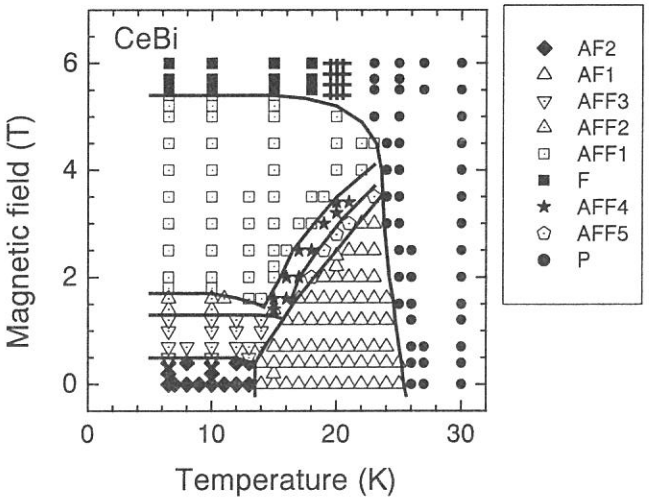

Fig. 3. Values of temperature and magnetic field at which magneto-reflectivity spectra of CeBi were measured. The same marks indicate the values at which same spectra are observed. The lines are where the spectrum changes. The legends have the same notation as those of neutron scattering.

scattering. One peak at 0.27 and one shoulder at 0.53 eV appear at 16 K and the energy separation of these structures increases as the temperature increases. At last, the spectrum continuously changes to that in the P-phase. The data indicate that the electronic structure in the AF1-phase strongly changes with the temperature and the electronic structure in the AF1-phase continuously connects to that in the P-phase.

The temperature dependence of the MCD optical conductivity spectrum at 6 T is shown in Fig. 2. Below 15 K, the $\sigma_+(\omega)$ and $\sigma_-(\omega)$ spectra are different from each other, *i.e.*, the peak of $\sigma_-(\omega)$ is located at 0.85 eV which is higher energy than that of $\sigma_+(\omega)$ at 0.6 eV. These spectra indicate that the electronic structure is the strong polarization. The state is assigned to be in the induced ferro-magnetic phase. However, these peaks approach each other around 20 K, and finally the $\sigma_+(\omega)$ and $\sigma_-(\omega)$ spectra become almost equal above 24K. Since the $\sigma_+(\omega)$ and $\sigma_-(\omega)$ spectra at 30 K are equal to the $\sigma(\omega)$ spectrum in the paramagnetic phase, the state at 6 T above 24 K is in the P-phase. Therefore the spectra indicate the state changes around 23 K from the induced ferro- to the para-magnetic phases. This is the first observation, because the phase transition has not been observed in neutron scattering experiment.[3]

According to the MR and MCD spectra, magnetic phase diagram was determined and is shown in Fig. 3. The outline of the diagram is almost equal to the previous one determined by neutron scattering.[3] Therefore the MR and MCD spectra reflect the electronic structure in the magnetically ordered states.

---

[1] S, Kimura *et al.*, J. Phys. Soc. Jpn. **69** (2000) in press.
[2] S. Kimura: Jpn. J. Appl. Phys. **38** (1999) Suppl. 38-1, 392.
[3] H. Bartholin *et al.*, J. de Phys. Colloq. **40** (1979) C5-130.

(BL6A1)

Optical response of RRu$_4$P$_{12}$ (R=La,Ce,Pr and Sm) due to metal-insulator transition

Masaya Nakayama[a] ,Masato Hayashi[a], Takao Nanba[a], Itimin Shirotani[b], and Chihiro Sekine[b]

a Graduate school of Science and Technology, Kobe University, Nada-ku, Kobe 657-8501, Kobe,Japan

b Muroran Institute of Technology, 27-1, Mizumoto,Muroran 050-0071, Japan

RRu$_4$P$_{12}$ (R=La,Ce,Pr and Sm) are ones of ternary metal phosphides with the skutterudite structure ($CoAs_3$-type) which is represented as RT_4P_{12} (R=rare earth element and T=transition metal). Recently, their stable compounds have been successfully synthesized using a wedge-type cubic anvil high pressure apparatus under a high pressure of 4 GPa and high temperature of 1100 ℃[1] According to the electric resistivity data, CeRu$_4$P$_{12}$ and CeFe$_4$P$_{12}$ are a semiconductor [1,2], LaRu$_4$P$_{12}$ shows a superconductivity at 7K, PrRu$_4$P$_{12}$ and SmRu$_4$P$_{12}$ show a metal-insulator (M-I) transition, respectively, at Tc=60K [3] and 16K.

After the success of the synthesis, many experiments has started on these compounds but the optical measurements has not yet been done.for these materials. We measured the reflection spectrum in order to know the electronic structure close to the Fermi energy level of these materials. The temperature dependence of the optical reflection spectra of RRu$_4$P$_{12}$ (R=La,Ce,Pr and Sm) were measured in the energy region of 0.005 -4 eV. The optical conductivity spectrum ($\sigma(\omega)$) was obtained from a Kramers-Kronig transformation of the reflectivity spectrum.

Figs.1 and 2 show the measured reflection and the optical conductivity spectra of these materials at 300 K (dashed line) , 78K (dotted line) and 8 K (solid line). We can see that the onset of the interband transition as the abrupt rise in the intensity of σ-spectra around 0.4 eV for La, Pr, and Sm compounds, and the spectral profile in the higher energy region than 0.4eV has a similar structure with three peaks. The similarity of the spectral profile means that the overall electronic structure of these three compounds (La,Ce,Pr and Sm) does not change. In CeRu$_4$P$_{12}$, the σ-spectrum did not show a temperature dependence. Then we can see that CeRu$_4$P$_{12}$ is semiconductor with an energy gap of about 0.2 eV. In addition, the spectrum profile in the higher energy region than 0.7eV has similar structure with those of other three compounds although the energy positions of three peaks shift to a higher energy side , and an additional peak exists at 0.4 eV. We found that the effective electron number which contributes to the Drude component of other three compounds is almost same with the effective electron number which contributes to the interband transition at 0.4 eV of CeRu$_4$P$_{12}$. In the insulating phase of PrRu$_4$P$_{12}$ and SmRu$_4$P$_{12}$ at 8K, on the other hand, the Drude component below 0.3eV disappeared and a new band, which corresponds to an interband transition, appeared , respectively, around 0.06eV and 0.025 eV. The effective electron number which contribute to the transition below 0.3 eV was estimated and found to be kept constant at both metallic and insulating phases. This means that the band which the Fermi level crosses underwent a very small amount of energy splitting due to the M-I transition and consequently a new interband transition at 0.4 eV appeared.

References

[1] I.Shirotani *et al.*, J.Phys.Chem.Solids **57**, (1996)211. [2] G.P.Meisner, *et al.*, J.Appl.Phys.**57**, (1985)3073.
[3]C.Sekine, T.Uchiumi, I.Shirotani, and T.Yagi, Phys.Rev.Lett.**79**, (1997)3218.

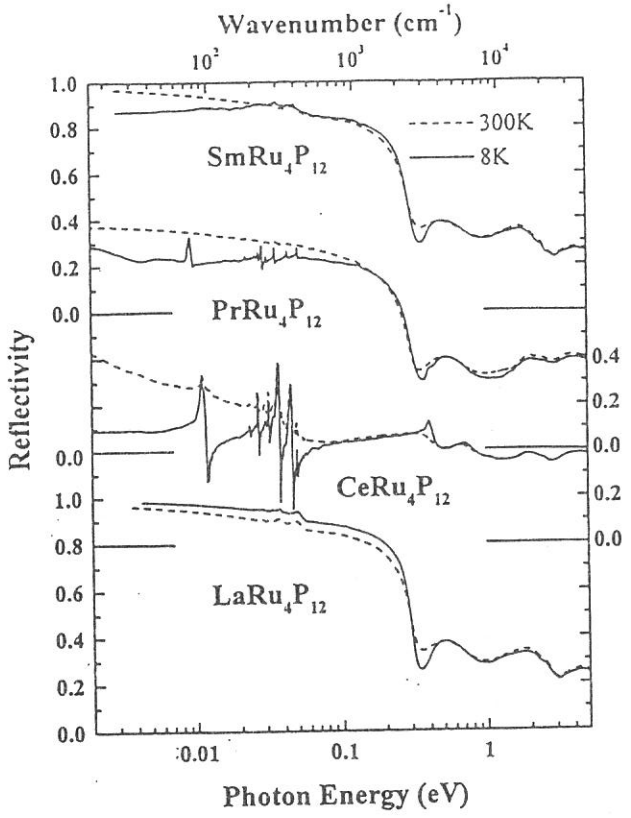

Fig.1

Reflection spectra of RRu$_4$P$_{12}$ (R=La,Ce,Pr and Sm) at 300 K (dashed line) ,78 K(dotted line) , and 10 K (solid line).

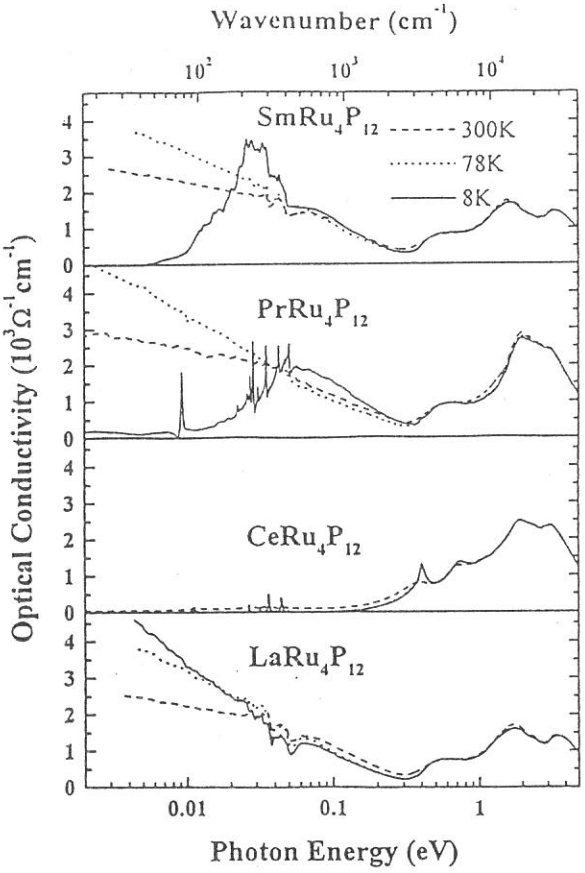

Fig.2 σ spectra of PrRu$_4$P$_{12}$ of RRu$_4$P$_{12}$ (R=La,Ce,Pr and Sm).

(BL6A1)

Infrared Magnetic Linear Dichroism of CeSb

Mitsuru Okuno[1], Shin-ichi Kimura[1,2], Hideaki Kitazawa[3], Giyu Kido[3], and Takashi Suzuki[3]

[1]*Graduate School of Science and Technology, Kobe University, Nada-ku, Kobe 657-8501*
[2]*PRESTO, Japan Science and Technology Corporation*
[3]*Physical Properties Division, National Research Institute for Metals, 1-2-1 Sengen, Tsukuba, 305-0047*

When magnetic field is applied to a material, the physical properties parallel and perpendicular to the magnetic field become different from each other. For instance, the anisotropy has been observed in electrical resistivity[1] and de Haas van Alphen experiments[2] and so on. The anisotropy originates from the electronic structure near the Fermi level. Here, the investigation of the anisotropic electronic structure is main theme.

We have started reflectivity measurement using linear polarized infrared synchrotron radiation which electric vector was set parallel ($\boldsymbol{E}$ // $\boldsymbol{H}$) and perpendicular ($\boldsymbol{E} \perp \boldsymbol{H}$) to an applied magnetic field (infrared magnetic linear dichroism, IRMLD). In our previous experiment of magnetic circular dichroism in infrared region (IRMCD), the light is irradiated from the same direction of magnetic field, *i.e.*, the electric vectors with right and left circularly polarizations is perpendicular to the magnetic field. Then the spectrum of $\boldsymbol{E} \perp \boldsymbol{H}$ is equal to the average of the spectra with both circularly polarizations, on the contrary, the spectrum of $\boldsymbol{E}$ // $\boldsymbol{H}$ provides us new information of electronic structure along the magnetic field. For instance of the AFP1-phase of CeSb, the configuration of magnetic structure, applied magnetic field and electric vector are shown in Fig. 1. In CeSb, magnetic layers are stacked along the magnetic field like a sandwich. In the AFP1-phase case, the magnetic structure has the wave number of k = 2/3, *i.e.*, the periodic magnetic structure with three layers (+ 0 −) appears. Here, + and − indicate the direction of the

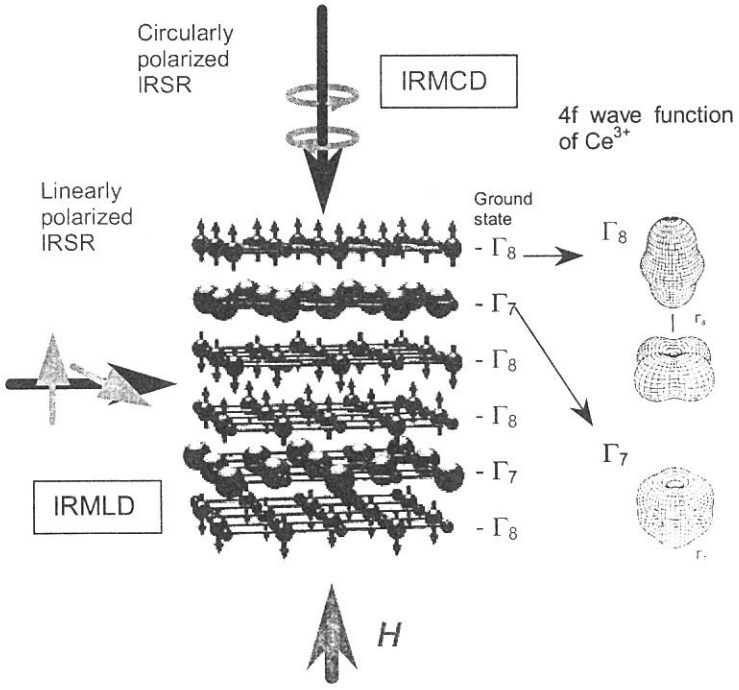

Fig. 1. Magnetic structure in AFP1-phase of CeSb and layered structure of Ce^{3+} 4*f* ground state of Γ_7 (largest sphere) and Γ_8 (middle-size sphere with an arrow). Smallest sphere indicates Sb-ion. Arrows indicate applied magnetic field, incident lights and electric vectors. Configurations of infrared magnetic circular dichroism (MCD) and infrared magnetic linear dichroism (IRMLD) experiments are also depicted.

magnetic moments of Ce $4f$ Γ_8 state and 0 the Ce 4f Γ_7 state. The IRMCD spectrum, as well as the spectrum of $\boldsymbol{E} \perp \boldsymbol{H}$, reflects the electronic structure along the layer of the sandwich structure. The spectrum of $\boldsymbol{E} // \boldsymbol{H}$ only detects the electronic structure along the magnetic field.

We measured the IRMLD spectra of CeSb. The material shows anomalous magnetic phase diagram and also magnetic structure as described in a previous report.[3] Here, we cleaved along the (100)-plane to obtain the clean surface and set the [001] direction parallel to the magnetic field. The light was irradiated from the [100] direction and the electric vector was parallel and perpendicular to the [001] direction.

The reflectivity spectra in some magnetic phases of CeSb with the configurations of $\boldsymbol{E} // \boldsymbol{H} //$ [001] and $\boldsymbol{E} \perp \boldsymbol{H} //$ [001] are shown in Fig. 2. The legends of the magnetic phase have the same notations as those of neutron scattering.[4] In the AF-, AFPx- (x = 1 ~ 5) and P-phase, the spectra in two configurations are similar to each other. However, the spectra are different in the F-, FPx- and AFFx-phase. This indicates that the electronic structure has strong anisotropy due to the different Ce^{3+} $4f$ Γ_8 ground state and the periodic structure.

---

[1] Ex.) T. Terashima, J.S. Qualls, T. F. Stalcup, J. S. Brooks, H. Aoki, Y. Haga, A. Uesawa and T. Suzuki, Phys. Rev. B **60**, 15285 (1999).

[2] Ex.) H. Kitazawa, Y. S. Kwon, A. Oyamada, N. Takeda, H. Suzuki, S. Sakatsume, T. Satoh, T. Suzuki and T. Kasuya, J. Magn. Magn. Mater. **76-77**, 40 (1988).

[3] S. Kimura, H. Kitazawa, G. Kido and T. Suzuki, UVSOR Activity Report 1998, 160 (1999); J. Phys. Soc. Jpn. **69** (2000) in press.

[4] J. Rossat-Mignod *et al.*, J. Magn. Magn. Mater. **52**, 111 (1985).

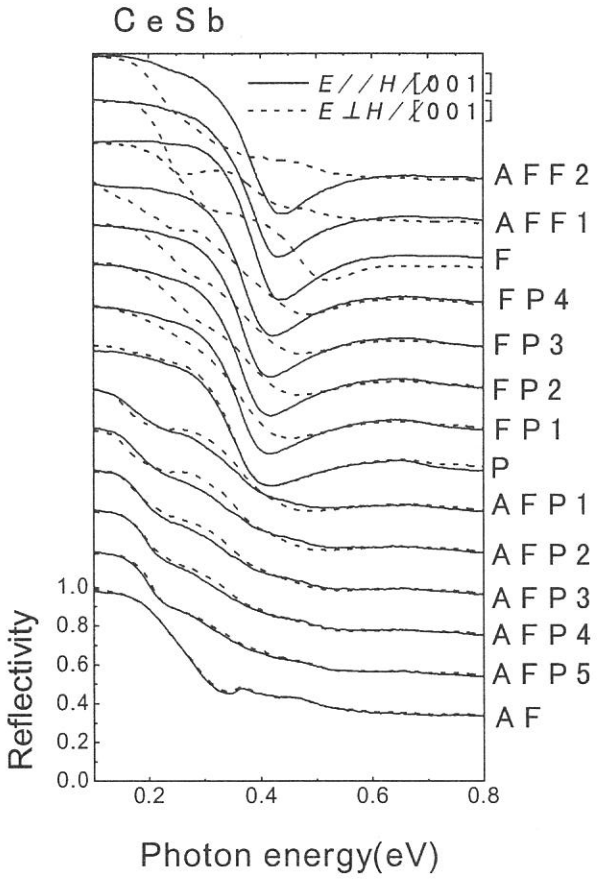

Fig. 2. Reflectivity spectra in some magnetic phases of CeSb with the configurations of $\boldsymbol{E} // \boldsymbol{H} //$ [001] and $\boldsymbol{E} \perp \boldsymbol{H} //$ [001]. The legends have the same notation as those of neutron scattering. Successive curves are offset by 0.2 for clarity.

(BL6A1)

Low Energy Electronic Structure of $Yb_4(As_{0.85}P_{0.15})_3$

Shin-ichi Kimura[1], Mitsuru Okuno[1], Hidekazu Aoki[2] and Akira Ochiai[2]

[1]*Graduate School of Science and Technology, Kobe University, Nada-ku, Kobe 657-8501*
[2]*Department of Material Science and Technology, Niigata University, Niigata 950-2181*

In Yb_4As_3, the relation between transport and magnetic properties is open to question because there is no relation between them at first sight. The magnetic susceptibility does not change in spite that the carrier density is controlled by the substitution of Sb and P for As.[1,2] Then we consider the key to solve the contradiction, we are investigating the electronic structure near the Fermi level using a reflectivity measurement in the infrared region.

In Yb_4As_3, the optical conductivity indicates the transport property continuously changes from the high carrier density and the short relaxation time above 200 K to the low carrier density and very long relaxation time below 100K.[3] The origin of the carriers at high temperature is considered to originate from the Yb 4*f* state because the state crosses the Fermi level observed by a photoemission experiment.[4] However, the origin of carrier at low temperature is still unresolved.

We have investigated the temperature dependence of the electronic structure very near the Fermi level as well as that of the carrier character at low temperature of Yb_4As_3 using far-infrared reflectivity measurement.[5] At the result, we found a new absorption peak at 30 meV and it becomes sharp coincident with the growing-up of the Drude-like carrier absorption with decreasing temperature. To clarify the origin of the absorption at 30 meV, we measured far-infrared reflectivity spectra of a semiconducting material $Yb_4(As_{0.85}P_{0.15})_3$ with a tiny energy gap.

Figure 1 indicates the temperature dependence of optical conductivity ($\sigma(\omega)$) spectra, which are derived from the Kramers-Kronig analysis of the reflectivity spectra of $Yb_4(As_{0.85}P_{0.15})_3$. We are not concerned with some peaks of 10 – 35 meV here because they originate from TO-phonons. The temperature dependence below 0.6 eV is strong. However, the temperature dependence is almost linearly, *i.e.*, the metallic $\sigma(\omega)$ spectrum simply changes into the semiconducting with decreasing temperature. This is not equal to the situation of Yb_4As_3, in which another Drude-like carrier absorption appears at low temperature and also an absorption peak at 30 meV appears. This result means that the absorption peak at 30 meV of Yb_4As_3 is accompanied with the Drude-like absorption at low temperature. Therefore it is considered that the carriers at low temperature originate from the quasiparticle after hybridization between As-4*p* and Yb-4*f* states and the absorption between the hybridization gap appears at 30 meV.

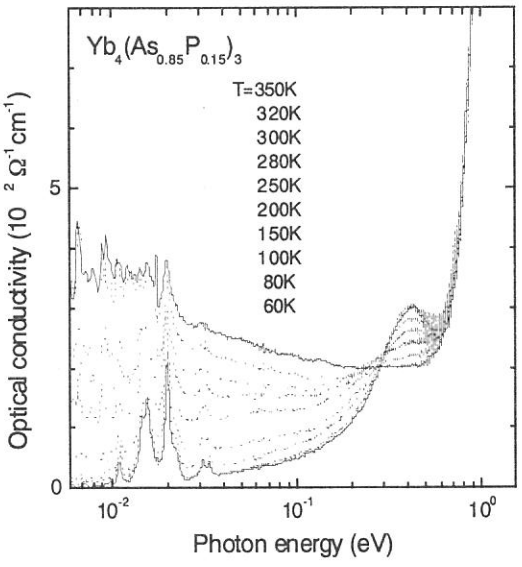

Fig. 1. Temperature dependence of optical conductivity spectrum of $Yb_4(As_{0.85}P_{0.15})_3$ in the infrared region.

[1] H. Aoki, A. Ochiai, T. Suzuki, R. Helfrich and F. Steglich, Physica B **230-232** (1997) 698.
[2] A. Ochiai, H. Aoki, T. Suzuki, R. Helfrich and F. Steglich, Physica B **230-232** (1997) 708.
[3] S. Kimura, M. Ikezawa, A. Ochiai and T. Suzuki, J. Phys. Soc. Jpn. **65** (1996) 3591.
[4] S. Suga *et al.*, J. Phys. Soc. Jpn. **67** (1998) 3552.
[5] S. Kimura, A. Ochiai and T. Suzuki, UVSOR Activity Report 1997 (1998) 124.

(BL7A) Temperature dependence of AlN reflectivity in VUV region

Q.X. Guo[1], A. Okada[1], M. Nishio[1], H. Ogawa[1], K. Fukui[2], H. Miura[3], and A. Yoshida[4]

[1]*Department of Electrical and Electronic Engineering, Saga University, Saga 840-8502*

[2]*Institute for Molecular Science, Okazaki, 444-8585*

[3]*Department of Electrical and Electronic Engineering, Fukui University, Fukui 910-8507*

[4]*Department of Electrical and Electronic Engineering, Toyohashi University of Technology, Toyohashi 441-8580*

Aluminum nitride (AlN), one of the III-V compound semiconductors with a wurtzite crystalline structure, is promising not only for the use of passivation of semiconductor surfaces and insulators for high temperatures, but also for the use of optical devices at ultraviolet spectral region and surface acoustic wave devices, because it has wide band gap and high sound velocity. Recently, it has received more attention from the properties of its alloys with GaN and InN which permit the fabrication of AlGaInN based shortest-wavelength semiconductor laser diode. In spite of the prospects of AlN in device applications, experimental data on the optical properties are surprisingly scarce, although several theoretical studies were performed. We have reported reflectance spectra measured with synchrotron radiation on AlN single crystals in the energy from 6 to 120 eV at room temperature [1,2]. In this work, we investigated the temperature effect on the reflectance spectra of AlN single crystal.

AlN films were grown epitaxially on (0001) α -Al_2O_3 substrates using the chemical reaction of trimethylaluminum with ammonia [3]. Reflection high-energy electron diffraction results showed all the AlN samples to be a single crystal and to have an orientation relationship of (0001)AlN//(0001) α -Al_2O_3. The samples were placed in a continuous-flow cryostat with a coolant (liquid helium) from a storage vessel to a vacuum-insulated sample space. The sample temperature could be maintained at any temperature with an accuracy of 0.1 K in the range of 4.2 to 300 K by controlling the flow of the coolant and the power supplied to the electrical heater. Reflectance spectra were measured in the photon energy range from 6 to 10 eV as a function of temperature. The results show that with decreasing temperature, the energy positions of the dominant structures in the reflectance spectra shift towards higher energies. The shifts of these dominant structures can be well described by the Bose-Einstein expression and the calculated parameters by fitting the experimental data to the expression have a good agreement with those obtained by absorption spectra measurements [4].

The authors would like to thank Professor K. Tsubouchi of the Research Institute of Electrical Communication, Tohoko University, for supplying the samples of AlN single crystal.

References:

[1]Q.X. Guo, M. Nishio, H. Ogawa, and A. Yoshida, Phys. Rev. B 55, R15987 (1997).

[2]Q.X. Guo, M. Nishio, H. Ogawa, and A. Yoshida, J. Crystal Growth 189/190, 457 (1998).

[3]M. Morita, N. Uesugi, S. Isogai, K. Tsubouchi, and N. Mikoshiba, Jpn. J. Appl. Phys. 20, 17 (1981).

[4]Q.X. Guo and A. Yoshida, Jpn. J. Appl. Phys. 33, 2453 (1994).

(BL7B)

Optical reflectivity study of $(Fe_{1-x}V_x)_3Al$ intermetallic alloys

H. Okamura, J. Kawahara, T. Nanba, S. Kimura,
K. Soda[A], U. Mizutani[A], Y. Nishino[B], M. Kato[B]

Department of Physics and Graduate School of Science and Technology, Kobe University, Kobe 657-8501.
[A]Department of Crystalline Materials Science, Nagoya University, Nagoya 464-8603, Japan
[B]Department of Materials Scienceand Engineering, Nagoya Institute of Technology, Nagoya 466-8555, Japan.

The Heusler-type intermetallic compound Fe_2VAl has recently attracted much interest since it possesses several anomalous properties [1]. Fe_2VAl shows semiconductor-like transport data at temperatures above ~ 400 K, but it shows highly metallic photoemission data at low temperatures (40 K). In addition, it shows an anomalous enhancement of specific heat below 4 K, which is reminiscent of typical behaviors shown by the f-electron heavy electron systems [1]. In order to probe the electronic structures of Fe_2VAl and related compounds, we have performed optical reflectivity experiments of $(Fe_{1-x}V_x)_3Al$ ($0 \leqq x \leqq 0.33$) at photon energies between 0.08 eV and 30 eV and at temperatures between 9 K and 300 K [2]. The optical reflectivity spectra above 2 eV were measured at BL7B of UVSOR, while the spectra at lower energy were measured at Kobe University. Figures 1 and 2 show the measured optical reflectivity spectra $R(\omega)$ and the corresponding optical conductivity spectra $\sigma(\omega)$, respectively, measrued at room temperature. $\sigma(\omega)$ were obtained from $R(\omega)$ using the Kramers-Kronig relations. With increasing x, $R(\omega)$ shows large decreases below ~ 1 eV, and correspondingly $\sigma(\omega)$ also decreases below 0.5 eV. This demonstrates the formation of a well-developed pseudogap with increasing V content. For the Heusler composition Fe_2VAl ($x=0.33$), the spectra show only minor temperature dependence down to 9 K [2], showing that the pseudogap results from the band structure of Fe_2VAl rathre than from temperature-sensitive electron correlation effect. Based on the present results, we have proposed a simple model of electronic structures that accounts consistently for both the semiconductor-like transport and the metallic photoemission data of Fe_2VAl [2].

References

[1] Y. Nishino *et al.*, Phys. Rev. Lett. **79**, 1909 (1997).

[2] H. Okamura *et al.*, to appear in Phys. Rev. Lett. (2000).

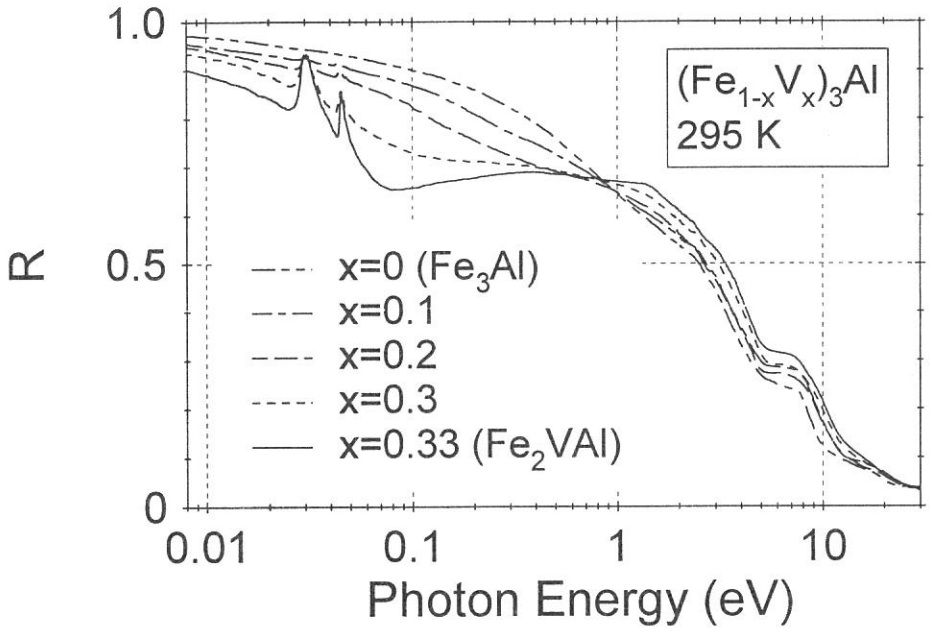

FIG. 1. The optical reflectivity (R) spectra of $(Fe_{1-x}V_x)3Al$ at room temperature.

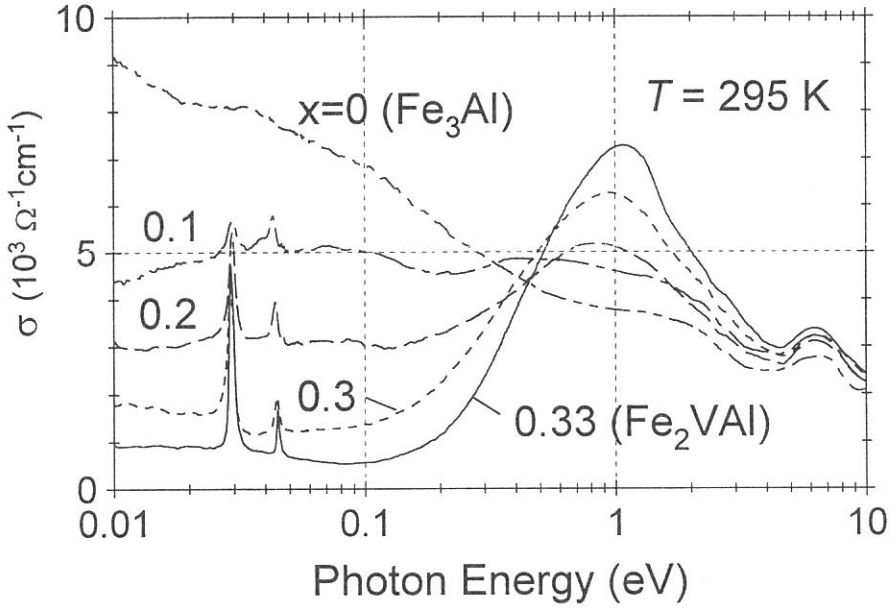

FIG.2 : Optical conductivity (σ) of $(Fe_{1-x}V_x)_3Al$ at room temperature, which are obtained from the spectra in Fig. 1 using the Kramers-Kronig relations.

(BL-7B)

Photo-Dissociation Process of tetraethoxysilane, tetraethoxygermanous and tetraethylsilane induced by Vacuum Ultraviolet Radiation

Hideaki Yanagita, Yasuhiro Kawasaki, Yoshihiro Maesono[a], Ryo Nomura[a],
Noritaka Takezoe, Atsushi Yokotani[a] and Kou Kurosawa

Institute for Molecular Scinece, Myoudaiji, Okazaki 444-8585
[a]Miyazaki University, Miyazaki 889-2192

Tetraethoxysilane (TEOS:Si $(OC_2H_5)_4$) or tetraethoxygermane (TEOG:Ge $(C_2H_5)_4$) is one of the promising materials for preparing SiO_2 or GeO_2. These films have been prepared by photo-chemical vapor deposition using VUV excimer lamp from TEOS or TEOG at room temperature. We have measured absorption spectra of TEOS and TEOG using synchrotron radiation (BL-1B and 7B) with the aim to search suitable wavelength of the light souce for films preparation, and also measured absorption spectrum of tetraethylsilane (TES:Si $(C_2H_5)_4$) which is expected to be a source material for preparing amorphous-Si and SiO_2 films. We have tried to prepare SiO_2 thin films from TEOS using five diffrent excimer lamps (λ =126 ~ 308nm).

Figures 1, 2 and 3 show absorption spectra of TEOS, TEOG and TES at gas pressure of 50mTorr. In the absorption spectra in the region of 115nm to 300nm, TEOS showed absorption in the region shorter than about 180nm, TEOG and TES showed absorption in the region shorter than 200nm. Figure 4 shows FT-IR spectrum from SiO_2 films prepared with five different excimer lamps. SiO_2 films were deposited in case of using Ar_2^* (126nm), Kr_2^* (146nm) and Xe_2^* (172nm), but not with KrCl* (222nm) and XeCl* (308nm), which is consistent with the absorption spectra.

We are planning to investigate photo-dissociation process of TEOS, TEOG and TES with UVSOR by means of mass and FT-IR spectroscopy.

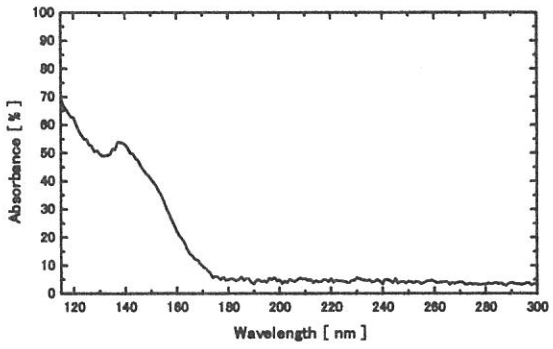

Figure 1 Absorption spectrum of TEOS

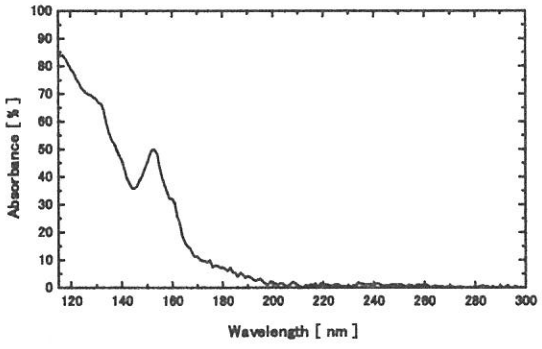

Figure 2 Absorption spectrum of TEOG

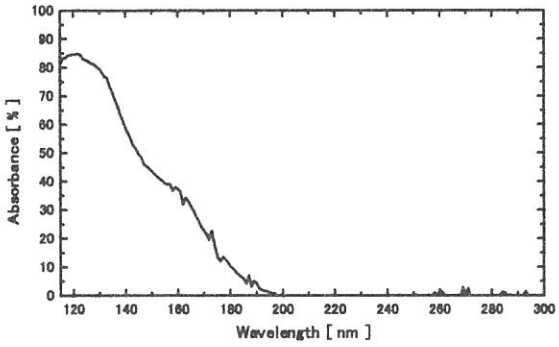

Figure 3 Absorption spectrum of TES

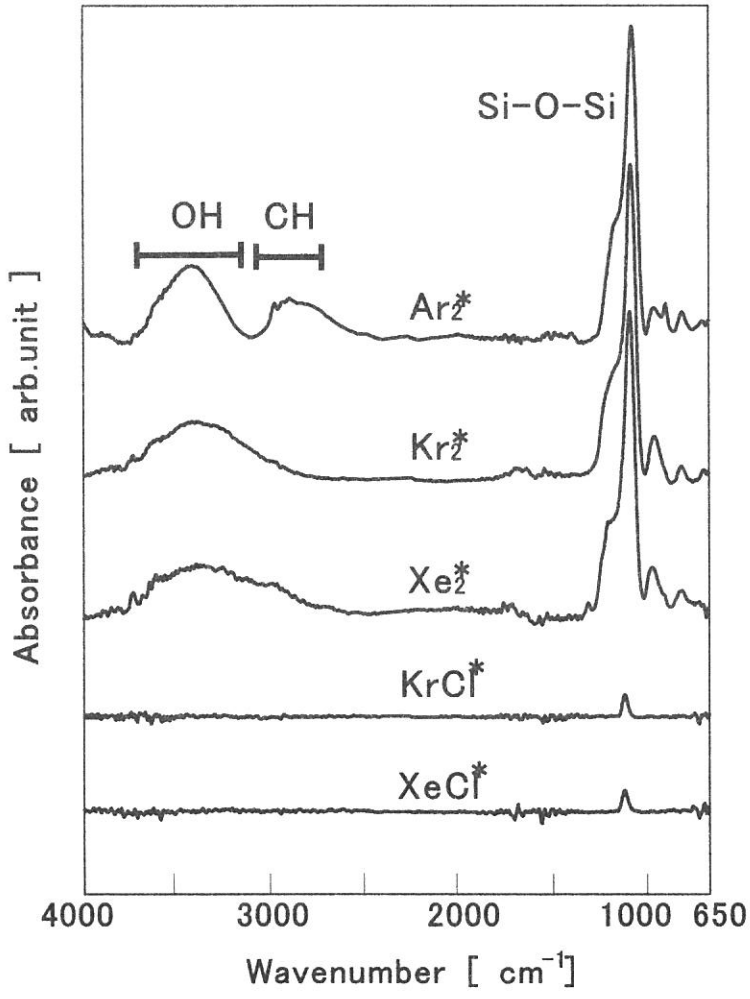

Figure 4 FT-IR spectra from SiO_2 films prepared with five different excimer lamps.

(BL8B2)

Angle-resolved UPS of In/PTCDA interface

K. K. Okudaira, Y. Azuma, S. Akatsuka, Y. Harada[A], and N. Ueno

Graduate School of Science and Technology, Chiba University, Chiba 263-8522
[A]Life Culture Department, Seitoku University, Iwase, Matsudo, 271-8555

The archetypal organic semiconductor, perylene-3,4,9,10-tetracarboxylic dianhydride (PTCDA), has recently gained increasing interest as a promising material for organic electroluminescence devices. It was reported that a thin film of PTCDA provides a new state in the PTCDA band gap due to the reaction between the film and orverlayer materials such as In, Al, Ti, and Sn.[1] This result is very important because the new band is located very close to the Fermi level, and therefore it is expected that it plays an important role in organic devices properties.

In this work, In-PTCDA system was measured by angle-resolved ultraviolet photoelectron spectroscopy (ARUPS) with synchrotron radiation in order to study the origin of the band gap state. We report the results of quantitative analysis of the take-off angel (θ) dependence of the photoelectron intensity from the new band using single-scattering approximation combined with *ab initio* molecular orbital calculation (SS/MO).[2]

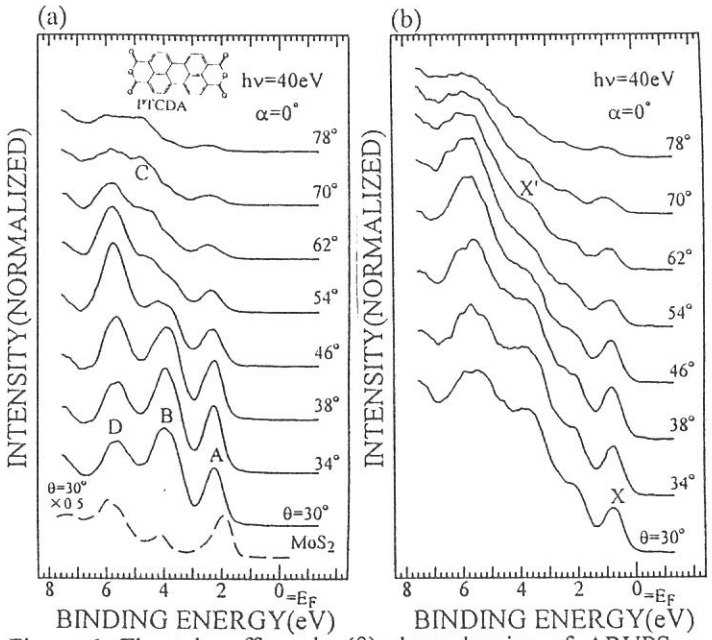

Figure 1 The take-off angle (θ) dependencies of ARUPS spectra of a 3−Å−thick PTCDA film on MoS_2 before (a) and after In overlayer deposition (b). The thickness of the In overlayer is 1Å. The intensity is normalized to the incidence photon flux. The molecular structure of PTCDA is also shown in Fig.1(a).

ARUPS measurements were carried out at the beamline BL8B2 of the UVSOR at the Institute for Molecular Science. ARUPS spectra were measured at photon energy hν=40eV and at incidence angle of photon α=0°. All measurements were carried out at room temperature under UHV conditions (~10^{-10} Torr). Purified PTCDA was evaporated onto a MoS_2 substrate obtained by *in situ* cleavage. The In overlayer was deposited onto the PTCDA film by vacuum evaporation.

In Fig.1(a), we show the θ dependence of the ARUPS of PTCDA thin film (3Å thick; ~monolayer) on the MoS_2 surface, where the binding energy is measured from the Fermi level. These spectra are in good agreement with previously reported results, indicating that PTCDA molecules lie flat on the MoS_2.[3] The assignment for each band in the spectra was already made with *ab initio* calculation and the quantitative analysis of the photoelectron intensity.[3]

Figure 1(b) shows the θ dependence of the ARUPS of an In/PTCDA interface which was prepared by evaporating the In onto the 3-Å-thick PTCDA film. The thickness of the In overlayer was 1 Å. From the comparison between Figs.1(a) and 1(b), some spectral changes can be clearly seen. First, a new band X appears at E_B = ~ 0.8eV in the PTCDA band gap after the In deposition. Second, the band C in Fig. 1(a) ($n_{O\parallel}$:oxygen 2p nonbonding states distributed

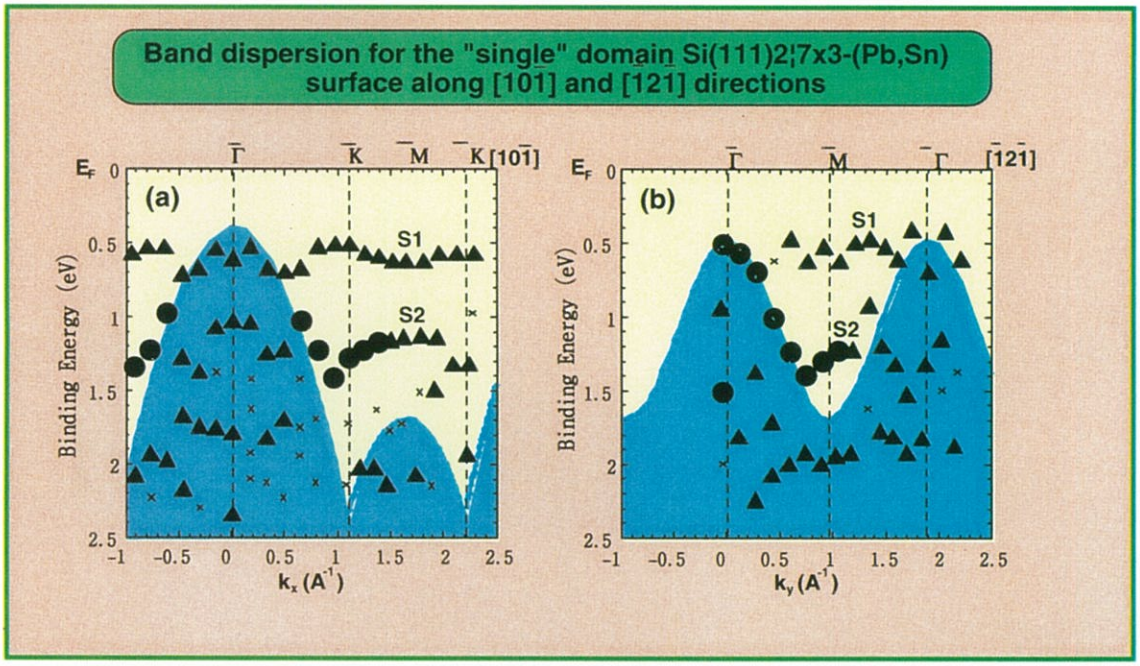

Solid State Spectroscopy Ⅱ

(XAFS, PES)

BL1A, 2B1, 5A, 5B, 6A2, 7A, 8B1, 8B2

parallel to the molecular plane at C=O parts) was not resolved after the In deposition, while new band X' (E_B = ~ 3.6eV) is observed at θ = ~ 62° . These spectral changes originate from a chemical reaction between the PTCDA molecules and the In atoms. The disappearance of the $n_{O\parallel}$ band in Fig.1(b) suggests that the chemical reaction between PTCDA and In takes place at the C=O parts to change the $n_{O\parallel}$ states. It is expected the band X' originates from the molecular orbital which is distributed parallel to the surface, since the band X' observed at a large value of θ.

On the other hand, we performed Penning ionization electron spectroscopy of the In/PTCDA interface. The result suggested that four In atoms react with the one PTCDA molecule.[4]

In Fig.2, we compared the observed ARUPS of the In/PTCDA with the results of *ab initio* MO calculation (STO-6G) on an expected model compound of the reaction product, In_4PTCDA. In Fig.2 θ-averaged spectrum is shown. From the calculation we found that band 1 consists of a single MO of π character with large contribution from C 2pz, O 2pz, and In 5pz atomic orbitals (AOs). On the other hand, the band 3 is related to four σ MOs with the contributions of O 2s, In 5s, 5px, and 5py AOs. The calculated density-of-states (DOS) curve agrees well with the measured ARUPS, indicating that the X and X' are assigned to the π and σ orbitals of In_4PTCDA, respectively. The agreement indicates that the electronic structure of the In/PTCDA is well simulated by that of the model compound In_4PTCDA.

In Fig.3, the observed θ dependence of the band X intensity is compared with the calculated one for molecular tilt angle of β = 0°, 10°, and 20° using the SS/MO method. Among these, the calculated θ pattern for β = 10° agrees better with the observed one in the value of θ_{max} and the width of the angular distribution. The calculated θ dependence for various β with a long molecular axis parallel to the surface showed remarkable disagreement from the observed results. These results indicate that molecules become tilted by the reaction, and the averaged tilt angle is considered to be approximately 10° as shown in Fig.3.

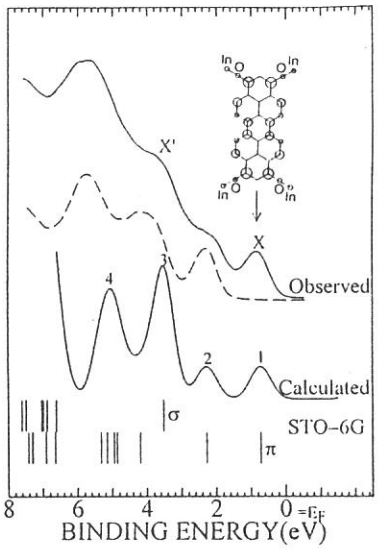

Figure 2 Comparison between observed UPS and the DOS calculated for a model system of the reaction product, In_4PTCDA. The vertical bars show the calculated MO levels. The upper and lower bars indicate σ and π states respectively. The calculated DOS was obtained by a Gaussain broadening of the MO levels. The observed ARUPS's of the pristine PTCDA (– – – – –) and the In/PTCDA (————) are shown for comparison. The molecular orbital coefficients of the π-band X in the reacted system are shown schematically.

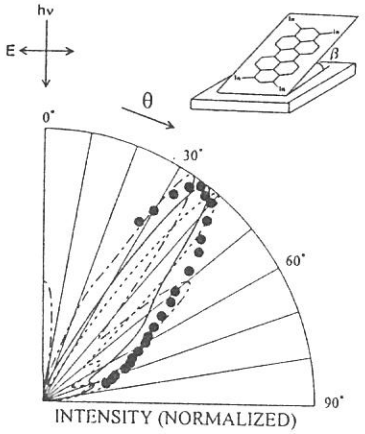

Figure 3 Comparison between calculated and observed θ dependencies of the photoelectron intensities for the band gap state. The SS/MO results at hν=40eV and α=0° are shown for β=0° (– – – – –), 10° (————), and 20° (----------). The calculation was made by assuming azimuthal disorder of the reaction product, In_4PTCDA. The tilt direction of the molecule is also shown.

REFERENCES

[1]Y.Hirose, A.Kahn, V.Aristov, P.Soukiassian, V.Bulovic, and S.R.Forrest, Phys. Rev. B 54. 13748(1996).

[2]N.Ueno *et al.*, J.Chem.Phys. **107**, 2079 (1997).

[3]Y.Azuma *et al.*, J. Synchrotron Radiation **5**, 1044 (1998).

[4] S.Kera *et al.*, to be published.

(BL8B1)

Faraday Rotation Measurement on a Co film around $M_{2,3}$ Edges

K. Saito, W. Hu, T. Hatano, T. Ejima and M. Watanabe
Research Institute for Scientific Measurements, Tohoku University
Katahira 2-1-1, Aoba-ku, Sendai 980-8577

We had developed a polarimeter which enables Faraday rotation measurements in the 55-90 eV region by the use of Al/YB_6 multilayer polarizers[1]. It consists of a transmission multilayer polarizer, a magnetic circuit composed of Sm-Co permanent magnets and a rotating analyzer unit consisting of a reflection multilayer analyzer, a multi-channel plate and a pulse motor. In our previous experiment on Ni films around $M_{2,3}$ edges[2], the Faraday rotation angles obtained by using the polarimeter were larger than those calculated from MCD spectrum measured by the total photoelectron yield (TY) method[3], through Kramers-Krönig analysis. It was concluded that the Faraday rotation measurements are transmission measurements, so that they are scarcely affected by surface conditions and reflect bulk properties.

In this experiment, the Faraday rotation measurement on a 21 nm Co film has been performed around $M_{2,3}$ edges under an applied magnetic field of 0.82 T at room temperature. Figure 1 shows the preliminary result of the Faraday rotation spectrum obtained by the present experiment and the calculated one from MCD spectrum measured by the TY method, through Kramers-Krönig analysis. The former spectrum is similar to the latter one. However, the measurement of MCD was performed under a magnetic field of 1.2 T at 140 K (the saturation magnetic field of Co : 1.8 T), so that the absolute value calculated from MCD should be larger than the present result. This means that the MCD measurement was affected by the surface condition and the Faraday rotation measurement reflects bulk properties well as in the case of Ni. However, it is necessary to carry out additional experiments to confirm this conclusion.

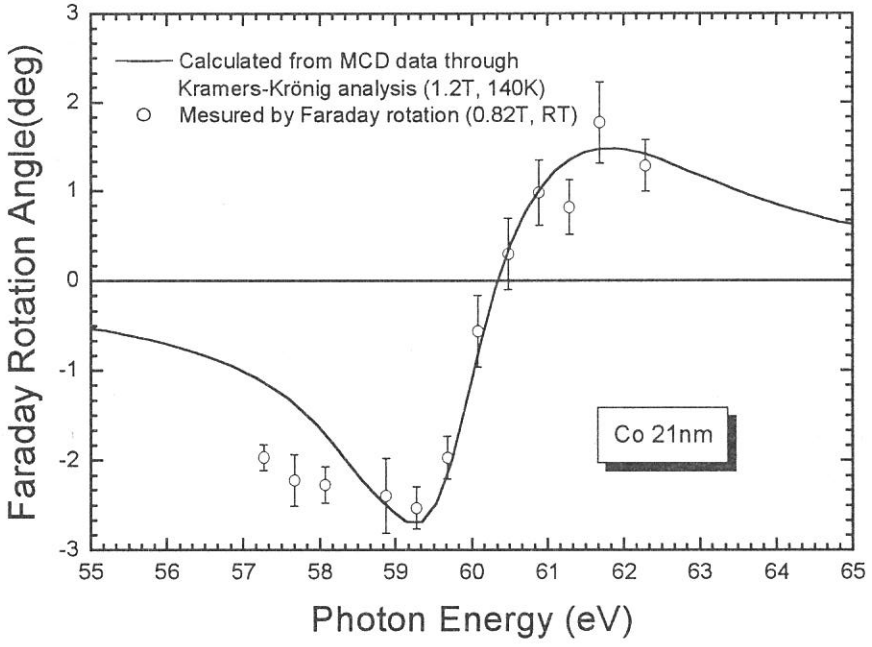

Fig. 1. Faraday rotation spectra of Co around $M_{2,3}$ edges.

References

1) W. Hu, T. Hatano, M. Yamamoto and M. Watanabe, J. Synch. Rad. **5** (1998) 732.
2) T. Hatano, W. Hu, K. Saito, M. Watanabe, J. Electr. Spectr. Rel. Phenom. **101-103** (1999) 287.
3) T. Hatano, S.Y. Park, T. Hanyu, T. Miyahara, J. Electr. Spectr. Rel. Phenom. **78** (1996) 217.

(BL1A)

Mg and Al K-Edge XAFS Measurements with a KTP Crystal Monochromator

Yasutaka Takata and Nobuhiro Kosugi

Institute for Molecular Science,
Myodaiji, Okazaki 444-8585

There has been a strong demand for the monochromator crystals with a large lattice spacing in order to measure the EXAFS spectra for Mg and Al K-edges. At BL1A, beryl ($10\bar{1}0$) [2d=15.965Å] and quartz ($10\bar{1}0$) [2d=8.512Å] are used as the crystal monochromator for the Mg and Al K-edge X-ray absorption fine structure (XAFS) spectra, respectively, and serve soft X-rays with high quality in the near edge region. However, the energy range (k range) is limited because beryl and quartz contain Al and Si, respectively. In the EXAFS analysis, the reliability and accuracy depend strongly on the k range. At the XAFS-X conference (Chicago, 1998), Rogalev et al. reported that KTP, $KTiOPO_4$, (011) [2d=10.95Å] crystal can be used in the crystal monochromator at the ESRF ID12A beamline (circularly polarized undulator) [1]. We have introduced KTP crystal (Crystal Laser Co., France) at BL1A and tested the performance in the energy range below 2100eV including the applicability to the EXAFS measurements for Al and Mg K-edges.

Figure 1 shows the throughput spectra of the KTP double crystal monochromator. The solid line indicates the photon flux measured by the Si photodiode (IRD Co.). The Si K-edge jump at around 1840 eV originates from the photodiode. The total electron yield spectrum of Au plate (broken line) is also shown as a reference. It should be noticed that there is no structure up to 2140eV (P K-edge). On the other hand, YB_{66} (400) [2d=11.72Å] crystal monochromator covering the same energy range shows undesirable structures at around 1400eV due to the anomalous (600) reflection [2-4]. Furthermore, as pointed out by Rogalev et al., the reflectivity of KTP was higher than that of YB_{66}. The energy width of the monochromatized beam was 0.5~0.6 eV in the energy range from 1200 to 2100 eV. We must mention about the radiation damage of the KTP crystal. At the ESRF ID12A, the damage was not noticeable: on the other hand, the present first crystal suffered the damage at BL1A similarly to the case of beryl and quartz crystals. Fortunately, the damage was not so serious and we could measure the EXAFS spectra.

Figure 2 and 3 shows the Mg and Al K-edge XAFS spectra of MgO and α-Al_2O_3, respectively, measured by monitoring the sample drain current. These samples are powder and spread on adhesive conduction tapes. For both spectra, the energy range is extended considerably in comparison with the spectra measured with the beryl and quartz monochromator. In the latter cases, Mg and Al K-edge XAFS spectra are limited up to 1560 eV (Al K-edge) and 1840 eV (Si K-edge).

References

[1] A. Rogalev et al., Abstract of XAFS X, (1998) R5.1-20.
[2] M. Rowen et al., Synchrotron Rad. News, **6** (1993) 25.
[3] T. Tanaka et al., J. Appl. Cryst., **30** (1997) 87.
[4] A. D. Smith et al., J. Synchrotron Rad., **5** (1998) 716.

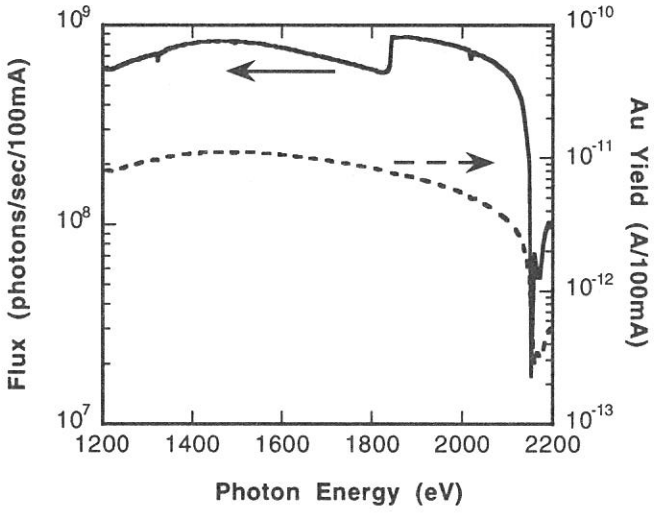

Figure 1. Throughput spectra of the KTP double crystal monochromator at BL1A.

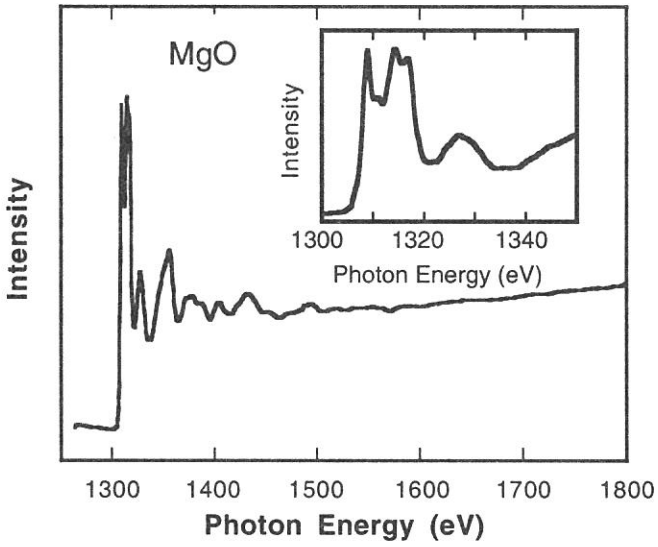

Figure 2. A Mg K-edge XAFS spectrum of MgO.

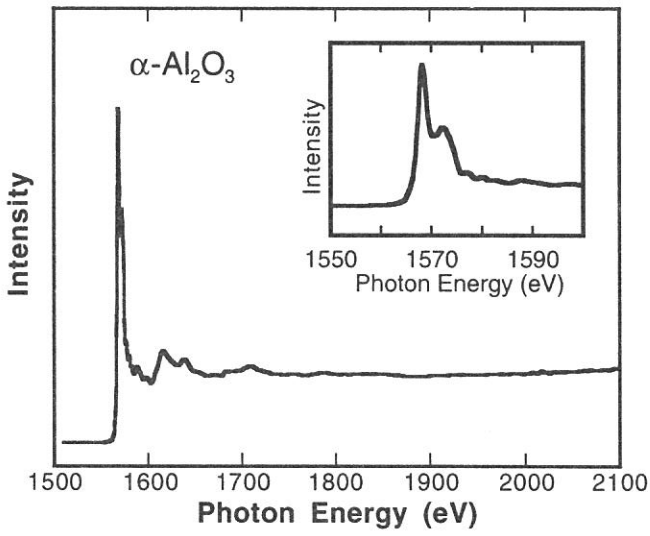

Figure 3. An Al K-edge XAFS specrum of α-Al_2O_3.

(BL1A)

Ni 2p Photoabsorption and Resonant Photoionization of Ni(*NN'*-dimethylethylenediamine)$_2$Cl$_2$

Yasutaka Takata, Takaki Hatsui and Nobuhiro Kosugi

Institute for Molecular Science,
Myodaiji, Okazaki 444-8585

We have reported that the planar Ni complexes with a $3d^8$ low-spin ground state show distinct satellite structures in the Ni 2p photoabsorption spectra [1, 2], and show characteristic resonant behavior in the Ni 3p and 3s resonant photoelectron spectra in comparison with Ni metal and NiO [3-5]. The observed characteristics can be interpreted within a one electron picture taking the ligand vacant orbitals into account. In the present study, we have measured Ni 2p photoabsorption and resonant photoelectron spectra of Ni(*NN'*-dimethylethylenediamine: DED)$_2$Cl$_2$ with a $3d^8$ high-spin state in order to investigate how the spin state influences the spectra.

Experiments were performed at BL1A soft x-ray beamline. A pair of beryl $(10\bar{1}0)$ crystals was used in the double crystal monochromator. The Ni(DED)$_2$Cl$_2$ powder was spread on an adhesive conduction tape. The Ni 2p photoabsorption spectra were measured by monitoring the total electron yield. A SCIENTA SES200 electron energy analyzer was used to measure the photoelectron spectra. The total energy resolution in the photoelectron spectra was about 0.7 eV.

The Ni 2p photoabsorption spectrum of Ni(DED)$_2$Cl$_2$ (Fig.1) shows two strong peaks at the $2p_{3/2}$ edge, and is quite similar to the spectrum of Ni(cyclam)Cl$_2$ [6]. In Ni(DED)$_2$Cl$_2$, Ni is in a D_{4h} symmetry with the apical Cl atoms. The spectrum is quite different from the planar Ni complexes with a $3d^8$ low-spin ground state such as $K_2Ni(CN)_4H_2O$ [1]and Ni(Hdmg)$_2$ [2].

Figure 2 shows the resonant photoelectron spectra in the Ni 3p and 3s ionization regions measured at the excitation energies (0-3) marked in Fig. 1. The intensity was normalized referring that of the Cl 2p photoelectron peaks which are independent of the resonant condition. In the non-resonant spectrum (0), strong satellite bands appear, and are strongly enhanced by the resonant excitation. All the enhanced satellite bands in the spectra (1-3) have constant binding energies, and no noticeable binding energy shift was observed; i.e., there is no clear relation between the photoexcited states and the resonantly enhanced satellite states. These results are similar to those for NiO [3], in which the correlation and multiplet interaction are very important, but are quite different from those for the low-spin planar complexes. In $K_2Ni(CN)_4$[3, 4]and Ni(Hdmg)$_2$[5] weak or hidden satellite bands in the non-resonant spectra are enhanced by the resonant excitation, and show clear one-to-one correspondence between the photoexcited state and the satellite state. The present results indicate that the resonant behavior is strongly influenced by the spin state.

References

[1] T. Hatsui et al., Chem. Phys. Lett., **284** (1998) 320.
[2] T. Hatsui et al., J. Synchrotron Rad., **6** (1999) 376.
[3] Y. Takata et al., J. Electron Spectrosc. and Relat. Phenom. **101-103** (1999) 443.
[4] Y. Takata et al., Chem. Phys. Lett., **287** (1998) 35.
[5] Y. Takata et al., J. Electron Specrosc. and Relat. Phenom. **93** (1998) 109.
[6] J. van Elp et al., J. Am. Chem. Soc., **116** (1994) 1918.

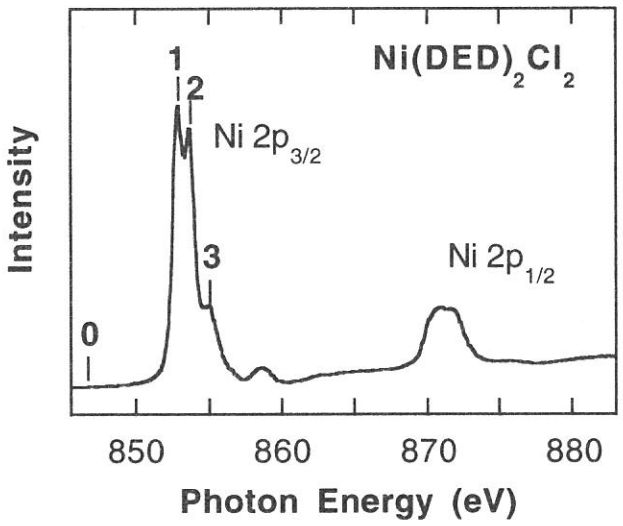

Fig. 1. Ni 2p photoabsorption spectrum of $Ni(DED)_2Cl_2$.

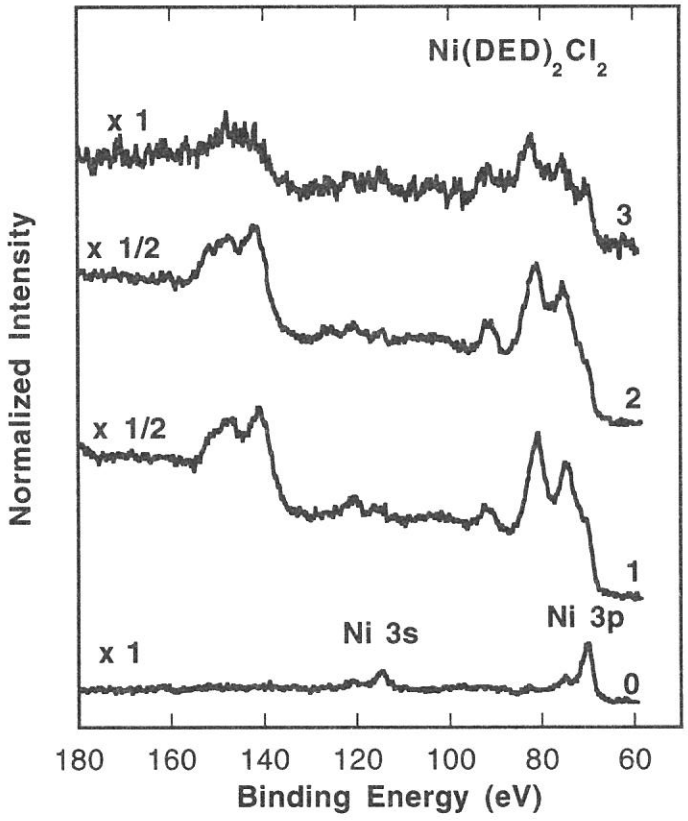

Fig. 2. Resonant photoelectron spectra in the Ni 3p and 3s regions of $Ni(DED)_2Cl_2$ at the photon energies marked in Fig. 1.

(BL2B1)

Removal of time-structure background in coincidence spectrum

Shin-ichi Nagaoka, Kazuhiko Mase,[A] Mitsuru Nagasono[B] and Shin-ichiro Tanaka[C]

Institute for Molecular Science, Okazaki 444-8585, [A]Photon Factory, Institute of Materials Structure Science, High Energy Accelerator Research Organization, 1-1 Oho, Tsukuba 305-0801, [B]MAX-lab, Beamline I511, Lund University, P.O. Box 118, 221 00 Lund, Sweden, [C]Department of Physics, Graduate School of Science, Nagoya University, Chikusa-ku, Nagoya 464-8602

In an energy-selected-photoelectron photoion coincidence (ESPEPICO) experiment, the pulses in the ion channel, triggered by a pulse in the energy-selected electron channel, are displayed as a function of the time delay between the two channels (i.e., the TOF). The TOF depends on the mass of the ions. By tuning to a peak of the photoelectron spectrum and measuring only the ions coincident with the electron emission, we can correlate an ionized-state with observation of an ionic fragment.

However, one experimental difficulty in ESPEPICO, as well as in any coincidence experiment, is differentiating between true and accidental coincidences [1,2]. Using a synchrotron-radiation apparatus operated in partial-filling mode makes this problem even more severe because the periodic accidental coincidences originating from the time-structure of the synchrotron radiation are superimposed on the ordinary accidental coincidences that are nearly independent of the TOF.

Figure 1a shows an ESPEPICO spectrum measured for (trifluorosilyl)(trimethylsilyl)methane (FSMSM) condensed on a Si(111) surface. The periodic structure is essentially the spectrum of the accidental coincidences, which show the modulation due to the time structure of the synchrotron radiation. Eberhardt et al. removed such a time-structure background by subtracting from the measured spectrum the shifted part of the spectrum containing only accidental coincidences [1,2]. We removed the time-structure background by performing fast-Fourier-transformation (FFT) on the ESPEPICO spectrum (that is, subtracting the ±177-ns component from the transformed spectrum), then performing an inverse FFT [3]. Figure 1b shows the time-structure background that was extracted with our method, and Figure 1c shows the difference between the spectra in Figures 1a and b. This technique worked so well that we were able to discern even weak true coincidence features very well. For example, a weak true coincidence peak can be seen at around 1.9 μs in Figure 1c, although it is difficult to discern the peak in Figure 1a.

When an ion is produced coincidentally with an energy-selected electron, the integrated intensity of a peak in the ESPEPICO spectrum (I) corresponds to the accumulated ion count. To estimate integrated intensity I, the time-structure background intensity (B) and the ordinary accidental-coincidence intensity (Z) should be subtracted from the total coincidence intensity (A). The error (r) for I inherent in the procedure described in the preceding paragraph was evaluated

as follows. I is given by

$$I = \sum_t \{A(t) - B(t) - Z(t)\}, \quad (1)$$

where t, $A(t)$, $B(t)$ and $Z(t)$ denote TOF, A measured at t, B at t and Z at t, respectively, and $A(t)>0$ and $Z(t)>0$. This summation is carried out over the TOF region of the corresponding peak. In the TOF region, $A(t)>B(t)+Z(t)>0$. Figures 1a and b show plots of $A(t)$ and $B(t)$ versus t, respectively. Assuming that the coincidence count obeys the Poisson distribution, error r is given by

$$r = \sqrt{\sum_t [A(t) + \{B(t) + Z(t)\}]}. \quad (2)$$

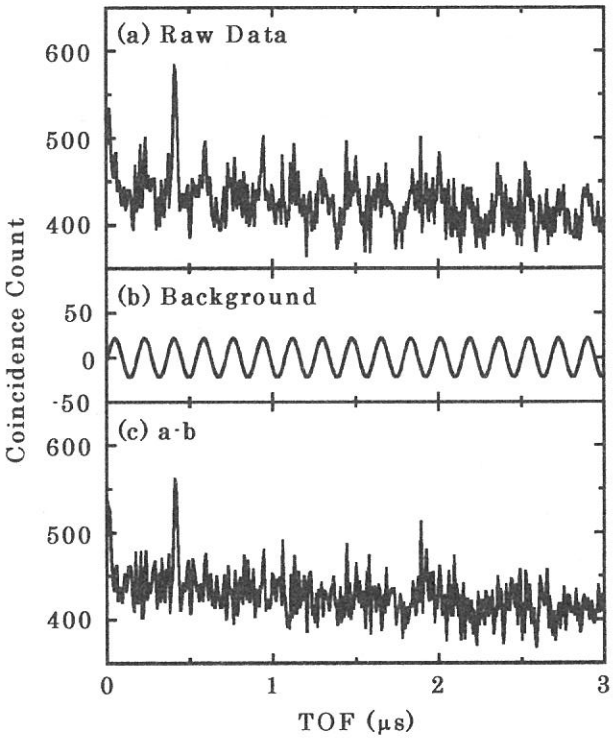

Let the total coincidence intensity at t in Figure 1c be $C(t)$. Because Figure 1c shows the difference between the spectra in Figures 1a and b, $C(t)$ can be written as

$$C(t) = A(t) - B(t), \quad (3)$$

where $C(t)>0$ in the corresponding TOF region. Equations (1) and (2) can thus be rewritten as

$$I = \sum_t \{C(t) - Z(t)\} \quad (4)$$

and

$$r = \sqrt{\sum_t \{C(t) + Z(t) + 2B(t)\}}. \quad (5)$$

In Figure 1, $r - \sqrt{\sum_t \{C(t) + Z(t)\}}$ was calculated to be 1.3 % of r for the peak at around 0.4 μs, but it was negligible for the peak at around 1.9 μs.

[1] W. Eberhardt, E. W. Plummer, I.-W. Lyo, R. Reininger, R. Carr, W. K. Ford, D. Sondericker, Aust. J. Phys. 39, 633 (1986).

[2] W. Eberhardt, E. W. Plummer, C. T. Chen, R. Carr, W. K. Ford, Nucl. Instrum. Methods Phys. Res., Sect. A 246, 825 (1986).

[3] S. Nagaoka, K. Mase, M. Nagasono, S. Tanaka, T. Urisu, J. Ohshita and U. Nagashima, Chem. Phys. 249, 15 (1999).

Figure 1. (a) ESPEPICO spectrum measured for FSMSM condensed on a Si(111) surface. This spectrum was obtained in coincidence with the electron emissions at a photon energy of 206 eV. Data collection time was 1200 s. The accidental coincidence reflects the time structure of the synchrotron radiation that was operated in a partial-filling mode with a period of 177 ns. (b) Time-structure background with a period of 177 ns. This time-structure background was extracted by using FFT. (c) Difference between spectra in Figures 1a and b.

(BL2B1)

Occurrence of different chemical shifts in Si:2*p* ionized state of $X_3Si(CH_2)_nSi(CH_3)_3$ (X=F or Cl, *n*=0-2) condensed on a Si(111) surface

Shin-ichi Nagaoka, Kazuhiko Mase,[A] Mitsuru Nagasono,[B] Shin-ichiro Tanaka,[C] Tsuneo Urisu, Joji Ohshita[D] and Umpei Nagashima[E]

Institute for Molecular Science, Okazaki 444-8585, [A]Photon Factory, Institute of Materials Structure Science, High Energy Accelerator Research Organization, 1-1 Oho, Tsukuba 305-0801, [B]MAX-lab, Beamline I511, Lund University, P.O. Box 118, 221 00 Lund, Sweden, [C]Department of Physics, Graduate School of Science, Nagoya University, Chikusa-ku, Nagoya 464-8602, [D]Department of Applied Chemistry, Faculty of Engineering, Hiroshima University, Higashi-Hiroshima 739-8527, and [E]National Institute of Advanced Interdisciplinary Research, Agency of Industrial Science and Technology, Ministry of International Trade and Industry, 1-1-4 Higashi, Tsukuba 305-8562

Synchrotron radiation has provided a powerful means to obtain information about core-level excitations, and the dynamic processes following the core-level excitations in molecules have long been a subject of interest. In contrast to valence electrons that are often delocalized over the entire molecule, the core electrons are localized near the atom of origin. Although core electrons do not participate in the chemical bonding, the energy of an atomic core-level in the molecule depends on the chemical environment around the atom. A shift in the energy levels of core electrons that is due to a specific chemical environment is called a chemical shift.

To elucidate the occurrence of different chemical shifts, we have studied the photoelectron spectroscopy and the *ab initio* calculation in the Si:2*p* core-ionized state of $X_3Si(CH_2)_nSi(CH_3)_3$ (X=F or Cl, *n*=0-2) [1-3]. The chemical environments of a Si atom bonded to three halogen atoms (Si[X]) and of Si bonded to three methyl groups (Si[Me]) are different from each other, so it seems likely that $X_3Si(CH_2)_nSi(CH_3)_3$ will show occurrence of different chemical shifts.

Figure 1 shows the photoelectron spectrum of $X_3Si(CH_2)_nSi(CH_3)_3$ condensed on a Si(111) surface. The high-resolution spectrum of the Si:2*p* peak is shown in the inset. The photoelectron spectra of the $F_3SiCH_2Si(CH_3)_3$ (FSMSM) and $F_3SiCH_2CH_2Si(CH_3)_3$ (FSMSE) have two peaks in the region of Si:2*p* electron emission (Figs. 1b and c). The peaks at the lower- and higher-energy sides are respectively assigned to Si[Me]:2*p* and Si[F]:2*p* electron emissions. In contrast, the peak due to the Si:2*p* electron emission of $Cl_3SiSi(CH_3)_3$ (MCDS) is not split (Fig. 1a), although the same energy-resolution of CMA was used for these three molecules. From these experimental results, we conclude that the occurrence of different chemical shifts at the two Si sites is clearly observed in molecules in which the two sites are located far apart. However, they are unlikely to be observed in molecules in which the two Si sites are closely located. To clarify the reason for the absence of these different chemical shifts in the latter molecules, we have made *ab initio* calculations.

Let the calculated energy gap between the Si[Me]:2p and Si[X, X=F or Cl]:2p core-eigenvalues be ΔE. In Fig. 2, the ΔEs of MFDS (X=F and n=0), MCDS (X=Cl and n=0), FSMSM (X=F and n=1), FSMSE (X=F and n=2) and FSMSP (X=F and n=3) are plotted as a function of the number of CH_2 groups between the two Si sites (n). For reference, the calculated energy difference between the Si:2p core-eigenvalues of SiF_4 ($SiCl_4$, CH_3SiF_3 and CH_3SiCl_3) and $Si(CH_3)_4$ is also plotted (assuming that n is ∞). Although ΔE is nearly constant or decreases slightly when going from FSMSP to FSMSE to FSMSM, it decreases rapidly when going from FSMSM to MFDS (MCDS). In MCDS, the small ΔE (Fig. 2) is thus consistent with the absence of different chemical shifts (Figs. 1a). The qualitative features of the present computational results are fully consistent with the experimental ones, so interpretation of the observed features of photoelectron spectra can be made on the basis of computational results [3].

[1] S. Nagaoka, K. Mase, M. Nagasono, S. Tanaka, T. Urisu and J. Ohshita, J. Chem. Phys. **107**, 10751 (1997).

[2] S. Nagaoka, K. Mase and I. Koyano, Trends Chem. Phys. **6**, 1 (1997).

[3] S. Nagaoka, K. Mase, M. Nagasono, S. Tanaka, T. Urisu, J. Ohshita and U. Nagashima, Chem. Phys. **249**, 15 (1999).

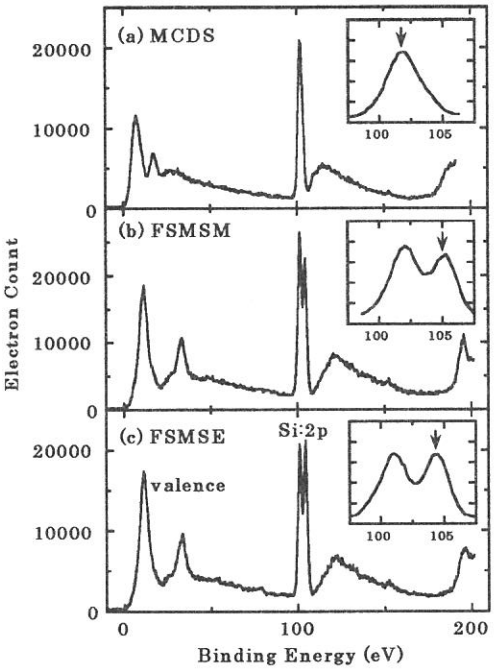

Figure 1 (left-hand side). Photoelectron spectra of (a) MCDS, (b) FSMSM and (c) FSMSE condensed on a Si(111) surface. The spectra a, b and c were taken at photon energies of 196.2, 206.6 and 206.6 eV, respectively. The horizontal scale of the spectra in the region of Si:2p electron emission is enlarged and shown in the insets. Each of the channels in the main spectra was measured for 0.2 s at a step of 0.5 eV, and each of those in the insets was measured for 0.5 s at 0.2 eV. In the measurement shown in the insets, an electric field across the ionization region was applied during the measurement.

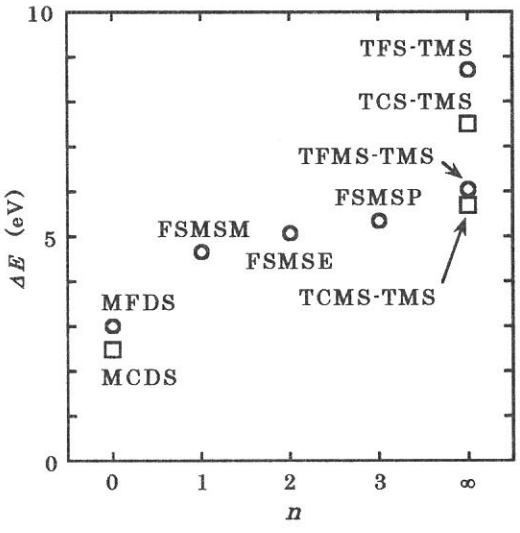

Figure 2 (right-hand side). Plot of ΔE versus n in MFDS, MCDS, FSMSM, FSMSE and FSMSP.

(BL2B1)

Layer-resolved photoemission study of $CF_3CD(OH)CH_3$ on a Si(100) surface

Shin-ichi Nagaoka, Arinobu Nakamura,[A] Kazuhiko Mase[B] and Shin-ichiro Tanaka[C]

Institute for Molecular Science, Okazaki 444-8585

[A]Department of Chemistry, Faculty of Science, Ehime University, Matsuyama 790-8577

[B]Photon Factory, Institute of Materials Structure Science, High Energy Accelerator Research Organization, 1-1 Oho, Tsukuba 305-0801

[C]Department of Physics, Graduate School of Science, Nagoya University, Chikusa-ku, Nagoya 464-8602

The study of adsorbate properties and behaviors on substrates has attracted considerable attention. Chiang et al. previously reported the observation of layer-resolved shifts of photoemission spectra from physisorbed rare-gas multilayers [1]. The shifts were explained in terms of difference in final-state hole-screening energy. However, such a shift has not yet been found for molecules adsorbed on surface. In the present study, we have studied the photoemission spectra of $CF_3CD(OH)CH_3$ (TFIP-d_1) on Si(100) and have found that similar shifts can be revealed in the binding energies of the C:1s core-level, the O:1s core-level and the valence level. TFIP-d_1 is expected to be adsorbed on Si(100) like $CF_3CD(O(H)Si\{substrate\})CH_3$ [2], which is consistent with the results of NEXAFS.

TFIP-d_1 was prepared with the reaction of CF_3COCH_3 and $LiAlD_4$. The amount-regions of gas exposure corresponding to the monolayer coverage and the multiplayer coverage were determined by observing the development of the ion intensity as a function of the amount of gas exposure; the plot of the ion intensity versus the amount of gas exposure was discontinuous between the two regions. The experiments were performed using a double-pass cylindrical-mirror electron-energy analyzer (ULVAC-PHI) and a home-built time-of-flight ion-detection assembly coupled to a grasshopper monochromator (Mark XV) installed on the BL2B1 beamline [3].

Figure 1a shows the C:1s core-level photoemission spectrum of TFIP-d_1 monolayer on a Si(100) surface. The spectrum has three peaks whose assignments are given in the figure. The occurrence of different chemical shifts at the three C sites can clearly be revealed. The site-specific fragmentation of this molecule is very interesting [4].

Figure 1b shows the C:1s core-level photoemission spectrum of TFIP-d_1 condensed on a Si(100) surface (multilayer). The peaks in the spectrum of the multilayer are shifted by about 0.5 eV to higher binding energies from those of the monolayer. Similar shifts can also be found in the O:1s core-level and valence photoemission spectra (Figures 2 and 3); the amounts of the shifts are 0.7 and 1.4 eV, respectively. As in the case of rare-gas [1], the shifts might be explained in terms of difference in final-state hole-screening energy.

Further investigations are clearly needed on the reason of the spectral shift and the

site-specific fragmentation in this molecule.

[1] T.-C. Chiang, G. Kaindl and T. Mandel, Phys. Rev. B 33, 695 (1986).

[2] J. Yoshinobu, S. Tanaka and M. Nishijima, Appl. Phys. 60, 1196 (1991).

[3] S. Tanaka, N. Takahashi, K.-P. Lee and M. Kamada, J. Electron Spectrosc. Relat. Phenom. 80, 205 (1996).

[4] A. Nakamura, S. Nagaoka, K. Mase, S. Tanaka and T. Urisu, UVSOR Activity Report, 26, 100 (1998).

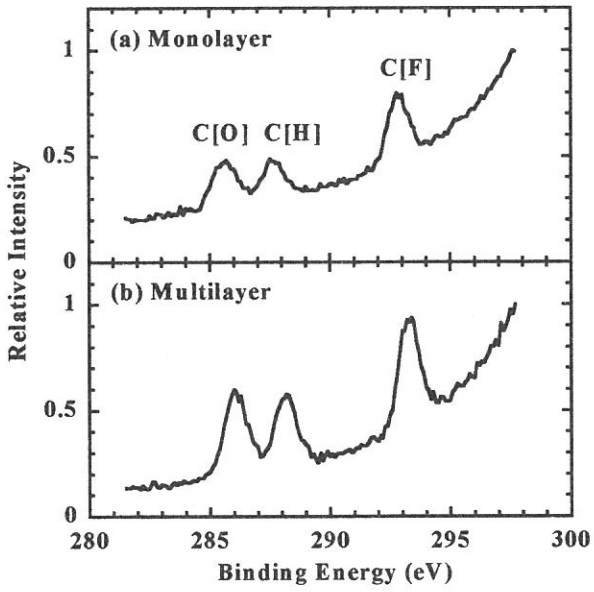

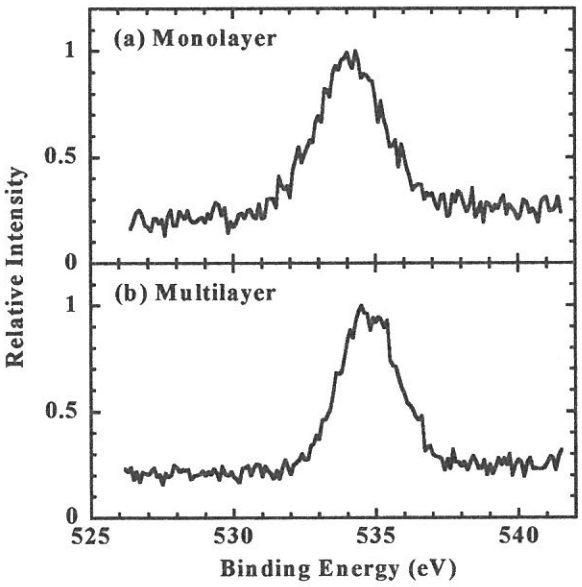

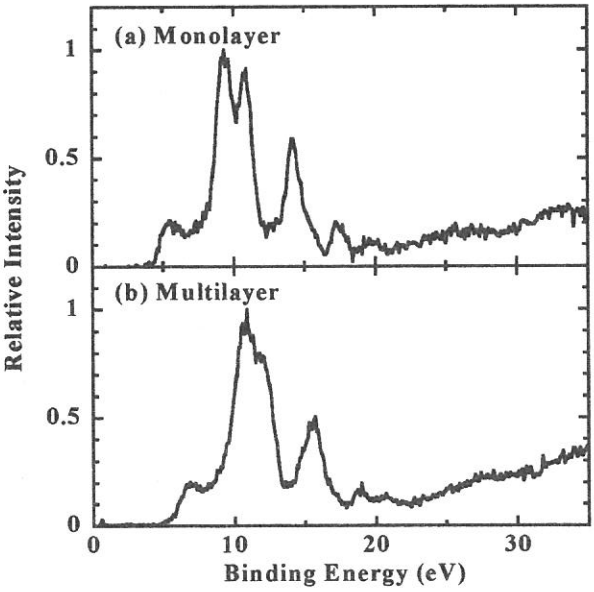

Figure 1 (upper left-hand side). C:1s core-level photoemission spectrum of TFIP-d_1 on a Si(100) surface. (a) Monolayer. (b) Multilayer. The assignments are given in the figure.

Figure 2 (upper right-hand side). O:1s core-level photoemission spectrum of TFIP-d_1 on a Si(100) surface. (a) Monolayer. (b) Multilayer.

Figure 3 (bottom). Valence-level photoemission spectrum of TFIP-d_1 on a Si(100) surface. (a) Monolayer. (b) Multilayer.

(BL5A)

Ultraviolet Photoelectron Spectra of $D0_3$-related $(Fe_{1-x}V_x)_3Al$ and $Fe_2VAl_{1-z}Si_z$ Alloys

Osamu YOSHIMOTO, Hideyoshi TANAKA, Shintaro YUASA, Masahiko KATO, Kazuo SODA, Masaaki KATO[A], Yoichi NINSHINO[A], Shin-ichiro TANAKA[B], and Masao KAMADA[B]

Graduate School of Engineering, Nagoya University, Furo-cho, Chikusa, Nagoya 464-8603

[A]*Nagoya Institute of Technology, Gokiso-cho, Showa, Nagoya 466-8555*

[B]*Institute for Molecular Science, Myodaiji, Okazaki 444-8585*

Recently, the $D0_3$-related pseudo-binary alloys $(Fe_xV_{1-x})_3Al$ have been received much attention because of their fascinating electronic and magnetic properties [1,2]. The alloy of the V composition $x = 0$, *i.e.* Fe_3Al is a well-ordered ferromagnetic metal of the $D0_3$ crystal structure with the Curie temperature T_C of 720 K. As the composition x is increased, T_C and magnetization of the pseudo-binary alloys are rapidly reduced, and their electrical resistivities exhibit a maximum at a temperature T_m near T_C and hence negative temperature dependence above T_m. Finally, the alloy with $x = 1/3$, *i.e.* the Heusler-type Fe_2VAl compound is in a marginally magnetic state, and its electrical resistivity shows semiconductorlike behavior suggesting an energy gap of about 0.1 eV and reaching 30 μΩm at 2 K. Low-temperature specific heat studies indicate a large enhancement of the effective electron mass and a substantial decrease in carrier concentration in Fe_2VAl. The Hall effect [3] and nuclear magnetic resonance [4] measurements also support the low carrier concentration. Several theoretical studies predict that Fe_2VAl is a nonmagnetic semimetal with a pronounced pseudogap of about 0.5 eV in its width across the Fermi level E_F [5-10]. The anomalous transport property is thought to arise from the spin fluctuation as well as the low carrier concentration rather than the existence of the band gap [1,2]. However, its ultraviolet photoelectron spectrum reveals a clear metallic Fermi edge with fairly large intensity [1,11]. Thus we have systematically investigated the valence-band photoelectron spectra of $(Fe_xV_{1-x})_3Al$ and $Fe_2VAl_{1-z}Si_z$. In $(Fe_xV_{1-x})_3Al$ with x larger than 1/3, its resistivity is higher than in Fe_2VAl, which may show a wider (pseudo)gap. In $Fe_2VAl_{1-z}Si_z$, E_F might be shifted by several hundreds meV in the rigid band model with a calculated density of states [10] at the Si composition $z = 0.2$. Here, we will report some preliminary results.

Photoelectron measurement was performed at BL-5A with a helical undulator [12], a spherical grating monochromator SGM-TRAIN [13] and a hemispherical analyzer (Omicron EA125HR) in an angle-integrated mode (the acceptance angle of 18°) under a pressure of 3×10^{-8} Pa. Specimens used in the present study were polycrystalline $(Fe_xV_{1-x})_3Al_{1-z}Si_z$ alloys prepared in the $D0_3$-related structure [1,2]. Specimens of 3 x 3 x 3 mm^3 in size were attached on a sample holder with conductive epoxy glue and cooled down to a temperature of about 80 K. Their surfaces were *in situ* cleaned with a diamond file for the photoelectron measurement. The total energy resolution was estimated to be 0.10 eV at the photon energy $h\nu$ of 40 eV and 0.12 eV at $h\nu = 75$ eV by measuring the Fermi edge of Au evaporated onto a plate of the sample holder. The origin of the binding energy *i.e.* E_F was also determined with the Au Fermi edge.

Figure 1 shows the valence-band photoelectron spectra of Fe_2VAl obtained at the first run after each cleaning procedure. The excitation photon energy $h\nu$ is indicated in the figure. The spectrum measured at $h\nu$

= 75 eV is similar to that reported so far [1]. However, a feature is noticed around the binding energy E_B of 6 eV in the spectrum obtained at $h\nu = 40$ eV. This feature seems to be attributed to the oxygen contamination due to the sample oxidation or condensation of molecules containing oxygen, and to become prominent at the low photon energy [14]. Unfortunately, we could not completely remove or prevent it in the present measurement.

The valence-band photoelectron spectra near E_F of Fe_2VAl, $(Fe_{0.62}V_{0.38})_3Al$ and $Fe_2VAl_{0.8}Si_{0.2}$ as well as Au are shown in Fig.2, where they are plotted so that the intensity may coincide with each other at $E_B \approx 0.15$ eV. As seen in the figure, no large gap can be recognized either in $(Fe_{0.62}V_{0.38})_3Al$ nor in $Fe_2VAl_{0.8}Si_{0.2}$, and the intensity at E_F is slightly low in Fe_2VAl compared with other compounds. For $Fe_2VAl_{0.8}Si_{0.2}$, these features seem consistent with a preliminary result on the temperature dependence of its resistivity, which shows a maximum at about 600 K. No indication of the gap and the relatively large intensity at E_F might show that the increase of the resistivity in $(Fe_xV_{1-x})_3Al$ with $x > 1/3$ arises from further spin fluctuation due to the lack of long range ordering. Rather sharp Fermi edge of Fe_2VAl, in comparison with Au, as well as its low intensity at E_F indicates a possibility of its low density of states above E_F [15]. Although the unoccupied states have not been investigated yet and the effect of the above-mentioned contamination is not clear, the present results suggest that the pseudogap in Fe_2VAl, if any, may be located higher in energy or its width may be smaller than expected.

References

[1] Y. Nishino *et al.*, Phys. Rev. Lett. **79**, 1909 (1997).
[2] M. Kato *et al.*, J. Phys.: Condens. Matter, *in press*.
[3] M. Kato *et al.*, J. Japan Inst. Metals **62**, 669 (1998).
[4] C.-S. Lue and Jr. J. H. Ross, Phys. Rev. B**58**, 9763 (1998).
[5] G.Y. Guo *et al.*, J. Phys.: Condens. Matter **10**, L119 (1998).
[6] D.J. Singh and I.I. Mazin, Phys. Rev. B**57**, 14352 (1998).
[7] R. Weht and W.E. Pickett, Phys. Rev. B**58**, 6855 (1998).
[8] M. Weinert and R.E. Watson, Phys. Rev. B**58**, 9732 (1998).
[9] A. Bansil *et al.*, Phys. Rev. B**60**, 13396 (1999).
[10] G. A. Botton *et al.*, Intermetallics, *in press*.
[11] K. Soda *et al.*, Jpn. J. Appl. Phys. Suppl. **38-1**, 496 (1999).
[12] S. Kimura *et al.*, J. Electron Spectrosc. Relat. Phenom., **80**, 437 (1996).
[13] M. Kamada *et al.*, Rev. Sci. Instrum. **66**, 1537 (1995).
[14] J.J. Yeh and I. Lindau, Atomic Data and Nuclear Data Tables **32**, 1 (1985).
[15] T. Sato *et al.*, Phys. Rev. Lett. **79**, 2254 (1999).

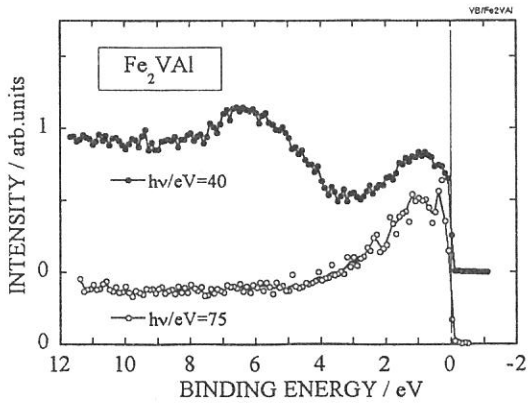

Fig.1 Valence-band photoelectron spectra of Fe_2VAl.

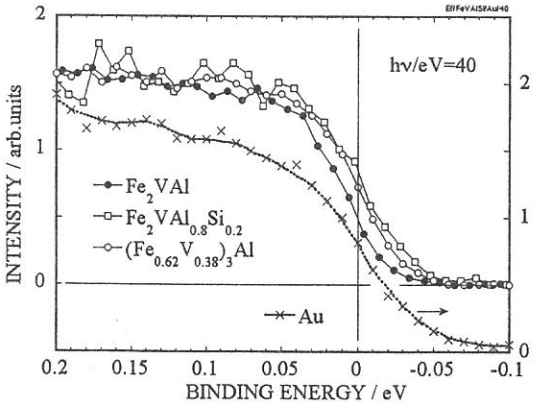

Fig. 2 Photoelectron spectra near the Fermi level.

(BL-5B)

Electronic Structures of Organic Salt DMTSA-BF_4 Using Photoelectron Spectromicroscopy

Yuichi HARUYAMA, Toyohiko KINOSHITA[A], Kazuo TAKIMIYA[B], Tetsuo OTSUBO[B], Chikako NAKANO[C] and Kyuya YAKUSHI[C]

Labortory of Advanced Science and Technology for Industory, Himeji Institute of Technology, 3-1-2 Kouto, Kamigori, Ako 678-1205

[A]*Synchrotron Radiation Laboratory, Institute for Solid State Physics, University of Tokyo, Tokyo 106-8666*

[B]*Faculty of Engineering, Hiroshima University, 1-4-1, Kagamiyama, Higashi-Hiroshima, 739-8527*

[C]*Institute for Molecular Science, Myodaiji, Okazaki 444-8585*

The 1:1 charge-transfer organic salt DMTSA-BF_4, where DMTSA is 2,3-dimethyltetraseleno-anthracene, have attracted the interest of many researchers because of the high electrical conductivity and metallic physical properties [1]. The electrical resistivity of DMTSA-BF_4 decreases from the room temperature to ~150K with a positive slope and DMTSA-BF_4 behaves as a metal. At about 150K the metal insulator transition is caused and the electrical resistivity below ~150K turn to increase with a negative slope as an insulator. It has been considered that the 1:1 charge-transfer salt becomes a Mott insulator due to the Coulomb interaction since the 1:1 charge-transfer salt has half-filled band. The origin of the metallic physical properties is not clear at present. In order to obtain the information on the electronic structures such as the band structure, density of states, and the orbital characters, we have performed the photoemission experiments for the organic salts DMTSA-BF_4. Since the size of DMTSA-BF_4 is not large enough to carry out the ordinary photoemission experiments, we used the photoelectron spectromicroscopy instrument as reported in Ref. 2.

Photoemission experiments were carried out by using a conventional UHV system (FISONS, ESCALAB-220i-XL) at a base pressure of 2×10^{-8} Pa [2]. Total instrumental energy resolution was 0.3~0.6 eV full width at half maximum (FWHM), depending on the photon energy ($h\nu$) in the energy range of 30~100 eV. Needlelike shaped single crystals of DMTSA-BF_4 and DMTSA were synthesized by electrochemical reduction [1]. The typical sample size used here was less than $2\times0.2\times0.1\mu m^3$. These samples were characterized by x-ray diffraction, electrical resistivity, magnetic susceptibility and ESR measurements [1]. The clean surface was obtained by scraping the sample surface using an edge of a razor. The cleanliness was confirmed by x-ray photoemission spectroscopy for the absence of extra features arising from the contaminations.

Figure 1(a) shows the photon energy dependence of the photoemission spectra for DMTSA-BF_4. From the photon energy dependence of the photoionization cross-section, the atomic orbital characters of the observed spectral features are determined. The features at ~1 eV, ~3 eV, and ~6 eV are predominantly derived from Se 4*p* states. The broad feature at ~8 eV is predominantly derived from C 2*p* and F 2*p* states. The features between 12 and 18 eV are predominantly from Se 4*s* and C 2*s* states. As shown in Fig. 1(b), the clear Fermi edge was not observed. It is suggested from the previous polarized reflection experiment [1] that DMTSA-BF_4 has a pseudo-one-dimensional band structure. No clear Fermi edge may be due to one dimensional electronic

structure for DMTSA-BF_4. In Figure 2, the Se 3*d* core-level photoemission spectrum for DMTSA-BF_4 is compared with that for DMTSA. The Se 3*d* core-level photoemission spectrum for DMTSA-BF_4 showed the tail at the higher binding energy side as compared with that for DMTSA. Although the difference of the Se 3*d* core-level photoemission spectra between DMTSA and DMTSA-BF_4 is not clear at present, there are some possibilities that the tail originates from the Doniach-Sunjic tail by the metallic nature and another component such as the different charge state and/or the surface component.

References

[1] J. Dong, K. Yakushi, K. Takimiya and T. Otsubo, J. Phys. Soc. Jpn. **67**(1998)971.

[2] T. Kinoshita, K. G. Nath, Y. Haruyama, M. Watanabe, S. Yagi, S. Kimura, and A. Fanelsa, J. Electron Spectrosc. Relat. Phenom. **92**(1998)165; T. Kinoshita, K. G. Nath, M. Watanabe, S. Yagi, S. Kimura, and A. Fanelsa, UVSOR Activity Report 1996, p.154.

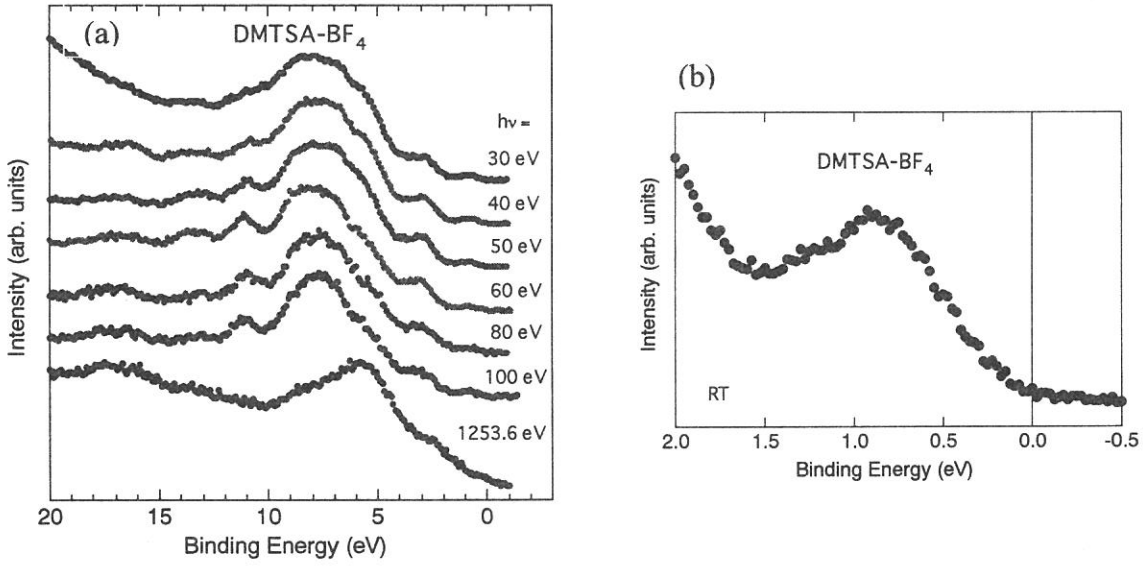

Figure 1 (a) The photon energy dependence of the photoemission spectra for DMTSA-BF_4. (b) The photoemission spectrum near the Fermi level. The detection area was ϕ50 μm.

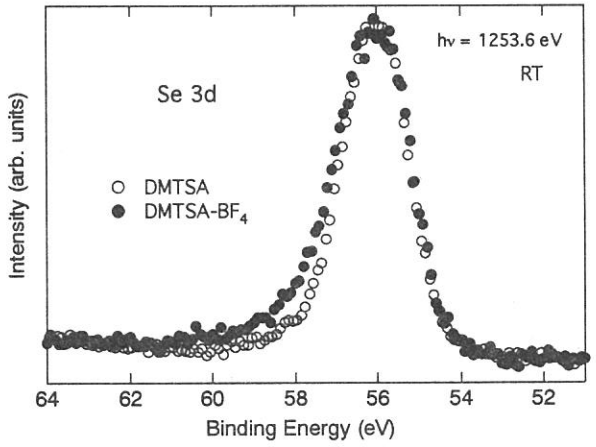

Figure 2 The Se 3*d* core-level photoemission spectra for DMTSA-BF_4(closed circles) and DMTSA(open circles). The detection area was ϕ50 μm.

(BL5B)

Photoelectron spectroscopic study on photo-induced phase transition in a spin crossover complex $Fe(2\text{-}pic)_3)Cl_2EtOH$

Masao Kamada, Yoichiro Doi,[A] Kazutoshi Fukui,[B] Yuichi Haruyama,[C] Syuji Asaka,[D] Takeshi Tayagaki,[E] Naoki Yonemura,[E] and Kouichiro Tanaka[E]

UVSOR Facility, Institute for Molecular Science, Okazaki 444-8585
[A] College of Engineering, Fukui University, Fukui 910-8507
[B] VUV-PhotoScience, Institute for Molecular Science, Okazaki 444-8585
[C] LASTI, Himeji University, Hyogo 678-1201
[D]Equipment Develop Center, Institute for Molecular Science, Okazaki 444-8585
[E]Faculty of Science, Kyoto University, Kyoto606-8502

In recent years, photon-induced phenomena attract much interest. For examples, photon excitation changes the crystal structures, magnetic and optical properties, and so on. These new phenomena are called as photo-induced phase transitions, which are expected to produce new properties of condensed matters.

In order to investigate the photo-induced phase transitions, optical spectroscopic techniques such as optical absorption and reflection have been mostly used, since these techniques can monitor the phenomena in a fast time domain. However, these techniques have some limitation. For examples, only narrow energy range in the valence electrons can be observed by the optical spectra. The purpose of the present study is to investigate the photo-induced effects on electronic states in wide energy range using photoelectron spectroscopy. We have been developing new techniques based on the combination of synchrotron radiation and laser in recent years. We will show the application of the technique to the present purpose.

Experiments have been carried out at a beam line BL5B, where a plane-grating monochromator provides photons in a wide energy range from 6 to 260 eV with a moderate resolving power and intense fluxes. A VG-microESCA system , which consists of XPS and UPS components with multi-channel detectors, was installed to this beamline during our beam time. A single crystal of $[Fe(2\text{-}pic)_3]\ Cl_2EtOH$ was grown at Kyoto university and was filed in a preparation chamber. The sample was attached on the holder of a flow-type He cryostat and was cooled down to about 40 K. The cw Ar^+ laser light was introduced in an analyzing chamber using an optical fiber to excite the sample during photoelectron measurements.

Figure 1 shows XPS spectra of Cl-2p states of $Fe(2\text{-}pic)_3]Cl_2EtOH$. Solid and broken lines represent the spectra observed at room temperature and 40K, respectively, while a dotted line shows the spectrum with laser excitation at 40K. It

is noted that the spectra are shifted to higher binding-energy side with cooling the sample, but no photo-induced effect is observed on Cl-2p state. Figure 2 shows N-1s spectra obtained under the same condition. It is obvious that the N-1s spectra are shifted to lower binding-energy side with cooling the sample and laser excitation causes the shift of N-1s to higher binding-energy side. The photo-induced spectrum at 40K is also in good agreement with the spectrum observed at RT. On the other hand, photoelectron spectra of Fe element, for examples Fe-3d spectra, are very complicate to explain (not shown here). The spectral structures were remarkably changed with temperature and laser excitation. The photo-induced spectrum at 40K is not agreement with that observed at RT.

It has been believed from the optical spectroscopic studies that $Fe(2\text{-pic})_3]$ Cl_2EtOH shows high-spin and low-spin states in Fe ions at RT and low temperatures, respectively, and that the low-spin state (low-temperature phase) is changed by photo-excitation to the high-spin state (high-temperature phase). However, the present experimental results indicate that the photo-induced phase transition of $Fe(2\text{-pic})_3]$ Cl_2EtOH is closely related to both Fe and N ions and is more complicate and interesting co-operative phenomenon.

Fig. 1. Photoelectron spectra of Cl-2p level in $Fe(2\text{-pic})_3]$ Cl_2EtOH. Solid and broken lines show the spectra at 40K and RT, respectively, while a dotted line represents the spectrum induced by laser excitation at 40K.

Fig. 2. Photoelectron spectra of N-1s level in $Fe(2\text{-pic})_3]$ Cl_2EtOH . Solid and broken lines show the spectra at 40K and RT, respectively, while a dotted line represents the spectrum induced by laser excitation at 40K.

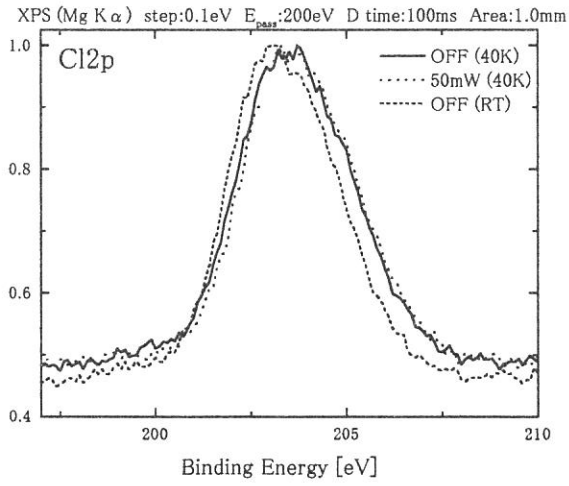

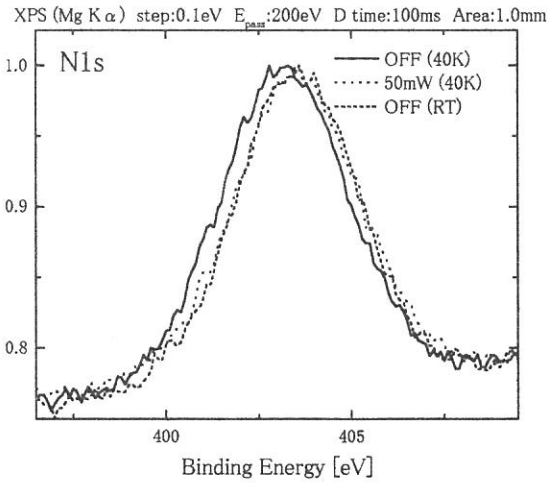

(BL-5B)

A Combined Study of Photoelectron Specrtomicroscopy and Laser Annealing For Si(111) Clean Surface

Yuichi HARUYAMA, Toyohiko KINOSHITA[A], Shin-ichiro TANAKA[B], Hideo MAKINO[C], Katsuo WADA[C], and Shinji MATSUI

Labortory of Advanced Science and Technology for Industory, Himeji Institute of Technology, 3-1-2 Kouto, Kamigori, Ako 678-1205

[A]*Synchrotron Radiation Laboratory, Institute for Solid State Physics, University of Tokyo, Tokyo 106-8666*

[B]*Faculty of Science, Nagoya University, Furo-cho, Chikusa-ku, Nagoya 464-8602*

[C]*Silicon Technology LTD, 897-20 Kyowa, Mochizuki, Kitasaku-gun, Nagano 384-2204*

The photoelectron spectromicroscopy is one of the attractive methods to investigate the electronic structure for various materials because a lot of applied usages are possible as compared with the ordinary photoelectron spectroscopy [1]. One of the advantages of the photoelectron spectromicroscopy is to measure the specific small area of the sample. Making the most of the advantage, we have performed the combined study of the photoelectron spectromicroscopy and the laser annealing. A merit of the laser annealing is that it is possible to anneal the specific small area of the sample by irradiating the focused laser light to the sample with less degassing and without the heating unit in the vacuum. In addition, the effect of the electric field used to keep the sample to high temperature is not needed if we use the laser annealing. Therefore, it is considered that the electronic structure at high temperature can be easily measured. As a typical example of the laser annealing, we report the electronic structure at high temperature for the Si (111) surface.

Figure 1(a) shows the experimental setup. Photoelectron spectromicroscopy experiments were carried out by using a conventional UHV system (FISONS, ESCALAB-220i-XL) at a base pressure of 2×10^{-8} Pa [1]. Total instrumental energy resolution at room temperature was 0.1~1.0 eV full width at half maximum, depending on the photon energy ($h\nu$) in the energy range of 21.2~1486.6 eV. The clean surface was obtained by annealing the sample at ~1200°C using the laser light irradiation ($h\nu$ = 1.165 eV) and checked by x-ray photoemission spectroscopy and LEED as shown in Figure 1(b). The temperature of the sample was measured with an optical pyrometer.

Figure 2(a) shows the temperature dependence of the photoemission spectra for n-Si (111) surface (P-dope, 9-14Ω) from room temperature to ~1200°C. At room temperature, three surface states were observed at ~0.2, ~0.8 and ~1.8 eV. With increasing the annealing temperature, the surface state at ~0.8 eV disappears. The temperature dependence of the spectral features obtained in our measurements is essentially identical to that previously obtained by Yokotsuka et al. [2]. However, we found that the shift of the photoemission spectra was observed at ~0.2 eV higher binding energy side under 0.04~0.89 W laser irradiation. With increasing the annealing temperature, the shift disappears at the laser power of 2.00 W. The shift at ~0.2 eV higher binding energy side was also observed at the Si 2p core level photoemission spectra as shown in Figure 2(b). It is considered that the observed rigid shift is caused by the surface photovoltage effect [3] induced by the laser irradiation.

Although we introduced the electronic structure at high temperature for the Si(111) surface, a lot of materials and surface systems cause the phase transition at high temperature. The combined study of the photoelectron spectromicroscopy and the laser annealing would become an effective method to investigate the electronic structure at high temperature.

References

[1] T. Kinoshita, K. G. Nath, Y. Haruyama, M. Watanabe, S. Yagi, S. Kimura, and A. Fanelsa, J. Electron Spectrosc. Relat. Phenom. **92**(1998)165; T. Kinoshita, K. G. Nath, M. Watanabe, S. Yagi, S. Kimura, and A. Fanelsa, UVSOR Activity Report 1996, p.154.

[2] T. Yokotsuka, S. Kono, S. Suzuki and T. Sagawa, Solid State Commun. **39**(1991) 1001.

[3] J. E. Demuth, W. J. Thompson, N. J. DiNardo and R. Imbihl, Phys. Rev. Lett. **56** (1986) 1408.

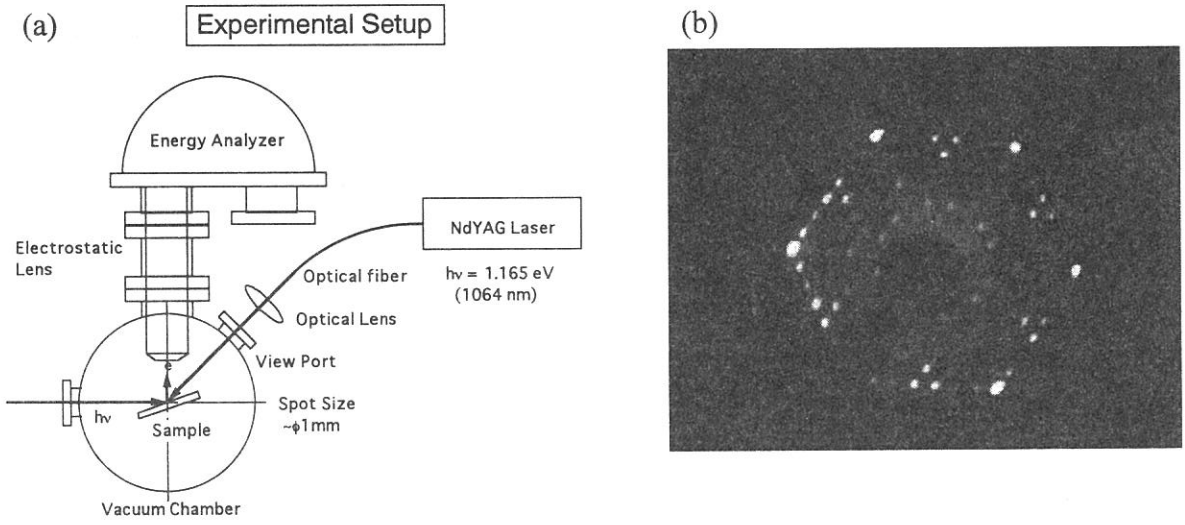

Figure 1(a) Schematic experimental setup. (b) A LEED pattern observed at ~54 eV electron energy after ~1200°C laser annealing.

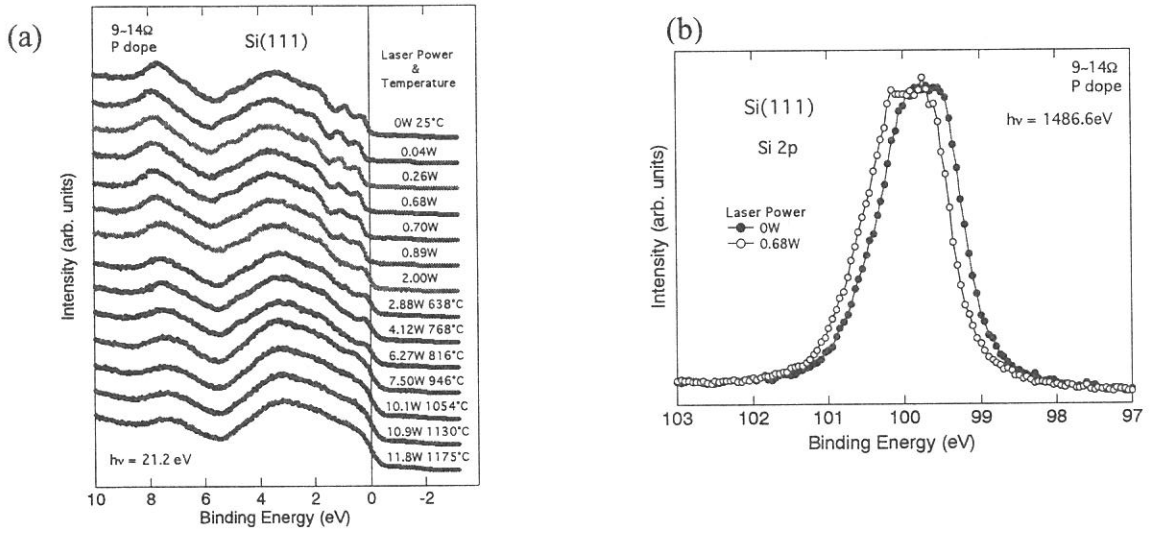

Figure 2(a) The temperature dependence of the photoelectron spectra in the valence band region for n-Si (111) surface. (b) Si 2p core level photoelectron spectra of n-Si (111) with and without laser irradiation.

(BL6A2)

Angle-resolved Photoelectron Spectroscopy of Si(111)-2√7x3-(Pb,Sn) Surface

J. Yuhara, K. Soda [1], S. Yuasa [1], O. Yoshimoto, K. Morita, M. Kamada [2]

Dept. of Cryst. Mat. Sci., School of Eng., Nagoya Univ., Chikusa-ku, Nagoya, 464-8603

[1] *Dept. of Nucl. Engineering, School of Eng., Nagoya Univ., Chikusa-ku, Nagoya, 464-8603*

[2] *Institute for Molecular Science, Myodaiji, Okazaki 444-8584*

Recently, it has been shown by means of LEED, AES, and RBS techniques that binary metal adsorbates of Pb and Sn on the Si(111) surface form a Si(111) 2√7x3-(Pb,Sn) surface at both Pb and Sn coverages of 0.5ML (1ML for Si(111) face = 7.8×10^{14} atoms/cm^2). STM images of the 2√7x3-(Pb,Sn) surface showed that there exist constant bright lines along [101] direction at both empty and filled states. The 2√7x3-(Pb,Sn) surface intrinsically has domain boundary, as shown in Fig.1. In this paper, ARUPS of the 2√7x3-(Pb,Sn) surface has been performed to study the dispersion relationship of the bright lines, with use of "single" domain 2√7x3-(Pb,Sn) surface .

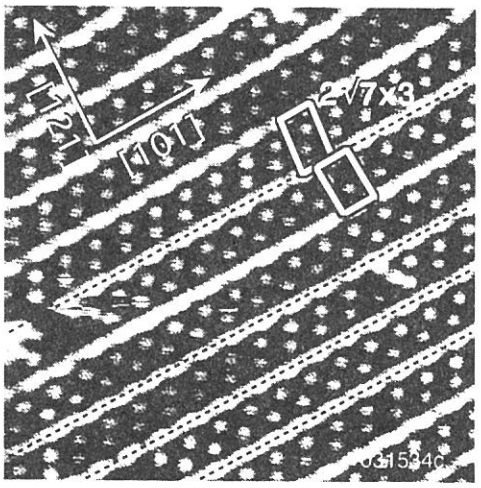

Fig.1 STM image of the Si(111)2√7x3-(Pb,Sn) surface at sample bias of -1.0eV. Dotted lines are domain boundary.

All the experiments were performed in the UHV chamber (8×10^{-10} Torr) at BL6A2. For ARUPS measurements, we used excitation photon energy of 26.1eV. The energy resolution and angular resolution at ARUPS measurements were 0.15eV and 1°, respectively. Specimens used were mirror-polished n-type Si(111) wafers with a miscut angle of ~2°. The "single" domain 2√7x3-(Pb,Sn) surface was prepared as followed. First, Sn of 0.8ML was deposited onto the Si(111)-7x7 surface at RT, and annealed at 550°C for 5min to form the 2√3x2√3+√3x√3-Sn surface at the Sn coverage of 0.5ML. Next, Pb of 0.8 ML deposited onto the 2√3x2√3+√3x√3-Sn surface was annealed at 300°C for 2 min.

A LEED pattern of the "single" domain 2√7x3-(Pb,Sn) surface is shown in Fig.2. The other domains are hardly seen. Surface Brillouin zones (SBZs) of the single domain 2√7x3 surface and 1x1 surface are shown in Fig.3. Symbols are 1x1 symmetry points. Typical spectra along the [101] direction are shown in Fig.4. The dispersion relationships along the [101] direction and [121] direction are shown in Fig.5 (a) and (b). Gray lines represent the projected bulk bands of the Si structures. Unique 2√7x3-(Pb,Sn) surface bands of S1 and S2 are clearly seen. The S1 band has peaks at Γ and K points, and the S2 band has peak at M point. The periodicity of S1 band does not match SBZs of both 2√7x3 and 1x1. Since there is no surface band across the Fermi level, the Si(111) 2√7x3-(Pb,Sn) surface is not metallic but semiconducting.

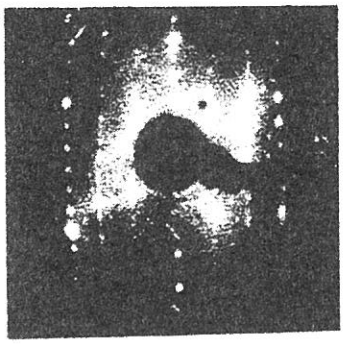

Fig.2 LEED pattern of a "single" domain Si(111)2√7x3-(Pb,Sn) surface.

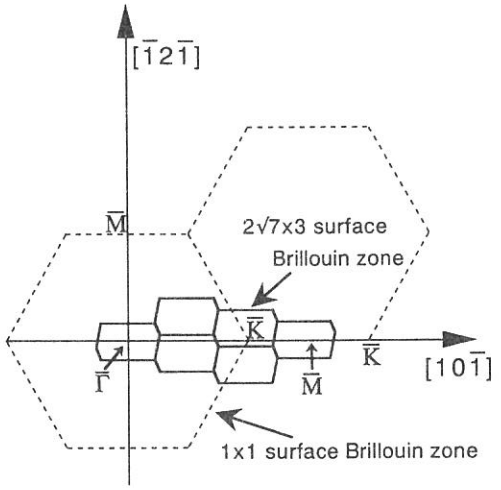

Fig.3 Surface Brillouin zones (SBZs) of the single domain Si(111)2√7x3-(Pb,Sn) surface and Si(111)1x1 surface.

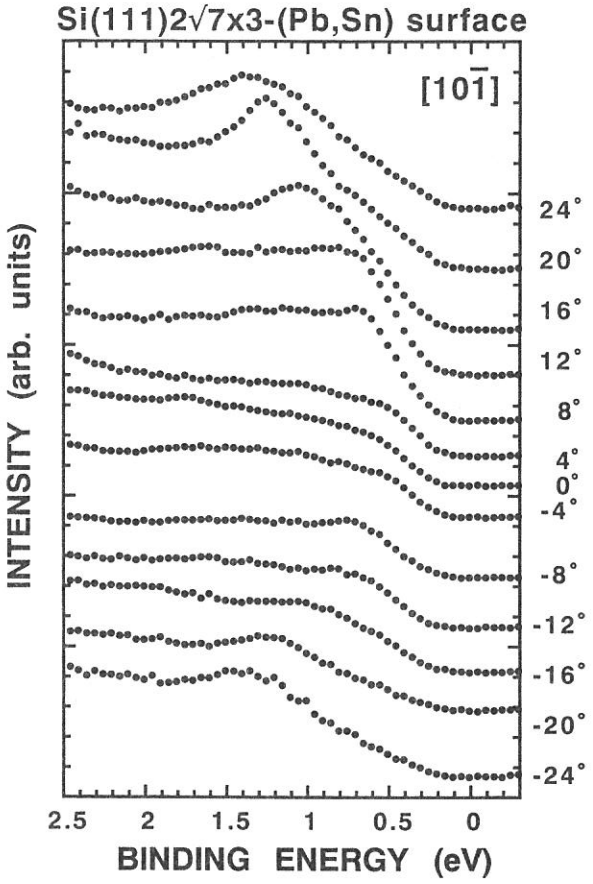

Fig.4 Typical ARUPS spectra for the "single" domain Si(111)2√7x3-(Pb,Sn) surface measured along the [101̄] direction.

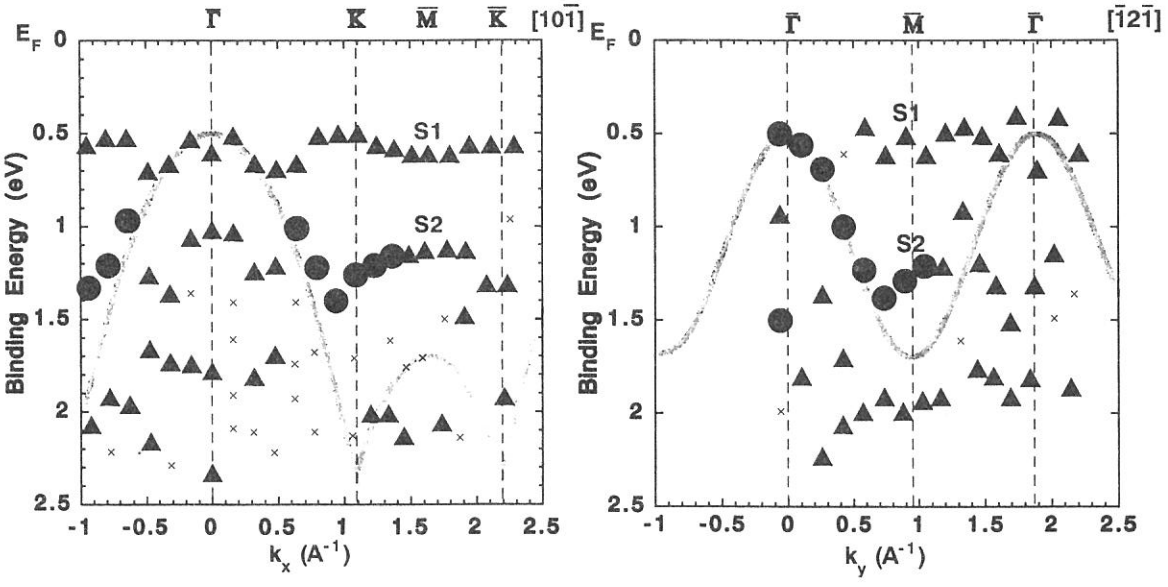

Fig.5 Band dispersion relationship along the [101̄] direction (a) and along the [1̄2̄1̄] direction (b).

(BL7A)

Structural analysis of molybdena/silica-alumina by means of Mo L_{III}-edge XANES

Hirofumi Aritani, Osamu Fukuda, Takashi Nishio, Hideyuki Yamane, and Seiichiro Imamura

Faculty of Engineering and Design, Kyoto Institute of Technology, Sakyo-ku, Kyoto 606-0962

Molybdenum-containing heterogeneous catalysts for olefin metathesis have been a great interest since Banks et al.[1] had reported the first observation. It is accepted fundamentally that reduced Mo ions such as Mo^{4+} and/or Mo^{5+} need to exist as the active center for metathesis. In the case of molybdenum-containing oxide catalysts, reductive pretreatment (with H_2 or CO) needs generally to reduce Mo^{6+} ions. However, we proposed previously that MoO_3/SiO_2-Al_2O_3 catalysts exhibit high activity for propene metathesis even at room temperature without reductive pretreatment.[2] In order to obtain the structural information details about the active molybdenum species for metathesis, the Mo L_{III}-edge XANES was applied to the supported molybdena systems. The XANES spectrum probes the orbitals of 4*d* character participating in the Mo-O bonds. The white lines of the spectrum are split, corresponding to the ligand field splitting of Mo 4*d* orbitals.[3]

Supported molybdenum catalyst samples were prepared by impregnation of each metal oxide support with an aqueous solution of ammonium heptamolybdate ($(NH_4)_6Mo_7O_{24}\cdot 4H_2O$) or acetone solution of bis(acetylacetonato)dioxomolybdenum ($MoO_2(acac)_2$). The oxide supports were SiO_2 (Aerosil), γ-Al_2O_3 (Nacalai, calcined at 873 K), and amorphous SiO_2-Al_2O_3 containing 28.6 wt% (JRC-SAH-1, indicated as SAH-1) and 13.8 wt% (JRC-SAL-2, indicated as SAL-2) Al_2O_3. The impregnating solution was stilled at room temperature and evaporated at 343 K for 6 h, and then, the paste was dried for overnight and calcined at 773 K for 6 h. The Mo *L*-edge XANES spectra were collected on a facility of BL-7A station of soft X-ray beam line at UVSOR, in the Institute for Molecular Science with 750 MeV of a ring energy. Each powdery sample was mounted on a carbon-tape, and then attached on a beryllium-copper dynode which was set to the first-stage of electron multiplier placed into a vacuum chamber. After the chamber had been evacuated ($< 3.0\cdot 10^{-7}$ Torr), the spectrum was recorded in a total electron yield (TEY) mode at room temperature, using the Ge(111) double-crystal monochromator ($2d$ = 0.6532 nm). The photon energy was calibrated by using Mo metal sample at Mo L_{III}-edge (2520 eV).

MoO_3/SiO_2-Al_2O_3 exhibit high activity for propene metathesis even at 293 K without reductive pretreatment, as described above. The metathesis reactivity (at 293 and 473 K) is summarized as (MoO_3/SAH-1 > MoO_3/SAL-2 > MoO_3/Al_2O_3 > MoO_3/SiO_2). Molybdena-rich MoO_3/SAH-1 (7.5 - 10.0 wt% as MoO_3) shows the highest catalytic activity. By the results of UV-Vis and ESR, it is concluded that molybdenum ions on SAH-1 can be easily reduced to form active species even by contact with propene, and thus, it shows a high activity without reductive pretreatment. The Mo L_{III}-edge XANES (TEY mode) of supported molybdena samples and reference compounds are shown in Fig. 1. The detailed interpretation of the spectra was described elsewhere.[4] In the case of MoO_3/SiO_2 and MoO_3/Al_2O_3 (prepared by means of AHM), tetrahedral Mo-O_4

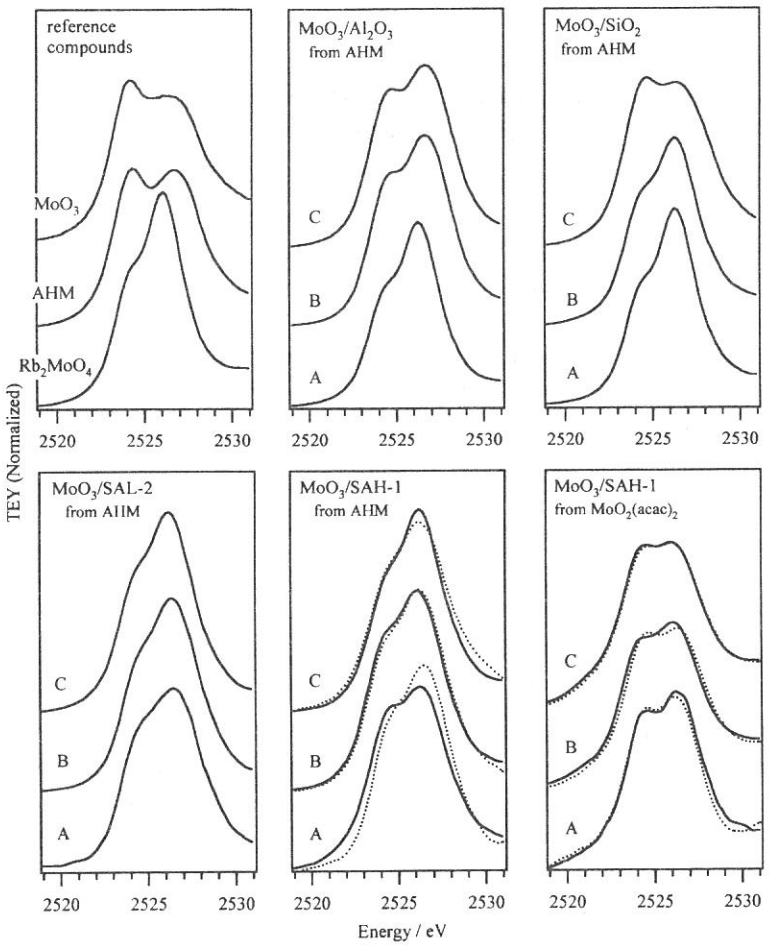

Fig. 1 Mo L_{III}-edge XANES of supported molybdena samples and reference compounds. Contents of MoO_3 are (A) 2.5, (B) 7.5, and (C) 15.0 wt%. Dotted lines are the spectra of each sample after the metathesis reaction at 293 K.

species are dominant at a low MoO_3 content (2.5 wt%). With an increase in MoO_3 content, polyanion-like Mo-O_6 octahedra coexist with tetrahedra. For 15.0 wt% MoO_3/SiO_2, the octahedral species exist mainly. These results support the conclusion reported previously by several workers.[5] On the other hand, the molybdena species supported on SiO_2-Al_2O_3 (SAH-1 and SAL-2) is almost occupied by the tetrahedron even at the higher MoO_3 contents. It is likely that the molybdena species in 2.5 wt% MoO_3/SiO_2-Al_2O_3 contains poly-anion-like octahedra partly, and it is almost absent after the catalytic reaction. For 7.5 and 15.0 wt% MoO_3/SAH-1, structural change of tetrahedral species is scarcely brought about by the reaction. It can be suggested that the formation of the bulk MoO_3 phase and/or large polyanion clusters proceeds hardly on SiO_2-Al_2O_3 because of peculiar support-interaction as reported.[6] In contrast, the polyanion-like octahedra coexist with tetrahedra on SAH-1 when $MoO_2(acac)_2$ is employed as the precursor. The structure of these species is little affected by the reaction. The study of the structural difference between these MoO_3/SAH-1 samples prepared from AHM and $MoO_2(acac)_2$ is now in progress.

We acknowledge Dr. E. Shigemasa and staffs of UVSOR for helpful assistance and support of the works in the BL-7A beamline.

1 R. L. Banks and G. C. Bailey, *Ind. Eng. Chem., Prod. Res. Develop.*, **3**, 170 (1964).

2 H. Aritani et al., *Chem. Lett.*, in press.

3 J. Evans et al., *J. Phys. Chem.*, **95**, 9673 (1991).

4 H. Aritani et al., *UVSOR Activity Report*, 1996, 208.; H. Aritani et al., *UVSOR Activity Report*, 1997, 210.; H. Aritani et al., *J. Phys. Chem.*, **100**, 19495 (1996).

5 H. Shimada et al., *J. Catal.*, **138**, 746 (1992).; H. Praliaud, In *Proc. 2nd International Conference on Chemistry and Uses of Molybdenum*, Climax Molybdenum Co., London, p. 195 (1976).

6 S. Rajagopal et al., *J. Catal.*, 147, 417 (1994).; S. Rajagopal et al., *J. Catal.*, 151, 192 (1995).

(BL7A)

Structural Analysis of Oxygen-coordinated Al(III) in Mullite by Means of X-ray Absorption Fine Structure

Hikoshiro ICHIHASHI, Shuji MATSUO, Tsutomu KURISAKI,
Takushi YOKOYAMA[1], and Hisanobu WAKITA*

Department of Chemistry, Faculty of Science, Fukuoka University, Nanakuma, Jonan-ku, Fukuoka 814-0180, Japan
[1]*Department of Chemistry, Faculty of Science, Kyushu University, Hakozaki, Higashi-ku, Fukuoka 812-8581, Japan*

*Corresponding author: wakita@SUNSP1.sc.fukuoka-u.ac.jp

Introduction

Light metal oxides are noticed as functional materials recently, and applied for ceramics and various catalyses. In particularly, aluminosilicate minerals as the light metal oxides are used well as materials of ceramics. However, the aluminosilicate minerals have not been made a fundamental study in detail, especially for a correlation between coordination and electronic structures around Al(III) or Si(IV), though there are aluminosilicate minerals with various oxygen-coordinated Al(III) in nature. We have investigated the electronic structures around Al(III) in the aluminosilicate minerals by an X-ray absorption fine structure (XAFS) method. A region of X-ray absorption near edge structure (XANES) on XAFS spectrum is useful to contain the structural information of the electronic state around an absorbing atom. In previous studies, we carried out the Al *K*-edge XAFS measurement for anorthite [$CaAl_2Si_2O_8$: four-coordinated to Al(III)], andalusite [Al_2SiO_5 : five- and six- (1 : 1) coordinated to Al(III)], and kaolinate [$Al_2Si_2O_5(OH)_4$: six-coordinated to Al(III)] in a series of aluminosilicate minerals, and obtained the relationship between the features of the XANES spectra for Al(III) in their aluminosilicate minerals and the coordination number around the Al(III). In this study, we investigate the structure around the Al(III) in mullite, one of a series of aluminosilicate minerals, by the XAFS method with being based on the result mentioned above. Strength of ceramics made of mullite depends on the structure and composition of mullite. However, the structure of mullite has been insufficiently studied, since mullite has a complicating structure. Therefore, it is worth study to reveal the structure of mullite.

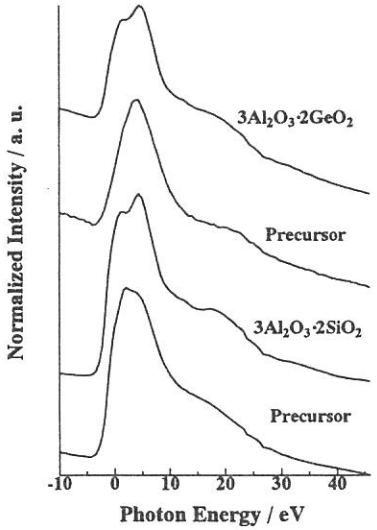

Fig. 1. Al K XANES spectra of noncrystalline mullites and noncrystalline mullite precursors.

Experimental

The Al *K* XAFS measurements were carried out at the BL7A of UVSOR in the Institute for Molecular Science. Two YB_{66} crystals as a monochromator are used combining with Si mirror. The storage ring was operated at 750 MeV. All of XANES spectra were measured by the total electron yield method. The samples in powder were mounted on CuBe photo dynode, and were attached to the photomultiplier tube. A series of mullites were prepared by adsorption of silicic acid on aluminium hydroxide. The detailed preparation method is described in a previous paper[1]. All samples (noncrystalline mullite precursors and noncrystalline mullites) are represented in terms of their composition as $3Al_2O_3 . 2(Si_xGe_{1-x}O_2)$.

Table 1. The enegy values of the Al K edge for $3Al_2O_3 \cdot 2(Si_xGe_{1-x}O_2)$ noncrystalline Mullites.

Composition	First peak(eV)	Second peak(eV)
Ge only	1.6271	4.4276
Si : Ge = 1 : 5	1.3179	4.7308
Si : Ge = 1 : 5	1.6271	3.8803
Si : Ge = 1 : 5	1.3043	4.7308
Si : Ge = 1 : 5	1.6271	3.8803
Si : Ge = 1 : 5	1.3179	4.7308
Si only	1.6271	4.4276

Results and discussion

Main peak positions on the Al K XANES spectra of a series of noncrystalline mullites and noncrystalline mullite precursors are presented in Fig. 1 and 2. In Fig. 1 and 2, the energy of abscissa axis was normalized with respect to the first peak top of aluminium metal as 0 eV. All of the XANES spectra of a series of model aluminosilicates present one maximum when aluminium is tetracoordinated, and two maxima when aluminium is hexacoordinated[2]. Their spectra of noncrystalline mullite precursors are not clearly observed two maxima, but their features are present an inflexion points in the spectra. Therefore, we conclude that all spectra contain two peaks, and the Al atoms of their noncrystalline mullites and noncrystalline mullite precursors are hexacoordinated.

Table 1 shows the peak top energy value of Al K edge for all samples. It was reported that slight variations in positions of the first maximum can be related to the Al-O bond character[3]. Their first maximum peak exists the slight variations, but the tendency of variations can not be explained satisfactorily. It is maybe due to the limit of the energy resolution of the beamline. Therefore, in our measurements, it is difficult to discuss the term of energy shift.

Fig. 3 shows the Fourier transformed EXAFS spectra of six samples. For gibbsite, the Fourier transformed EXAFS spectrum shows clearly the presence of the second neighbor atoms at about 3 Å. But all of the others do not show them clearly, and the comparison of thier first peaks didn't shift. It is maybe due to the limit of the energy resolution of the beamline. Because we consider that the Al-O distance of noncrystalline mullites and noncrystalline mullite precursors arise from compositional variation of silicon and germanium.

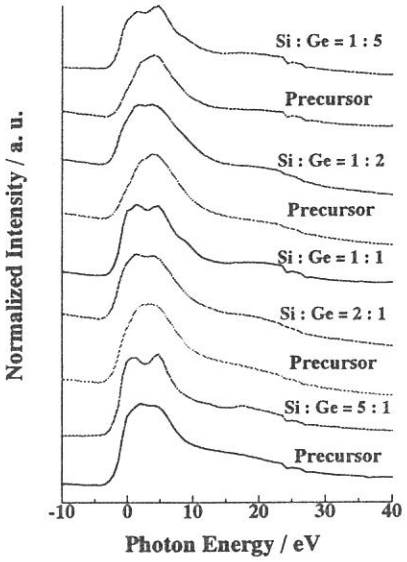

Fig. 2. Al K XANES spectra of noncrystalline mullites and noncrystalline mullite precursors. The compositions of them are represented as $3Al_2O_3 \cdot 2(Si_xGe_{1-x}O_2)$.

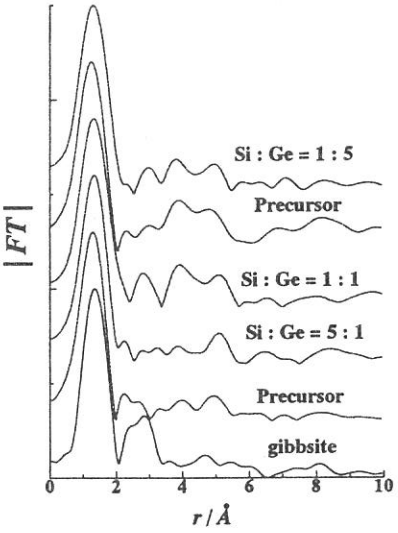

Fig. 3. The Fourier transforms of a series of noncrystalline mullites and noncrystalline mullite precursors. The com positions of them are represented as $3Al_2O_3 \cdot 2(Si_xGe_{1-x}O_2)$.

Conclusion

The Al K XANES spectra of a series of noncrystalline mullites and noncrystalline mullite precursors were measured. All Al atoms of them are hexacoordinated. The Fourier transformed EXAFS spectra of six samples derived, and the spectra didn't obtain a significant tendency. Further theoretical study is required.

References

1) Y. Ikeda, T. Yokoyama, S. Yamashita and H. Wakita, *Jpn. J. Appl. Phys.*, 32 (1993) 670-672.
2) J. Wong, Z. U. Rek, M. Rowen, T.Tanaka, F. Schäfers, B. Müller, G. N. George, I. J. Pickering, G. Via, B. DeVries, G. E. Brown Jr and M Fr ba, *Phys.*B 208&209 (1995) 220-222.
3) D. J. Jones, D. Grandjean and A. M. Flan *J. Non-crs. So.*, 147&148, (1992) 134-140.

(BL7A)

Analysis of Local Structure around Al(III) and Si(IV) in Mullite Containing Gerumanium(IV) by means of X-ray absorption fine structure

Hikoshiro ICHIHASHI, Shuji MATSUO, Kaori SHIROUZU, Tsutomu KURISAKI, Takushi YOKOYAMA[1], and Hisanobu WAKITA*

Department of Chemistry, Faculty of Science, Fukuoka University, Nanakuma, Jonan-ku, Fukuoka 814-0180, Japan
[1]Department of Chemistry, Faculty of Science, Kyushu University, Hakozaki, Higashi-ku, Fukuoka 812-8581, Japan

*Corresponding author: wakita@SUNSP1.sc.fukuoka-u.ac.jp

Introduction

Mullite is one of the aluminosilicates, and is excellent material for functional ceramics. The strength and crystallinity of the ceramics change by the ratio of Al (III) with Si (IV) and/or calcination temperature of mullite. As described in the UVSOR Activity report in 1998 and 1999, the Al *K* X-ray Absorption Near edge Structure (XANES) spectra of a series of model aluminosilicates, noncrystalline mullites and noncrystalline mullite precursors $\{3Al_2O_3 \cdot 2(Si_XGe_{1-X}O_2)\}$ were measured and analyzed in terms of Al-O distances and their bond characters. In particular, for noncrystalline mullites and noncrystalline mullite precursors $\{3Al_2O_3 \cdot 2(Si_XGe_{1-X}O_2)\}$, we conconcluded that the character changes of the mullites are particularly due to the change of Al-O bond character with the composition change of silicon and germanium. In this study, the Si *K* XANES spectra of a series of noncrystalline mullites and noncrystalline mullite precursors $\{3Al_2O_3 \cdot 2(Si_XGe_{1-X}O_2)\}$ were measured and discussed the electronic structures, especially, the properties of $3Al_2O_3 \cdot 2(Si_XGe_{1-X}O_2)$ mullites with the changes of Al-O, Si-O bond character were discussed.

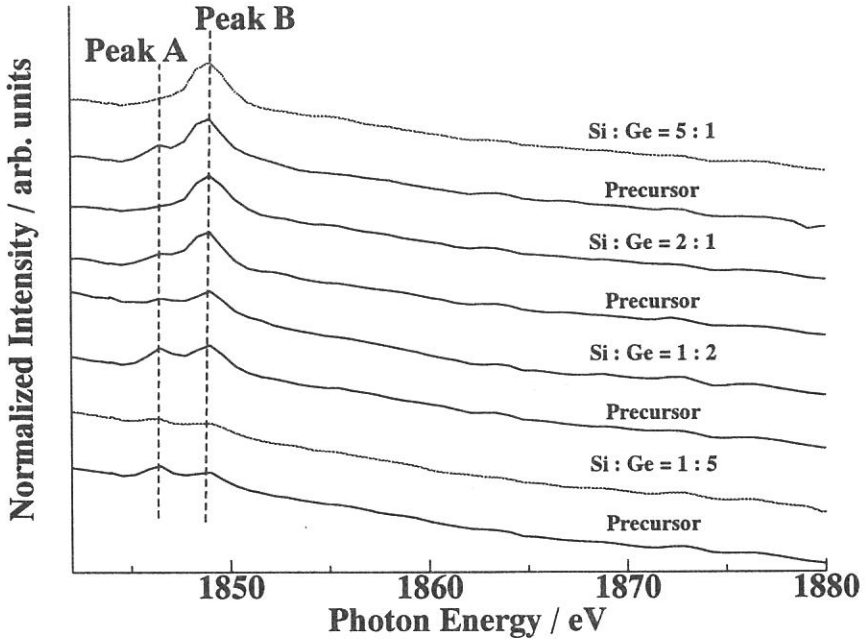

Fig. 1 Si *K* XANES spectra of a series of $3Al_2O_3 \cdot 2(Si_XGe_{1-X}O_2)$ noncrystalline mullites and noncrystalline mullite precursors.

Experimental

The Si *K* XANES spectra were measured at the BL7A in the UVSOR of the Institute for Molecular Science (Okazaki, Japan), a crystal monochromater beam line with Two YB_{66} crystals as a monochromator are used combining with Si mirror. The storage ring was operating at electron energy of 750 MeV. Powdered samples were dispersed on double-faced adhesive carbon tape mounted on copper slide and the signal detected as the total electron yield.

Results and discussion

Fig. 1 shows Si *K* XANES spectra of a series of $3Al_2O_3 \cdot 2(Si_XGe_{1-X}O_2)$ noncrystalline mullites and noncrystalline mullite precursors. It is immediately apparent that two peaks are present in the XANES spectra of all samples. As the results, the peak positions of the two peaks A and B on the Si *K* XANES spectra were nearly the same in the series. Therefore, from a simple fingerprint basis, the Si atoms seem to consist of the SiO_4 tetrahedral structure[1]. The presence of two peaks on the XANES spectra probably is due to two different Si-O distances. It was noted from previous report that the strength of peak B on Si *K* edge increases with increasing the Si composition of mullite. So, the first, it is due to the increase of Si component, that is the strength of observed spectra increases with increasing the composition of the absorbing atom Si. The second, it is reported that Peak B can be assigned the transition from Si 1s orbital to Si 3p-like orbital (3s/3p)[2], therefore, the feature of the Si *K* XANES spectra of mullite depends on a distribution of Si 3p-like orbital.

Conclusion

The Si *K* XANES spectra of a series of noncrystalline mullites and noncrystalline mullite precursors $\{3Al_2O_3 \cdot 2(Si_XGe_{1-X}O_2)\}$ were measured. These XANES spectra were used as a fingerprint study of the structure of the mullites and mullite precursors. All Si atoms of them are tetracoordinated. The feature of the Si *K* XANES spectra of the mullites probably depends on a distribution of Si 3p-like (Si 3s/3p) orbital. But it is not observed that the effect of Al-O bond character is due to the Si-O bond character change. Further theoretical study is required.

References

1) P. Colomban, D. J. Jones, D. Grandjean and A. M. Flank, *J. Non-Cryst. Sol.*, 147&148 (1992) 135.
2) D. Li, G. M. Bancroft, M. Kasrai, M. E. Fleet, X. H. Feng, K.H. Tan and B. X. Yang, *Sol. Sta. Com.*, 87(1993) 613.

(BL7A)

Thickness effects of photoluminescence from lithium bromide film excited with soft x-rays in Br-L edge energy.

Tokuo MTSUKAWA, Fumiaki MITANI and Toyohiko KINOSHITA*

Naruto University of Education, Naruto 772-8502

**Institute for Solid State Physics, The University of Tokyo, Tokyo 106-8666*

(5:Solid- & liquid-phase spectroscopy; soft x-ray, absorption, photo-luminescence)

We have measured sample thickness dependence of photoluminescence excitation spectra from vacuum evaporated LiBr film excited in the photon energy region of Br-L_3 absorption edge. Br-L spectra had become possible to measure by the use of YB_{66}[1] crystal as monochromator crystals at the BL7A beam line. We had obtained Br-L absorption spectra of alkali bromides by the transmission methods and photoluminescence yield spectra from thin samples excited in the energy region. In the case of fine powder samples, the excitation spectra show inverted profiles of absorption spectra in the case of LiBr fine powder sample, whereas other alkali bromides show same profile as the absorption spectra. It had been considered that it might be due to the difference of the effective sample thickness In order to observe the change with sample thickness, excitation spectra were measured on LiBr thin films prepared by vacuum evaporation with different thickness. Although the results show no existence of inverted feature, the intensity of excitation spectra are found to show characteristic variation with sample thickness.

Experiments were performed at the BL7A with YB66 monochromator crystal. Several modification were applied for the beamline. A sample preparation chamber were attached to the sample chamber to evaporate samples in separated place. Sample were prepared with vacuum evaporation on to a collodion film and transferred to the sample chamber for each measurements on every sample with different thickness. Evaporation were repeated over the one sample film after a measurement. The thickness of evaporated film was monitored by a quartz frequency monitor.

A photo-multiplier tube was installed at 45 degree to incident light direction through a quartz focusing lens of 20mm diameter at 200mm from the sample position. A electron-multiplier with Be-Cu anode was set behind the sample film, and absorption spectra were simultaneously obtained by a transmission method getting along with the excitation spectra.

Figure 1 shows a comparison of the excitation spectra with different film thickness . The thickness were given by the frequency shift of the quartz thickness monitor. No correction, nor estimation of the thickness was made because of lack of reference value of the density of dehydrate LiBr. In the figure the absorption spectrum is also shown with a dashed curve for a comparison. Spectral features are all common among the samples of the different thickness and with the absorption spectrum except the intensity distribution. As the thickness are small, it is apparent that the photoluminescence intensity increases rapidly.

Figure 2. shows a change of luminescence intensity measured at the energy below the absorption edge, the first absorption peak and second peak, which are shown by arrow A, B and C in figure 1, respectively. It is found that the change is presented quite well by a quadratic curve as shown in the figure by solid curves. That of C is given by a bold dashed curve, which has not minimum point whereas the other have minimum at around 2 kHz thickness. Intensity of the photoluminescence from thin film, excited with x-ray, increases as a function of quadratics of film thickness, not but linear function.

The luminescence intensity depends on the whole amount of creation of inner core holes, and the amount may depends on dose of absorbed x-ray, thus it may be considered to be proportional to the thickness of the sample. The intensity of the light may be unchanged since alkali halides are transparent in visible and uv region, thus no self-absorption effects are considered. We had obtained quantum efficiency spectra, ratio spectra of the luminescence and the dose spectra. The dose spectra are given by (I_0-I) spectra, where I_0 is incident x-ray spectra and I is transmitted x-ray spectra. They increase with sample thickness and appear to have maxmum structures at the same position as the excitation spectra. Figure 3 shows plots of the quantum efficiency at the point A,B and C against sample thickness. The figure show that quantum efficiency of A, B and C are not only linearly changes against the sample thickness as the samples are thin, but also they appear to converge to zero at thickness of about 2.5kHz commonly among A, B and C,. If it is true, it suggest that there is a threshold in the sample thickness to excite the photoluminescence by x-ray.

Fig.1

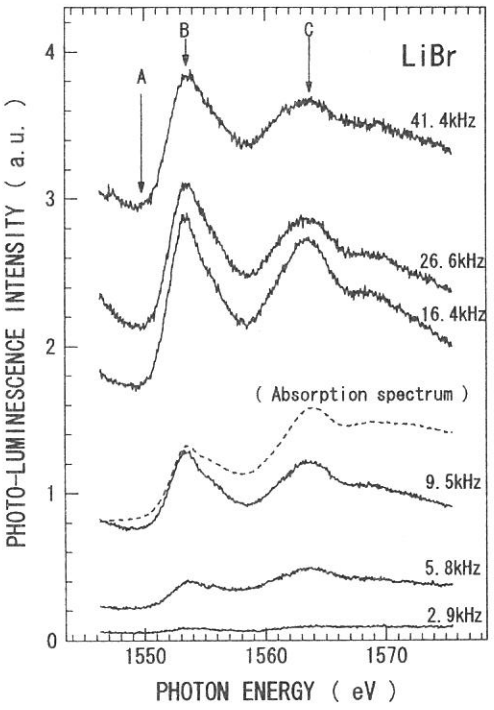

Fig.2

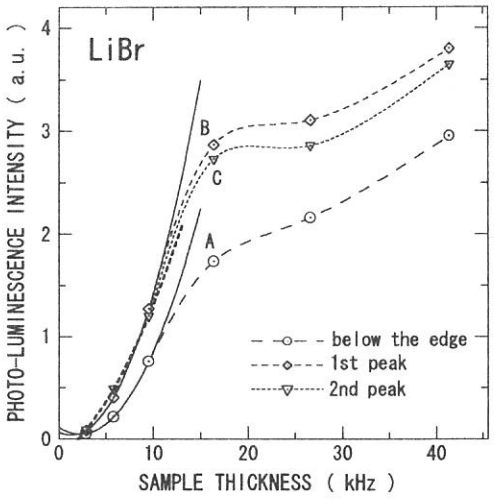

Fig.3

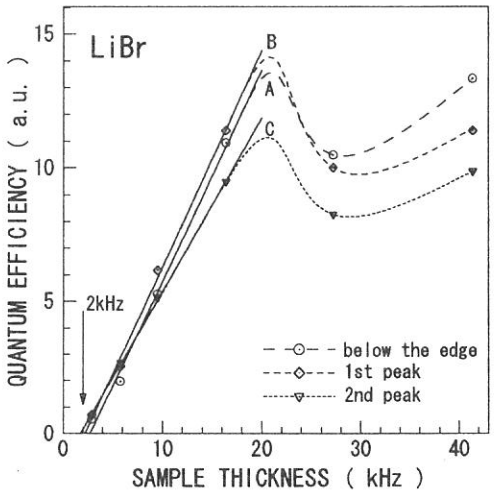

(BL7A)

Br-L_3 absorption spectra and excitation spectra of photoluminescence of alkali bromides.

Tokuo MATSUKAWA, Hiroaki OKUTANI and Toyohiko KINOSITA*)

Naruto University of Education, Naruto 772-8502

**Institute for Solid State Physics, The University of Tokyo, Tokyo 106-8666*

(5: Solid- & liquid-phase spectroscopy 2; soft x-ray, absorption , photo-luminescence)

Soft x-ray excitation spectra of luminescence were measured in Br-L_3 region as well as soft x-ray Br L_3 absorption spectra of alkali bromides. The photon energy of Br L edge exist at around 1500eV, where only few spectroscopic study is reported. One of the reason is that a proper monochromator crystal has been poor. At the BL7A beam line, stable spectroscopic works had become possible by the use of YB_{66} crystal in the region. The beam line was operated at the 4T-wiggler mode. The beam line is composed with a double crystal monochromator. By using wiggler, usable energy extends up to about 5 KeV and the intensity raises of the two order in the 1500eV region. The YB66 crystals used were commercial products synthesized by the Crystal Systems Inc.,Yamanashi, Japan. We had performed Br L absorption measurements on alkali bromides in order to check the availability. The experiments were performed on thin powder samples. The absorption spectra were obtained by the total photoelectron yield. The excitation spectra were obtained simultaneously with recording the intensity of the visible (ultraviolet) light from the sample.

Figures 1 to 4 show comparisons of the excitation spectrum and the absorption spectrum of four bromides, respectively. Thin curves show the absorption spectra and bold ones the excitation spectra. The absorption spectra have a series of fine structures at the edge commonly. The intensity distribution and the number are the similar to Cl-L spectra of alkali chlorides, though the Br spectra don't show sharp peak structures as Cl spectra. This is due to the restricted resolution at much more higher energy and the difference of the life time broadening of the core-level. The Br L spectra show no overlap structures because of the large separation of around 50eV between L_2 and L_3 levels. Thus the week and shallow structures in Br spectra may be explained as the exiton absorption peaks as chlorides.

The excitation spectra appear to follow the features of the absorption spectra, except that of LiBr. In the case of LiBr, the luminescence intensity drops at the threshold of the absorption edge. In the higher energy region luminescence yields shows some structures which corresponds absorption structures as peaks to dips. Thus the luminescence excitation spectrum of LiBr shows inverted profiles of the absorption spectrum. It is a well known phenomenon in the case the luminescence excitation spectra excited with x-ray. Emura et al. discussed the phenomena according to a phenomenological model. They showed that the excitation spectra changes the profiles among the effective thickness of samples. The results shows that the excitation spectra

change their spectral features as the effective thickness change, and finally reach the inverted profiles of absorption spectra. If it is true, our results of NaBr, KBr and RbBr are the case of the samples with enough thin effective thickness. Then, LiBr is a special case or might be due to a different condition of the sample preparation. Although we prepared the sample with fine powders as thin as possible, LiBr is deliquescence and fine powders crystallize to form a hydrate. Then effective thickness of the sample might be increase. Even though the sample in this case is that of a hydrate, the spectral features of the absorption spectrum presents the same features of non-hydrate which had been measured on a vacuum evaporated thin film using a dehydrate sample.

Fig.1

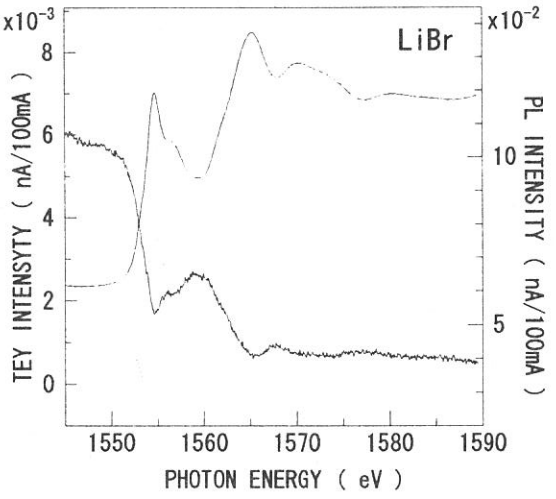

Fig.2

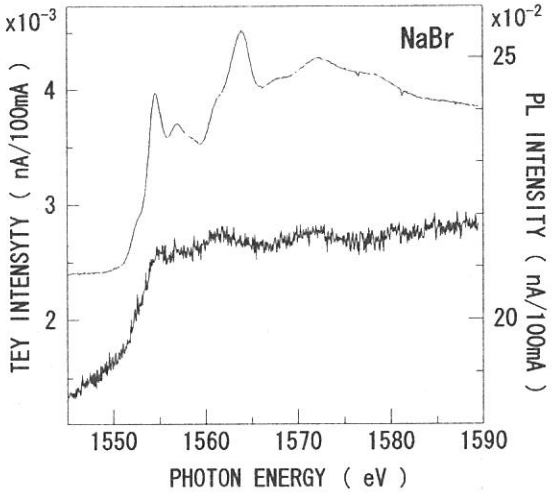

Fig.3

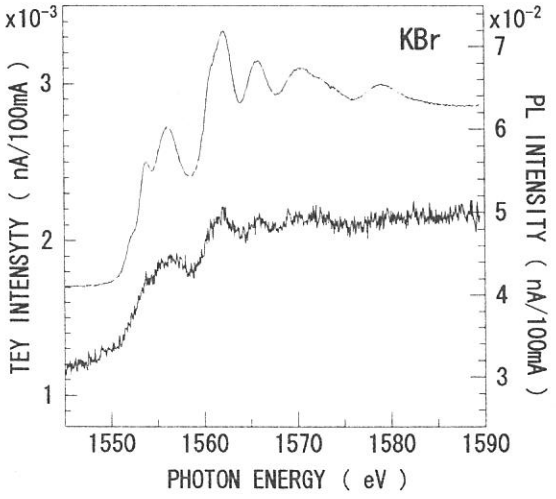

Fig.4

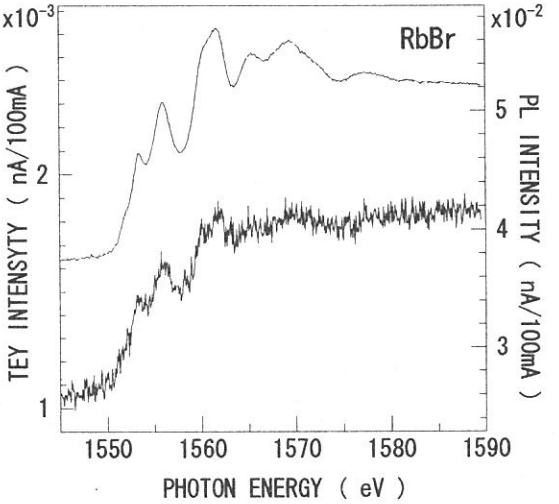

(BL7A)

Local structure around S in permanently densified GeS_2 glass

*Koichi MIYAUCHI, Masanori SHOJIYA, Yoji KAWAMOTO and Noriyuki KITAMURA**
Division of Molecular Science, Graduated School of Science and Technology, Kobe University, Nada, Kobe 657-8501, Japan
**Department of Optical Materials, Osaka National Research Institute, AIST, Midoriga-oka Ikeda 563-8577, Japan*

When glasses are treated under high pressures, significant increases in density are observed even after removal of the applied pressures. This permanent densification phenomenon of glass was demonstrated for the first time by Bridgman and Simon [1]. This permanent densification phenomenon is of importance from a practical point of view because it may be applied to control functions such as optical, electrical and mechanical properties without changing glass composition. The permanent densification phenomena have been investigated on various kinds of oxide and chalcogenide glasses [2,3]. On chalcogenide glasses, for example, the effects of high-pressures on various properties have been extensively investigated [3]. However, structural studies of permanently densified chalcogenide glasses are very few. On the structure of densified GeS_2 glass, for example, there is only one report, though the presumed structural changes are based on a change of the optical absorption-edges measured in situ under high-pressures [4].

GeS_2 glass was prepared from metallic Ge and elementary S according to the procedure described previously [5]. The prepared glass was annealed at the glass-transition temperature determined by a DTA analysis. Permanent densification of the GeS_2 glass was carried out with a 6-8 multi-anvil high-pressure apparatus under 1.5, 3.0, 4.5, 6.0 and 9.0 GPa at 270°C. The permanent densification was retained after the removal of the pressure and temperature. The densities and the absorption-edge energies in the visible region on permanently densified GeS_2 glasses are shown in Fig. 1. The density increased with pressure until 6.0 GPa and then reached to a constant value under further increased pressure. The absorption-edge energies in the visible region shifted toward low energies with pressure until 6.0 GPa and then reached a constant value under further increased pressure.

All the densified GeS_2 glasses have the same composition so that the changes of physicochemichal properties are attributable to structural changes by high-pressure treatments. Especially the shift of the absorption-edge energies is related to the molar volume and the Ge-S bond distance, as referred by Xu and Ching [6]. Therefore we investigated the local structure around S in undensified and densified GeS_2 glasses.

The XAFS measurements were carried out at BL-7A under ambient temperature using a Total Electron Yield method. A monochromater with two flat Ge(111) (d = 3.266) was used. The S-K XAFS absorption data were collected in the energy range from 400 eV on the low energy side of S-K absorption edge (2471 eV) to about 1200eV on high energy side. Analyses of EXAFS data were performed by using the program WinXas97. In the least square curve fitting procedure, the theoretical EXAFS parameters calculated from FEFF7 code [7] were used.

Fig. 2 shows the S-Ge atomic distance plotted against the applied pressure, together with the experimental error bar. The S-Ge atomic distance extended slightly with pressure untill 6.0 GPa and then reached a constant value under further increased pressure. The pressure dependence of S-Ge bond length corresponds to that of absorption-edge energy in the visible region. Thus, both are strongly related.

The XANES spectra of undensified and densified GeS_2 glasses and the α- and β-GeS_2 reference crystals were shown in Fig. 3. In the figure, solid lines indicate experimental spectra and dashed lines indicate combined spectra of α- and β-GeS_2 with given ratios. As the linkage manner of GeS_4 tetrahedra there are two kinds of manners; corner-sharing (linkage by one S) and edge-sharing (linkage by two S). The former exists in α- and β-GeS_2; while the latter is present only in α-GeS_2. A comparison of both spectra indicates that the S-K XANES spectra profile of GeS_2 glass varied from α-GeS_2 glass-like to β-GeS_2-like. Therefore it is concluded that the fraction of edge-sharing in the linkage of GeS_4 tetrahedra decreases with densification. This is also supported by a decrease of the peak due to Ge-Ge distance in edge-shared GeS_4 tetrahedra observed in X-ray differential radial distribution curves of undensified and densified GeS_2 glasses.

References

[1] P. W. Bridgman and I. Simon, J. Appl. Phys. 24 (1953) 405
[2] S. Sakka and J. D. Mackenzie, J. Non-Cryst. Solids 1(1969) 107
[3] G. Parthasarathy and E. S. R. Gopal, Bull. Mater. Sci. 3&4 (1985) 271
[4] R. Zallen, B.A. Weinstein and M. L. Slade, J. Phys. 42(1981) C4-241; B.A. Weinstein, R. Zallen, M.L. Slade and J. C. Mikkelsen Jr., Phys. Rev. B 25(1982) 781

[5] Y. Kawamoto and S. Tsuchihashi, J. Am. Ceram. Soc. 52 (1961) 626; 54 (1971) 131
[6] Y. Xu and W. Y. Ching, Phys. Rev. B44 (1991) 11048
[7] S. I. Zabinsky, J. J. Rehr, A. Ankudinov, R. C. Albers and M. J. Eller, Phys. Rev. B52 (1995) 2995

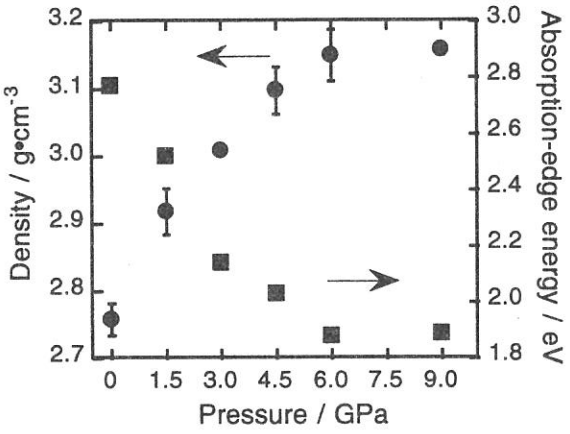

Fig. 1. Pressure dependence on density (●) and absorption-edge energy in visible region (■) in undensified and densified GeS_2 glasses.

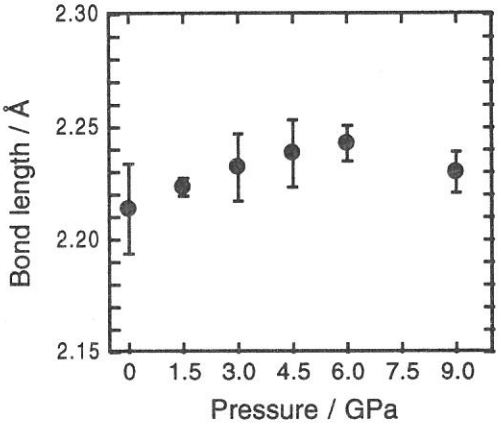

Fig. 2. Pressure dependence of S-Ge bond length in undensified and densified GeS_2 glasses.

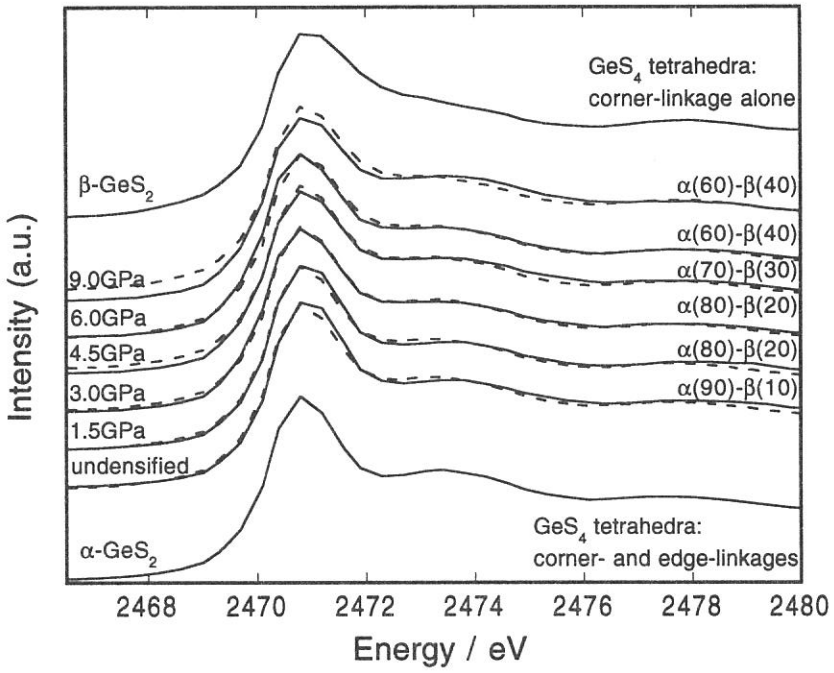

Fig. 3. Pressure dependence of S-K XANES spectra of undesified and densified GeS_2 glasses. (solid line: experimental, dashed line: simulated)

(BL7A)

Crystalline structure of impurity-doped multinaly compound semiconductor

Tooru Tanaka, Qixin Guo*, and Akihiro Wakahara

Department of Electrical and Electronic Engineering, Toyohashi University of Technology, Toyohashi 441-8580, Japan

**Department of Electrical and Electronic Engineering, Saga University, Saga 840-8502, Japan*

I -III-VI_2 chalcopyrite semiconductors, such as $CuInSe_2$ and $Cu(In,Ga)Se_2$, have been one of the leading candidates for absorbers in hetero-junction photovoltaic devices because of their direct bandgap and high absorption coefficient[1]. These devices have been demonstrated to exhibit high conversion efficiency close to 19%[2].

The electrical properties, both the conductivity type and the carrier concentration, of $CuInSe_2$ strongly depend on the Cu/In and Se/(Cu+In) compositional ratio. $CuInSe_2$ thin films for high efficiency solar cells are fabricated by co-evaporation technique with precise control of the Cu/In ratio. In order to achieve a solar cell with higher efficiency and larger area, it is important to establish the doping technique using extrinsic dopants. However, the detailed roles of doped impurity in $CuInSe_2$ have not yet been clarified.

Recently, We have investigated the effect of implanted Mg on the electrical properties of $CuInSe_2$ epitaxial films[3]. It was found that Mg atoms act as donor in $CuInSe_2$, and that the electron concentration increased linearly with increasing the Mg concentration in the films. However, the concentration ratio of the implanted Mg to carrier electron at room temperature was as low as about 1%, and thus, all of the Mg atoms seem not necessarily to be present on donor site. As the next step, we should clarify the doping mechanism by Mg in $CuInSe_2$. In this work, we measured Mg K-edge XANES spectra of Mg-implanted $CuInSe_2$ thin films in order to investigate the local structure around Mg atoms.

Epitaxial $CuInSe_2$ thin films were grown on semi-insulating GaAs(001) substrate at the substrates temperature of 450℃ for 180min by RF diode sputtering. Mg atoms were implanted into the films at room temperature using three kinds of accelerating energies, 60, 140, and 200keV, in order to fabricate the box profile of Mg atoms within a depth of 300nm from the surface. The mean Mg concentration in the implanted layer of the films used in this measurements were $5\times10^{19}cm^{-3}$ and $5\times10^{20}cm^{-3}$. After implantation, the films were annealed at 400℃ for 60min in N_2 atmosphere to eliminate implantation damage, and activate Mg atoms electrically.

Soft X-ray absorption experiments were carried out on the beam line BL7A station at the Ultraviolet Synchrotron Radiation Facility (UVSOR) in the Institute for Molecular Science, Okazaki, Japan, with a ring energy 750MeV and stored current of 80-200mA. Mg K-edge X-ray absorption spectra were recorded using a beryl two-crystal monochromator. Data were collected in a total electron

yield mode under high vacuum (<10^{-7}Torr) at room temperature. The samples were put on the first photocathode made of Cu-Be of the electron multiplier by using adhesive carbon tape.

Figure 1 shows Mg K-edge XANES spectra of Mg-implanted $CuInSe_2$ thin. We have obtained clear XANES spectra. By analyzing the spectra, local structure around Mg atoms would be characterized, and it has been now in progress.

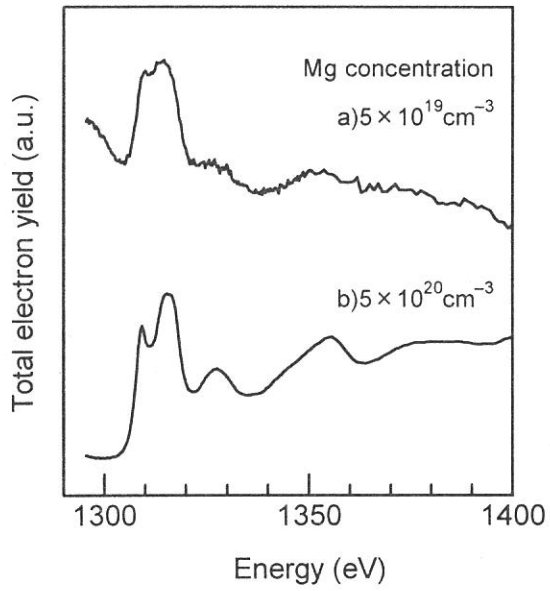

Fig.1 Mg K-edge XANES spectra of Mg-implanted $CuInSe_2$ films with a mean Mg concentration of (a)$5\times10^{19}cm^{-3}$ and (b)$5\times10^{20}cm^{-3}$.

Acknowledgements

The authors would like to thank Professor T.Kinoshita and other staff members of the UVSOR facility for the useful advice and technical support. We are also grateful to Mr. H.Sato and Mr. M.Nakajima for their help in the experiment.

References

[1] D.Haneman, Crit. Rev. Solid State Mater. Sci. **14,** 377 (1988).
[2] M.A.Contreras, B.Egaas, K.Ramanathan, J.Hiltner, A.Swartzlander, F.Hasoon, R.Noufi, Progress in Photovoltaics, **7**, 311 (1999).
[3] T.Tanaka, A.Wakahara, A.Yoshida, T.Ohshima, H.Itoh, and S.Okada, J.Appl.Phys. (in press).

(BL7A)

Al K-edge study for Al doped Lithium Manganese Spinel Oxides for Lithium Secondary Batteries

Yoshiharu UCHIMOTO, Takeshi YAO, and Taiji SASADA
Department of Fundamental Energy Science,
Graduate School of Energy Science, Kyoto University,
Yoshida, Sakyo-ku, Kyoto 606-8501, JAPAN

Secondary lithium batteries using intercalation compounds as the cathode active material have been studied intensively. Among many intercalation compounds, $LiMn_2O_4$ based spinel type oxides are one of the most promising cathode materials used in lithium ion batteries because their low cost, high theoretical energy density. (1-5) However the capacity of the battery using $LiMn_2O_4$ fades out during charge-discharge cycling at around 4 V. Recently, Al doped $LiMn_2O_4$ material have shown better cycle performance at around 4 V compared with the cycleability of undoped $LiMn_2O_4$. (6-7)

The unit cell of the ideal spinel structure (space group: *Fd3m*) is given in Fig. 1. In this ideal structure, oxide ions form a cubic close packing, in which cations partly occupied tetrahedral and octahedral interstices. The unit cell of $LiMn_2O_4$ contains 56 atoms; 32 O, 16 Mn, and 8 Li. The oxide ions occupied 32e position, lithium ions occupied tetrahedral 8a positions, and manganese ions occupied octahedral 16d positions. In order to understand the improvement of cycleability by Al doping, it is important to clarify doping site of Al cations on the cubic spinel structure. In the present study, Al cation doped spinels ($LiAl_xMn_{1-x}O_4$) were prepared. X-ray diffraction (XRD), X-ray Absorption Fine Structure (XAFS), and electrochemical studies were carried out. Especially, Al K-edge X-ray Absorption Near Edge Structure (XANES) analysis was used to determine the Al doping site; 16d (octahedral position) or 8a (tetrahedral position).

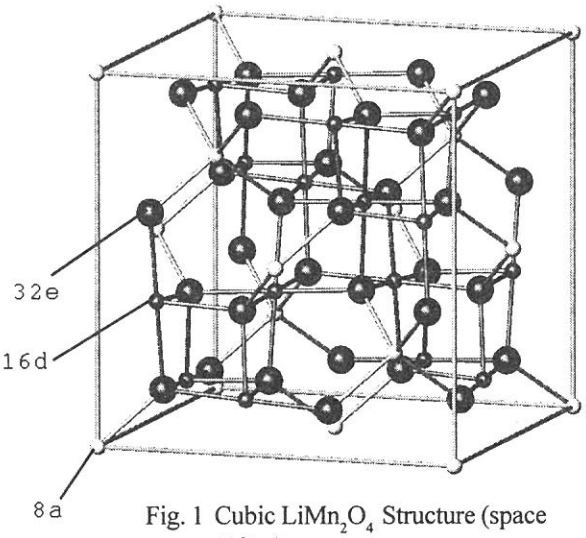

Fig. 1 Cubic $LiMn_2O_4$ Structure (space group *Fd3m*).

$LiAl_xMn_{1-x}O_4$ spinels were prepared from lithium carbonate, manganese carbonate, and aluminium hydrate. The mixture was calcined for 48 hours at 850°C. The crystal structure of the product was determined by XRD using MoKα radiation. Fig. 1 shows XRD pattern of $LiAl_xMn_{1-x}O_4$. The $LiAl_xMn_{1-x}O_4$ (x=0.0, 0.05, 0.1, 0.2) were indexed to an cubic lattice. Above x=0.3, unknown peaks appeared. The lattice parameters and other

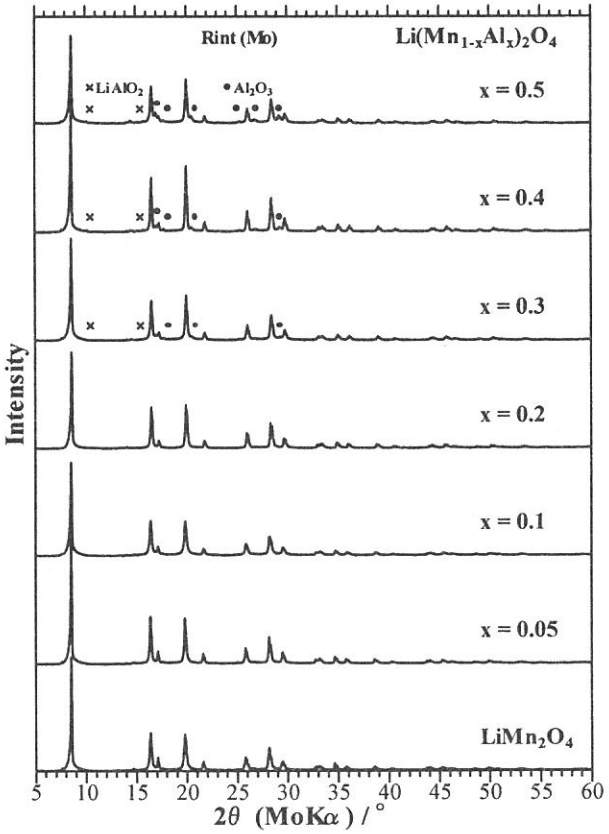

Fig. 2 XRD pattern of $LiAl_xMn_{1-x}O_4$.

structural parameters for samples below x=0.2 were refined by the Rietveld method. The Rietveld analysis was confirmed that the samples were belonging to cubic *Fd3m* space group.

Al K-edge XANES spectra were measured at room temperature in a total electron yield mode at BL-7A at UVSOR line with two quartz crystals. The Al K-edge XANES spectra were powerful tool to determine the coordination number of Al cations. (8-10) Fig. 3 shows a Al K-edge XANES of $AlPO_4$ and Al_2O_3. In the $AlPO_4$, AlO_4 (tetrahedra) is dominant, whereas in the Al_2O_3, AlO_6(octahedra) is dominant.

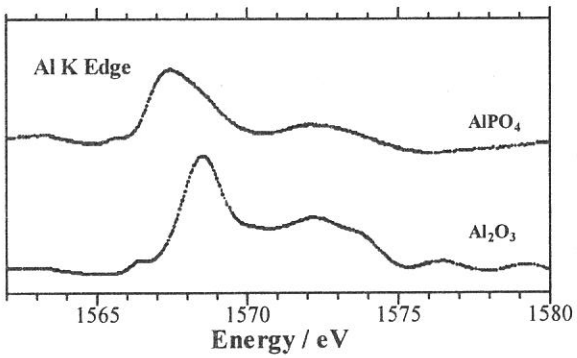

Fig. 3 Al K-edge XANES of $AlPO_4$ and Al_2O_3.

Fig. 4 shows Al K-edge XANES of $LiAl_xMn_{1-x}O_4$ (x = 0.0, 0.05, 0.075, 0.1, 0.2, 0.3, 0.4, and 0.5) together with those of reference compounds of $AlPO_4$ (AlO_4 :tetrahedra) and Al_2O_3 (AlO_6 :octahedra). The figure clearly indicates that the AlO_6 octahedra is predominant for $LiAl_xMn_{1-x}O_4$ (x=0.0, 0.05, 0.1, 0.2) which were belonging to cubic *Fd3m* space group. This means that Al doping site is mainly 16d (octahedral position) in the cubic spinel structure. From the data of the standard Gibbs energy of the information of Al_2O_3 and Mn_2O_3, the Al-O bond is stronger than Mn-O bond in the octahedra. (6) The M-O bond at 16d (octahedral position) in the cubic spinel structure are stronger by Al doping, so that the Al doping improve the cycleability of the lithium secondary battery.

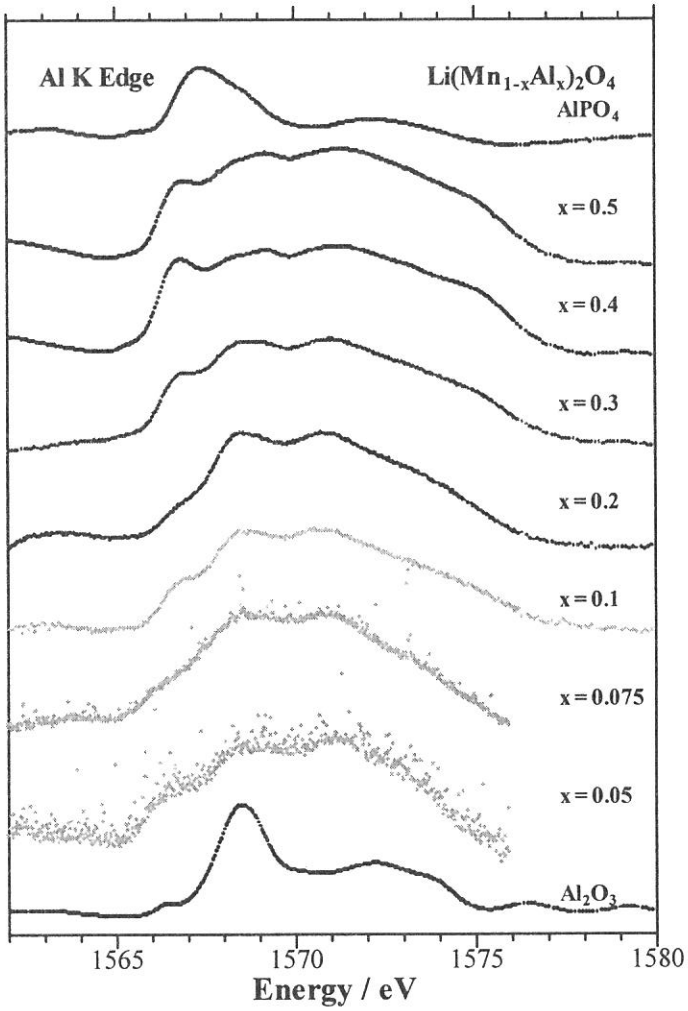

Fig. 4 Al K-edge XANES of $LiAl_xMn_{1-x}O_4$ (x = 0.0, 0.05, 0.075, 0.1, 0.2, 0.3, 0.4, and 0.5) together with those of reference compounds of $AlPO_4$ and Al_2O_3.

REFERENCES

1) D. Guyomard, J.M. Tarascon, *Solid State Ionics*, **69**, 222 (1996).
2) W. Liu, G.C. Farrington, F. Chaput, and B. Dunn, *J. Electrochem. Soc.*, **143**, 879 (1996).
3) Y. Xia, H. Takeshige, H. Noguchi, and M. Yoshio, *J. Power Sources*, **56**, 61 (1995).
4) H. Ohzuku, M. Kitagawa, T. Hirai, *J. Electrochem. Soc.*, **137**, 769 (1990).
5) K. Kanamura, H. Naito, T. Yao, and Z. Takehara, *J. Mater. Chem.*, **6**, 33 (1996).
6) D. Song, H. Ikuta, T. Uchida, and M. Wakihara, *Solid State Ionics*, **117**, 151 (1999).
7) F. Le Cras, D. Bloch, M. Anne, and P. Strobel, *Solid State Ionics*, **89**, 203 (1996).
8) G.A. Waychnas and G.E. Brown Jr., *EXAFS and Near Edge Structure III*, Springer-Verlag, Berlin, 336 (1984).
9) J. Wong, Z.U. Rek, M. Rowen, T. Tanaka, F. Schafers, B. Muller, G.N. George, I.J. Pickering, G. Via, B. DeVries, G.E. Brown Jr, M. Froba, *Physica B*, **208&209**, 220 (1995).
10) K. Shimizu, Y. Kato, T. Yoshida, H. Yoshida, A. Satsuma, and T. Hattori, *UVSOR Activity Report*, 174 (1998).

(BL-7A)

XAFS study on Al coordinations in silica-alumina prepared by sol-gel method

Hisao Yoshida,[a] Norimitsu Matsushita,[a] Yuko Kato,[a] Ken-ichi Shimizu,[a] Tomoko Yoshida[b] and Tadashi Hattori[a]

[a] *Department of Applied Chemistry, Graduate School of Engineering, Nagoya University, Nagoya, 464-8603, Japan*

[b] *Center for Integrated Research in Science and Engineering, Nagoya University, Nagoya, 464-8603, Japan*

Abstract

By means of Al K-edge XANES study at UVSOR, it was clarified that the AlO_4 species in silica-alumina catalysts were responsible for their activity in photoinduced non-oxidative methane coupling at room temperature.

Introduction

In order to convert natural gas into useful chemicals, the oxidative methane coupling is an expedient reaction. However, it is quite difficult to obtain the coupling products in high selectivity, because the oxidation of coupling products to CO_x proceeds more selectively than the coupling reaction. When the oxidant molecules are removed to avoid the complete oxidation, the reaction should require very high temperature [1]. Recently, photoinduced non-oxidative methane coupling was found to proceed on silica-alumina in yields as high as 5 % without formation of CO and CO_2 [2]. The active sites on silica-alumina were proposed to be the highly dispersed Al species in the silica matrix. In the present study, we focussed the coordination states of Al species in the silica-alumina prepared by sol-gel method and their photoactivity.

Experimental

The samples of silica-alumina were prepared by sol-gel method. After a mixture of $Si(OEt)_4$ and ethanol (mol ratio, 1/5) was stirred for 1 h, another mixture of ethanol, distilled water, $Al(NO_3)_3$ and nitric acid (mol ratio, 5/50/x/0.02, x=0.02-2) was added dropwise, followed by stirring for 1 h. Dehydration proceeded at 353 K with suction. When geration started, the mixture was dried without stirring, followed by drying at 383 K for 12 h, grind and calcination in a flow of dry air (60 ml/min) at 773 K for 5 h to obtain the silica-alumina powder samples. Pure silica sample was prepared from $Si(OEt)_4$ by sol gel method in water-ethanol mixture at boiling point followed by grind and calcination. Pure alumina was prepared by calcination of $Al(NO_3)_3$. They were stored under ca. 80% humidity at room temperature.

Before the reaction test, the sample was heated in air up to 1073 K and then evacuated. Subsequently the sample were treated with 100 Torr oxygen (1 Torr=133.3 Nm^{-2}) at 1073 K for 1 h, followed by evacuation at the same temperature for 1 h. The reaction test was carried out under irradiation by using a 250 W Xe lamp for 6 h. No oxidant molecules was introduced into the reaction system. Under photoirradiation, the temperature of sample bed was measured to be around 310 K. Products in the gaseous phase were collected with a liquid-N_2 trap and analyzed by GC. BET specific surface area of the samples was measured after the reaction test.

Soft X-ray absorption experiments were carried out on the beam line 7A [3] at UVSOR, Institute for Molecular Science, Okazaki, Japan, with a ring energy 750 MeV and stored current of 130-200 mA. Two-crystals monochromator employing YB_{66} crystals were used for recording Al K-edge XAFS [4]. Data were collected in a total electron yield mode under high vacuum (residual pressure $<1\times10^{-6}$ Torr) at room temperature. The sample was put on the first Cu-Be dynode of the electron multiplier (-1.5 kV) by using adhesive carbon tape.

Table 1 Results of characterization and ethane yield in photoinduced non-oxidative methane coupling

Al composition (Al/(Si+Al)%) [a]	BET surface area (m^2g^{-1}) [b]	ethane yield (%) [c]	ethane yield per surface area ($x10^{-4}$ % /m^2g^{-1}) [c/b]	ethane yield per amount of surface Al ($x10^{-4}$ %/m^2g^{-1}/atom%) [c/b/a]
0.0	297	0.022	0.75	-
2.0	137	0.067	4.9	2.4
9.1	258	0.058	2.8	0.58
16.7	273	0.104	3.8	0.22
37.5	203	0.091	4.5	0.12
50.0	98	0.041	4.8	0.096
66.7	93	0.051	5.5	0.083
100	92	0.049	5.3	0.053

Results and discussion

The Al in the each silica-alumina sample prepared was confirmed to be homogeneously dispersed in bulk and surface since the surface Al concentration estimated by XPS was in good agreement with the bulk composition. The BET surface area of the samples containing Al of more than 50 % was obviously smaller than those of low Al content samples as shown in Table 1.

In the photoinduced non-oxidative methane coupling, only ethane was obtained as gaseous product in this condition. The ethane yield listed in Table 1 did not show a linear correlation with Al composition, which should be affected by the differences of specific surface area and Al composition. The activity normalized by them (the last column in Table 1) shows good relation to the Al composition; the lower Al composition sample exhibited the higher activity. It supports the proposal that highly dispersed Al species in silica-alumina would be active sites [2].

Fig. 1 shows the normalized Al K-edge XANES spectra of silica-alumina and alumina samples together with those of model compounds containing AlO_4 tetrahedra (mordenite) and AlO_6 octahedra (corundum) [5]. The spectra of the silica-alumina samples varied with their Al contents (Fig. 1 a-f). The low Al content samples (Fig. 1a, b) show a peak at around 1566 eV, which is assigned AlO_4 species as shown in the spectrum of mordenite (Fig. 1h). This peak broadened to higher energy and a broad peak at around 1572 eV became apparent as increase of Al contents (Fig. 1c-f). The alumina sample showed the obvious peaks at 1568 eV and 1572 eV(Fig. 1g). The peaks at 1568 and 1572 eV are assigned to AlO_6 species as shown in the spectrum of the corundum alumina (Fig. 1i). These results indicate that the fraction of AlO_6 species in the silica-alumina samples increased as increase of Al contents. In the other words, AlO_4 species are predominant in the lower Al content samples.The activity in photoinduced non-oxidative methane coupling to produce ethane mentioned above also showed the same tendency.

As a conclusion, it was claimed that the activity of the silica-alumina samples in this photoreaction would be responsible for the surface AlO_4 species.

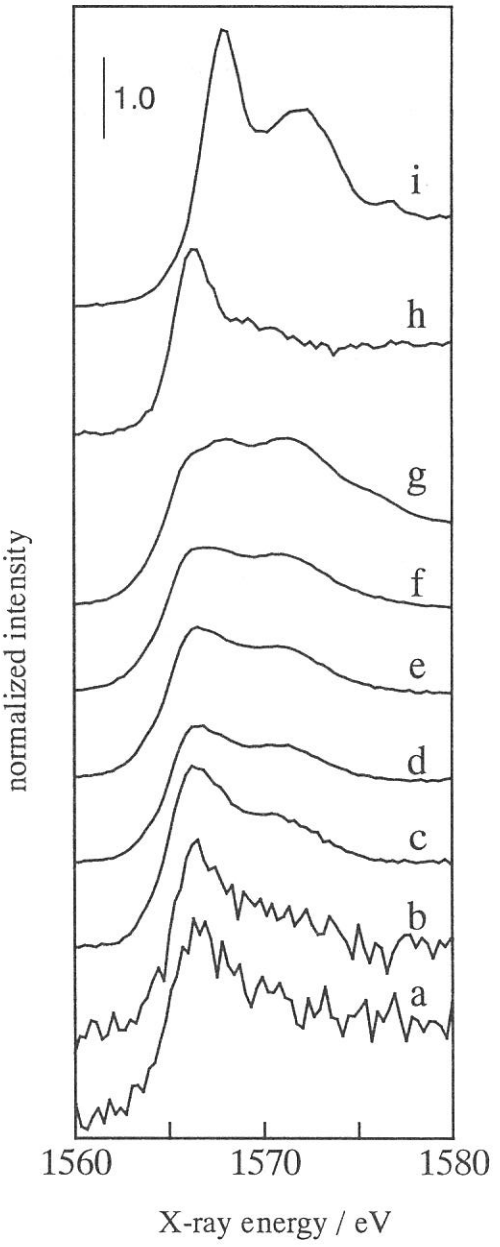

Fig. 1 Al K-edge XANES spectra of silica-alumina samples whose Al contents (mol%) of 2.0 (a), 9.1 (b), 16.7 (c), 37.5 (d), 50 (e) and 66.7 (f), and alumina calcined at 773 K (g), mordenite-type zeolite (JRC-Z-HM15, tetrahedral) (h) and alumina (corundum, octahedral) (i).

References

1. L. Guczi, R. A. Van Santen and K. V. Sarma, *Catal. Rev. Sci.-Eng.*, 38 (1996) 249.
2. Y. Kato, H. Yoshida and T. Hattori, *Chem. Commun.*, 1998, 2389.
3. T. Murata, T. Matsukawa, S. Naoe, T. Horigome, O. Matsudo and M. Watanabe, *Rev. Sci. Instrum.* 63 (1992) 1309.
4. T. Kinoshita, Y. Takata, T. Matsukawa, H. Aritani, S. Matsuo, T. Yamamoto, M. Takahashi, H. Yoshida, T. Yoshida, Y. Ufuktepe, K. G. Nath, S. Kimura, H. Kumigashira and Y. Kitajima, *J. Synchrotron Rad.*, 5 (1998) 726.
5. K. Shimizu, Y. Kato, T. Yoshida, H. Yoshida, A. Satsuma and T. Hattori, *Chem. Commun.*, (1996) 1681.

(BL 7A)

Study on D^+ irradiated Si surface by XAFS

Tomoko Yoshida,[a*] Hisao Yoshida,[b] Takanobu Hara,[c] Mikio Sakai[c] and Tetsuo Tanabe[a]

[a] *Center for Integrated Research in Science and Engineering, Nagoya University, Nagoya 464-8603, Japan*

[b] *Department of Applied Chemistry, Graduate School of Engineering, Nagoya University, Nagoya 464-8603, Japan*

[c] *Department of Nuclear Engineering, Graduate School of Engineering, Nagoya University, Nagoya 464-8603, Japan*

Introduction

Ion implantation is commonly used as a method to modify the near-surface properties of materials. By controlling the fluence and energy of incident ions, one can introduce the desired amount of foreign species into suitable depth in host materials. Simultaneously the kinetic energy of implanted ions introduces lattice damage through electron excitation and atomic displacement processes, sometimes resulting in undesirable modification of the near-surface structure. Therefore characterization of the implanted materials with fine depth resolution is a very important task. In the present work, we have applied an X-ray absorption technique for characterization of silicon samples implanted by deuterium with the difference in the depth distribution of implanted deuterium and produced damages.

Experimental

Deuterium ion irradiation was carried out in a standard vacuum chamber equipped with an ion source at room temperature[1]. With an aid of differential pumping system, the pressure of the target chamber was kept below 10^{-8} Torr during the irradiation. Mass analyzed deuterium ions (D^+) accelerated up to 5 keV were injected into a Si target (100) through a slit of 5 mm diameter with an incident angle of 22.5 degrees with respect to the target normal. Since the samples were stored in air, they were exposed to atmospheric oxygen.

Si K-edge XANES spectra were recorded under vacuum ($<10^{-7}$ Torr) at room temperature at the beam line 7A station attached with a two-crystal InSb monochromator at UVSOR, Institute for Molecular Science, Okazaki, Japan. The ring energy was 750 MeV and stored current was 100-200 mA during measurement. The sample was directly put on the first photocathode made of Cu-Be of the electron multiplier with the voltage of - 1.5 keV. Data were collected in a total electron yield mode, in which X-ray energy dependence of Si KLL Auger electron yield is mainly monitored.

Results and Discussion

Fig. 1 shows Si K-edge XANES spectra of unirradiated silicon (a) and deuterium irradiated silicons with incident energy of 5 keV (b-d). The XANES spectrum of a pure silica glass is also shown in Fig. 1 (e) as a reference. The features of the XANES spectrum changed with increase of D^+ ion fluence. After the irradiation of 1.6×10^{18} ions/cm^2, characteristic peaks of unirradiated silicon disappeared (Fig. 1 (b)), indicating that the regular tetrahedral structure of silicon was disordered by D^+ ion bombardment. In this spectrum, a pronounced peak at around 8 eV was also appreciable. Since the energy position of the peak agreed with that of the large characteristic peak of silica (Fig. 1 (e)), this result clearly indicates that the target surface was oxidized to SiO_2. As shown in Fig. 1(a), the peak corresponding to SiO_2 was not observed for the XANES spectrum of unirradiated silicon. Accordingly, the appearance of SiO_2 species can be regarded as an indication of displacement of surface silicon atoms, which easily attract or bind oxygen in residual gas during the irradiation and/or in atmosphere during the transfer for the XAFS measurements.

In addition to the surface oxidation, as shown in Fig. 1 (c, d), when D^+ ion fluence was over ca. 2×10^{18} ions/cm^2, a remarkable change was observed in the XANES spectra. This strongly indicates that the electronic and atomic structures of these samples changed to others from those of a pure silicon, i.e., such a change is much considerable compared with the merely disordering of the regular tetrahedral structure of silicon as shown in Fig. 1 (b). Since the edge due to Si(0) state almost disappeared and simultaneously a sharp peak was observed at around 5 eV, it is likely that most Si(0) atoms changed to new Si species which are in higher valence states by the irradiation. On the basis of the energy position of the new peak, they must be in the intermediate states between Si(0) and Si(4+). However, less valenced silicon oxide like SiO is known to be unstable.[2] Therefore the new Si species should correspond to Si-D (SiDn species) formation with implanted deuterium as follows. As mentioned above, under irradiation at 5 keV, the amount of implanted deuterium is less than the number of the displaced atoms. Accordingly the peak due to the Si-D formation appeared after the deuterium irradiation over 2×10^{18} ions/cm^2, whereas the peak due to SiO_2 was clearly observed for the irradiation of 1.6×10^{18} ions/cm^2. Rather drastic structural change as observed between Fig. 1 (b) and Fig. 1 (c) would indicate abrupt formation of SiDn local structure after the implantation of a certain amount of deuterium ions. The formation of the SiHn species in which Si ions are in the intermediate states between Si(0) and Si(4+) has been reported to occur by the assist of the bubble or crack formation under hydrogen irradiation.[3,4]

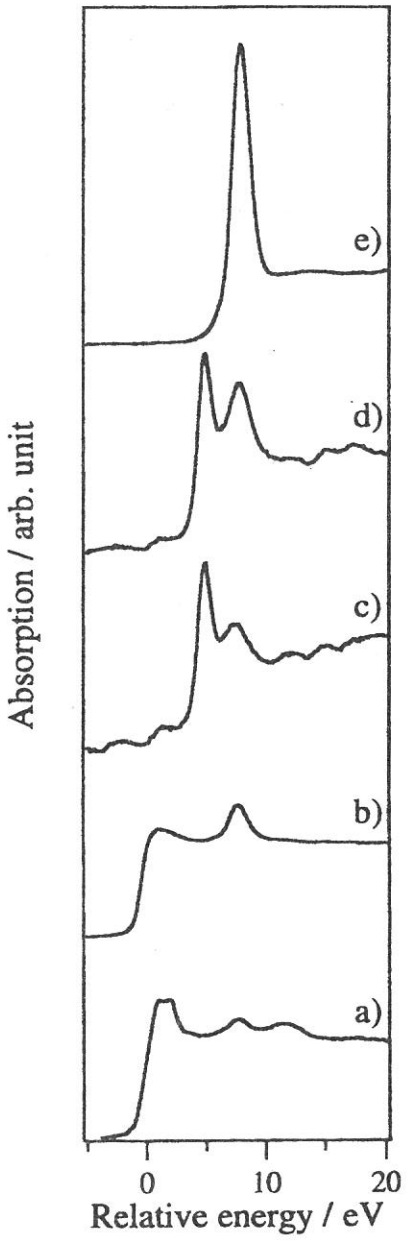

Figure 1
Si K-edge XANES spectra of a) unirradiated silicon, b-d) silicon samples irradiated by 5 keV deuterium ions, and e) a silica sample. The fluence of deuterium ions is b) 1.6×10^{18} / cm^2, c) 2.1×10^{18} / cm^2 and d) 2.9×10^{18} / cm^2. Energy offset is taken to be 1838 eV.

References

1) Tanabe, T., Tanaka, S., Yamaguchi, K., Otsuki, N., Iida, T., and Yamawaki, M. (1994) *J. Nucl. Mater.* **212-215**, 1050.
2) Yamamoto, H., Baba, Y., Sasaki, T. A. (1995). *Surf. Interf. Anal.* **23**, 381.
3) Doyle, B. L. (1982). *J. Nucl. Mater.* **111-112**, 628.
4) Varma, C. M. (1997) *Appl. Phys. Lett.* **71**, 3519-3521.

(BL8B1)

C K-edge XANES of Carbonaceous Materials on Catalysts

T. Shishido,[a] M. Kondo, H. Sameshima,[a] S. Takenaka,[b] and K. Takehira[a]

[a] *Department of Applied Chemistry, Faculty of Engineering, Hiroshima University, Kagamiyama 1-4-1, Higashi-hiroshima, Hiroshima 739-8527, Japan*

[b] *Department of Applied Chemistry, Graduate School of Engineering,, Tokyo Institute Technology, Ookayama, Meguro-ku, Tokyo 152-8522, Japan*

Introduction

In recent years, carbon fibers grown over metal species such as Fe, Co, Ni from the decomposition of hydrocarbons have been interesting materials [1-3]. Several novel carbon structures such as fullerens and nanotubes have been formed in similar systems, and bringing excitement to many fibers [4-6], due to their extraordinary physical and chemical properties. Efforts have been made to control the morphology and size of the nanotubes (or fibers) and to improve the efficiency of the production processes. It has been proposed that the growth process was composed of several steps such as adsorption, bulk diffusion, and formation of fibers. It has also proposed that the deactivations of metal species occur due to encapsulation by a graphite layer [2]. These results indicate that the catalytic activities of metal species strongly depend on the structure of carbonaceous materials.

The metal (Ni, Fe and Co) supported catalysts were prepared and testes for the methane decomposition at a high temperature. In this report, we attempted to characterize the structures of carbonaceous materials on the metal (Ni, Fe, Co) supported catalysts by means of C K-edge XANES spectroscopy.

Experimental

The metal supported catalysts were prepared by conventional impregnation method. The catalytic activity for decomposition of methane was carried out using a conventional flow system. The C K-edge XANES spectra of the catalysts were collected at room temperature in a total electron yield mode at BL-8B1 at UVSOR. In most part of experiments, the sample was put on a carbon tape and then the carbon tape was put on a Cu-Be dinode which is attached to the first position of the electron multiplier.

Results and Discussion

The C K-edge XANES spectra of the 5wt% metal/γ-Al_2O_3 catalysts used for methane decomposition at 900°C are shown in Figure 1. Figure 2 shows the C K-edge XANES spectra of 5wt% Ni/SiO_2 and Ni/MgO catalysts used for methane decomposition together with carbon tape. The shapes of the XANES spectra were almost same, regardless of kind of metal and support of the catalysts, suggesting that the

structures of the carbonaceous materials formed during the decomposition of methane on all the catalyst are almost same. In the C K-edge XANES spectra of all the catalysts, the band at 285eV and broad band between 290eV and 315eV could be confirmed. In general, the band at 285eV is assigned to $1s \rightarrow \pi^*$ resonance and the broad band around 300eV is assigned to $1s \rightarrow \sigma^*$. The negative band at 288ev was also observed in the C K-edge XANES spectra of all the catalysts. In this peak position, a sharp band was observed in the C-K-edge XANES spectrum of carbon tape, suggesting that the background subtraction is inappropriate in this energy region. In order to collect clear C K-edge XANES spectra, another method for background subtraction should be needed.

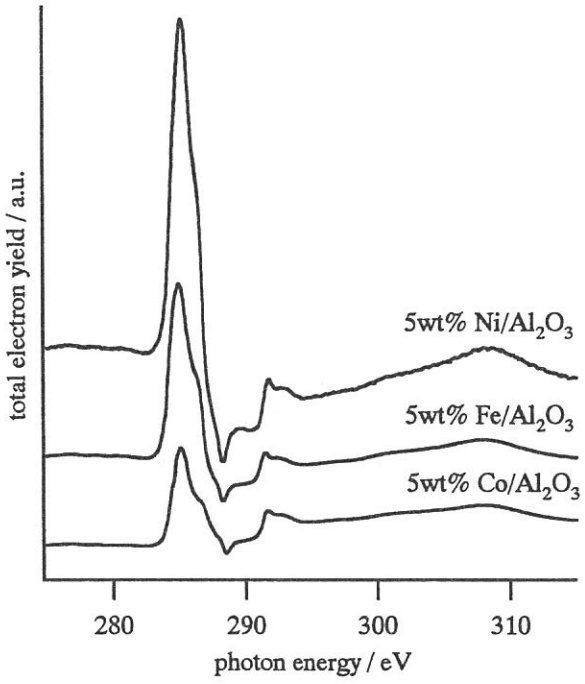

Figure 1 CK-edge XANES spectra of metal/Al_2O_3 catalysts

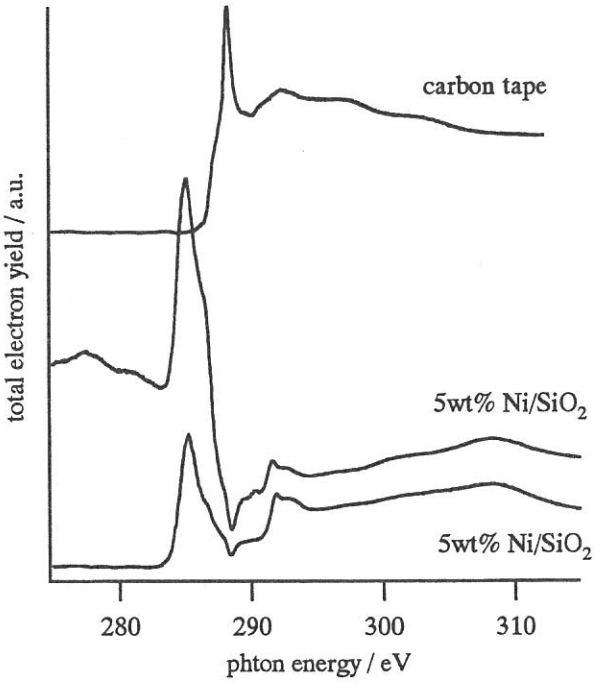

Figure 2 CK-edge XANES spectra of Ni/MgO and Ni/SiO_2 catalysts

References

[1] M. Endo, *Chemtech*, **Sept.**, 568 (1988).

[2] R. T. K. Baker, *Carbon*, **27**, 315 (1989).

[3] M. N. Rodriguez, *J. Mater. Res.*, **8**, 3233 (1993).

[4] S. Iijima, *Nature*, **354**, 56 (1991).

[5] T. W. Ebbesen, and P. M. Ajayan, *Nature*, **358**, 220 (1992).

[6] J. H. Weaver, *Science*, **265**, 611 (1994).

(BL8B1)

Electronic Structure in $Li_{1\pm x}Mn_2O_4$ Spinel Oxides from Mn *L*-edge and O K-edge XANES

Yoshiharu UCHIMOTO, Takeshi YAO, and Taiji SASADA
Department of Fundamental Energy Science,
Graduate School of Energy Science, Kyoto University,
Yoshida, Sakyo-ku, Kyoto 606-8501, JAPAN

$LiMn_2O_4$ based spinel type oxides are one of the most promising cathode materials used in lithium ion batteries because their low cost, high theoretical energy density. (1, 2) It is important to clarify the change of electronic structure during charge and discharge process in order to understand their electrochemical properties. In this study, the electronic structure of $LiMn_2O_4$ spinel oxide was determined by using a measurement of Mn L_{23}-edge and Oxygen K-edge X-ray Absorption Near Edge Structure (XANES). XANES spectra were measured on BL-8B1 at UVSOR with ring energy of 750 MeV in a mode of total electron yield.

$LiMn_2O_4$ spinel was prepared from lithium carbonate and manganese carbonate. The lithium carbonate and manganese carbonate were weighted with molar ratio as Li:Mn=1:2 and mixed for 5h. The mixture was pressed into disk and heated at 850°C for 48 hours. The crystal structure of the oxide was determined by XRD using MoKα radiation. These XRD patterns were indexed to a cubic lattice. The lattice parameters and other structural parameters were refined by the Rietveld method. The Rietveld calculation was performed on the vector processor (Cray Y-MP2E/264) at the Institute for Chemical Research, Kyoto University, by using 'Rievec' computer program (3, 4) Fig. 1 shows the results of the Rietveld analysis. The observed pattern agreed well with the calculated pattern. The obtained lattice parameters are given in Table 1. R_{wp}, R_F, and R_B are small enough to guarantee the reliability, and it was confirmed that $LiMn_2O_4$ is belonging to cubic *Fd3m* space group.

Figure 2 shows a low rate discharge curve of $LiMn_2O_4$ spinel. The $LiMn_2O_4$ spinel shows mainly 2 different plateau regions of a voltage range of 3.8-4.1 V and a voltage range of 2.8 V. XANES analysis were performed to clarify the oxidation

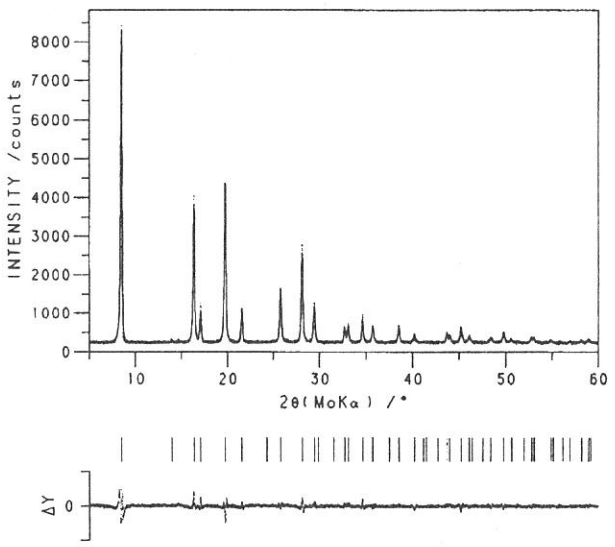

Cubic Spinel
Space group : *Fd3m*

Atom	site	x	y	z
Li	8a	0	0	0
Mn	16d	0.625	0.625	0.625
O	32e	0.3866(1)	0.3866(1)	0.3866(1)

a = 8.24941(4) Å

R_{wp},R_F,R_B = 0.0699,0.0340,0.0306

Fig. 1 The result of Rietveld analysis of $LiMn_2O_4$ .The observed and calculated XRD patterns are indicated by dots and solid, respectively. The differnce between observed snd calculated is plotted below.

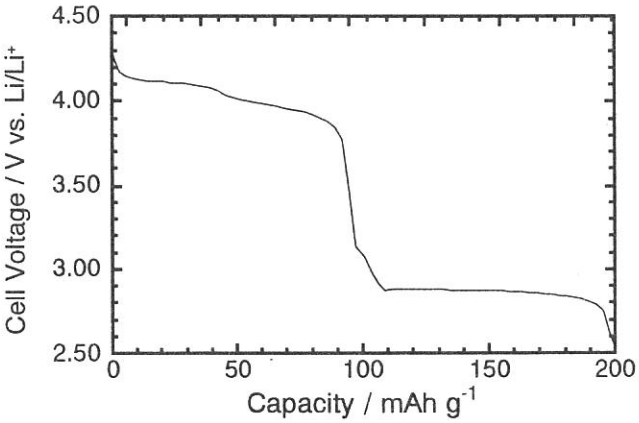

Fig. 2 Voltage versus capacity for $LiMn_2O_4$.The cell was cycled between 4.3V and 2.5V at 0.1mA / cm^2.

state of manganese and nickel for various x values in $LiMn_2O_4$ spinel.

Fig. 3 shows the Mn L-edge XANES of $Li_xMn_2O_4$ at various x values together with reference materials of MnO_2 (Mn^{4+}), Mn_2O_3 (Mn^{3+}), and $MnCO_3$ (Mn^{2+}). The spectra correspond to $Mn2p^63d^n$ to $Mn2p^53d^{n+1}$ transitions. This figure shows that the Mn L_3 absorption edge of Mn_2O_3 was about 642.0 eV and that of MnO_2 was 643.4 eV. These results indicate that increasing the oxidation state of manganese, the Mn L_3 absorption edge shifted to higher energy. As shown in Fig. 3, the peak of $LiMn_2O_4$ was a combination of peak of Mn_2O_3 and MnO_2. At low x value of the $Li_xMn_2O_4$, contribution of Mn^{4+} increased, whereas contribution of Mn^{3+} increased at large x values.

Fig. 4 shows the oxygen K-edge XANES of $Li_xMn_2O_4$ at various x. A peak at about 529 eV is attributed to the band derived from the mixing of the Mn 3d majority (spin-up) e_g and minority (spin-down) t_{2g} states with oxygen 2p states. A peak at about 531.5 eV is attributed to the band derived from the mixing of the Mn 3d minority (spin-down) e_g states with oxygen 2p states. The broad structure about 540-545 eV is attributed to band of Mn 4sp character. The peak at about 529 eV increased with decreasing lithium content. This results shows that oxidation also take place on oxygen 2p orbital and the ground state of $Li_xMn_2O_4$ ($x<1.0$) is mixed state of $3d^3$ and $3d^4L$, where L represents a ligand hole state. These results are in good agreement with the result of First-Principles calculation for $LiMn_2O_4$ spinel oxides. (5, 6) At x values above 1.2, the peak at about 534 eV appeared. The peak at about 534 eV is attributed to minority (spin-down) d_{x2-y2} state, which appeared by cubic-to-tetragonal phase transition.

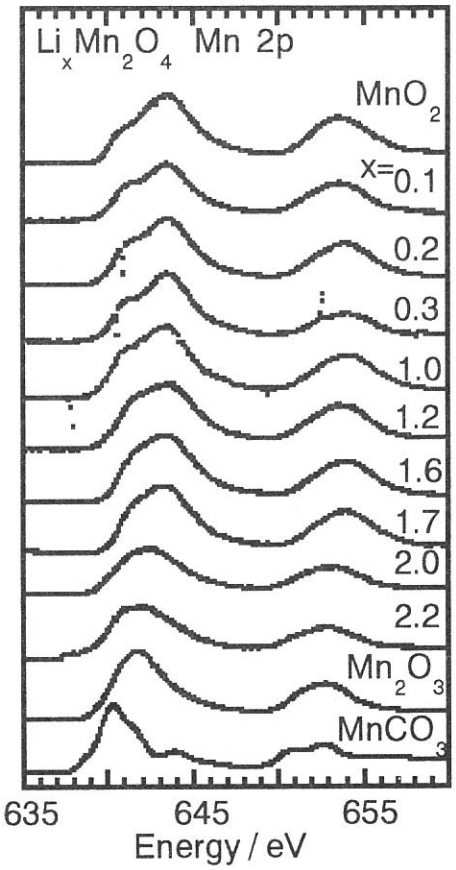

Fig.3 Mn 2p absorption spectra of $Li_xMn_2O_4$, the value of x is indicated in the figure.

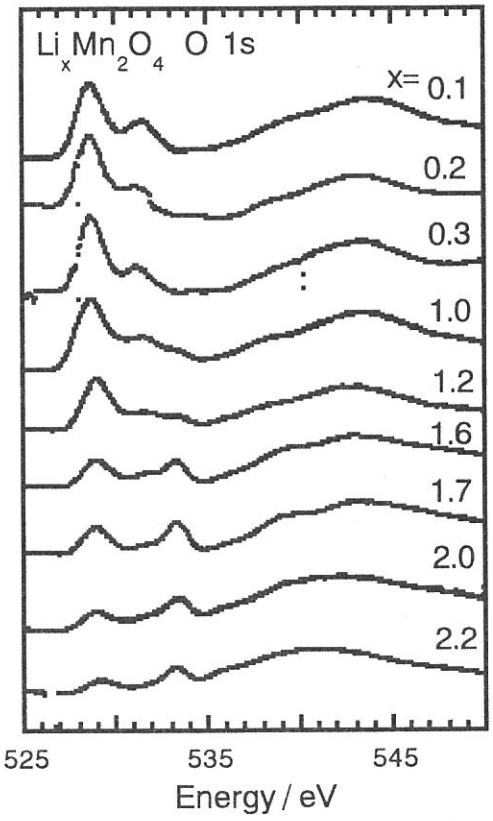

Fig.4 O 1s absorption spectra of $Li_xMn_2O_4$, the value of x is indicated in the figure.

REFERENCES

1) T. Ohzuku, M. Kitagawa, and T. Hirai, *J. Electrochem. Soc.*, **137**, 769 (1990).

2) K. Kanamura, H. Naito, T. Yao, and Z. Takehara, *J. Material Chem.*, **6**, 33 (1997).

3) T. Yao, Y. Oka, and N. Yamamoto, *J. Mater. Chem.*, **32**, 331 (1992).

4) T. Yao, T. Ito, and T. Kokubo, *J. Materials Research*, **10**, 1079 (1995).

5) S.K. Mishra and G. Cedar, *Physical Review B*, **45**, 1612 (1999).

6) M.K. Aydinol and G. Cedar, *J. Electrochem. Soc.*, **144**, 3832 (1997).

(BL8B1)

Nitrogen *K*-edge Absorption of AlInN

Kazutoshi FUKUI, Akio YAMAMOTO [1], Satoru TANAKA [2,3], Yoshinobu AOYAGI [3],
Shigeo YAMAGUCHI [4], Hiroshi AMANO [4,5] and Isamu AKASAKI [4,5]
Institute for Molecular Science, Okazaki 444-8585, Japan
Fax +81-564-54-7079, fukui@ims.ac.jp
[1] *Faculty of Engineering, Fukui University, Fukui 910-8507, Japan*
[2] *Research Institute for Electronic Science, Hokkaido University, Sapporo 060-0812, Japan*
[3] *Institute of Physical and Chemical Research (RIKEN), Wako 351-0198, Japan*
[4] *High-Tech Research Center, Meijo University, Nagoya 468-8502, Japan*
[5] *Department of Materials Science and Technology, Meijo University, Nagoya 468-8502, Japan*

The soft X-ray absorption (SXA) around nitrogen *K*-edge (N-*K*) have been measured to investigate the electronic structure of the wurzite III – V nitrides, especially the structure of the unoccupied states. The N-*K* absorption spectra of III – V nitrides near the N *K*-edge in principle represent the partial density of the final states with *p* symmetry according to the selection rule. Since the core levels are strictly localized in space, the N-*K* absorption spectrum gives us the site-specific information. The N-*K* absorption spectrum also gives us the information about the final states symmetry p_{xy} and p_z, because the incidence soft X-ray light is linearly polarized. In this report, we represent the first results of N-*K* SXA spectra of wurtzite $Al_{1-x}In_xN$ (x= 0, 0.53, 0.78, 1).

The experiments were carried out at BL8B1. Resolution power under the experimental conditions was about 0.5 eV at 400 eV. The soft X-ray absorption measurement was performed by using the total photoelectron yield (TY) method. Thin films were made by the MOCVD method at RIKEN on SiC substrates (x = 0), at Fukui University on GaAs(111) surface (x = 1) and at Meijo University (x = 0.53, 0.78) on α-Al_2O_3 substrates. All films were cleaned with organic solvents just before the installation in the vacuum chamber. No specific surface cleaning of the samples was performed in the vacuum chamber. The TY measurements were carried out at room temperature in the range of 10^{-9} Torr. Sample holder was able to rotate in the vacuum chamber for the angular dependent measurement. The incidence angle θ is defined as the angle between the incident light and the normal axis of the sample surface, i.e., c-axis. The incidence angle dependent SXA measurements were performed under the *p*-polarization configuration which means **E** parallel to *c*-axis at $\theta \sim 90^{\circ}$, where **E** was the electric field of the incident light.

Figure 1 shows the N-*K* absorption spectra of $Al_{1-x}In_xN$ (x= 0, 0.53, 0.78, 1). The energy scale is relative to the threshold energy corresponds to the conduction band minimum. The intensity is normalized at the maximum peak in each spectrum. The spectra features of AlN (x = 0) and InN (x = 1) are good agreement with the previous works [1-3]. The spectrum feature shows the structure-less spectra of x = 0.78 and, in particular, x = 0.53. Figure 2 shows the N-*K* absorption of $Al_{0.78}In_{0.22}N$ as

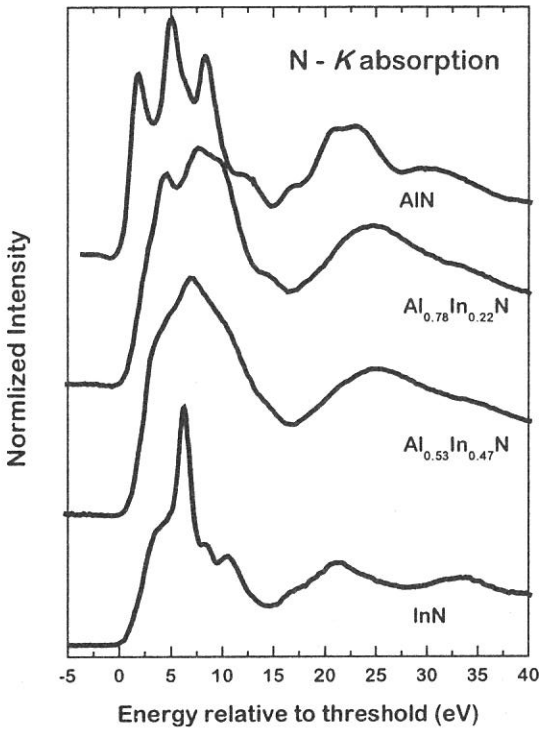

Fig.1 N-K absorption spectra of AlInN. The energy scale is relative to the threshold energy.

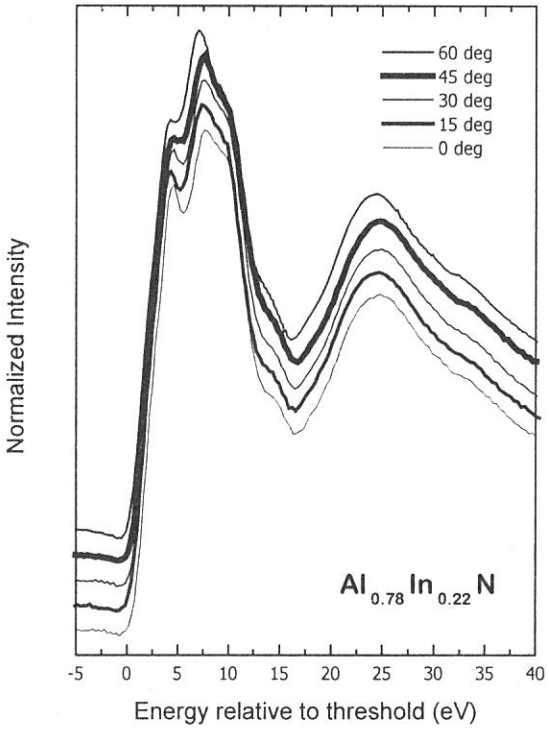

Fig.2 N-K absorption spectra of $Al_{0.78}In_{0.22}N$ as function of angle which is defined as the angles between the incident light and the normal to the sample surface (c–axis).

function of angle θ. All spectra are normalized at the peaks around 7.5 eV. The clear θ dependence can be seen at the lowest peaks and the higher energy side of the maximum peaks. These types of angular dependence are seen in $Al_{1-x}Ga_xN$ and $In_{1-x}Ga_xN$ [2,4]. However, in the spectra of $x = 0.53$ such θ dependence are not found. Both this result and the structure-less feature in Fig. 1 may correspond to the X-ray diffraction results which suggest the c-axis fluctuations of $x = 0.78$ and $x = 0.53$ samples are about 3 and 10 times larger than those of the typical $Al_{1-x}Ga_xN$ samples, respectively.

References

[1] L.-C. Duda, C. B. Stagarescu, J. Downes, K. E. Smith, D. Korakakis, T. D. Moustakas, J. Guo, J. Nordgren, Phys Rev. B **58** (1998) 1928.

[2] K. Fukui, M. Ichikawa, A. Yamamoto and M. Kamada, Solid State Electronics **41** (1997) 299.

[3] K. Fukui, R. Hirai, A. Yamamoto, S. Naoe and S. Tanaka, Jpn. J. Appl. Phys. **38** (1999) Suppl. 38-1, pp. 538.

[4] K. Fukui, R. Hirai and A. Yamamoto, UVSOR Activity Report 1998, 1999, p. 214.

(BL8B2)

Intramolecular Energy-Band Dispersion in Oriented Thin Films of n-$CF_3(CF_2)_{22}CF_3$ Observed by Angle-Resolved UV Photoemission

D. Yoshimura,[a] T. Miyamae,[b] S. Hasegawa,[b] H. Ishii,[a] N. Ueno,[c] and K. Seki [a,d]

a) Department of Chemistry, Graduate School of Science, Nagoya Univ., Chikusa-ku, Nagoya 464-8602 , Japan

b) Institute for Molecular Science, Myodaiji, Okazaki 444-8585, Japan

c) Department of Materials Technology, Faculty of Engineering, Chiba Univ., Inage-ku, Chiba 263-8522, Japan

d) Research Center for Materials Science, Nagoya University, Chikusa-ku, Nagoya 464-8602, Japan

Poly(tetrafluoroethylene) (PTFE) $(CF_2)_n$ is one of the most fundamental polymers, which is the perfluorinated analogue of polyethylene $(CH_2)_n$ with a simple repeating CF_2 unit. PTFE has been widely used for chemical, medical, and high-performance electronic applications due to its excellent chemical stability, low dielectric constant, small dielectric loss, low surface energy, and excellent charge-storage capability. Many of the above mentioned interesting chemical and physical properties of PTFE are related to its valence electronic structures, and its elucidation is important from the viewpoints of both basic science and practical applications.

The electronic structures of PTFE and its oligomers have been studied both experimentally and theoretically. The use of oligomers is based on the theoretical and experimental findings that oligomers more than ten repeating units have very similar electronic structures with infinite polymers. An interesting aspect of such calculations is that a chain in an extended ordered form can be regarded as a one-dimensional crystal, and we can expect the formation of intramolecular one-dimensional bands with intramolecular energy band dispersion ($E = E(\boldsymbol{k})$) relation, where $\boldsymbol{k}$ is the wavevector along the chain. Many calculations for a PTFE chain have indicated large widths of the bands of the order of 5 eV due to the strong interatomic covalent bond within the chain. Unfortunately, however, there were no experimental results to be compared with such calculated intramolecular energy band dispersion relation besides the indirect information of DOS.

In the present work, we report on ARUPS studies of oriented thin films of perfluorotetracosane n-$C_{24}F_{50}$ (PFT), an oligomer of PTFE, prepared by in-situ vacuum evaporation. Thin PFT films showed drastic spectral changes depending on various experimental parameters. In particular, from the $h\nu$ dependence of the normal emission spectra we could successfully determine the intramolecular energy-band dispersion.

ARUPS measurements were carried out at the beamline 8B2 of the UVSOR facility at Institute for Molecular Science. The sample of PFT supplied from Aldrich was used without further purification. Thin films of PFT were prepared by vacuum evaporation at room temperature onto n-doped Si(100) substrates. The pressure during the evaporation was about 4×10^{-9} Torr. Before introducing into the chamber, the substrates were rinsed by acetone for 10 min. The thickness of PFT was about 10 nm as monitored by a quartz oscillator, and the deposition rate was about 0.5 nm/min. For PFT, X-ray diffraction,[1] NEXAFS,[1] and VUV absorption measurements revealed that the molecules in evaporated films prepared in a similar way are well oriented with their long axes vertical to the substrate surface.

In order to minimize the radiation damage, the incident light intensity was reduced less than 50 pA, and the sampling position of specimen was changed after several runs. The absence of the damage effect was confirmed by remeasuring spectra under fixed experimental parameters.

The $h\nu$ dependence of the spectra of the PFT thin film for photoelectrons emitted normal to the surface at $22 \leq h\nu \leq 60$ eV is shown in Fig. 1. The emission intensities of these spectra are normalized by the photon flux of the incident photon energy. The main features show continuous and significant changes in both peak positions and intensities. In the upper part of the valence bands extending from 10.5 to 14.5 eV, the position of peak A slightly changes at around $h\nu = 30$ eV, and shifts towards higher binding energies with increasing photon energy for $h\nu \geq 34$ eV. Another feature B is observed for $h\nu \leq 28$ eV. In the F_{2p} region at 14.5 – 18 eV (peak C), drastic changes in the intensity are seen.

We attribute the peak shifts to the intramolecular energy-band dispersion. The dispersion relation can be determined according to the method reported in ref. 2 by assuming that the photoexcitation are dominated by direct transitions, and the final state follow the dispersion relation of a nearly free-electron-like parabola. Considering the initial state broadening of $\boldsymbol{k}$ (or relaxation of $\boldsymbol{k}$-conversation rule) due to the small number of repeating units, we can regard the PFT molecules have sufficient number of repeating units for mapping the energy band structure.[3] In Fig. 2, we display the experimentally derived band structure obtained by the procedure as described in ref. 2. In order to map out the energy-band dispersion, we took the second derivative of the ARUPS spectra after smoothing for specifying the energies of the spectral features. We assumed the length of repeating unit as 2.6 Å. In this figure, the bright regions correspond to the bands. For comparison, we also show the results of an ab initio band calculation for a PTFE chain in planar-zigzag geometry by Seki et al.[4] The energy-scale of the calculated band structure was 0.95 times contracted and shifted 1.8 eV to the higher binding energy side. We also compare another calculated band structures, but good correspondence is not obtained at the whole

energy region. The correspondence between the observed and calculated band structure is fairly good, although there are differences in details. In particular, the detailed shape of the topmost band is quite different.

There are several possible origins of such difference between the observed and calculated band structures. First, the calculation assumed a planar molecular structure, while the actual PTFE chain has a helical structure.[5] Energy band calculations for PTFE in helical- and planar-zigzag- configurations indicate dihedral-angle difference in the calculated DOS. Especially, the shape of the topmost band shows the dihedral-angle dependence, although the shapes of the topmost band in these calculations with helical form are still quite different from the observed one. The second is that the accurate band structure may not be directly observed because low $h\nu$ is used for the excitation. In the case of ARUPS measurements of polyethylene, the top portion of the valence bands is not observed when low $h\nu$ light was used for the excitation although the reason is unknown.[2] Thirdly, the interference pattern of electron waves leading to the $\boldsymbol{k}$ conservation rule may be different between the helical structure with a long repeating unit of ~ 13 carbons and that in the assumed planar-zigzag structure with a repeating period of only 2 carbon atoms.

Although no satisfactory quantitative explanation is available for the observed difference at present, these points may be clarified by better calculations. In particular, the calculation of photoemission intensity by using independent-atomic-center (IAC) and single-scattering approximations combined with molecular orbital (MO) calculations have been successfully applied to the analysis of the photoelectron angular distribution for oriented organic thin films and the energy-band dispersion of solid surface.[6,7] We are currently performing such calculations.

REFERENCES [1] K. Nagayama, R. Mitsumoto, T. Araki, Y. Ouchi, and K. Seki, Physica B **208/209**, 414 (1995).
[2] K. Seki, N. Ueno, U. O. Karlsson, R. Engelhardt, and E. E. Koch, Chem. Phys. **105**, 247 (1986).
[3] T. Miyamae, S. Hasegawa, D. Yoshimura, H. Ishii, N. Ueno, and K. Seki, J. Chem. Phys., in press.
[4] K. Seki, H. Tanaka, T. Ohta, Y. Aoki, A. Imamura, H. Fujimoto, H. Yamamoto, and H. Inokuchi, Phys. Scripta **41**, 167 (1990).
[5] C. W. Bunn and E. R. Howells, Nature **174**, 549 (1954).
[6] N. Ueno, A. Kitamura, K. K. Okudaira, T. Miyamae, S. Hasegawa, H. Ishii, H. Inokuchi, T. Fujikawa, T. Miyazaki, and K. Seki, J. Chem. Phys. **107**, 2079 (1997).
[7] D. Yoshimura, H. Ishii, Y. Ouchi, E. Ito, T. Miyamae, S. Hasegawa, K. K. Okudaira, N. Ueno, and K. Seki, Phys. Rev B **60**, 9046 (1999)

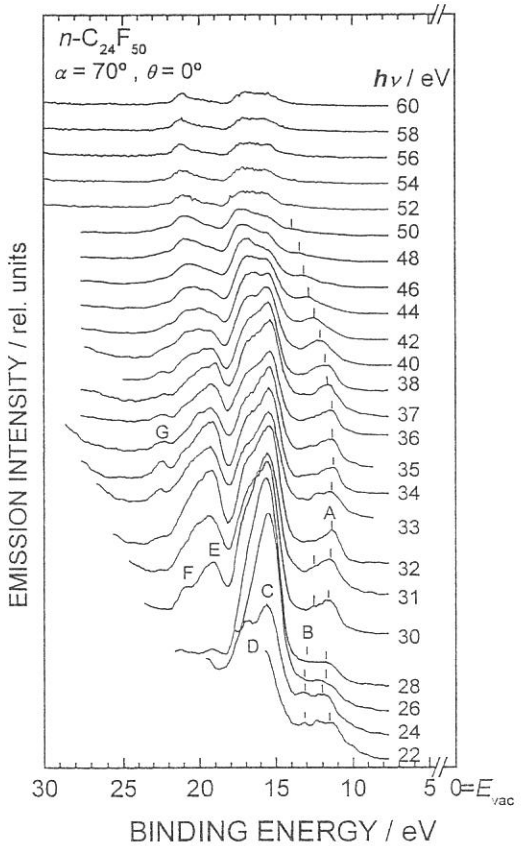

Fig. 1. $h\nu$-dependence of the normal-emission spectra of PFT thin films for $\alpha = 70°$.

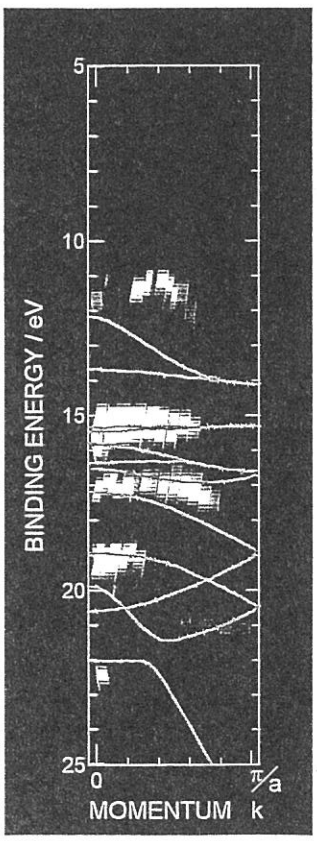

Fig. 2. Experimentally determined band structure for PFT.

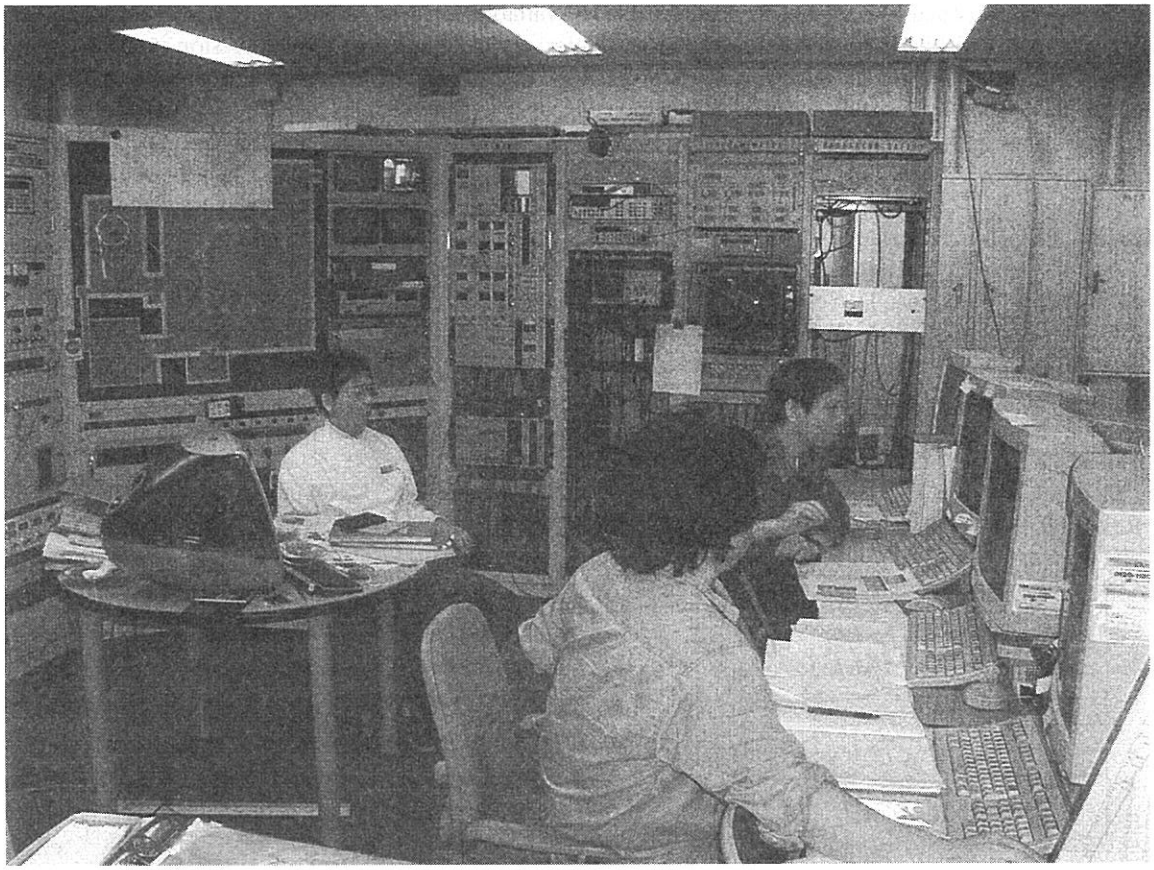

Injection is started!!

UVSOR

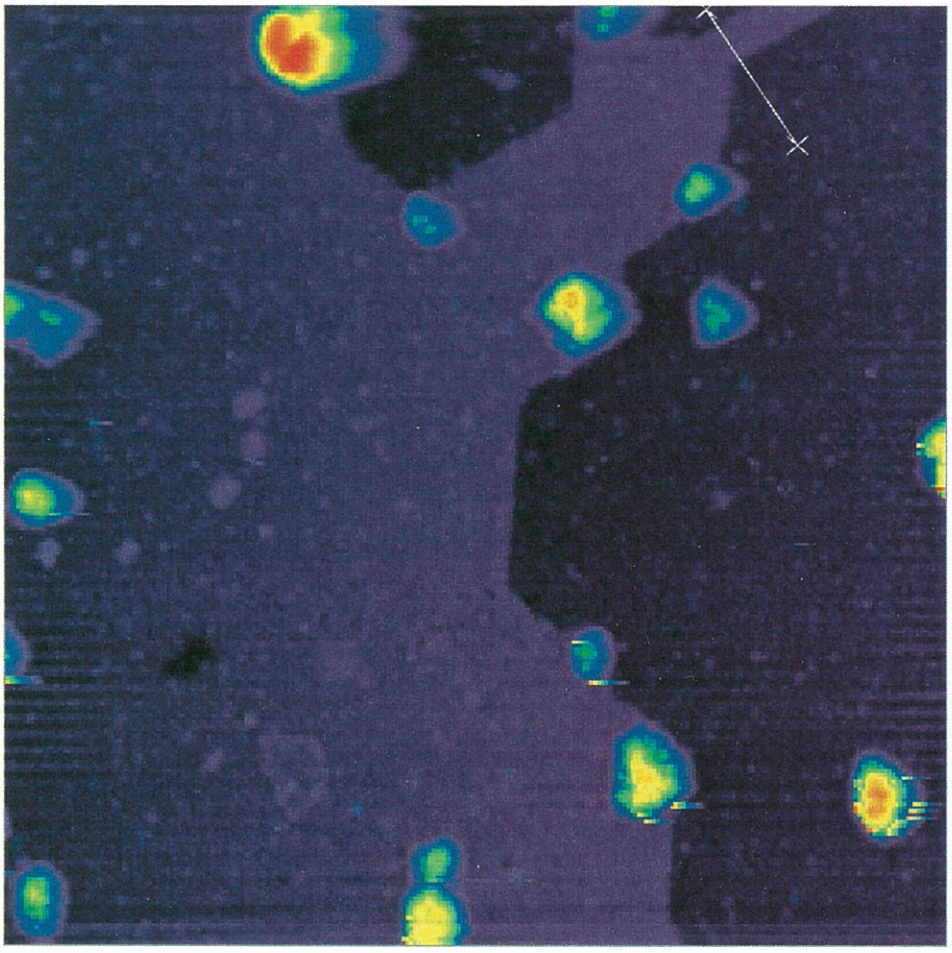

Surface & Photochemistry

BL2B1, 3A1, 4A1, 4B, 5A, 5B, 6A2, 8A

Electronic states of organic molecule/Si surface hybrid systems

Jun Yoshinobu, Yoshiyuki Yamashita, Kozo Mukai, Kanae Hamaguchi,
Shin-ichi Machida, Masashi Nagao and Fumiko Yasui

The Institute for Solid State Physics, University of Tokyo
7-22-1 Roppongi, Minato-ku, Tokyo 106-8666, Japan
(e-mail: yoshinobu@issp.u-tokyo.ac.jp)

In order to explore the candidate systems for nano-scale molecular device and chemical sensor, bonding and structures of several unsaturated hydrocarbons (ethylene, cyclopentene, cyclohexene, and 1,4-cyclohexadiene) chemisorbed on Si(100) have been investigated by means of photoelectron spectroscopy (PES) for both valence region and core level, scanning tunneling microscopy (STM) and high-resolution electron energy loss spectroscopy (HREELS).

Here we report some experimental results about adsorbed molecular systems using UVSOR-BL5A. Experiments have been performed in the UHV chamber including the apparatus for low energy electron diffraction (LEED), Auger electron spectroscopy (AES), photoelectron spectroscopy (PES) and gas dosing. The Si sample used was a Si(100) 5° vicinal surface. The clean one-domain Si(100)(2x1) surface was prepared by several flashing cycles up to ~1250℃ and annealing at ~600℃. The PES spectra of Si 2p and valence region were measured for the clean Si(100), saturated chemisorption layer and multilayer surfaces.

Ethylene on Si(100)(2x1) is a well established system which is di-σ bonded to the Si dimer [1]. The formation of this di-σ bond is due to the interaction between the π orbital of ethylene and the Si dangling bond. Adsorbed ethylene is stable up to 550-600K [1,2]. Thus, using such surface reaction including the di-σ bond formation, atomically controlled interface could be fabricated between an unsaturated hydrocarbon molecule and the Si(100) surface.

Hamers et. al. have reported that adsorbed cyclopentene molecules are well ordered on Si(100(2x1) and the molecule stands up on the surface by the use of STM and multiple internal reflection infrared absorption spectroscopy [3]. The present PES results have clearly indicated that the π orbital of cyclopentene and the Si dangling bond are interacted. Both PES and HREELS results indicate a single adsorption state. The electronic structure of the adsorbed cyclopentene is quite similar to cyclopentane.

In the case of cyclohexene adsorbed on Si(100), the situation is different. The PES spectra in valence and Si 2p regions are somewhat complex. Our STM observation shows that there are two adsorption states at least. According to the HREELS measurements, cyclohexene adsorbs molecularly. Two adsorbed states may originate from two different conformational isomers ("boat" and "chair" conformations) on the surface.

1,4-cyclohexadiene takes a single adsorption state on Si(100) according to the STM, HREELS and valence PES results. Valence PES shows that only one of two π orbitals of the molecule reacts with the Si dangling bond. Here an upright (standing-up) structure is proposed for the adsorbed molecule; the remaining π orbital protrudes towards the vacuum. Thus, this system may be a good candidate system for successive chemical reaction to fabricate more complex structure on the surface [4].

References

[1] J. Yoshinobu et.al., J. Chem. Phys. 87(1987)7332.
[2] L.Clemen et. al., Surf. Sci. 268(1992)205.
[3] R. J. Hamers et. al., J. Phys. Chem. 101(1997)1489.
[4] J. T. Yates, Jr., Science 229(1998)335.

(BL2B1)

Cs Adsorption on ZrC(111)

Kenichi OZAWA, Takashi YOSHII, Tetsu NODA, Kazuyuki EDAMOTO, Shinichiro TANAKA[1], Shigeki OTANI[2]

Department of Chemistry and Materials Science, Tokyo Institute of Technology, Meguro-ku, Tokyo 152-0033, Japan

[1] *Institute for Molecular Science, Okazaki-shi, Aichi 444-8585, Japan*

[2] *National Institute for Research in Inorganic Materials, Tsukuba-shi, Ibaraki 305-0044, Japan*

Room-temperature adsorption of Cs on the ZrC(111) surface has been studied by core-level photoemission spectroscopy. The work function of the substrate surface decreases monotonically upon Cs adsorption and approaches to the Cs metal value without showing a clear work function minimum. The Cs 4*d* core-level lineshape analysis indicates that the plasmon loss peak appears already in the very initial stages of adsorption. These results suggest that the adsorbed Cs atoms are in a metallic state by forming Cs islands and that adsorption proceeds via a growth of these islands.

1 Introduction

Alkali-metal adsorption has been attracted much attention because they are utilized for promoting a variety of surface chemical reactions, improving the electron emission from cathods, etc. Transition metal carbides (TMCs) are known to be a potential material for stable field electron emitters and catalysts which can be used in the extreme condition. Thus, adsorption of alkali metals on TMC surfaces are of great interest from the technological point of view.

Recently, we have investigated alkali-metal adsorption adsorption on the group IV and V TMC surfaces and found that the adsorption process is different depending on the low-index surfaces, i.e. (100) and (111) [1]. On the (100) surfaces, alkali metal adatoms tend to condence to form islands from the relatively low coverages. However, an ion-to-metal transition characterizes the adsorption process of alkali metals on the (111) surface. In the present study, we have investigated the adsorption process of Cs on ZrC(111) utilizing core-level PES in order further to elucidate the atom adsorption process on the TMC surface.

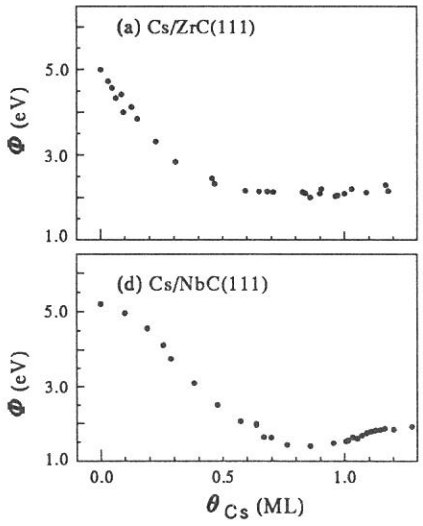

Fig. 1. (a) The work function change of ZrC(111) as a function of θ_{Cs}. (b) The work function change of NbC(111) as a function of θ_{Cs}.

2 Experimental

The core-level PES measurements utilizing synchrotron radiation were carried out at Beam Line 2B1, where the light was dispersed by a grasshopper monochromater. The photoelectron energy was analyzed by a double-pass cylindrical mirror analyzer. The ultrahigh vacuum (UHV) chamber was also equipped with an low energy electron diffraction (LEED) optics for the surface structural analysis and a mass spectrometer for the check of residual gases. The base pressure in the UHV system was less than 1.5×10^{-8} Pa.

A single crystal of $ZrC_{0.9}$ was grown by the floating-zone method at the National Institute for Research in Inorganic Materials. The (111) surface was cleaned by flashing to $\sim$ 1800 K in the UHV chamber with electron bombardment from the rear of the sample disk. The Cs atoms were deposited on the surface at room temperature using a thoroughly outgassed commercial SAES dispenser.

3 Results and Discussion

Fig. 1a shows the Cs coverage (θ_{Cs}) dependence of the work function Φ of the ZrC(111) surface. As the surface is covered with Cs, Φ first decreases and approaches to 2 – 2.2 eV at $\theta_{Cs} > 0.6$ monolayer (ML). The total decrease is ~ 3 eV. For comparison, the change in Φ for the Cs/NbC(111) system is shown in Fig. 1b. A similar behavior is seen in the Φ curve, i.e. a sharp decrease up to 0.8 ML. However, in contrast to the Cs/ZrC(111) system, further Cs adsorption on NbC(111) leads to a slight increase of ~ 0.5 eV in Φ, forming a clear work function minimum. Φ approaches to ~ 2 eV after the minimum for Cs/NbC(111) as in the case of Cs/ZrC(111). Considering that the work function of Cs metal is 2.14 eV [2], the property of the Cs overlayers at high coverages on both ZrC(111) and NbC(111) should be similar to that of Cs metal.

The metallization of the Cs overlayer at high θ_{Cs} is also proved from the Cs 4d core-level photoemission peak. The lower spectrum of Fig. 2a is the Cs 4d core-level spectrum for the 0.83 ML Cs-covered surface. The lineshape analysis reveals that the observed peak is composed of at least three components; one forms a main line and the other two components contribute to the tail structure to the high binding energy side of the main line. The latter two components are quenched by oxygen adsorption (upper spectrum of Fig. 2a). Moreover, the separation energies of these peaks from the main line are 1.9 and 4.7 eV, which are in good agreement with the energies of single and double losses of the Cs overlayer plasmon. Thus, the Cs overlayer at 0.83 ML has a metallic nature.

However, a similar tail structure is already observed at the Cs coverages of as low as 0.02 ML (Fig. 2b). A second component, shown as a shaded peak, is observed at the higher binding energy side of the main line by 1.9 eV. This is in good agreement of the plasmon energy, and thus the second component is attributed to the plasmon loss peak. In order to form a metallic overlayer in such a low coverage region, the Cs adatoms should condense to give a direct Cs–Cs interaction, which is requisite to form a Cs 6s metallic band. The work function change for this system also supports island formation from the low coverages. Fig. 1a shows that Φ decreases monotonically and approaches to the Cs metal value. This is in contrast to the work function change for Cs/NbC(111); the work function curve has a clear minimum at $\theta_{Cs} \simeq 0.8$ (Fig. 1b). Our recent study for the Cs/NbC(111) system has shown that, while the adsorbed Cs layer is metallic at high coverages, the Cs adatoms are partially ionized in the initial stages of adsorption [1]. Fig. 2c shows a lineshape

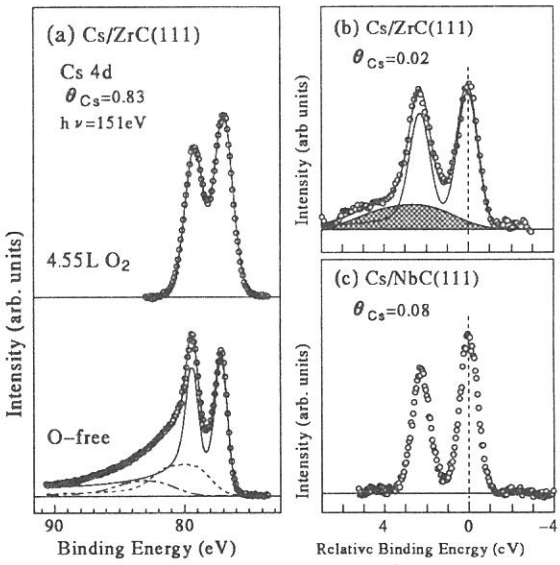

Fig. 2. Background-subtracted Cs 4*d* core-level spectra. Open circles are the observed data and the solid lines are the result of the lineshape analysis: (a) The Cs 4*d* spectra for the Cs-covered ZrC(111) surface ($\theta_{Cs} = 0.83$ ML) and for the 0.83 ML Cs-covered surface which is exposed to 4.55 L oxygen. (b) The Cs 4*d* spectrum for Cs/ZrC(111) at $\theta_{Cs} = 0.02$ ML. (c) The Cs 4*d* spectrum for Cs/NbC(111) at $\theta_{Cs} = 0.08$ ML.

of the Cs 4*d* peaks at $\theta_{Cs} = 0.08$, where adsorbed Cs is in an ionic state. Here, no tail structure associated with the plasmon loss is observed and the peaks are composed of two symmetric lines. This clearly demonstrates that the Cs adatoms are not in a metallic phase at low coverages. It is known that a depolarization process and the successive metallization of the alkali-metal overlayer lead to a minimum in the work function curve. Thus, the absence of the work function minimum for Cs/ZrC(111) implies that Cs adsorption proceeds without the formation of the surface dipole moment at low θ_{Cs} and its depolarization with increasing θ_{Cs}. The gradual approach of the work function to the value of Cs metal is, then, simply explained by a growth of the region covered with the Cs islands.

References

[1] K. Ozawa, S. Ishikawa, K. Edamoto, H. Kato and S. Otani: Surf. Sci. **419** (1999) 226, and references cited therein.

[2] H.B. Michaelson: J. Appl. Phys. **48** (1977) 4729.

(BL2B1)

Ion desorption from TiO_2(110) surface

Shin-ichiro Tanaka[A], Kazuhiko Mase[B], Mitsuru Nagasono[C], Shin-ichi Nagaoka[D] and Masao Kamada[D]

[A]*Department of Physics, Graduate School of Science, Nagoya University, Nagoya 464-8602, Japan*
[B]*Institute of Material Structure Science, 305-0801, Tsukuba, Japan*
[C]*MAX-lab, Lund University, Box 118, S-221 00 Lund, Sweden*
[D]*Institute for Molecular Science, Myodaiji, Okazaki, 444-8585, Japan*

Desorption induced by electronic transition (DIET) from solid surfaces has been extensively studied in these decades. A general mechanism of ion desorption induced by core-level excitation has been proposed by Knotek and Feibelman, and been widely accepted as a standard mechanism. In the KF mechanism, a Ti3p core hole is produced by a primary excitation, and decays via an inter-atomic Auger process, because there are no higher-lying occupied electronic states at the Ti site (i.e., "maximal valency"), and thus an intra-atomic Auger decay is prohibited. If two Auger electrons and an additional electron are emitted from the oxygen atom, the remaining O^+ ion desorbs as a result of the Coulomb repulsion from the surrounding Ti^{4+} ions. However, results which contradict the KF model have been observed in several materials, e.g., Ti_2O_3, Na_xWO_3, Cr_2O_3. In these materials, O^+ desorption has been observed although the "maximal valency" criterion is not satisfied. Furthermore, an electronic configuration of $(Ti3d)^0(O2p)^6$ which has been assumed in the KF mechanism is not true. Recent theoretical studies have shown that the electronic states of the TiO_2 can not be explained with a single configuration, but instead a mixture of $Ti3d^n\underline{L}^{10-n}$ configurations is present. Here $\underline{L}$ and n stand for a hole in the oxygen (ligand) 2p orbital, and a nominal number of transferred charge from O2p to Ti3d through the hybridization between them, respectively. Thus, the "maximal valency" condition is not satisfied in TiO_2.

The electron–ion coincidence spectroscopy has been recently developed, and proved to be a very powerful tool for investigating the dynamics of the ion desorption induced by the core-level excitation and decay process. In the present report, the ion desorption induced by the core-level excitation is investigated by using the synchrotron radiation and the electron-ion coincidence technique. All the experiments were carried out at the BL-2B1. The TiO_2(110) surface was cleaned by a number of cycles of Ar^+ ion sputtering and annealing. For removing the vacancy of oxygen at the surface, the sample was heated in the 10^{-6} Torr of oxygen once in three hours.

Figure 1 shows the photoelectron spectrum in the region of the O1s- and Ti2p-related Auger electrons (left part) and a series of electron-ion coincidence spectra (right part) of the photoelectron indicated by bars in the left part. The photon energy was 560 eV. Normalization were carried out using the total amount of signals mostly consisting of backgrounds, which were proportional to the photoelectron intensities. In fig.1, the peaks observed at about 1100 nsec are ascribed to the desorption of O^+. By assuming that the photoelectron intensity is proportional to the population of the final state of the Auger decay, the intensity of O^+ peak in the coincidence spectrum correlates to the desorption efficiency which is a function of the final state of the Auger decay. Peak area intensities derived from the summations of counts in the O^+ peaks (1048-1200 nsec) from the backgrounds and their errors derived from the standard deviation of the backgrounds are shown in figure 2 together with the photoelectron spectra.

At first, we discuss the ion desorption induced by the O1s core decay. Figure 2 indicates that O^+ yields does not correspond to the O-KVV Auger electrons. This can be related to the fact that oxygen in TiO_2 is nominally O^{2-}, therefore three electrons have to be removed from the oxygen atoms for the desorption of O^+. The final state of the normal Auger decay has only two holes at the valence band, and an additional process is necessary to produce O^+. The O^+ coincidence yield observed in the right panel of fig. 2 does not correspond to the normal Auger electron emission $[(O1s)^1(O2p)^6 \rightarrow (O1s)^2(O2p)^4]$ but to the shake-up Auger decay of O1s $[(O1s)^1(O2p)^6 \rightarrow (O1s)^2(O2p)^3(O3s)^1]$, which is minor process and can not be observed in the photoelectron spectrum. This is consistent with the recent photoelectron-photoion coincidence spectroscopy results, where the O^+ coincidence peak of the O1s shake-up satellite of O2p→O3s transition was larger than that of the O1s main peak. In this case, the shake-up excitation during the excitation and the following normal Auger decay $[(O1s)^1(O2p)^5(O3s)^1 \rightarrow (O1s)^2(O2p)^3(O3s)^1]$ produces three holes as a final state. This is a sort of an expansion of the KF mechanism although it is an intra-atomic process.

The desorption process induced by the Ti2p excitation, on the other hand, seems to be very different. In the photoelectron spectra, the Ti-$LM_{2,3}V$ and Ti-LVV electrons are observed (fig. 2). If the electronic configuration in the valence band of TiO_2 were assumed to be $(O2p)^6$ as in the KF model, this transition would be inter-atomic Auger transition. However, the O^+ desorption yield (normalized for the photoelectron intensity) does not result in a peak at the position of the (nominal) inter-atomic Auger transition or the shake-up transition. Instead, the O^+ desorption yield increases when a Ti3p hole is created as a final state of the Ti2p-initiated Auger decay. In fact, the Ti-LMV and Ti-LVV Auger transitions are not inter-atomic decay, but intra-atomic decay

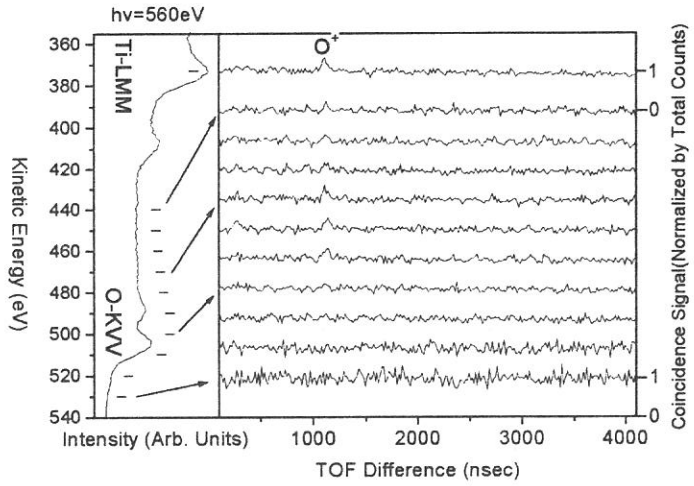

Figure 1

within the Ti site, because the charge transfer from O2p to Ti3d orbitals through their hybridization provides the Ti3d electron. Thus, the application of the KF model, in which the Ti3p:O2p:O2p inter-atomic Auger takes place because the Ti3p:Ti3d:Ti3d intra-atomic Auger decay is prohibited ("maximal valency"), is questionable.

Thus, another mechanism should be considered as the driving force for the creation of the O^+ and its desorption from TiO_2(110) surface. According to the systematic study of the 3d transition metal oxides, a cluster model calculation based on the impurity Anderson model could successfully simulate the core photoelectron spectra using only a limited set of parameters. In the final state of the core level photoemission of 3d transition metal oxide, the core hole potential (U_{dc}) at the metal site pulls down the energy of the 3d levels, enabling a charge transfer from the O2p to metal to screen the core hole. A charge transfer from O2p to Ti3d through their hybridization (V_{eff}) is therefore a good candidate for the driving force of the O^+ desorption from TiO_2(110) surface. It is likely to expect that a Ti3p core hole created by the Auger decay of Ti2p (and other core levels) can cause the charge transfer. This charge transfer may provide not only the change of the oxygen charge but also the re-arrangement of the valence electrons, which can add a repulsive potential due to an anti-bonding character of the new electronic states of the valence band. We would like to stress that this kind of re-arrangement of electronic configurations due to the core-hole potential is a multi-electron effect in solids. Therefore, a simple explanation such as that the main line corresponds to the single electron excitation and the satellite line corresponds to the two electron excitation in the photoelectron spectrum, which was valid in the O1s excitation, is not applicable to the excitation and decay of the Ti core level. Instead, the final state of the main line as well as the satellite line of Ti-related photoexcitation is due to a mixture of several electronic configurations, thus no shift was observed in fig. 2, and no enhancement of the O^+ yield was observed at the satellite line compared to the one at the main line of Ti-core levels in the photoelectron-photoion coincidence spectra.

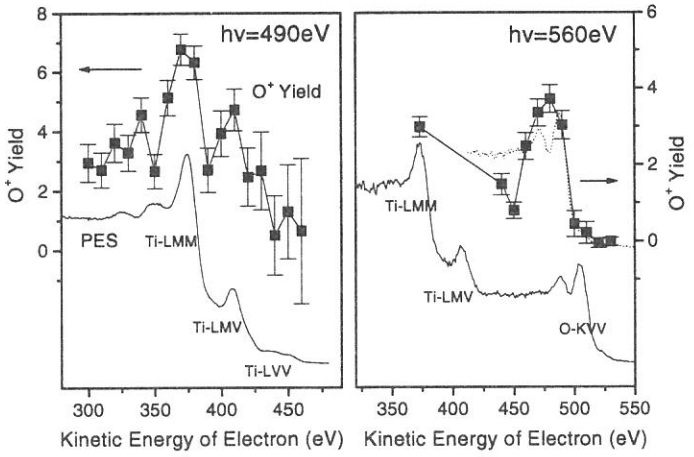

Figure 2

The new model can explain many of the results in the ion desorption from solid surfaces. This mechanism can be applied to early transition-metal compounds whose V_{eff} (mainly determined by number of the vacancy at the d orbital) is large. Thus, our model can explain the O^+ desorption not only from TiO_2, WO_3 and V_2O_5, but also from Ti_2O_3, Na_xWO_3 and Cr_2O_3, which could not be explained by the KF model. In late transition-metal compounds, V_{eff} is smaller, and thus the ion desorption is not expected, which is consistent with the experimental results. This model can also be applied to the early f-electron metal compounds like La_2O_3 and Er_2O_3 because the charge-transfer from O2p to metal f orbitals can be treated in a similar way as the one from O2p to metal d orbitals. In non-transition metal compounds, the mechanism can not be applied and it is expected that an excitation at the metal site does not yield the ion desorption. No ion desorption actually could observed in MgO and CaF_2 as a result of the Mg1s and Ca2p excitation. Thus, our model is more appropriate as a mechanism of the ion desorption from solid surfaces than the KF model.

(BL2B1)

O1s Core level shift on the Amorphous Ice Surface

Shin-ichiro Tanaka[A], Kazuhiko Mase[B], Mitsuru Nagasono[C], Shin-ichi Nagaoka[D] and Masao Kamada[D]

[A]*Department of Physics, Graduate School of Science, Nagoya University, Nagoya 464-8602, Japan*
[B]*Institute of Material Structure Science, 305-0801, Tsukuba, Japan*
[C]*MAX-lab, Lund University, Box 118, S-221 00 Lund, Sweden*
[D]*Institute for Molecular Science, Myodaiji, Okazaki, 444-8585, Japan*

Core-level photoelectron spectroscopy, also referred as XPS (X-ray photoelectron spectroscopy), has been used to investigate solids and solid surfaces. It is surface sensitive due to the small escape depth of the photoelectrons. The electron-ion coincidence (EICO) spectroscopy has been developed and used in order to investigate the mechanism of the ion desorption stimulated by the core excitation and to investigate the cite specific photochemistry in several systems. In EICO, only a photoelectron to correlate an ion desorption, i.e., a photoelectron ejected from the atoms from which ions desorb, can be detected. Considering the shorter escape depth of the ions than the electrons, the EICO spectroscopy is expected to give an information of electronic properties which is much more sensitive to the surface compared to the ordinal XPS. Thus, the EICO spectroscopy may be applicable not only to the investigation of the ion desorption from solid surfaces but also as a new tool for surface analysis.

In the present study, the EICO technique is applied to the ice surface for detecting the surface core level shift of the O1s level. Since the nature of the ice surface is of critical importance in many fields, extensive studies has been carried out. Although the photoelectron spectroscopy of the ice has been studied, there have been no study that reported the core level shift of O1s level on the ice surface to our knowledge. Ion desorption stimulated by the electron transition from the ice surface has been investigated theoretically, by the electron impact and by the photons of the O1s excitation region. According to these studies, the H^+ desorption after the O1s excitation is induced by the two hole final states of the Auger decay.

The experiments were carried out in a UHV chamber located at BL2B1 with a grasshopper monochromator (grating: 1800/mm). The chamber was equipped with a home-made EICO apparatus consisting of a cylindrical mirror analyzer (CMA) for electrons and a time-of-flight (TOF) mass analyzer for ions. Amorphous ice film was produced on the TiO_2(110) surface exposed to gaseous water at 100K. Water was dosed via a stainless steal tube located in front of the sample with a pulsed valve. Film thickness of the ice was thick enough to exclude the affect of the substrate on the ion desorption and thin enough to avoid the charging effect. Measurements were carried out at 100K.

The figure below shows a series of photoelectron-photoion coincidence (PEPICO) spectra of amorphous ice taken at hν=680eV in the region of the O1s phototelectron in 0.5 eV steps. The desorption of H^+ in coincidence with the O1s photoelectrons are observed at around 250 ns, the intensity of which shows a maximum near the kinetic energy of 139 eV. Any other species like O^+ and OH^+ were not observed due to

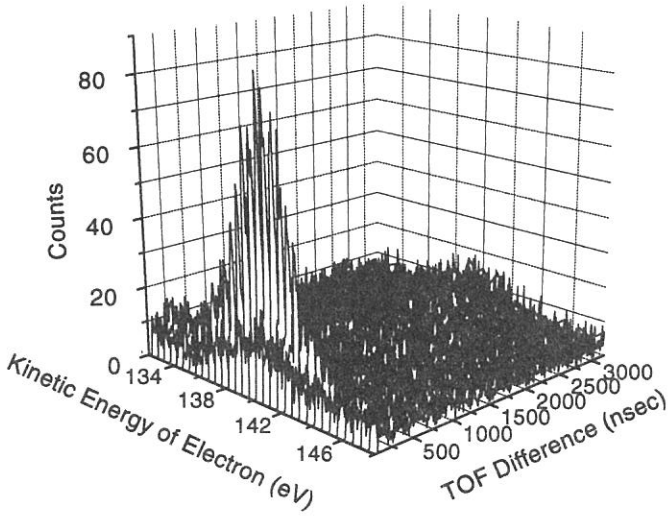

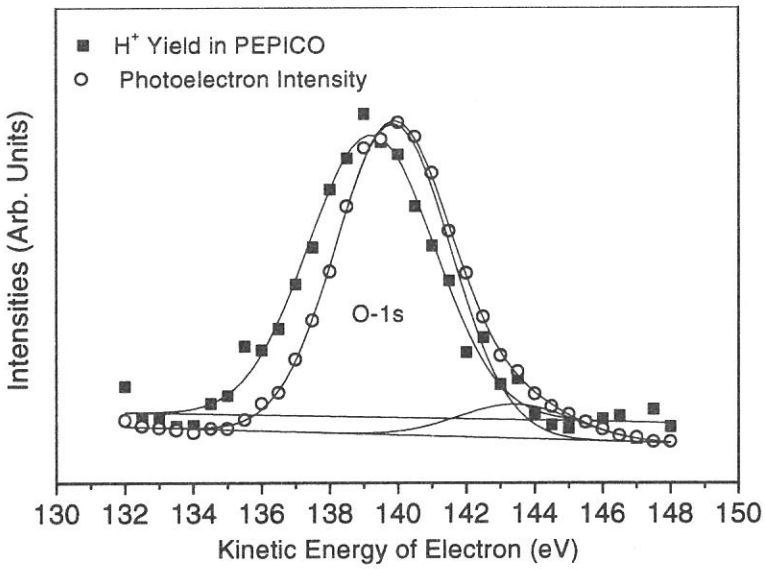

smaller desorption efficiencies. The desorption of H^+ is due to the repulsive final states as a result of the decay of the O1s hole. The energy of photons was far beyond the O1s threshold, and thus the effect of the excitation to the specific boundary state, e.g., $4a_1$ antibonding state, can be eliminated. The peak of the H^+ PEPICO yield spectrum, however, did not precisely agree with the peak in the photoelectron spectrum. In the figure above, area intensities of H^+ peak (200-320 nsec) in the PEPICO spectra (solid square) are plotted together with photoelectron intensities obtained simultaneously (open circle) as a function of the kinetic energy of photoelectrons. Lines are Gaussian curves with linear backgrounds as a result of the least square fitting calculation. A small component at ~144 eV in the photoelectron spectrum is due to the O1s emission from the TiO_2 substrate. Obviously, the H^+ yield is not in agreement with the photoelectron intensity. In fact, the peak position of the H^+ desorption yield is shifted to lower kinetic energy by about 0.7 eV compared to the photoelectron peak. This shift can be interpreted to the difference in the binding energy of the O1s level of H_2O from which the hydrogen atoms desorbs. According to the previous study, ice surface has several types of H_2O molecules, which are two- or three-coordinated molecules with a dangling hydrogen, two- or tree-coordinated molecules with a dangling oxygen coordination, and four-coordinated molecules with distorted tetrahedra. It seems to be likely to assume that the hydrogen ions desorbes from the molecule with a dangling hydrogen (probably with two coordination) due to the weaker bond between the hydrogen atom and the surface. Thus, the PEPICO spectroscopy only reflects the binding energy of oxygen atoms which is bonded to dangling hydrogen atoms at (and very close to) the surface layer. Meanwhile, the O1s photoelectron comes from all the oxygen atoms located near the surface, thus the observed peak in the photoelectron spectrum is a convolution of many peaks which correspond to several surface and bulk species.

It was reported that the O1s binding energy of ice (bulk) observed in the XPS spectrum was shifted by -7.1 eV (without a correction of the work function) or -2.3 eV (with a correction of the work function) compared to H_2O in the gas phase. The O1s binding energy of O1s the less coordinated molecules with the dangling hydrogen at the surface is expected to be between the bulk and the gas phase, because the effect which changes the binding energy in the bulk should be weaker in less coordinated molecules. The present study have shown that the binding energy of such H_2O is shifted by +0.7 eV from the bulk ice, which is thus quite reasonable. This component is not observed in the photoelectron spectrum, this is probably due to the fact that such water molecules with the dangling hydrogen are minor species at the surface of amorphous ice after heated at 60-120K.

In order to verify the above results, we have made a measurements on the H_2O-chemisorbed Si(100) surface at room temperature. The H^+ yield and photoelectron intensities made peaks at similar kinetic energies in the EICO and photoelectron spectra of H_2O/Si(100). This agreement is quite reasonable because all the oxygen on the Si(100) surface is present as OH species bonded to the Si atom as a result of the dissociation of the H_2O molecules at the surface. There is no reason to expect the surface core-level shift of O1s on H_2O/Si(100). This result confirms that the observed difference between the H^+ yield in PEPICO and the photoelectron intensity is due to the core level shift of the H_2O molecules from which hydrogen ion desorbes.

To our knowledge, this is the first observation of the core-level shift on the ice. It demonstrates the advantages and the possibilities of the electron ion coincidence spectroscopy for surface analysis. The EICO spectroscopy can be utilized for an extremely surface sensitive and cite-specific XPS. Moreover, the EICO spectroscopy will be useful to investigate the surface chemical condition because the ion desorption process is strongly related to the surface chemical bond and the relaxation process of the excited state.

(BL2B1)

ORIENTATION OF OXYGEN AD-MOLECULES ON STEPPED PLATINUM (112)

Sugio WAKO,[a] Manami SANO,[a] Yuichi OHNO,[b] Tatsuo MATSUSHIMA,[b] Shin-ichiro TANAKA[c] and Masao KAMADA[d]

[a] *Graduate School of Environmental Earth Science, Hokkaido University, Sapporo 060-0810, Japan*
[b] *Catalysis Research Center, Hokkaido University, Sapporo 060-0811, Japan*
[c] *Department of Physics, Nagoya University, Senju, Nagoya 464-0814, Japan*
[d] *Institute for Molecular Science, Myodaiji Okazaki 444-8585, Japan*

Oxygen molecules on platinum surfaces emit hot atoms parallel to the surface plane when these are photolytically or thermally dissociated. The emission can be directed in a one-dimensional way if the ad-molecules are uni-directionally oriented, which is useful for designing surface aligned reactions. Thus, the orientation of oxygen ad-molecules was examined on stepped Pt(112) at 105 K by near-edge X-ray absorption fine-structure (NEXAFS) [1]. The π^* resonance due to O_2 was major when the electric vector, $\boldsymbol{E}$, of the incident X-ray was in a plane perpendicular to the step edge. On the other hand, when $\boldsymbol{E}$ was in the plane parallel to it, the σ^* resonance was major at the normal incidence and was attenuated with increasing incidence angle of the X-ray whereas the π^* resonance was enhanced. It was concluded that most oxygen was oriented along the step edge, although some oxygen molecules were oriented differently.

EXPERIMENTAL

The angle of X-ray incidence (θ) was varied by rotating the sample crystal such that $\boldsymbol{E}$ was oriented in a plane parallel to or perpendicular to the step edge. The sample crystal was kept at around 105 K during the NEXAFS measurements. The spectra were recorded by an Auger electron yield mode with the kinetic energy of the oxygen KLL Auger electrons at 520 eV. The oxygen coverage (Θ_{O2}) was determined by thermal desorption and normalized to the literature value.

RESULTS

On a clean surface, no signal peaks were found in raw NEXAFS spectra in a photon energy range from 525 eV to 550 eV (Fig. 1a). The difference between this signal and that observed with oxygen yielded NEXAFS due to oxygen ad-molecules (Fig. 1b). The π^* and σ^* resonance states were clearly seen at 530 ± 1 and 535 ± 1 eV. The base line was drawn by considering the edge jump and the energy resolution of the instrument of 2 eV. The energy of the continuum level was considered to begin at 531 eV. The resonance intensity curve was deconvoluted into two Gaussians with a fixed peak position and constant half width.

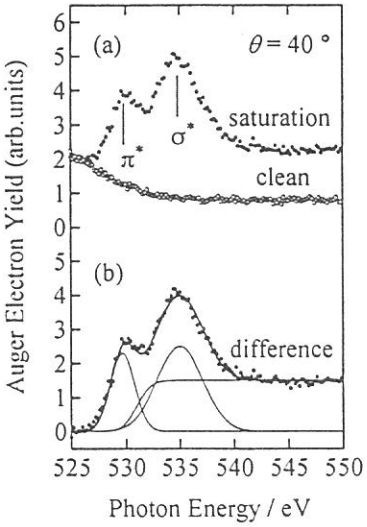

Fig. 1 NEXAFS spectra of oxygen ad-molecules at saturation. $\boldsymbol{E}$ was oriented 40 degrees from the surface in a plane along the step edge. (a) Raw NEXAFS spectra for clean and O_2-saturated surfaces and (b) their difference spectrum. Typical deconvolutions into two Gaussians are shown by the thin curves. The thick solid line indicates the sum of these components.

Both of the resonance peaks showed strong dependence on θ and the crystal azimuth. Furthermore, no coverage dependence was found in NEXAFS spectra over Θ_{O2} = 0.05 to 0.50 (saturation). A series of the spectra at Θ_{O2} = 0.4 is summarized in Fig. 2. The σ^* resonance was major at θ =10° when ***E*** was in a plane along the step edge whereas the π^* resonance was much less (Fig. 2a). The former decreased quickly with increasing θ and disappeared at around θ =80°, whereas the latter increased with increasing θ. This indicates that oxygen is lying along the step-edge direction. This orientation was supported from NEXAFS when ***E*** was in the plane perpendicular to the step edge (Fig. 2b). The π^* resonance was intense irrespective of the incident angle and the σ^* resonance was always small. However, it is noteworthy that the latter was always noticeable. Furthermore, the π^* resonance was also noticeable at θ =10° when ***E*** was along the step edge. This suggests that some oxygen molecules do not align along the step-edge. When ***E*** was in the plane perpendicular to the step edge, the σ^* resonance should disappear when all oxygen molecules align along the step edge. Step edges on stepped platinum surfaces may not be uniform as observed by STM. The molecular axis of oxygen on structural defects may be oriented $\pm 60°$ from the edge direction because of the terrace with a (111) structure. These oxygen molecules can contribute the σ^* resonance even when ***E*** is in the plane perpendicular to the step edge.

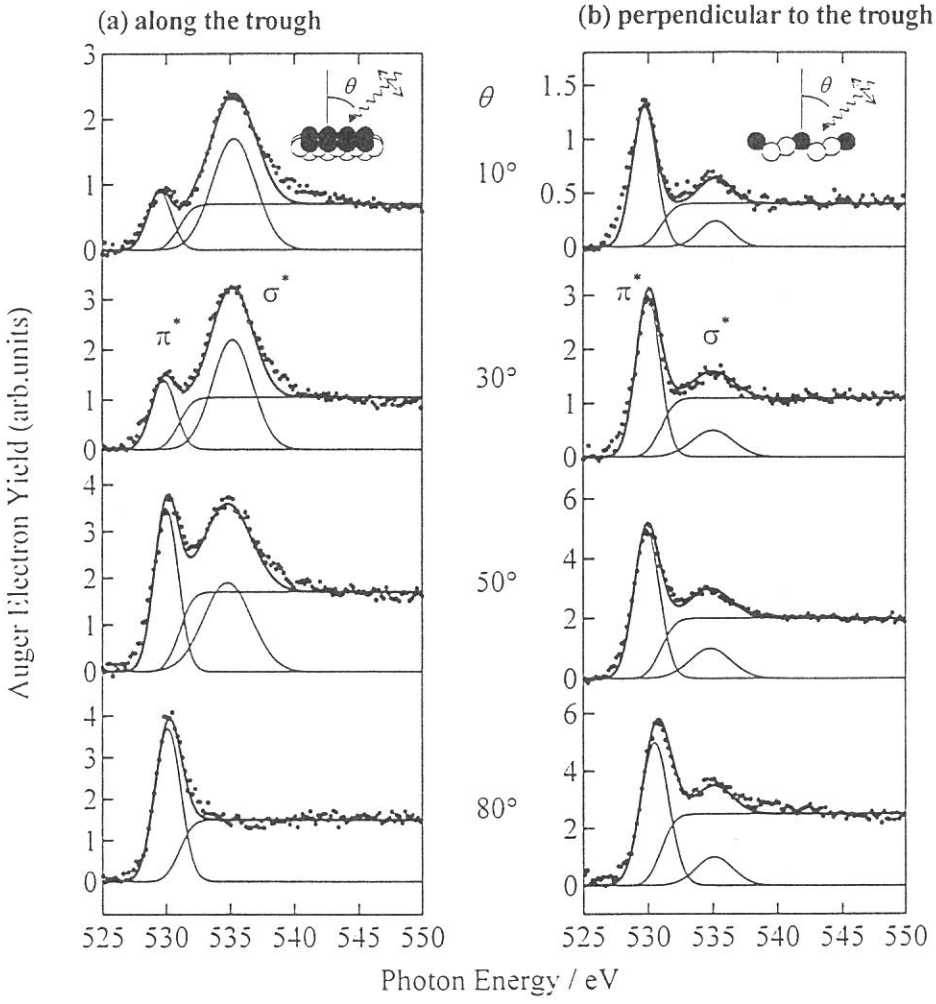

Fig. 2 NEXAFS spectra of oxygen ad-molecules at Θ_{O2}= 0.4 and at various X-ray incident angles. θ is the incidence angle. (a) The electric vector ***E*** was in a plane along the step edge and (b) perpendicular to it. Typical de-convolutions into two Gaussians are also shown.

Reference

[1] M. Sano, Y. Seimiya, Y. Ohno, T. Matsushima, S.I. Tanaka and M. Kamada, Surface Science, **421** (1999) 386.

(BL3A-1)

Deposition of Cu thin films by photo-chemical vapor deposition with Undulator Radiation

H.Sato, M.Uchida, A.Wakahara, A.Yoshida, A.Hoshino* and H.Machida*

Toyohashi University of Technology, Tenpaku, Toyohashi, *441-8580*

*TRI CHEMICAL LABORATORY INC, Japan

Recently, large-scale integrated circuits (LSIs) have been developed remarkably, and mass production in the intrachip connection of 0.25 μ m is advanced. The next step after 0.25 μ m rule, such as 0.15 μ m, are planned on the road map. However, the Al metal as the intrachip circuit wiring material shows the electro-migration, and the resistivity is high. These facts degrade the high speed operation of LSIs. Cu is one of the attractive material, because Cu has an excellent electro-migration tolerance and low resistivity compared with Al. The film growth at low temperature process is possible in the photo-enhanced chemical vapor deposition (photo-CVD), and since low damage and low contamination are expected, it attracts much attention as a process technology in the following generation.

In this study, copper films were deposited on Corning 7059 glass substrates by using photo-chemical vapor deposition with Cu(hfac)(TMVS) (Hexafluoroacetylacetnato Cu(I) · Vinyltrymathylsilane : $(O_2C_5HF_6)Cu \cdot (CH_3)_3Si(CH=CH_2)$). Undulator Radiation Light was used as the source excitation light source.

The experimental set-up is shown in Fig.1. In this experiment, Corning 7059 glass substrate was installed in the reaction chamber, and Cu(hfac)(TMVS) was supplied by 3×10^{-3} Torr on the substrate. The substrate temperature was always kept below 130 ℃ during the experiments to avoid themal deposition of Cu(hfac)(TMVS). Cu(hfac)(TMVS) is liquid at R.T., and the tube line was heated to 30℃ to avoid condensation of the Cu(hfac)(TMVS). The undulator gap was 60mm, corresponding to the photon energy of 36eV. This photon beam was introduced on the substrate. The average photon density on the surface of the substrate was 7.2 $\times10^{15}$photon/cm^2 · sec, and the total dose was 30000 mA·min.

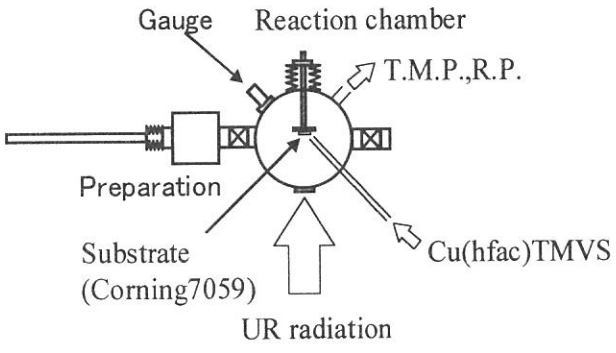

Fig.1. Experimental set-up

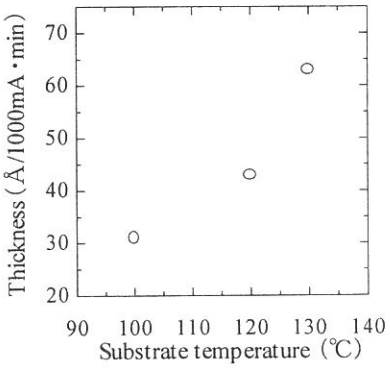

Fig.2. Thickness of the deposited Cu film as a function of the substrate temperature

The relation of the substrate temperature and the film thickness is shown in Fig.2. When the substrate temperature was 130℃, the resistivity of Cu film was very high, but it became 4.7 $\mu\Omega\cdot$cm after annealing (N_2atmosphere, 250℃, 30min, 0.03Torr). When the substrate temperature was 120℃, the resistivity wasn't improved even after annealing.

The surface morphology of the Cu thin-film was observed by atomic force microscope(AFM). The AFM images after annealing are shown in a Fig.3(a), and Fig.3(b). From these images, the grain size was larger with increasing the substrate temperature.

AES spectra after sputter cleaning with Ar ions and annealing are shown in a Fig.5. Carbon was found in the film produced at the substrate temperature of 120℃, but not observed in the film at the substrate temperature of 130℃.

From the above results, it was concluded that the after-annealing is effective in improving the resistivity in the films deposited at higher substrate temperature, resulting in the increase of the grain size and reduction of the impurities in the film.

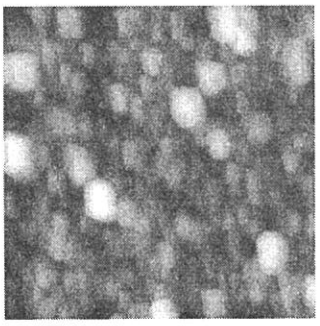

(a)substrate temperature 120℃

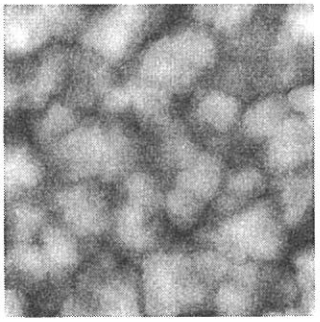

(b)substrate temperature 130℃

Fig.3 AFM images of Cu films after annealing (1000nm × 1000nm)

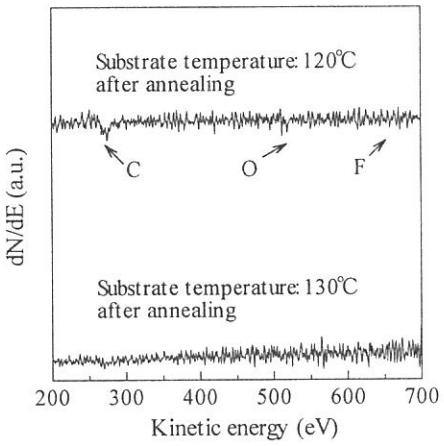

Fig.5. AES spectra after sputter cleaning and annealing.

(BL-4A1)

X-ray photoemission spectroscopy study of Si(111) Surface after Removal of SiO_2 by Synchrotron Radiation Illumination

Yongli Gao[a'], Harutaka Mekaru[a], Tsuneo Urisu[a] and Toshio Horigome[b]

[a]*Institute for Molecular Science, Myodaiji, Okazaki, 444-8585*
[b]*Machine Shop, Japan Advanced Institute of Science and Technology, Tatsunokuchi, Ishikawa, 923-1292*
a' : On sabbatical from Univ. Rochester

X-ray photoemission spectra (XPS) were measured for the native oxide / Si(111) surface after the synchrotron radiation stimulated desorption at the beam line 4A of UVSOR. The optics of the beam line are consisted of one Pt coated elliptically bent cylindrical quartz mirror with 4 degrees grazing incident angle and the horizontal beam divergence of about 15 mrad, and two Pt coated quartz plane mirrors with 2 degrees grazing incident angle. The XPS sample was set about 0.5 m upstream of the focus point. The unmonochromatized XPS apparatus is CL150 from VSW Inc. The resolution of the XPS measurements was about 1.46 eV.

The sample was resistively heated by passing through it a current and the temperature was maintained within ±10 °C as monitored with an optical pyrometer. The structure of the sample holder is shown in Fig. 1. Shown in Fig. 2 are the XPS spectra of Si 2p from oxidized Si(111) surface before and after 8 hours of SR irradiation at beam line 4A. The observed spectrum width is explained by the resolution (about 1.46 eV) of the apparatus. The difference of the spectra is manifested in the part of relative binding energy 2-6 eV. While the spectrum prior to SR irradiation shows the SiO_2 peak at 3.9 eV, the one after SR irradiation has the oxide peak appeared to be centered at 3.6 eV. Previous work by Himpsel et al. shows that SiO_2/Si interface is characterized by intermediate-oxidation states for about two Si layers, twice of that expected for an atomically abrupt interface. The intermediate states, Si^{1+}, Si^{2+}, Si^{3+}, are of relative binding energy 0.95 eV, 1.75 eV, and 2.48 eV, respectively. The observed shift of the oxide peak toward lower relative binding energy therefore reflects the breaking of the bond between Si and O, resulting in the increase of the lesser oxidized Si intermediate states. The benign desorption of the SiO_2 layer by SR stimulated desorption can also contribute to the formation of the steps in registry to the underlying crystal structure and bilayer stripes, since it is less disruptive to the Si surface in comparison to thermal desorption where the consumption of Si to form volatile SiO is taking place.

In Fig. 2, the difference of the intensities of the oxide peaks before and after SR irradiation is quite small in spite of the prolonged SR exposure. One possible factor is the SR photon distribution, since the XPS and STM measurements were performed in two different beam lines, beam lines 4A and 4B, respectively. Not only due to the difference of the calculated total photon flux, the photon flux in beam line 4A is much weaker than beam line 4B in energies larger than 100 eV. For example, at 531 eV (O 2s binding energy), beam line 4A flux is about 6 times weaker than that of beam line 4B. Slower desorption rate observed in XPS result suggests that the core electron excitations of Si (2s : 150 eV and 2p: 108 eV) and O (1s: 531 eV) contribute significantly to the SiO_2 desorption. Another factor may be due to the size of the XPS measurement area, about the 4 mm in diameter, which is larger than the calculated elliptical 7 x 3 mm beam spot and inevitably some areas outside the SR irradiation region were also sampled. Finally, the chamber is turbo-pumped and of base pressure $2x10^{-9}$ Torr, and some contamination of the sample may have occurred.

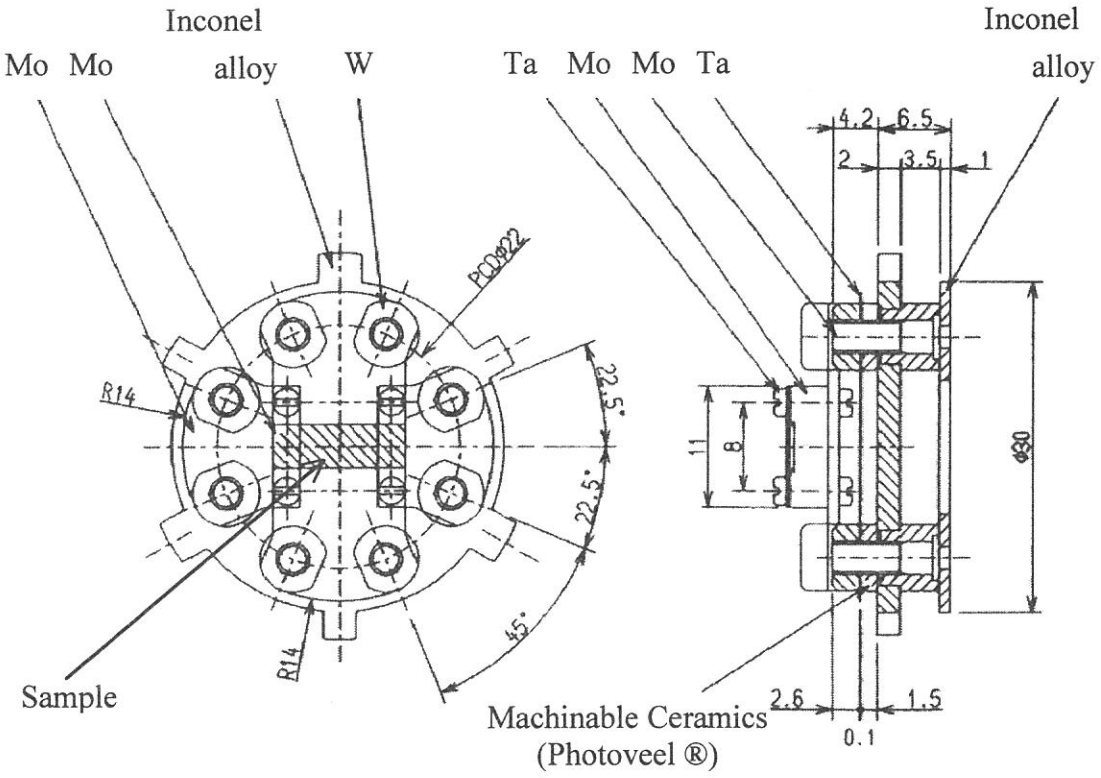

Figure 1. Top and side views of a new type of an XPS sample holder that can be heated at about 1000 K by passing an electric current through the sample.

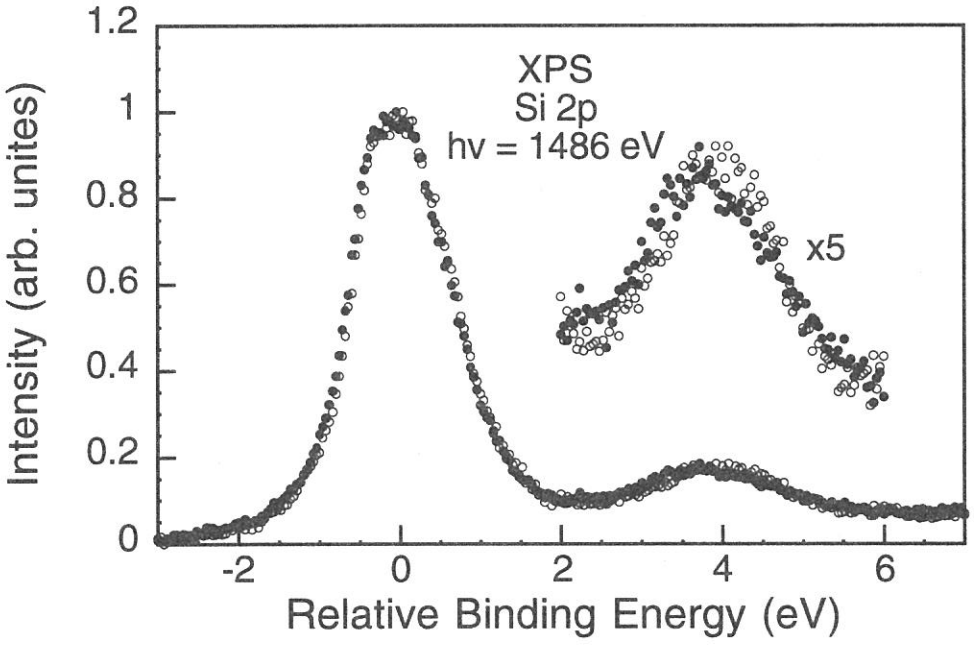

Figure 2. XPS spectra of Si 2p from oxidized Si(111) surface before and after 8 hours of SR irradiation in BL4A. The resolution was 1.46 eV. The difference of the spectra is manifested in the part of relative binding energy 2-6 eV. While the spectrum prior to SR irradiation shows the SiO_2 peak at 3.9 eV, the one after SR irradiation has the oxide peak shifted to 3.6 eV.

(BL-4B)

Scanning Tunneling Microscopy Study of Si(111) Surface Morphology after Removal of SiO_2 by Synchrotron Radiation Illumination

Yongli Gao[a'], Harutaka Mekaru[a] and Tsuneo Urisu[a]

[a]*Institute for Molecular Science, Myodaiji, Okazaki, 444-8585*
a' : On sabbatical from Univ. Rochester

We report the first investigations using scanning tunneling microscopy (STM) on the surface morphology of Si(111) after cleaning (complete removal of surface SiO_2) by SR irradiation. The surface shows large regions of an atomically flat and coherent 7×7 structure. An interesting feature of the surface is the formation of single bilayer steps nicely registered to the underlying crystal structure and the width quantized (to the units of 7×7 unit cell) of stripes formed by the bilayer steps. This indicates that the surface after cleaning reaches thermodynamic equilibrium under SR irradiation at temperatures much lower or by a much shorter time than that necessary for thermal desorption.

The experiment was done at the beam line 4B. The STM measurements were performed with a Rasterscope-3000 from DME Co.. The base pressure of the STM chamber was 5×10^{-10} Torr. Details of the experimental conditions are descrived in Ref. 1. The sample (3×8 mm^2) was an boron doped p type Si(111) wafer of misorientation within ±0.1 degree, with thickness of 0.5 mm and resistivity 8 Ω/cm. A native oxide layer was formed on the Si substrate by a conventional wet process.[1] The thickness of the native oxide layer was about 1 nm.[2] The sample was resistively heated by passing through it a current and the temperature was maintained within ±10 °C as monitored with an optical pyrometer. The sample temperature was decreased after cleaning by the rate of 1degree/s down to 700 °C and below this by 2 degrees/s.

The regular shape of the bilayer steps is not associated with the SR stimulated oxide desorption. The topograph of a Si(111) surface prepared by thermal desorption at 880 °C for 2 minutes is shown in Fig. 1(a). No registry of the steps with respect to the underlying crystal structure can be observed. Instead, the steps form arched curves with the ends pinned by particles. In comparison, the Si(111) surface with 2 hour SR irradiation at 700 °C after the oxide layer had been removed by thermal desorption at 880 °C presents the registered steps as shown in Fig. 1(b). This observation indicates that the registered bilayer steps are created through an SR stimulated annealing process. We have also tested 2 hours thermal annealing at 700 °C of Si(111) after thermal desorption of SiO_2 at 880 °C, but could only observe roughened surfaces.

More detailed information about the bilayer steps can be obtained by using finer resolution. Fig. 2 shows the atomic image of a single bilayer step from a Si(111) sample with 2 hours of SR irradiation at 700 °C. The 7×7 structure is clearly visible. The displacement vector g(a,b) between upper and lower terrace 7×7 structures defined by J.L.Goldberg et.al.[3] is measured to be g(1 + 1/3, 3+2/3) at this step. This indicate that this step is F1a (according to the definition by H. Tochihara *et. al.* [4]) descending along [11$\underline{2}$]. The 7×7 reconstruction structure is coherent on all over the surface observed by STM (max. 100 x 100nm), and the width of the bilayer stripes are all quantized to the units of the 7×7 cell width similarly as observed in the terrace width of thermal equilibrium Si(111) surface.[5] These facts indicate that the SR irradiated surface is in thermal equilibrium equivalent to the 700 ℃-20 hours thermal annealing. In summary, we have shown that the SR illumication of Si(111) under elevated temperatures generates a near perfect 7×7 surface with regular shaped bilayer steps. The shape of the steps intend to be hexagonal. The inequivalence of [$\underline{1}$12] and [11$\underline{2}$] steps observed in dry chemical etching is absent in the SR irradiation case. The mechanism of the formation of the regular shaped steps can be attributed to the enhancement of the surface migration of Si atoms under SR irradiation and elevated temperatures, which is considered to be induced by the direct photo-excitation of surface adatoms and/or the inelastic cascade scattering of photoexcited electrons. The results may be particularly relevant to the fabrication of Si nanostructures, as nice bilayer stripes of a few unit cell width can be observed.

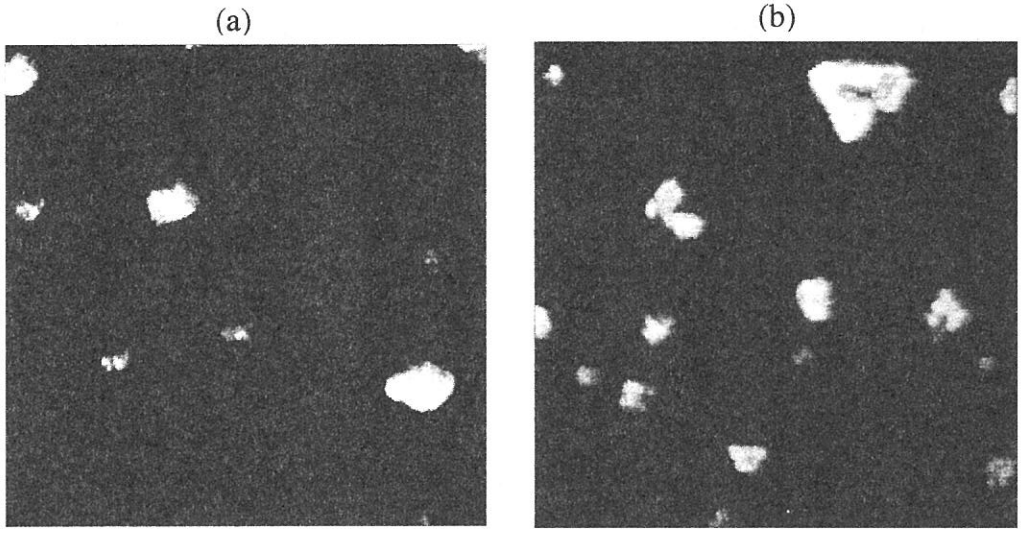

Figure 1. (a) 500 nm×500 nm topograph of a Si(111) surface prepared by thermal desorption at 880 °C for 2 minutes. No registry of the steps with respect to the underlying crystal structure can be observed. Instead, the steps form arched curves with the ends pinned by particles. (b) 200 nm×200 nm topograph of a Si(111) surface with 2 hours SR irradiation at 700 °C after the oxide layer removal by thermal desorption at 880 °C. The registered steps are clearly visible.

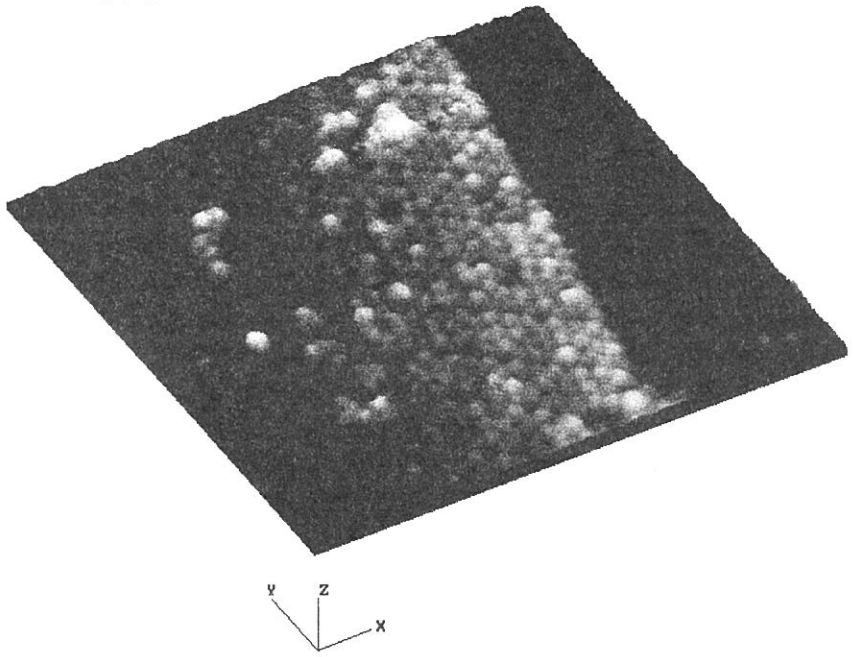

Figure 2. The 3-D atomic image of a bilayer step descending along [11$\bar{2}$] from a Si(111) sample with 2 hours of SR irradiation at 700 °C.
The 7×7 structure is clearly visible in the 20 nm×20 nm image.

1) T. Miyamae, H. Uchida, I.H. Munro, and T. Urisu, J. Vac. Sci. Technol. A17, 1 (1999).
2) Y. Kobayashi and K. Sugii, J. Vac. Sci. Technol. A10, 2308 (1992).
3) J.L.Goldberg, X.-Swang, J.Wei, N.C.Bartelt, and E.D.Williams, J.Vac.Sci. Technol. A9, 1868 (1991).
4) H.Tochihara, W.Shimada, M.Itoh, H.Tanaka, M.Udagawa, and I.Sumita, Phys. Rev. **B45**, 11332 (1992).
5) X.-S.Wang, J.L.Goldberg, N.C.Bartelt, T.L.Einstein, and E.D. Williams, Phys. Rev. Lett. **65**, 2430 (1990).

BL5A: Formation mechanisms of NEA surface on p-GaAs(100) studied by photoelectron spectroscopy

S. D. More, S. Tanaka), Y. Fujii*) and M. Kamada*

UVSOR Facility, Institute for Molecular Science, Okazaki 444-8585,
**College of Engineering, Osaka City University, Osaka 558-8585*

A dielectric field generated either by an external source or by a heterojunction or a surface dipole can lower the vacuum level of a semiconductor surface below the bulk conduction band level and thus generate a "negative electron affinity" NEA surface.

Negative electron affinity (NEA) surfaces have found applications as efficient photocathodes and the NEA surface of O/Cs/GaAs(100) is known to be a useful emitter of spin-polarized electrons with a high degree of polarization and efficiently. NEA occurs on semiconductors once the vacuum level is pulled below the conduction band minimum.
The photo-induced change in the semiconductor-vacuum interface of a negative electron affinity (NEA) surface prepared by coadsorption of Cs and O on GaAs(100) has been investigated with core level photoelectron spectroscopy using synchrotron radiation and laser light. A mode-locked Ti:Saphire laser with a pulse width of about 160 fs was triggered with a signal from a master oscillator of the UVSOR storage ring. Fundamental light of the laser (photon energy of 1.50 eV) was focused on the sample in a vacuum chamber and spectra have been measured with and without laser irradiation, thus allowing a direct observation of possible band-bending. As substrate a Zn doped ($1x10^{19}$ atoms/cm^3) p-type GaAs(100) wafer was used.

Fig. 1 shows the core level shifts for Ga, As and Cs as a function of sample treatment. The direction of the shifts implies an overall decrease of the band-bending with sample treatment. Superimposed on this trend are corelevel shifts for Ga and As towards lower kinetic energies when Cs is deposited and toward higher kinetic energies when the sample surface is exposed to O. At later stages the direction of the shift is reversed. Cs core level shifts are always towards higher kinetic energies at Cs deposition and lower kinetic energies for O deposition. The amounts of the energy shifts were strongly dependent on the sample treatment [1].

As core level peak shifts do not only indicate band-bending but are also influenced by changes in the chemical environment changes in band-bending have additionally spectra with and without irradition from laser light for clean GaAs, Cs covered GaAs(100) and two surfaces which have been treated with multiple, alternating dosages of Cs and O. They different however in the amount of photocurrent, yielding currents of 0.07 nA and 2 nA.
Both Ga-3d and As-3d photoelectron peaks of the surfaces which have been treated with multiple dosages of Cs and O surface show transient energy shifts of 0.08 eV and less than 0.03 eV, respectively. This compares to values of 0.35 eV for the clean surface and 0.25 eV for the cesium treated sample. This measurement confirms the core-level shift derived observation, indicate that the bands are flattened once the NEA surface condition is approached. It becomes clear however that band flattening itself is not sufficient to achieve NEA surface formation, but might rather be a byproduct of the O interaction at the substrate-Cs interface.

This is contrary to the expectations of previous models and rules out a dipole induced field in the substrate as the origin of NEA surface formation and relocates the workfunction lowering dipole towards a position inside the overlayer.

As Cs-oxide layers exhibit work-functions between 0.6 and 1.5 eV the workfunction of this material is sufficient as a coating to lower the overall work-function of the system. Oxygen-deposition thus first serves to generate Cs-oxide to lower the workfunction, but also interacts with the GaAs substrate. As the height of the interface barrier is critically dependent on the degree of chemical interaction between the substrate and overlayer, oxygen deposition should decrease the interface energy between the overlayer and the substrate.
Conditions for optimal electron yield would therefore be reached when both the workfunction and the interface barrier reach an optimal value.

A synergy of the interface barrier lowering chemical interaction between Cs, O and GaAs, the inherent low electron affinity of Cs-oxides and a possible electron confinement due to surface roughness and micro-domains is proposed to dominate NEA surface formation on GaAs(100) and related surfaces.

A quantitative determination of the interface barrier as a function of oxygen deposition will follow in near future, using the new laser system at BL5A.

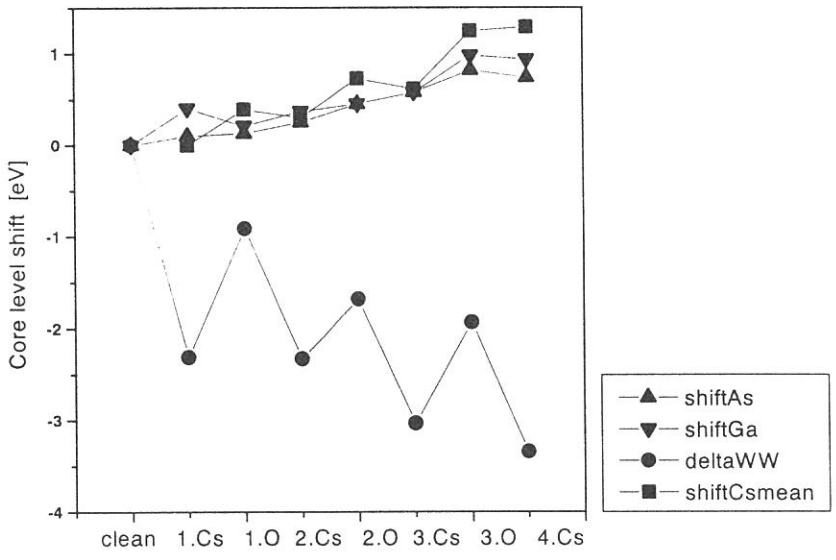

Fig. 1: Core level shifts and workfunction development during NEA surface formation on GaAs(100) [1]

[1] S. More, S. Tanaka, S. Tanaka, Y. Fudjii and M. Kamada, Surf. Sci. in print
[2] N. Takahashi, S. Tanaka, M. Ichikawa, Y.Q. Cai and M. Kamada, J. Phys. Soc. Jap. 66 (1997) 2798

(BL5B)

Absolute Measurements of the Total Yields of Photo-Desorption at the Surface of Solid Argon by Excitonic Excitations

Takashi Adachi*, Satoshi Ishii*, Takato Hirayama*, Ichiro Arakawa*,** and Makoto Sakurai***

**Department of physics, Gakushuin University , Mejiro, Toshima, Tokyo 171-8588.*

***Institute for Molecular Science, Myodaiji, Okazaki, Aichi 444-8585.*

****Department of Physics, Kobe University, Rokkodai-cho, Nada-ku, Kobe 657-8501.*

1. Introduction

Electron or photon irradiation of a solid surface leads the electronic excitations which are followed by the desorption of various kinds of particles. The desorption at the surface of a rare gas solid has been extensively investigated for last two decades[1]. Investigation of this phenomena will reveal dynamics of the electronic excitations and the relaxation processes in the solid. As to the desorption of excited neutral particles from rare gas solids, various desorption mechanisms were proposed and some of them were confirmed experimentally and theoretically. On the other hand, the desorption mechanism of the ground state atom has not been clarified yet, though it is the main component of the desorbed particles. In this report, we present the preliminary results of the absolute measurements of the total photo-desorption yields of argon. The "total" means that we detected all the argon particles desorbed, i.e., atoms and clusters in ground, electronically excited, and ionized states.

2. Experiments

Experiments have been carried out at the beam line BL5B in UVSOR of the Institute for Molecular Science, Okazaki. The wavelength resolution, $\lambda/\Delta\lambda$, was about 500 $\pm$ 200 in the range of λ between 20 and 110 nm. Argon gas was deposited on the surface of a Pt (111) substrate, which is attached to a liquid helium cryostat, at the temperature of 6K or lower. The cryostat was installed in an ultrahigh-vacuum chamber with a base pressure of 5×10^{-9} Pa. The thickness of an argon film was calculated from the exposure on the assumption that the condensation coefficient of the argon on the sample surface was unity. The thickness of argon film was in the range between 1 and 500 atomic monolayers (ML).

Desorption rate was calculated from the rise of the argon partial pressure in the vacuum chamber during the irradiation of the sample. The pumping speed for argon of a turbo molecular pump and the cold surface of the cryostat is 0.09 $\pm$ 0.01 m^3/s in total. The partial pressure of argon was measured by a quadrupole mass spectrometer which was calibrated for argon with an extractor type ionization gauge at each run of the experiments. The absolute intensity of the incident monochromatic vacuum ultraviolet light was monitored by measuring photoelectron current emitted from a gold mesh which was installed in the beam line.

3. Results

The dependence of the absolute photo-desorption yields of argon on the incident wavelength is shown in fig. 1. In case the film thickness is 4 ML film (fig. 1 (a)), a peak is observed at 106 nm which corresponds to the excitation energy for the first order surface exciton (S1). For the film of 100 ML in thickness (fig. 1 (b)), peaks appear at the wavelength corresponding to the second order surface (S2, 96 nm), the first order bulk (B1, 103 nm, 101 nm) and the second order bulk (B2, 91 nm, 90 nm) exciton excitations. The desorption yields which are directly due to excitonic excitations are estimated by the peak height above the continuous background which is thought to be due to the desorption caused by the higher order light from the monochromator. The present systematic measurements of the thickness dependence show that the desorption yields at B1 and B2 excitation increase with the thickness of argon film and reach ~0.07 and ~0.09 Ar/photon, respectively, at 100 ML. The desorption yield at S1 excitation has no thickness dependence and is ~0.03 Ar/photon. On the other hand, the desorption yield at S2 excitation increases gradually with the film thickness and reaches ~0.02 Ar/photon at 50 ML. The origin of the thickness dependence at S2 excitation has not been clarified yet.

In the case of solid neon[2], the absolute total desorption yields were about 1 and about 2~4 Ne/photon at the bulk exciton excitation and the bulk ionization, respectively. Such large desorption yields of neon were explained by the desorption mechanism which is called "Cavity Ejection (CE)"; the excited atom is pushed out by the repulsive force between the excited atom, which has an expanded electronic orbit, and the surrounding ground state atoms which has negative electron affinity. In the case of neon, the excited atom created at the 2nd or 3rd layer under the surface can desorb via CE mechanism and blow up a number of atoms in over layers because of a small cohesive energy (0.019 eV/atom[3]) in comparison with the kinetic energy of desorbing excited atoms (~0.2 eV[4]). This model, however, can not be applicable in the case of argon because the cohesive energy (0.08 eV/atom[3]) is larger than the kinetic energy of the desorbing excited atom via CE mechanism (~0.035 eV[5]). Other desorption channel of argon atom are thought to be as follows. The dissociation of an excited dimer produces two energetic atoms. The kinetic energy of the dissociated energetic atom is ~0.4 eV[5], which is enough to blow up a number of atoms in over layers. The quantitative analysis of the absolute desorption yields is now in progress.

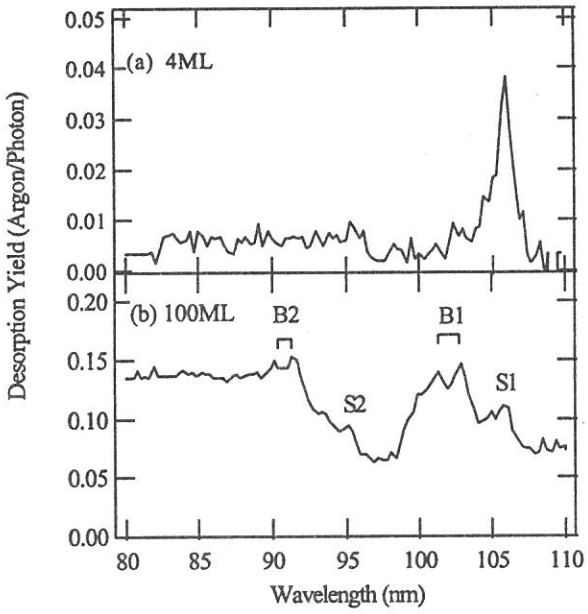

Fig.1 Absolute desorption yields of argon by photon excitation. The thicknesses of argon films are (a) 4 ML and (b) 100 ML.

[1] for recent review, see I. Arakawa, Molec. Crystal Liq. Crystal, **314**, 47 (1998), M. Runne and G. Zimmerer, Nucl. Instrum. Meth. Phys. Res. B **101**, 156 (1995).

[2] I. Arakawa, T. Adachi, T.Hirayama and M.Sakurai, Surf. Sci., accepted for publication.

[3] N. Schwentner, E. -E. Koch and J. Jortner, Electronic Excitations in Condensed Rare Gases, (Springer-Verlag, 1985).

[4] T. Hirayama, A. Hayama, T. Koike, T. Kuninobu, I. Arakawa, K. Mitsuke, M. Sakurai and E. V. Savchenko, Surf. Sci., **390**, 226 (1997).

[5] I. Arakawa and M. Sakurai, in "Desorption Induced by Electronic Transitions IV", eds. G. Betz and P. Varga, (Springer, Berlin, 1990) p. 246.

(BL5A & 6A2)

Time-response of photo-induced core-level shifts in GaAs (100) studied with combination of SR and laser

Masao Kamada, Senku Tanaka[A], Sam Dylan More,
Shuji Asaka[B], and Yasuo Fujii[A]

UVSOR Facility, Institute for Molecular Science, Okazaki 444-8585
[A]College of Engineering, Osaka City University, Osaka 558-8585
[B]Equipment Develop Center, Institute for Molecular Science, Okazaki 444-8585

In recent years, we have been studying the non-equilibrium electronic states at semiconductor surfaces using synchrotron radiation and laser. Electric potentials at semiconductor surfaces and interfaces are very important to understand a variety of electrical properties and phenomena of semiconductors and to control semiconductor devices. However, few works have been carried out to understand the dynamics of non-equilibrium charge distribution at the semiconductor surfaces. Long *et al.* have first reported the transient surface photo-voltage on Si (111) using synchrotron radiation (SR) and laser pulses.[1] They obtained non-equilibrium electron density induced by laser pulses in the space charge layer, but the agreement between their experiments and theoretical simulations is not good for a low power laser. In recent years, Marsi *et al.* have reported the time response of the transient surface photo-voltage on Si (111)2x1.[2] The purpose of the present work is to investigate the dynamics of photo-induced carriers on p-GaAs (100), since this surface provides spin-polarized electrons after Cs- and oxygen treatments.

Experiments were carried out at 6A2 and 5A, where a plane-grating monochromator (PGM) and a spherical-grating monochromator (SGM-TRAIN) provide EUV photons, respectively. We used mode-locked Nd:YAG and Ti:Sapphire lasers at BL6A2 and 5A, respectively. Lasers were triggered with a signal from a master oscillator of the UVSOR storage ring. The spatial and temporal overlaps were carefully adjusted by using a MCP-PM/TAC system. The surface of p-type GaAs (100) doped with Zn was prepared *in situ* using usual way.

Figure 1 shows the temperature dependence of the peak shift of Ga-*3d* photoelectron. The observed points can be well fit to the theoretical straight line which was derived on the basis of a thermionic emission model with some approximation. However, this good agreement does not mean that the thermionic emission model is perfect. It is important to obtain temporal information in order to understand the meaning of the carrier density, potential in the surface layer, and so on. Figure 2 shows the temporal structure of the energy shift which was obtained by adjusting the delay time between SR and laser. The observed data can be composed into a fast component in nano-second region and a slow component in the micro- or milli-second region. Hot electrons and holes produced by laser pulses are separately distributed in the surface space-charge layer, and then they will be recombined again to recover the band bending of GaAs. The present result may indicate two pathways at least in the recovering process.

This work was partially supported by a Grant-in-Aid from the Ministry of Education, Science, Culture, and Sports.

Reference: 1) J.P.Long et al., PRL.. 64 (1990) 1158. 2) M. Marsi et al.,APL.. 70 (1997) 895.

Fig. 1. Temperature dependence of the photo-induced energy shift of Ga-3d photoelectron.

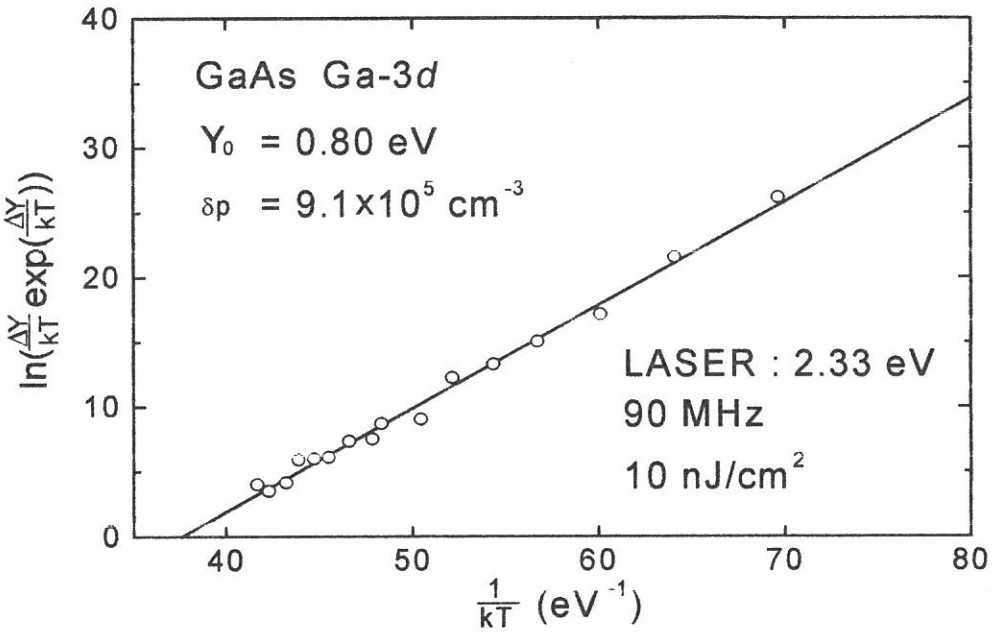

Fig. 2. Temporal structure of the photo-induced energy shift of Ga-3d photoelectron.

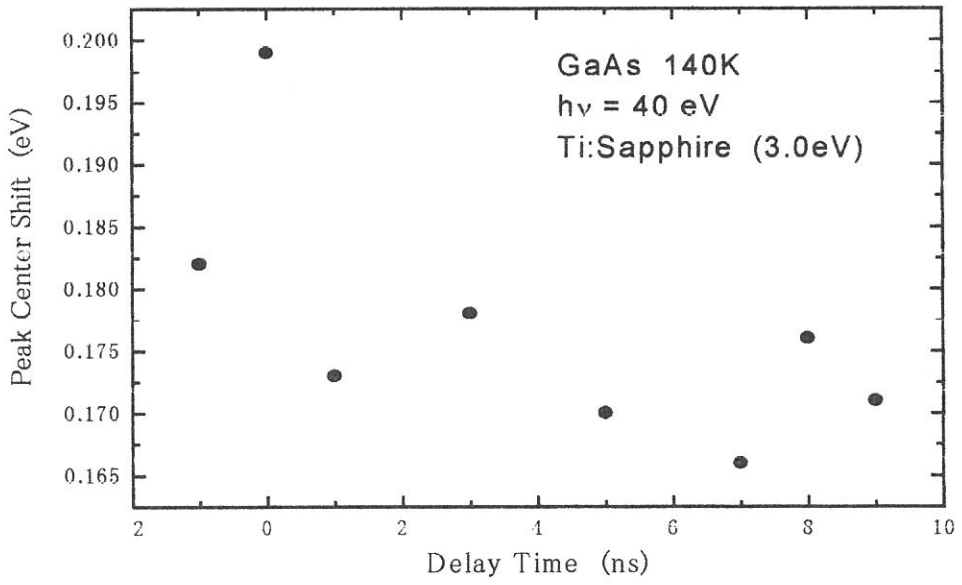

(BL8A)

Ablation of Metal Fluoride Film by Synchrotron Radiation

Hisao NAGAI, Masaru OKUMURA, Seiji ICHIYANAGI, Takumi SHIOMI,
Mineo HIRAMATSU, Masahito NAWATA,
Masaru HORI* and Toshio GOTO*

Department of Electrical and Electronic Engineering, Meijo University,
Tempaku-ku, Nagoya, 468-8502
**Department of Quantum Engineering, Nagoya University,*
Chikusa-ku, Nagoya, 464-8603

INTRODUCTION

Fluorine-compound materials including Teflon well absorb photons with energies in vacuum ultraviolet region in synchrotron radiation (SR) beam. Previously, we demonstrated the anisotropic micromachining and film formation of Teflon using the SR ablation process [1,2]. In addition, by selecting the photon energy of SR beam with filter, we indicated that photon energies absorbed by carbon (C) and fluorine (F) atoms contribute to the ablation of Teflon [3]. From results of SR ablation of Teflon, metal fluoride materials consisting of metal and fluorine atoms would be easily etched by the SR irradiation. In this report, the SR ablation process is applied to the etching of metal fluoride films. The anisotropic etching of three types of metal fluoride films, AgFx, MgFx, and AlFx, are systematically demonstrated using the SR ablation.

EXPERIMENT

The experiments were carried out at beam line BL-8A of UVSOR. Three types of metal fluoride films (AgFx, MgFx, AlFx) were prepared on Si substrate by electron beam evaporation. These samples were set perpendicularly to the SR beam in the reaction chamber (base pressure of 10^{-4} Pa). A Nickel (Ni) mesh (square pattern of 77 μm) was used as the contact mask. The SR beam irradiated the samples through the Ni contact mask in vacuum at a room temperature. The etched depth was measured using a surface profiler. The SR-irradiated films were analyzed by scanning electron spectroscopy (SEM) and micro electron spectroscopy for chemical analysis (micro-ESCA).

RESULTS AND DISCUSSION

Micro-pattern of metal fluoride films (AgFx, MgFx, AlFx) were fabricated by SR ablation process. Figure 1 shows the SEM photograph of fine pattern created in the 50 nm thick AlFx film with the dose of 5000 mA·min. As seen in Fig. 1, the fine pattern of 77 μm square holes was successfully produced in the AlFx film by the SR irradiation. Figure 2 shows the etched depth of AlFx film on Si substrate as a function of SR irradiation time. The thickness of AlFx film prepared on the Si substrate was 50 nm for each sample, and the SR beam current was constant at 190 mA in Fig. 2. When the SR irradiation

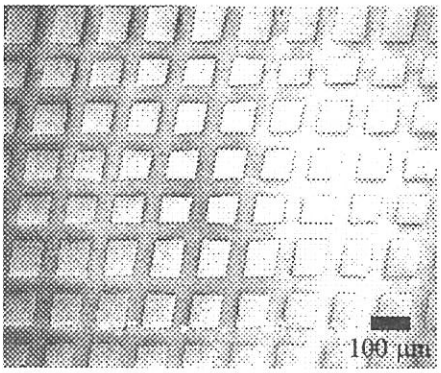

Fig. 1. SEM photograph of fine pattern with 77 μm square holes created in the AlF_x film by SR ablation

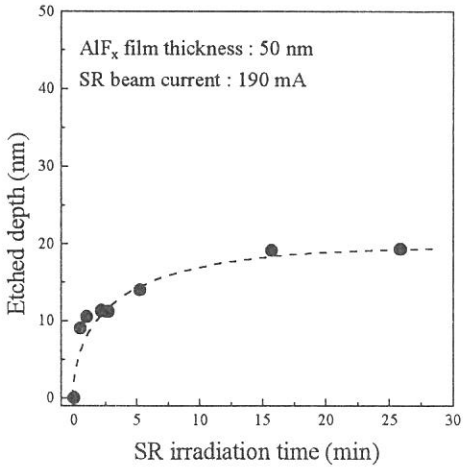

Fig. 2. Etched depth of AlF_x film on Si substrates of a function of SR irradiation time.

time increased, the etched depth of AlFx film increased rapidly at first, then became saturated with further increase of SR irradiation time, resulted in the termination of etching.

Figure 3 shows the F/Al ratios of the SR-irradiated and non-irradiated surfaces of AlFx film on Si substrate measured using micro-ESCA. The change of F/Al ratio corresponds to the created pattern by the SR ablation. Fluorine content of the SR-irradiated area was lower than that of the non-irradiated surface, which suggests that the fluorine atoms would be easy to remove from surface by the SR irradiation compared to the metal atoms.

Figure 4 shows etched depth of AlFx film at which the etching terminated as a function of film thickness of AlFx prepared on Si substrate. In the range of AlFx film thickness investigated, etched depth increased almost linearly with the increase of AlFx film thickness.

Figure 5 shows the etched depth of AlFx film on Au, Ni, SiO_2 and Si substrates as a function of SR irradiation time. The thickness of AlFx film on each substrate was 50 nm, and the SR beam current was constant at 190 mA in Fig. 5. As the SR irradiation time increased, the etched depth increased at first. With further increase of SR irradiation time, however, the etched depth became saturated in all cases. The maximum value of etched depth depended on the substrate materials. In the cases of Au and Ni substrates, Auger electrons ejected from substrates by the SR irradiation would enhance the etching of AlFx film. In the case of SiO_2 substrate, on the other hand, thermal energy due to the absorption of SR in the SiO_2 substrate would enhance the etching of AlFx film.

The SR ablation mechanism including etch termination and effect of substrate materials is under investigation.

SUMMARY

Anisotropic etching of metal fluoride films using the SR-induced reaction was successfully demonstrated. The saturation of etching depended on the thickness of metal fluoride films as well as the substrate materials.

REFERENCES

[1] M. Inayoshi, M. Ito, M. Hori, T. Goto, M. Hiramatsu, and A. Hiraya, Jpn. J. Appl. Phys., 34, L1675 (1995).

[2] M. Inayoshi, M. Ito, M. Hori, T. Goto, and M. Hiramatsu, J. Vac. Sci. Technol., B 17, 949 (1999).

[3] M. Inayoshi, H. Nagai, M. Hori, T. Goto, and M. Hiramatsu, J. Vac. Sci. Technol., submitted.

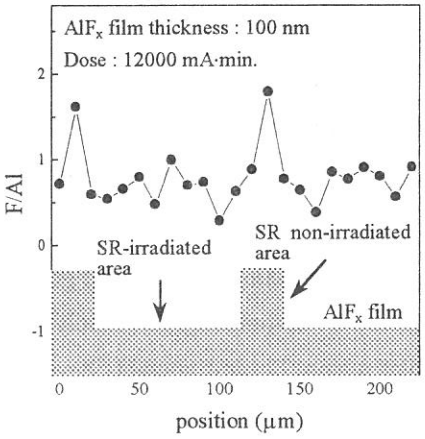

Fig. 3. F/Al ratio of surface of SR irradiated AlF_x film on Si substrate by Micro-ESCA.

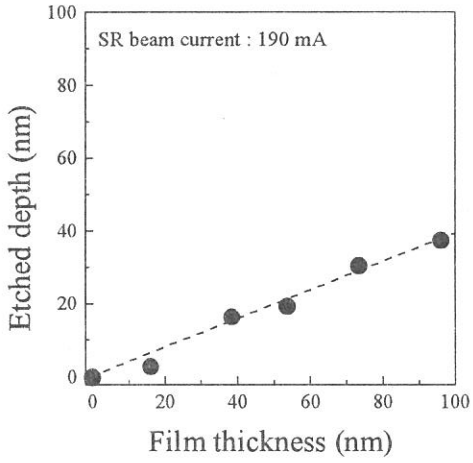

Fig. 4. Etched depth of AlF_x film on Si substrate as a function of prepared film thickness.

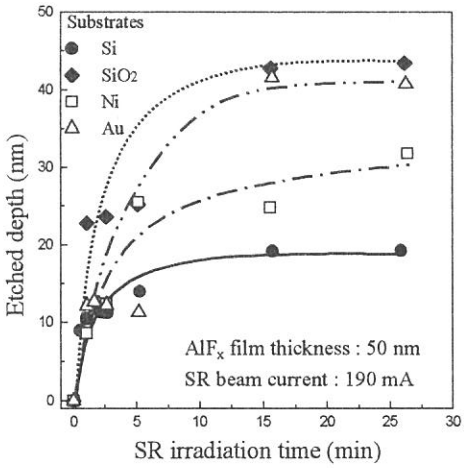

Fig. 5. Etched depth of AlF_x film on Au, Ni, SiO_2 and Si substrates of a function of SR irradiation time.

(BL8A) Growth characteristics and photoluminescence properties of ZnTe homoepitaxial films deposited by synchrotron-radiation-excited growth

Mitsuhiro Nishio, Kazuki Hayashida, Hiroki Harada, Yoshiaki Mitsuishi, Qixin Guo, Hiroshi Ogawa

Department of Electrical and Electronic Engineering, Saga University, Saga 840-8502, Japan

Synchrotron-radiation (SR) excited growth is promising as a new non-thermal technique, since virtually any reactants can be decomposed effectively at low temperature by using a high photon flux density in the vacuum ultraviolet region. Several attempts have so far been carried out using SR light to perform the deposition of semiconductors at low temperatures. In order to improve the film quality, it is important to investigate the photoluminescence (PL) spectrum of the film deposited by SR-excited growth. However, such investigations do not exist except for our previous paper, which described luminescence of ZnTe films deposited under only a confined growth condition. In this study, we describe PL spectra of the ZnTe films deposited under a wide variety of conditions.

The growth experiments were carried out using the SR beam line, BL8A. The beam line supplies only white light. Diethylzinc (DEZn) and diethyltelluride (DETe) were used as source materials. These source materials were independently fed into the chamber together with hydrogen or nitrogen carrier gas by means of mass flow controller and variable leak valve. The deposition of ZnTe was carried out at very low pressure of 10^{-5}～10^{-4} Torr in the growth chamber.

Figure 1 shows the relationship between the growth rate and DEZn transport rate when DETe transport rate is kept at 1 μ mol/min. The growth rate increases rapidly with increasing DEZn transport rate and then it eventually becomes saturated at low DEZn transport rate around 0.5 μ mol/min. The saturated tendency of the growth rate indicates that the rate-limiting step is due to the supply of DETe. Also, it is suggested that adsorption coefficient of DEZn is very high compared to DETe at room temperature. As shown in the figure, no difference is found in the growth rate between hydrogen and nitrogen carrier gases. Thus, hydrogen seems not to play an important role in the growth reaction due to a use of the low pressure. The PL spectra of ZnTe films as a function of DEZn transport rate are shown in Fig.2 (a), (b), and (c). It is noticeable that the substrate was not heated during growth during growth. The spectra for all samples have a sharply excitonic emission (I_a) at 2.375 eV. The I_a line is attributed to shallow acceptors, namely Li, Cu, and Na. This peak is observed widely for undoped ZnTe grown by another growth methods. The PL spectrum of the film grown at a DEZn transport rate of 1 μ mol/min exhibits the strong deep level emissions with two broad bands centered at around 2.1 eV and 1.85 eV (Fig. 2(a)). The deep-level luminescence may be due to the generation of defects such as vacancy-impurity complex in the film. The deep-level luminescence obtained here can be found in the experimental results by Tews *et al.*, who have attempted laser-induced diffusion in ZnTe with Cl. Thus, a Zn rich condition may facilitate Cl inclusion into a Te lattice site. Actually, a decrease of DEZn transports rate seems to bring about significant reduction of deep level band, as shown in Fig.2 (b), (c). At a DEZn transport rate of 0.5 μ mol/min, only I_a peak can be detected in the spectrum, indicating the relatively good quality film. However, a further decrease in DEZn transport rate leads to two broad bands centered around 2.32 and 2.28 eV in the spectrum of the film, as shown in Fig.2(c). The result for the film obtained at a high transport rate of DETe, which ensures Te rich condition, is given in Fig.2 (d). In the case, the spectrum shows almost the same feature as shown in Fig.2(c). A Te rich condition may occur the contamination of shallow acceptor and/or donor impurities related to these emission

bands. Thus, it seems that the quality of ZnTe film becomes deteriorated under Zn rich and Te rich conditions. Figure 3 shows the PL spectra of ZnTe films as a function of substrate temperature. The PL spectrum depends upon the substrate temperature. The film grown at 60℃ exhibits a strong I_a peak. Two broad bands centered around 2.32 and 2.28 eV are not detected in the spectrum, whereas these are clearly observed in the spectrum of the film deposited at 27℃. However, a further increase in substrate temperature induces enhancement of the deep-level luminescence, as shown in the figure. The spectrum of the film deposited at 100℃ resembles that obtained under a Te rich condition. We have already reported that the growth rate gradually decreases with increasing substrate temperature up to 60℃ and then shows a rapid decrease above this substrate temperature. This behavior will be closely related to the decrease in the adsorbed molecules regarding metalorganic sources with increasing substrate temperature. The PL properties of the films as a function of substrate temperature may be explained with the difference in the temperature dependency of adsorption coefficient between DEZn and DETe molecules.

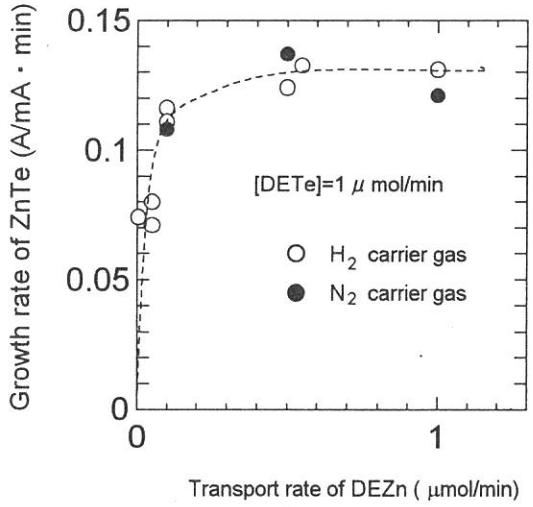

Fig.1. The relationship between the growth rate and DEZn transport rate when DETe transport rate is kept at 1 μ mol/min and substrate temperature at 27℃.

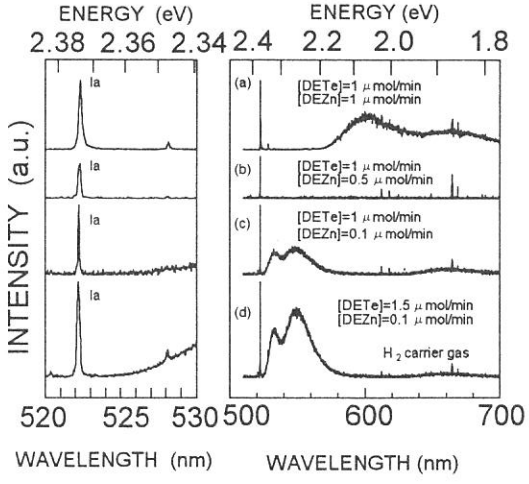

Fig.2. PL spectra of ZnTe films for different DEZn and DETe transport rates when substrate temperature was kept at 27℃.

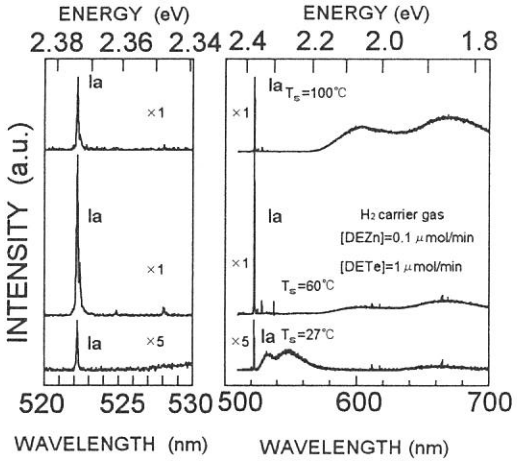

Fig.3. PL spectra of ZnTe films for different substrate temperatures.

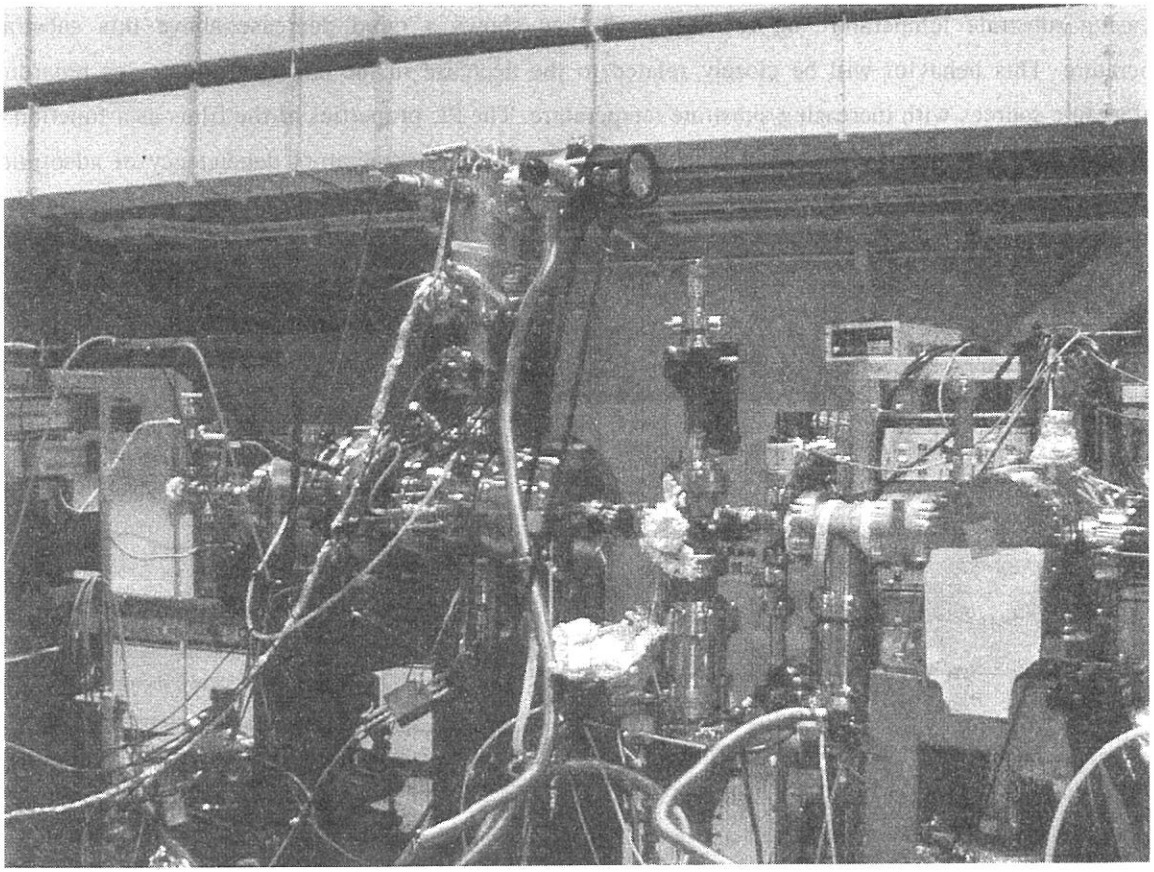

VARTMAN at BL8B1

List of Publication

LIST OF PUBLICTIONS (1999)

H. Aritani, H. Yamada, T. Nishio, S. Imamura, S. Hasegawa, T. Tanaka and S. Yoshida
Formation of Defects in Near-Surface Region over Li or Mn-Doped MgO Studied by Mg K-Edge XANES
Chemistry Letters, (1999) 359.

T. Ejima, K. Ouchi and M. Watanabe
Si-L absorption spectra of Si/CaF_2 and Si/LiF multilayers
J. Electron Spectrosc. Relat. Phenom., **101-103** (1999) 833.

T. Ejima, K. Ouchi and M. Watanabe
Simulation Study of Si-L Total Electron Yield Spectra of Some LiF/Si/LiF Multilayer Using Trial Anisotropic Optical Constants
Jpn. J. Appl. Phys., **38** (1999) Suppl. 38-1, 222.

K. Fukui, R. Hirai, A. Yamamoto, S. Naoe and S. Tanaka
Soft X-ray Absorption Study of III-V Nitrides
Jpn. J. Appl. Phys., **38** (1999) Suppl. 38-1, 538.

H. Hama and M. Hosaka
Longitudinal beam dynamics and FEL interaction on a negative momentum compaction storage ring
Nucl. Instr. and Meth., **A 429** (1999) 172.

Y. Haruyama, K. G. Nath, S. Kimura, Y. Ufuktepe, T. Kinoshita, K. Hiraki and K. Kanoda
Electronic structures of organic salts (DI-DCNQI)$_2$M(M = Cu and Ag) using photoelectron spectromicroscopy
Solid State Commun., **110** (1999) 17.

T. Hatano, W. Hu, K. Saito and M. Watanabe
Faraday rotation measurement around Ni $M_{2,3}$ edges using Al/YB_6 multilayer polarizers
J. Electron Spectrosc. Relat. Phenom., **101-103** (1999) 287.

T. Hatsui, Y. Takata and N. Kosugi
Metal-to-ligand charge transfer bands observed in polarized Ni 2p photoabsorption spectra of $[Ni(mnt)_2]^{2-}$
J. Electron Spectrosc. Relat. Phenom., **101-103** (1999) 827.

T. Hatsui, Y. Takata and N. Kosugi
Strong metal-to-ligand charge transfer bands observed in Ni K- and L-edge XANES of planar Ni complexes
J. Synchrotron Rad., **6** (1999) 376.

T. Hatsui, Y. Takata and N. Kosugi
Polarization Ni K-and L-edge XANES study of $[Ni(III)(mnt)_2]^{1-}$
J. Synchrotron Rad., **6** (1999) 379.

Y. Hikosaka, H. Hattori and K. Mitsuke
Spectator- and participant-like behavior of a Rydberg electron on predissociation of superexcited states of OCS
J. Chem. Phys., **110** (1999) 335.

M. Hosaka, J. Yamazaki and H. Hama
Influences of electron beam properties on spontaneous radiation from an optical klystron
Nucl. Instr. and Meth., **A 429** (1999) 191.

T. Ibuki, K. Okada, T. Gejo and K. Saito
K shell excitations of some organic molecules
J. Electron Spectrosc. Relat. Phenom., **101-103** (1999)149.

Y. Ishii, J. Murakami, and M. Itoh
Optical Spectra of Excitons in Lithium Oxide
J. Phys. Soc. Jpn., **68** (1999) 696.

M. Itoh, Y. Bokumoto and H. Yoshida
Time-Resolved Spectroscopic Studies of Localized Excitons in CsCl:I and CsCl:Br
J. Phys. Soc. Jpn., **68** (1999) 1731.

M. Itoh, J. Murakami and Y. Ishii
Intrinsic Luminescence from Li_2O Crystals Excited in the Exciton-Band Region
Phys. Stat. Sol. (b), **213** (1999) 243.

M. Itoh, H. Nakagawa, M. Kitaura, M. Fujita and D. Alov
Photoluminescence of orthorhombic and cubic PbF_2 single crystals
J. Phys.: Condens. Matter, **11** (1999) 3003.

M. Itoh and N. Ohno
Exciton-Polariton Dispersion of Alkali Bromides Observed with Interference Method
J. Phys. Soc. Jpn., **68** (1999) 2857.

T. Gejo, K. Okada, T. Ibuki and N. Saito
Photodissociation of Ozone in the K Edge Region
J. Phys. Chem. A, **103** (1999) 4598.

M. Kamada, N. Takahashi and S. Hirose
Nanosecond desorption of alkali fluorides excited by synchrotron radiation pulses
J. Electron Spectrosc. Relat. Phenom., **101-103** (1999) 599.

K. Kanda, T. Nagata, T. Ibuki
Photodisscciation of some simple nitriles in the extreme vacuum ultraviolet region
Chem. Phys., **243** (1999) 89.

T. Kawai, E. Takao, S. Shimanuki, M. Iwata, A. Miyashita and Y. Ishibashi
Effect of Phase Transition on the Optical Absorption Edge and Electronic States in Ferroelectric Materials of $(CH_3NH_3)_3M_3Br_9$ (M: Sb, Bi)
J. Phys. Soc. Jpn., **68** (1999) 2848.

N. Kida, N. Ohno, K. Deguchi and M. Kamada
VUV optical spectra of hydrogen-bonded ferroelectrics $PbHPO_4$ and $PbHAsO_4$
J. Electron Spectrosc. Relat. Phenom., **101-103** (1999) 603.

S. Kimura
Infrared Magnetic Circular Dichroism of Strongly Correlated 4f Electron Systems with Synchrotron Radiation
Jpn. J. Appl. Phys., **38** (1999) 392.

S. Kimura, D. Li, Y. Haga and T. Suzuki
Magneto-Optical Study on GdAs in the Intrared Region
Physics of Strongly Correlated Electron Systems JJAP Series 11, (1998) 126.

S. Kimura, K. G. Nath, Y. Haruyama, T. Kinoshita, S. Yoshii and M. Kasaya
Anisotropic optical conductivity of RPtAs (R=La, Ce)
Physica B, **259-261** (1999) 1163.

S. Kimura, H. Okamura, T. Nanba, M. Ikezawa, S. Kunii, F. Iga, N. Shimizu and T. Takabatake
Optical spectra of RB_x (R=rare-earth, x=4,6,12)
J. Electron Spectrosc. Relat. Phenom., **101-103** (1999) 761.

T. Kinoshita, K. G. Nath, Y. Haruyama, M. Watanabe, S. Yagi, S. Kimura and A. Fanelsa
Photoelectron spectromicroscopy experiment at the UVSOR facility
J. Electron Spectrosc. Relat. Phenom., **92** (1999) 165.

N. Kitamura, K. Fukumi, J. Nishii, M. Makihara, T. Sasaki and N. Ohno
High pressure effect on optical properties of cerium ion in fluoroaluminate glass
J. Non-Cryst. Solids, **259** (1999) 68.

M. Kitaura and H. Nakagawa
Thermal Behavior of holes in Lead-Chloride Crystal
Radiation Effects & Defects in Soleds., **150** (1998) 115.

K. Mase, M. Nagasono and S. Tanaka
Mechanism of ion desorption induced by core-electron transitions of condensed molecules and adsorbates studied by electron ion coincidence spectroscopy
J. Electron Spectrosc. Relat. Phenom., **101-103** (1999) 13.

K. Mase and S. Tanaka
An Electron-Ion Coincidence Spectroscopy Study of Ion Desorption Induced by Core-Electron Transition of Surfaces
Jpn. J. Appl. Phys., **38** (1999) Suppl. 38-1, 233.

H. Mekaru, Y. Tsusaka, T. Miyamae, T. Kinoshita, T. Urisu, S. Masui, E. Toyota and H. Takenaka
Construction of the multilayered-mirror monochromator beam line for the study of synchrotron radiation stimulated process
Rev. Sci. Instrum., **70** (1999) 2601.

T. Miyamae, S. Hasegawa, D. Yoshimura, H. Ishii, N. Ueno and K. Seki
Intramolecular energy-band dispersion in oriented thin films of n-$CF_3(CF_2)_{22}CF_3$ observed by angle-resolved photoemission with synchrotron radiation
J. Chem. Phys., **112** (2000) 3333.

T. Miyamae, N. Ueno, S. Hasegawa, Y. Saito, T. Yamamoto and K. Seki
Electronic structure of poly (1,10-phenanthroline-3, 8-diyl) and its K-doped state studied by photoelectron spectroscopy
J. Chem. Phys., **110** (1999) 2552.

T. Miyamae, H. Uchida, I. H. Munro and T. Urisu
Synchrotron-radiation stimulated desorption of SiO_2 thin films on Si(111) surfaces observed by scanning tunneling microscopy
J. Vac. Sci. Technol. A, **17** (1999) 1733.

T. Miyamae, H. Uchida, I. H. Munro and T. Urisu
Direct observation of synchrotron-radiation-stimulated desorption of thin SiO_2 films on Si(111) by scanning tunneling microscopy
Surface Science, **437** (1999) L755.

T. Miyamae, T. Urisu, H. Uchida and I. H. Munro
Scanning Tunneling Microscopy for the Study of the Synchrotron-Radiation Stimulated Processes; Synchrotron-Radiation Stimulated Desorption of SiO_2 Films on Si(111) Surface
Jpn. J. Appl. Phys., **38** (1999) Suppl. 38-1, 249.

S. Nagaoka, K. Mase, M. Nagasono, S. Tanaka, T. Urisu, J. Ohshita and U. Nagashima
Site-specific phenomena in Si:2p core-level photoionization of $X_3Si(CH_2)_n(Si(CH_3)_3$(X=F or Cl, n=0-2) condensed on a Si(111) surface
Chem. Phys., **249** (1999) 15.

T. Nanba, M. Hayashi, I. Shirotani and C. Sekine
Optical response of Pr Ru_4P_{12} due to metal-insulator transition
Physica B, **259-261** (1999) 853.

K. G. Nath, Y. Haruyama, S. Kimura, Y. Ufuktepe and T. Kinoshita
Study of magnetic linear dichroism (MLD) for different thickness of Ni thin film grown on ferromagnetic Co (001) in element specific photoemission
J. Electron Spectrosc. Relat. Phenom., **101-103** (1999) 257.

M. Niibe, A. Miyafuji, H. Kinoshita and T. Watanabe S. Inoue and K. Koterazawa
Fabrication of an aspherical mirror for Extreme Ultra-Violet Lithography (EUVL) optics
Proc. SPIE, **3447** (1998) 32.

M. Nishio, T. Enoki, Q. Guo and H. Ogawa
Growth Characteristics of Homoepitaxilal ZnTe Films Deposited by Synchrotron Radiation Using Metalorganic Sources
Jpn. J. Appl. Phys., **38** (1999) 568.

M. Nishio, T. Enoki, Y. Mitsuishi, Q. Guo and H. Ogawa
Homoepitaxial growth of ZnTe by synchrotron radiation using metalorganic sources
Thin Solid Films, **343-344** (1999) 504.

A. Ohnishi, K. Tanaka and T. Yoshinari
Exciton Self-Trapping in Two-Dimensional System of $(C_2H_5NH_3)_2CdCl_4$ Single Crystal
J. Phys. Soc. Jpn., **68** (1999) 288.

N. Ohno and N. Kida
Optical Study on the Ferroelectric Transition in $PbHPO_4$
Ferroelectrics, **223** (1999) 389.

I. Ouchi, I. Nakai, M. Kamada and S. Tanaka
Excitation Spectra of Polyester Films in the Ultraviolet and Vacuum Ultraviolet Regions
Rep. Progr. Polym. Phys. Jpn., **42** (1999) 467.

I. Ouchi, I. Nakai, M. Kamada, S. Tanaka and T. Gejyo
Structure and Core Electron Absorption Spectra of Polyester Films
Jpn. J. Appl. Phys., **38** (1999) Suppl. 38-1,183.

K. Ozawa, T. Noda, T. Nakane, M. Yamazaki, K. Edamoto and S. Otani
Photoemission study of K adsorption on ZrC(111)
Surface Science, **433** (1999) 700.

K. Ozawa, T. Noda, T. Nakane, K. Edamoto and S. Tanaka
Interaction of oxygen with potassium-covered ZrC(111) surface: photoemission spectroscopy study
Surface Science, **438** (1999) 223.

L. G. M. Pettersson, T. Hatsui and N. Kosugi
Ni 2p-3d photoabsorption and strong charge transfer satellites in divalent Ni complexes with molecular ligands. Evaluation of π-back donation based on the density functional theory approach
Chem. Phys. Lett. **311** (1999) 299.

K. S. Seol, M. Fujimaki, Y. Ohki and H. Nishikawa
Temperature dependence of the lifetime of 4.3-eV photoluminescence in oxygen-deficient amorphous SiO_2
Phys. Rev. B, **59** (1999) 1590.

K. S. Seol, M. Fujimaki, T. Watanabe and Y. Ohki
Effects of ion implantation and thermal annealing on the photoluminescence in amorphous silicon nitride
J. Appl. Phys., **85** (1999) 6746.

K. Shimizu, H. Maeshima, H. Yoshida, A. Satsuma and T. Hattori
Deconvolution Analysis of Cu L-edge XANES for Quantification of Copper (II) Coordinations in Copper-aluminate Catalysts
Jpn. J. Appl. Phys., **38** (1999) Suppl. 38-1, 44.

K. Shimizu, Y. Kato, T. Yoshida, H. Yoshida, A. Satsuma and T. Hattori
Al K-edge XANES study for the quantification of aluminium coordinations in alumina
Chem. Commun., (1999) 1681.

K. Tabayashi, J. Aoyama, M. Matsui, T. Hino and K. Saito
Dissociative excitation of HCOOH by Single-vacumm ultraviolet and two-ultraviolet photon
J. Chem. Phys., **110** (1999) 9547.

Y. Tamenori, B. H. Boo and I. Koyano
Dissociative photoionization of ferrocene in the Fe:3p inner-valence region
J. Electron Spectrosc. Relat. Phenom., **101-103** (1999) 87.

H. Tanaka, M. Takao, K. Soutome, H. Hama and M. Hosaka
A perturbative formulation of nonlinear dispersion for particle motion in storage rings
Nucl. Instr. and Meth., **A 431** (1999) 396.

Y. Takata, T. Hatsui and N. Kosugi
A unified view of resonant photoemission of metallic, molecular, and correlated solid systems
J. Electron Spectrosc. Relat. Phenom., **101-103** (1999) 443.

T. Tsujibayashi, M. Watanabe, O. Arimoto, M. Itoh, S. Nakanishi, H. Itoh, S. Asaka and M. Kamada
Resonant enhancement effect on two-photon absorption due to excitons in alkaline-earth fluorides excited with synchrotron radiation and light
Phys. Rev. B, **60** (1999) 8442.

(Japanese)
H. Aritani and T. Tanaka
Characterization of High Performance Materials by L-edge XANES in Soft X-ray Region
Hyomen, **19** (1998) 314.

M. Kamada
Safety Systems in the UVSOR Facility
J. Jpn. Soc. Synchro. Rad. Res., **12** (1999) 12.

M. Kamada, S. Asaka, T. Tsujibayasahi, O. Arimoto, M. Watanabe, S. Nakanishi, H. Itoh, S. Hirose and M. Itoh
Combination of Synchrotron Radiation and Lasers for Solid-and Surface-Researches
J. Jpn. Soc. Synchro. Rad. Res., **12** (1999) 48.

H. Ogawa, M. Nishio
Homoepitaxial growth of semiconductors with synchrotron radiation
Synchrotron Radiation and Industry, **81** (1999) 19.

Y. Uchimato and T. Yao
Electronic Structure of Cathode Materials for 5V Lit hium Ion Batteries
Material Integration, **12** (1999) 43.

Work Shops

UVSOR Workshop VI

"Current Status of Atomic and Molecular Science using Synchrotron Radiation and its future view at UVSOR"

13 and 14 March, 2000

13 Mar. (Mon) 13:00-19:00 (coffee break included)

<First half> Chair and discussion leader: **N. Kosugi (IMS)**

1. Present status of photochemical and molecular spectroscopic investigations at HiSOR

   A. Hiraya (Hiroshima Univ.)

2. Studies on dynamics of core excited atoms and molecules at ETL

   I.H. Suzuki (ETL)

3. Two-dimensional photoelectron spectroscopy of multi-atomic molecules; vibration and dissociation of excited molecules

   K. Mitsuke (IMS)

<Second half> Chair and discussion leader: **E. Shigemasa (IMS)**

1. Photoion spectroscopy for molecular targets in their valence excitation regions at UVSOR

   T. Masuoka (Osaka City Univ.)

2. Photoelectron spectroscopy using circularly polarized radiation at PF

   K. Soejima (Niigata Univ.)

3. Current status of the soft x-ray photochemical beamline at Spring-8 and future plans

   H. Ohashi (JASRI)

4. Photodissociation dynamics of ozone

   T. Gejo (IMS)

14 Mar. (Tue) 9:00-15:00 (coffee break included)

<Morning session> Chair and discussion leader: **E. Shigemasa (IMS)**

1. Studies on atomic and molecular inner-shell excitations and their subsequent processes, utilizing Spring-8 and PF

   K. Ueda (Tohoku Univ.)

2. Present status of studies on atomic and molecular physics at PF

J. Adachi (PF)

3. New electron spectroscopy for realizing resolutions with sub-natural widths

K. Ito (PF)

<Afternoon session> Chair and discussion leader: **N. Kosugi (IMS)**

1. Dynamics and spectroscopy of superexcited molecules; experiments at PF

N. Kochi (Tokyo Institute Tech.)

2. Inner-shell excitations in large molecules

T. Ibuki (Kyoto Univ. Education)

Appendix

ORGANIZATION

Director		
Nobuhiro Kosugi	Professor	kosugi@ims.ac.jp
Accelerator Division		
Masahiro Katoh	Associate Professor	mkatoh@ims.ac.jp (Mar. 2000-)
Hiroyuki Hama	Associate Professor	hama@ims.ac.jp (-Mar. 2000)
Masahito Hosaka	Research Associate	hosaka@ims.ac.jp
Shigeru Kouda	Research Associate	kouda@ims.ac.jp
Toshio Kinoshita	Unit Chief Engineer	kinoshita@ims.ac.jp
Jun-ichiro Yamazaki	Engineer	yamazaki@ims.ac.jp
Beamline Division		
Masao Kamada	Associate Professor	kamada@ims.ac.jp
Eiji Shigemasa	Associate Professor	sigemasa@ims.ac.jp (May. 99-)
Shin-ichiro Tanaka	Research Associate	stanaka@ims.ac.jp(-Oct. 99)
Tatsuo Gejo	Research Associate	gejo@ims.ac.jp
Kazutoshi Takahashi	Research Associate	ktakahashi@ims.ac.jp(Apr. 2000)
Osamu Matsudo	Section Chief Engineer	mastudo@ims.ac.jp
Masami Hasumoto	Unit Chief Engineer	hasumoto@ims.ac.jp
Tadanori Kondo	Engineer	kondo@ims.ac.jp
Suekichi Matsuo	Supporting Engineer	mastuo@ims.ac.jp
Bunichi Kamimoto	Supporting Engineer	kamimoto@ims.ac.jp
Guest Scientist		
Shin-ichi Kimura	Associate Professor	skimura@kobe-u.ac.jp (Apr. 99-)
Sam Dylan More	JSPS Research Fellow	more@ims.ac.jp
Secretary		
Hisayo Hagiwara		hagiwara@ims.ac.jp
Naoko Onitake		onitake@ims.ac.jp
Graduate Students		
Senku Tanaka		senku@ims.ac.jp (Apr.2000-)

STEERING COMMITTEE

(April 1998 – March 1999)

Nobuhiro Kosugi	UVSOR IMS	Chairperson
Masao Kamada	UVSOR IMS	
Hiroyuki Hama	UVSOR IMS	
Eiji Shigemasa	UVSOR IMS	
Tatsuhisa Katoh	IMS	
Masaaki Fujii	IMS	
Hayao Kobayashi	IMS	
Tsuneo Urisu	IMS	
Makoto Watanabe	Tohoku Univ.	
Yukihide Kamiya	Univ. of Tokyo	
Takatoshi Murata	Kyoto Univ. of Edu.	
Yasuo Udagawa	Tohoku Univ.	
Keiichiro Nasu	KEK	
Takao Nanba	Kobe Univ.	
Ken-ichiro Tanaka	Hiroshima Univ.	

JOINT STUDIES

(Financial Year 1999)

Special Projects	:1
Cooperative Research Projects	:17
Invited Research Projects	:2
Use-of-UVSOR Projects	:147
Workshop	:1
Machine Time for Users	:36 weeks

UVSOR staffs

Plane view of the UVSOR Facility

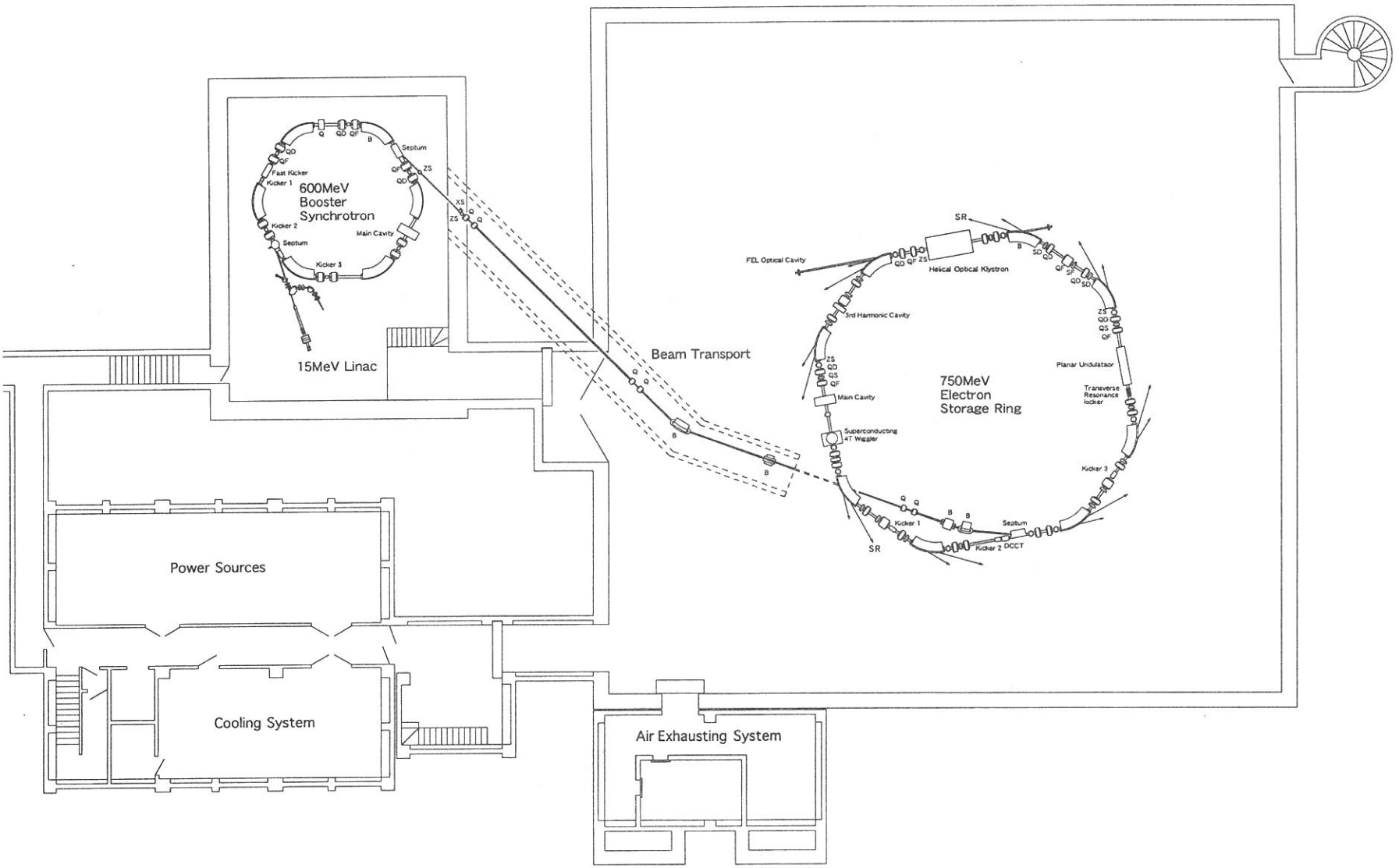

Storage Ring Room

Location

Ultraviolet Synchrotron Orbital Radiation (UVSOR) is located at Okazaki.Okazaki (population 320,000) is 260km southwest of Tokyo, and can be reached within 3 hours from Tokyo via the Tokaido Shinkansen and the Meitetsu line.

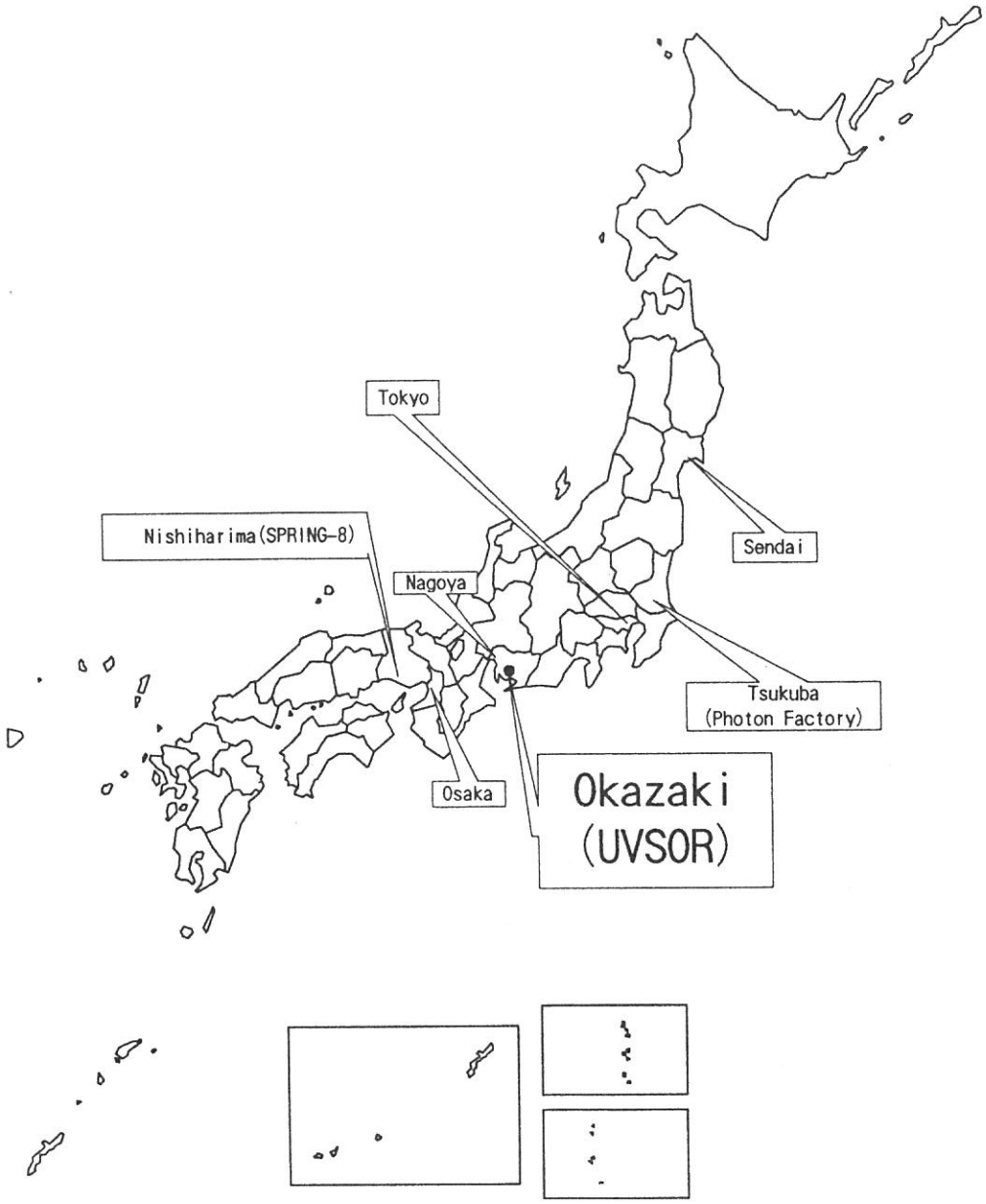

ADDRESS

UVSOR Facility
Institute for Molecular Science
Myodaiji, Okazaki, 444-8585, JAPAN

PHONE: +81-564-55-7402(Secretary)
+81-564-52-6101
FAX:+81-564-54-7079
Telex 4537475 KOKKEN J (IMS)
Homepage: http://www.uvsor.ims.ac.jp/